Res Electricae Magdeburgenses

MAgdeburger FOrum zur Elektrotechnik

Interaction of converter-interfaced components and other grid components can introduce wide-frequency range of resonances, thus induce massive harmonic distortions and even endanger system stability. Their consequences might be the tripping of renewable and conventional generation units or the physical damage of sensitive grid assets. Motivated by recent years' resonance incidents in wind-integrated power systems, this study investigates the resonance-induced harmonic distortion and stability issues in HVDC connected DFIG-based OWF. The objective of this study is to accurately characterize the resonances, evaluate their risks and provide solutions for the design of mitigation strategy.

To accurately capture the dynamic characteristics of DFIG-based wind farm, a comprehensive wind farm impedance model considering detailed converter control dynamics and wind farm grid topology is developed, aggregated and validated suitable for wide band resonance analysis.

On this basis, both Bode-plot method and RMA approach have been adopted to address the resonance issues taking into account various wind farm operating conditions. Their impacts on resonance frequency, harmonic amplification and damping level are investigated. The locations where resonances can be most easily excited are identified through bus participation factor analysis. Moreover, the impact of the frequency-coupling effects from asymmetrical converter control and PWM switching process on SSR, middle- and high-frequency resonances is analyzed using the aggregated models derived from a practical HVDC connected DFIG-based OWF. Large harmonic distortion and stability issues are demonstrated for the frequency range from several Hz to a few kHz.

In order to prevent the negative impact of resonances on power quality and system stability, a series of active damping possibilites have been studied and implemented in the studied wind-integrated power system, and a coordinated damping strategy which can effectively damp wideband resonances is proposed. Finally, simulations in MATLAB/Simulink validate the results of impedance modelling, resonance analysis as well as the effectiveness of the wideband resonance damping strategy.

ISSN 1612-2526
ISBN 978-3-948749-05-7
DOI 10.24352/UB.OVGU-2021-061

Yonggang Zhang: Analysis and Control of Resonances in HVDC Connected OWF

MAFO 84

Yonggang Zhang

Analysis and Control of Resonances in HVDC Connected DFIG-based Offshore Wind Farm

Magdeburg 2021

MAFO
Band 84

Res Electricae Magdeburgenses
MAgdeburger FOrum zur Elektrotechnik

Analysis and Control of Resonances in HVDC Connected DFIG-based Offshore Wind Farm

Dissertation

zur Erlangung des akademischen Grades

Doktoringenieur
(Dr.-Ing.)

von M. Sc. Yonggang Zhang
geb. am 04.07.1983 in Hebei, China

genehmigt durch die Fakultät für Elektrotechnik und Informationstechnik der Otto-von-Guericke-Universität Magdeburg

Gutachter: Prof. Dr.-Ing. habil. Martin Wolter
Prof. Dr.-Ing. Krzysztof Rudion

Promotionskolloquium am 26. Mai 2021

MAFO
Band 84

Res Electricae Magdeburgenses

Magdeburger Forum zur Elektrotechnik, Jg. 19, Band 84, 2021

http://www.mafo.ovgu.de/

Impressum

Herausgeber:

- Prof. Dr.-Ing. Andreas Lindemann, Lehrstuhl für Leistungselektronik, Institut für Elektrische Energiesysteme
- Prof. Dr.-Ing. habil. Martin Wolter, Lehrstuhl für Elektrische Netze und Erneuerbare Energie, Institut für Elektrische Energiesysteme
- Prof. Dr. rer. nat. Georg Rose, Lehrstuhl für Medizinische Telematik/Medizintechnik, Institut für Medizintechnik
- Prof. Dr.-Ing. Ralf Vick, Lehrstuhl für Elektromagnetische Verträglichkeit, Institut für Medizintechnik

Gründungsherausgeber:

- Prof. Dr. rer. nat. habil. Jürgen Nitsch
- Prof. Dr.-Ing. habil. Zbigniew Antoni Styczynski

alle: Otto-von-Guericke-Universität Magdeburg
Postfach 4120, 39016 Magdeburg

V.i.S.d.P.:

Dr.-Ing. Yonggang Zhang
Otto-von-Guericke-Universität Magdeburg, Postfach 4120, 39106 Magdeburg

1. Auflage, Magdeburg, Otto-von-Guericke-Universität, 2021
Zugl.: Magdeburg, Univ., Diss., 2021

Auflage: 50

Redaktionsschluss: Juni 2021

ISSN: 1612-2526
ISBN: 978-3-948749-05-7
DOI: 10.24352/UB.OVGU-2021-061

Bezug über die Herausgeber

Druck: docupoint GmbH
Otto-von-Guericke-Allee 14, 39179 Barleben

Declaration of Honor

„I hereby declare that I produced this thesis without prohibited external assistance and that none other than the listed references and tools have been used. I did not make use of any commercial consultant concerning graduation. A third party did not receive any nonmonetary perquisites neither directly nor indirectly for activities which are connected with the contents of the presented thesis.

All sources of information are clearly marked, including my own publications.

In particular I have not consciously:

- Fabricated data or rejected undesired results
- Misused statistical methods with the aim of drawing other conclusions than those warranted by the available data
- Plagiarized data or publications
- Presented the results of other researchers in a distorted way

I do know that violations of copyright may lead to injunction and damage claims of the author and also to prosecution by the law enforcement authorities. I hereby agree that the thesis may need to be reviewed with an electronic data processing for plagiarism.

This work has not yet been submitted as a doctoral thesis in the same or a similar form in Germany or in any other country. It has not yet been published as a whole."

Magdeburg, Oct. 26, 2020

Yonggang Zhang

I Abstract

Interactions among the widely utilised converter-interfaced grid components and passive grid components can introduce wide-frequency range of resonances, thus induce massive harmonic distortions and even endanger system stability. Their consequences might be the tripping of renewable and conventional generation units or the physical damage of sensitive grid assets. Motivated by recent years' resonance incidents in wind-integrated power systems, this study investigates the resonance-induced harmonic distortion and stability issues in doubly fed induction generator (DFIG)-based offshore wind farm (OWF) with high-voltage direct current (HVDC) grid connection. The objective of this study is to accurately characterize the resonances, evaluate their risks and provide solutions for the design of mitigation strategy.

To accurately capture the dynamic characteristics of DFIG-based wind farm, a comprehensive impedance modelling considering the detailed PI control loop and DC dynamics of wind turbine as well as the cable connections of the medium-voltage (MV) collector system is conducted. Through stepwise simulation verifications, aggregated modelling of MV collector system is proved to be suitable for wideband resonance analysis.

On this basis, both Bode-plot method and resonance mode analysis (RMA) approach have been adopted to address the resonance issues taking into account various wind farm operating conditions and grid topology changes. Their impacts on resonance frequency, harmonic amplification level and damping level are investigated. The locations where resonances can be most easily excited are identified through bus participation factor analysis. Moreover, the impact of the frequency-coupling effects from asymmetrial converter control and switching operations on subsynchronous resonance (SSR), middle- and high-frequency resonances is analyzed using the aggregated models derived from a practical HVDC connected DFIG-based OWF. Large harmonic distortion and stability issues are demonstrated for the frequency range from several Hz to a few kHz.

In order to prevent the negative impact of resonances on power quality and system stability, a series of active damping possibilites have been studied and implemented in the studied wind-integrated power system, and a coordinated damping strategy which can effectively damp wideband resonances is proposed.

Finally, simulations in MATLAB/Simulink validate the results of impedance modelling, resonance analysis as well as the effectiveness of the wideband resonance damping strategy.

II Kurzfassung

Wechselwirkungen zwischen den weit verbreiteten wechselrichtergekoppelten Netzkomponenten und den passiven Netzkomponenten können einen breiten Frequenzbereich von Resonanzen aufweisen, wodurch massive harmonische Verzerrungen hervorgerufen und sogar die Systemstabilität gefährdet werden. Ihre Folgen könnten die Trennung erneuerbarer und konventioneller Stromerzeuger vom Netz oder die physische Beschädigung empfindlicher Netzanlagen sein. Motiviert durch die Resonanzereignisse der letzten Jahre in windintegrierten Stromversorgungssystemen, untersucht diese Dissertation die resonanzinduzierten harmonischen Verzerrungs- und Stabilitätsprobleme in einem Offshore-Windpark (OWF) mit doppelt gespeisten Asynchrongeneratoren (DFIG) und Netzanschluss mittels Hochspannungsgleichstromübertragung (HGÜ). Ziel dieser Dissertation ist es, die Resonanzen genau zu charakterisieren, ihre Risiken zu bewerten und Lösungen für die Gestaltung der Minderungsstrategie bereitzustellen.

Um die dynamischen Eigenschaften eines DFIG-basierten Windparks genau zu erfassen, wird eine umfassende Impedanzmodellierung unter Berücksichtigung des detaillierten PI-Regelkreises und der Gleichstromdynamik der Windkraftanlage sowie der Kabelverbindungen des Mittelspannungskollektorsystems (MV) durchgeführt. Durch schrittweise Simulationsüberprüfungen hat sich die aggregierte Modellierung des MV-Kollektorsystems für die Breitbandresonanzanalyse als geeignet erwiesen.

Auf dieser Grundlage wurden sowohl die Bode-Plot-Methode als auch der Ansatz der Resonanzmodusanalyse (RMA) angewendet, um die Resonanzprobleme unter Berücksichtigung verschiedener Betriebsbedingungen des Windparks und Änderungen der Netz-Topologie anzugehen. Ihre Auswirkungen auf die Resonanzfrequenz, die harmonische Verzerrungen und die Dämpfungen zu Resonanzen werden untersucht. Die Orte, an denen Resonanzen am einfachsten angeregt werden können, werden durch die Busbeteiligungsfaktoranalyse identifiziert. Darüber hinaus wird der Einfluss der Frequenzkopplungseffekte von Steuerungs- und Schaltvorgängen für asymmetrische Wandler auf subsynchrone Resonanz- (SSR), Mittel- und Hochfrequenzresonanzen unter Verwendung der aggregierten Modelle analysiert, die aus einem praktischen HGÜ-verbundenen DFIG-basierten OWF abgeleitet wurden. Für den Frequenzbereich von mehreren Hz bis zu einigen kHz werden große harmonische Verzerrungs- und Stabilitätsprobleme gezeigt.

Um den negativen Einfluss von Resonanzen auf die Stromqualität und die Systemstabilität zu verhindern, wurde eine Reihe aktiver Dämpfungsmöglichkeiten untersucht und in das untersuchte windintegrierte Stromnetz implementiert, und es wird eine koordinierte Dämpfungsstrategie vorgeschlagen, mit der Breitbandresonanzen effektiv gedämpft werden können.

Schließlich validieren Simulationen in MATLAB / Simulink die Ergebnisse der Impedanzmodellierung, der Resonanzanalyse sowie die Wirksamkeit der Breitbandresonanzdämpfungsstrategie.

III Table of Contents

IV List of Figures

V List of Tables

VI List of Symbols

R	resistance
L	inductance
C	capacitance
G	conductance
Z	impedance
Y	admittance
P	active power
Q	reactive power
S	apparent power
h	harmonic order
$\underline{s}$	Laplace operator
i	instantaneous current
u	instantaneous voltage
p	instantaneous active power
J	total moment of inertia of the rotating masses
m_d, m_q	d-axis and q-axis components of the modulation index
i_d, i_q	d-axis and q-axis components of three-phase currents
u_d, u_q	d-axis and q-axis components of three-phase voltages
k_p, k_i	proportional and integral coefficients of a PI controller
f_sw , ω_sw	switching frequency and switching angular frequency
f_s , ω_s	sampling frequency and sampling angular frequency
T_s , T_d	sampling period and time delay
T_e, T_m	electrical torque, mechanical torque
$\underline{\boldsymbol{T}}_\mathrm{M}$	transformation matrix for symmetrical components
$\underline{\boldsymbol{Y}}_\mathrm{NN}$	nodal admittance matrix
$\underline{\boldsymbol{Y}}_\mathrm{M}$	modal admittance matrix
$\underline{\boldsymbol{Z}}_\mathrm{NN}$	nodal impedance matrix
$\underline{\boldsymbol{Y}}_\mathrm{M}$	modal impedance matrix
N, $\underline{N}$	turn ratio and equivalent turn ratio taking into account phase shifting
$\boldsymbol{E}$	identity matrix
$\underline{H}$	transfer function
$\underline{\boldsymbol{H}}$	transfer function matrix

Greek symbols

α	rotation of 120°
θ	phase angle
θ_1	phase angle of grid voltage
θ_{PLL}	phase angle of phase-locked loop
θ_r	rotor phase angle
ω	angular frequency
ω_1	fundamental angular frequency
ϕ	initial phase angle
θ_{diff}	equivalent phase shifting of three-phase transformer
ψ	flux
δ	magnetic flux leakage coefficient of induction machine

Subscripts

a, b, c	variables of phase a, b and c
d, q	d-axis and q-axis variables under synchronous reference frame
1, 2, 0	symmetrical components
p, n	positive-sequence perturbation and its coupled frequency component
s, r	stator and rotor of a generator
A, B	terminals of a series component such as cable or transformer
m	magnetizing branch
W	transformer winding
E	earthing
u, i	voltage and current

Superscripts

s	system dq frame
c	controller dq frame
*	conjugation of complex value
ref	reference control value
'	referred parameter of a transformer
T	matrix transposition

VII List of abbreviations

AC	Alternating Current
AD	Active Damper
APF	Active Power Filter
DC	Direct Current
DFIG	Doubly-fed Induction Generator
EMT	Electromagnetic Transient
FFT	Fast Fourier Transformation
FLL	Frequency-locked Loop
FSC	Fixed Series Compensation
GSC	Grid Side Converter
GSVSC	Grid Side VSC
HF	High Frequency
HVDC	High Voltage Direct Current
LC	Inductive-Capacitive
LV	Low Voltage
LF	Low Frequency
MV	Medium Voltage
MF	Middle Frequency
MMC	Modular Multilevel Converter
MPPT	Maximum Power-Point Tracking
OWF	Offshore Wind Farm
PMSG	Permanent Magnet Synchronous Generator
P-ANF	Pre-filtered Adaptive Notch Filter
PLL	Phase-locked Loop
PCC	Point of Common Coupling
PoC	Point of Connection
PWM	Pulse Width Modulation
PF	Participation Factor
PI	Proportional-Integral
PR	Proportional-Resonant
PV	Photovoltaic
R-APF	Resistive-Active Power Filter
RSC	Rotor Side Converter
RMA	Resonance Mode Analysis

SSR	Sub-synchronous Resonance
SCR	Short Circuit Ratio
SRF	Synchronous Reference Frame
STATCOM	Static Synchronous Compensator
THD	Total Harmonic Distortion
VSC	Voltage Source Converter
WT	Wind Turbine
WFVSC	Wind Farm side VSC
WPP	Wind Power Plant

1 Introduction

1.1 Background and Motivation

Over the last decade, many offshore wind farms (OWFs) have been developed and integrated into power grids through voltage source converter based high voltage direct current (VSC-HVDC) transmission systems in the North and Baltic Seas, particularly in the power systems of Denmark, Germany, UK and Netherlands [1]. The newly developed VSC-HVDC links typically have the voltage level of ±320 kV, and transmission capacity of no less than 900 MW, which allows the integration of two or more OWFs [2]. In China, a multi-terminal ±500 kV VSC-HVDC transmission system with the capacity up to 3 GW has been constructed for the integration of several geographically distributed renewable energy sources, which includes wind farms and photovoltaic (PV) plants [3]. The increased complexity of such grid integration configurations and their flexible operation and control can cause resonance-induced power quality and stability issues.

Moreover, due to the ever-growing capacity of single wind turbine (WT) and the increasing size of newly installed OWF, the lengthy WT collecting cables introduce large aggregated capacitance effect and creates the conditions for the formation of inductive and capacitive (LC) resonance circuits. For the application of HVDC connected OWF employing doubly-fed induction generator (DFIG) based wind turbines (WTs), the interaction between DFIG-based WT and HVDC converter can also induce poor damped subsynchronous resonance (SSR) due to the induction generator effect (IGE) and subsynchronous control interaction (SSCI) [4].

Regarding the various grid integration configurations and OWF operating conditions, the stimulation of the possible resonances may cause unacceptable harmonic distortions as stipulated by IEEE Std 519-2014 [5] or IEC/TR 61000-3-6 2008 [6], or incur instability when under poor or negative damping conditions. Possible consequences are the harmonic pollution of grids, the deterioration of WT operating environments, the extra consumed harmonic power losses, the tripping of WTs, blocking of HVDC converter, or physical damages of sensitive grid components. Field experiences on such issues have been reported in [7]-[9].

1.2 Status of Resonance Study and Contribution of this Work

Resonance issues in converter-interfaced power systems have attracted intentions in industry and academia for years. In case of HVDC connected OWF, DFIG-based WTs are prone to SSR due to the LC interaction at SSR frequencies [10], and the damping of the SSR in the system is typically low or negative due to the negative resistance induced by the negative slip ratio of the induction generator and converter controls [11]. For large-scale OWFs, the widely distributed WT collecting cables have large cumulative capacitive effect, thus strongly participate in the resonances at hundreds or thousands of Hz [12]. Note, that the risk of above resonances is susceptible to the variation of grid topology and operating conditions [13], [14], comprehensive study is required to prevent the occurance of large harmonic distortion and stability issues.

On the resonances in wind-integrated power systems, the sub-synchronous resonance (SSR), middle- and high-frequency resonances (typically at the frequency range from one or several hundred Hz to a few kHz) between DFIG-based wind farm and AC grids, as well as the SSR between full-converter based wind farm and HVDC system have been intensively studied in recent years [15]-[19]. The used AC grids are usually series-compensated grids or weak grids. Additionally, the resonances between DFIG-based OWF and HVDC grid connection are investigated in [10], [12], [20], [21]. However, all the above studies that are related to DFIG-based WT have at least one of the following model simplifications: (1) simplified DFIG impedance model ignoring the converter outer loop control and DC side dynamics; (2) simple single-machine wind farm model without considering the internal cable connections; (3) aggregated wind farm model neglecting the capacitance effect of the collecting cables. These modeling simplifications made to DFIG-based wind farm are unfavorable of the accurate identification of the resonances in the large-scale DFIG-based OWF with tens of widely distributed WTs.

As for the impedance modelling of DFIG-based WT, most recent publications either have not incorporated the detailed double-loop PI control or neglect the DC side dynamics [22]-[24], which makes them incapable of capturing the exact low-frequency impedance responses of DFIG-based wind energy conversion system [25]. Additionally, the frequency coupling between the sequence impedances of DFIG-based WT are often neglected in stability analysis [10], [26], [27], which can lead to wrong judgement in the assessment of SSR stability [23], [25]. In order to accurately evaluate the risks of resonances for a wide frequency range, this thesis derives a detailed impedance model of DFIG-based WT taking into account of all relevant control dynamics. Unlike the impedance model derived in [25], where the dq frame impedances are linearly

transformed to modified sequence impedances, as defined in [28], this paper transforms the dq frame impedances to the real sequence impedances through both linear transformation and frequency shifting. Moreover, the more commonly applied outer-loop control with rotor speed PI controller [29], [30] instead of active power PI controller [25] is adopted in this paper.

Regarding the large number of WTs in modern OWFs, aggregated single-machine model is usually adopted for wind farms, and the most widely used aggregation model is based on the equivalent power loss or voltage drop aggregation technique [31], [32]. Additionally, detailed impedance models of wind farms are built according to the series and parallel circuit theories in [33], [34]. However, for a large-scale wind farm with tens of WTs, its wideband impedance characteristic can hardly be directly validated through electromagnetic transient (EMT) simulations due to the huge computational burden, thus a method for the convenient simulation validation of wind farm impedance model is needed. To tackle this issue, a stepwise simulation validation approach is proposed [35].

Based on the impedance modellings of DFIG-based OWF with HVDC connection, this thesis furtherly analyzes the resonances in the frequency-coupled multi-input multi-output (MIMO) system using the equivalent single-input single-output (SISO) sequence component systems. The Bode-plot method is applied to study resonances at the point of common coupling (PCC), which requires equalizing a system into load and source subsystems [36][37]. Since the severest harmonic distortion can occur at any bus of a system, simply investigating the PCC condition is obviously not in favor of identifying resonance source and developing mitigation strategies [38]. Therefore, this work also adopts the impedance network method, i.e. resonance mode analysis (RMA), to address the resonance issues related to wind speed variation and grid topology change. The locations where resonances can be most easily excited are identified through bus participation factor analysis [39]. Additionally, traditional impedance-based RMA only evaluates the amplitudes of modal impedances, this work also uses the damping information embedded in the angle or real part value of the modal impedances in assessing harmonic stability [10].

Facing the challenges of the emerging resonance issues, a bunch of mitigation strategies have been proposed, of which active damping strategies [40]-[43] are more preferred than passive damping solutions [44], [45] due to the prevention of extra power losses. For the resonance damping in HVDC connected DFIG-based OWF, the methods of optimal design of controller parameters, adding extra signal filters in existing control loops, or adding extended control paths are implemented either in HVDC converter [40], [41] or in WT converters [42], [43]. However, the proposed damping solutions are typically

intended to be effective in part of the frequency range that resonance may occur, an adaptive damping scheme suited for the wideband resonances has not been studied in sufficient detail up to now. To bridge this gap, a coordinated resonance damping strategy which utilises both the damping capability of HVDC converter (and or DFIG-based WT) and extra active dampers is proposed to mitigate the wideband resonances ranging from several Hz to a few kHz.

1.3 Objective and Structure of the work

In this dissertation, models for passive grid components, converter-interfaced components and wind-integrated power systems will be developed for resonance analyses. Using these models, the mechanisms of resonance-induced power quality and system stability issues in HVDC connected DFIG-based OWF will be clarified, and based on which, control strategies for mitigating harmonic distortion and improving system stability shall be developed. Partial results of the present work were published in advance in [10], [12], [35], [46].

The rest of the dissertation is organized as follows:

Chapter 2 presents the challenges, fundamental concepts and analysis methods of resonances. Main features of the emerging resonances in modern converter-dominated power systems are presented. Different resonance analysis methods are presented and compared.

Chapter 3 presents the small-signal impedance modelling for the involved grid components in HVDC connected DFIG-based OWF, which mainly includes cables, transformers, DFIG-based WTs and HVDC converter.

In Chapter 4, aggregated modelling of the wind farm collector system is investigated through a comparative study of several aggregation methods, and the suitability of using aggregated collector system models in resonance analysis is assessed through stepwise simulation validations.

In Chapter 5, resonances in a 400 MW DFIG-based OWF with a ±150 kV VSC-HVDC grid connection are analyzed using both the Bode plot and the RMA methods, and the impact of the sideband harmonics of the fundamental frequencey and PWM switching frequency are evalutated.

In Chapter 6, several damping possibilities suited for the application of DFIG-based OWF with HVDC connection are presented, and a coordiated resonance damping strategy is proposed for solving the harmonic distortion and stability issues.

Chapter 7 presents cases studies on how modelling deepness, the variation of wind farm operating condition and the change of switching states of system components influence the resonances of a HVDC connected OWF, and furtherly, the damping capabilities of converter-interfaced components and the proposed coordinated damping strategy are validated through simulations.

Chapter 8 concludes the dissertation and presents some future work.

2 Phenomena, Concepts and Analysis Methods of Resonances

This chapter presents the field experiences, concepts, main features and analysis methods of resonances. An overview of the real-world resonance incidents is firstly presented, then the concepts of resonances as well as the new features of resonances in emerging converter-dominated power systems are presented, which are followed by the description of the symmetrical component theory for analyzing three-phase power systems, and finally several widely adopted resonance analysis methods in recent years are compared.

2.1 Overview of Real-World Resonance Events

Over the last decade, a series of resonance incidents involving wind farm or HVDC transmission have been reported in power systems. The resonance incidents are featured with wide range of frequencies due to the multi-timescale dynamic interactions between converter-interfaced components and passive grid components. In this section, an overview of the resonance incidents occurred in various applications are presented.

2.1.1 Incidents in Wind-Integrated AC grid

In 2009, an around 20 Hz SSR incident induced by the interaction of two DFIG-based wind farms and a transmission line with fixed series-compensation (FSC) occurred in ERCOT power system, resulting a large number of wind turbines tripped out and the damage of crowbar circuits. The occurrence of the event is illustrated in Figure 2.1.

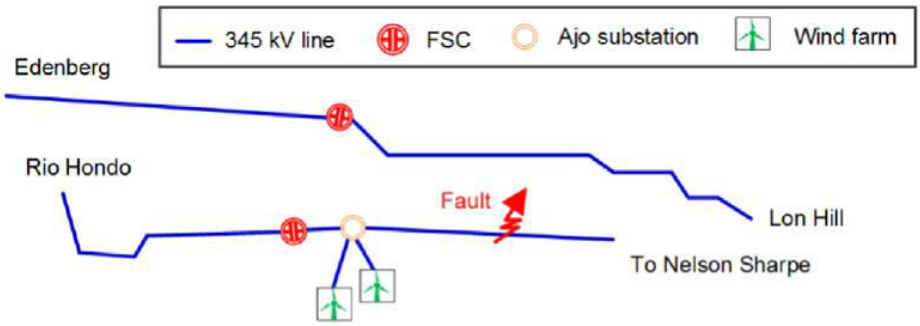

Figure 2.1 The event occured in ERCOT power system, Texas, USA in 2009 [4]

Along with the outage of the 345 kV line between To Nelson Sharpe substation and Ajo substation, where the two type-3 wind farms are integrated into grid, the wind power is only transmitted to the grid through the line from Ajo substation to Rio Hondo substation. As a result, the effective series compensation level of the transmission lines is increased and the induced sub-synchronous control iteraction (SSCI) between wind farms and the grid causes the current and voltage oscillations as shown in Figure 2.2.

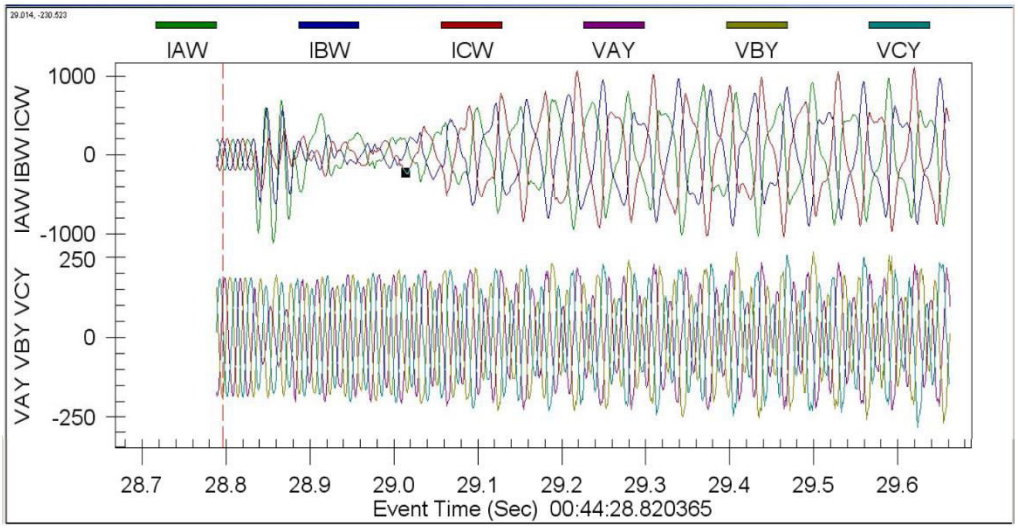

Figure 2.2 Recording of the sub-synchronous event in ERCOT power system in 2009 [47]

Since 2010, hundreds of SSRs in the frequency range of 3-10 Hz have occurred between the DFIG-dominated wind farms in Hebei Guyuan area and their series-compensated grid connections in Jibei region (China), resulting the trip-out of thousands of wind turbines. The Guyuan wind-integrated power system is shown in Figure 2.3.

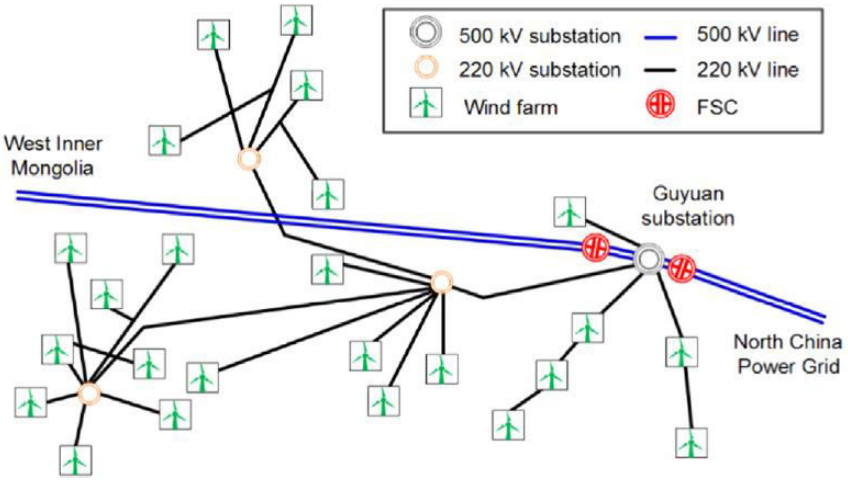

Figure 2.3 Hebei Guyuan wind-integrated power system, China [4]

The recorded active power waveform of a SSR incident occurred in 2013 is shown in Figure 2.4. As observed, the resonance firstly grew rapidly and then a large number of wind turbines were tripped off. Finally the resonance was stopped by bypassing the series compensation capacitor after lasted around 2 minutes. In this incident, about 145 MW power was lost.

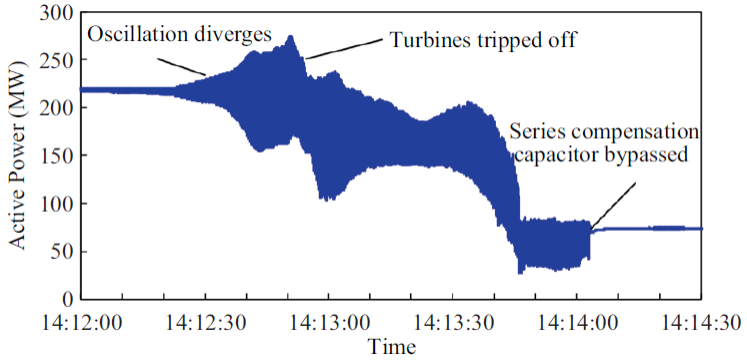

Figure 2.4 The power oscillation recording of a wind farm in Guyuan, China in 2013 [48]

In 2015, the Permanent Magnet Synchronous Generator (PMSG)-based wind farms and their grid connections without series-compensated lines in Xinjiang Hami area experienced an SSR incident, resulting the action of the torsional oscillation protection of a thermal generator and the trip out of the generation unit located 200 km away [49].

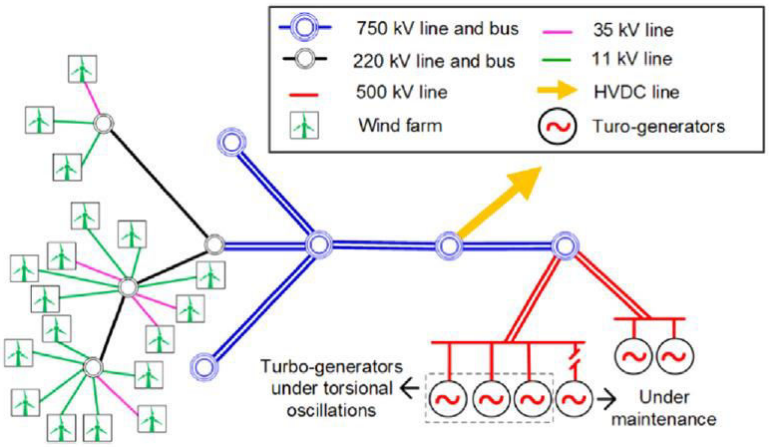

Figure 2.5 Xinjiang Hami wind-integrated power system, China [4].

The involved wind-integrated power system is shown in Figure 2.5. In the left side, the installed wind capacity at two of the three 220 kV substations reaches 1100 MW, causing the SCRs of these substations drop down to 1.3. As a result, the interaction of the type-4 wind farms and the weak grid connections introduces a SSR mode in the frequency range of 17-23 Hz. With the frequency variation of the SSR as illustrated by the blue curve in

Figure 2.6, in the time period of 11:50-11:55, the PMSG-grid SSR frequency matched with one of the thermal plant's shaft modes as illustrated by the red and green dotted lines, resulting in the shaft torsional vibration and the tripping of the generation unit.

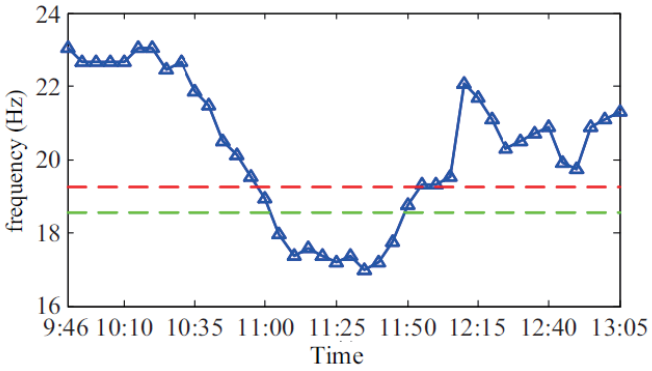

Figure 2.6 The SSR and torsional frequencies of the Xinjiang Hami incident in 2015 [48]

Besides, around 8.5 Hz SSR accidents occurred in a direct-drive PMSG-based OWF with weak grid connection in England as the power export of the OWF increased [8]. In 2017, several SSR incidents in the frequncy range of 20-30 Hz occurred again in ERCOT and all are related to DFIG-based WPPs with series-compensated grid connections and N-1 contigencies [50].

2.1.2 Incidents in Wind-Integrated HVDC grid

In 2011, the MMC-HVDC connected Shanghai Nanhui wind farm was put into operation. In the field tests, the interconnected system worked stably when the feed-in power of the wind farm was low. However, as the feed-in power of the wind farm increased, the system experienced multiple times of voltage and current oscillations, resulting in the shutdown of all the 11 wind turbines, and in the most serious cases, the converters of some wind turbines were damaged [51] [52].

In 2013, an around 250 Hz resonance occurred between the BARD Offshore1 OWF (400 MW) and its two-level VSC-based HVDC grid connection (BorWin1) in German North Sea. The harmonic current reached 40% of the fundamental component (see Figure 2.7), resulting the explosion of the filtering capacitor in the sending end HVDC converter station. The whole wind farm had been shut down for up to 10 months, causing enormous economic losses. Additionally, in German North Sea, another around 450 Hz resonance occurred in the MMC-HVDC integration of two PMSG-based OWFs during the period

of connecting a wind farm into the grid while the other wind farm is already connected to the grid. The recorded voltage waveform is shown in Figure 2.8.

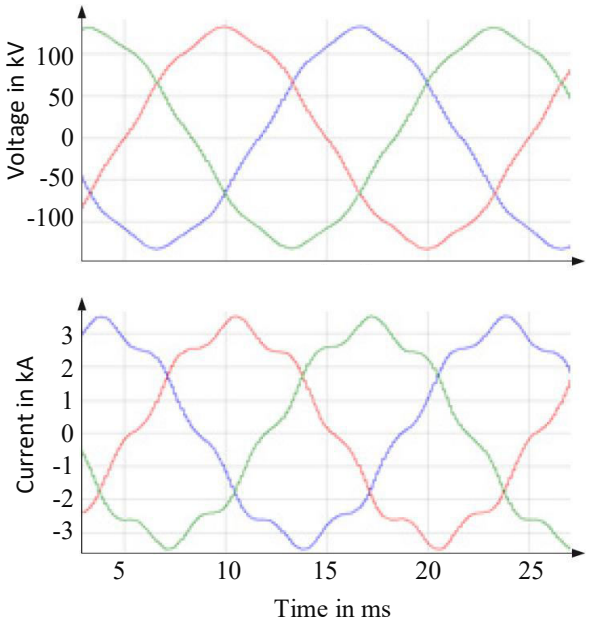

Figure 2.7 Reorded waveforms of the 250 Hz resonance experienced by the BARD Offshore1 wind farm and BorWin1 HVDC link in German North Sea in 2013 [7]

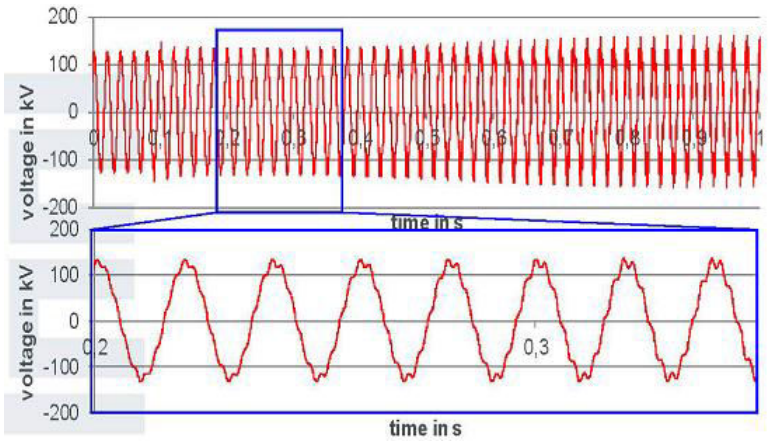

Figure 2.8 Recorded waveform of the 450 Hz resonance occurred in German North Sea [8].

In 2014, the China Nan'ao three-terminal MMC-HVDC for wind farm integration experienced an 20-30 Hz SSR as wind farm output power was gradually increased in the test stage, resulting the shutdown of the HVDC system and the trip out of wind turbines. The on-site recorded waveforms of the SSR in the MMC-HVDC system is shown in Figure 2.9.

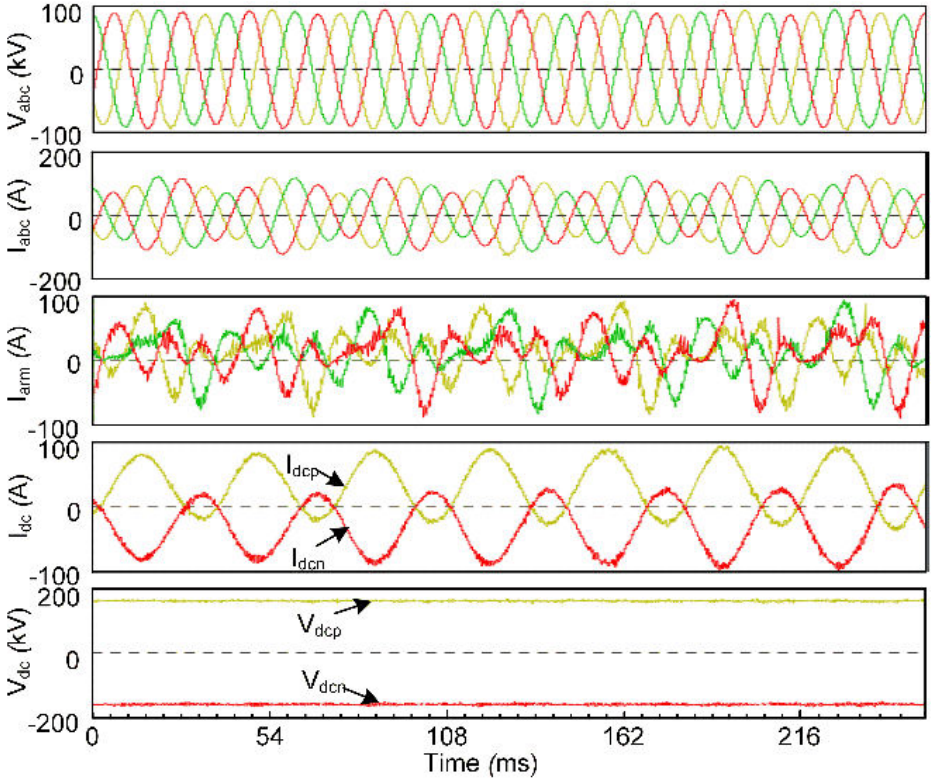

Figure 2.9 Recorded waveforms of the SSR in China Nan'ao in 2014 [53].

2.1.3 Incidents in HVDC connected AC grid

In 2015, the China Xiamen point-to-point VSC-HVDC transmission system experienced an around 23.6 Hz DC current oscillation, the amplitude of which reached 12.2% steady-state value, when the sending-end transfered 100 MW power under single-pole operation mode. Similarly, an 25.2 Hz DC current oscillation occurred when the sending-end transfered 500 MW power under single-pole operation mode [52].

In 2017, China Luxi back-to-back HVDC link experienced an around 1270 Hz high frequency resonance after several AC transmission lines were disconnected from the Guangxi side AC grid. Figure 2.10 shows the Guangxi side AC network of the Luxi HVDC project. The red dotted lines represents the transmission lines that were disconnected in the event. The recorded grid voltage and current waveforms of the Guangxi side HVDC converter station and the FFT analysis of the phase B current in the 1270 Hz resonance incident are shown in Figure 2.11.

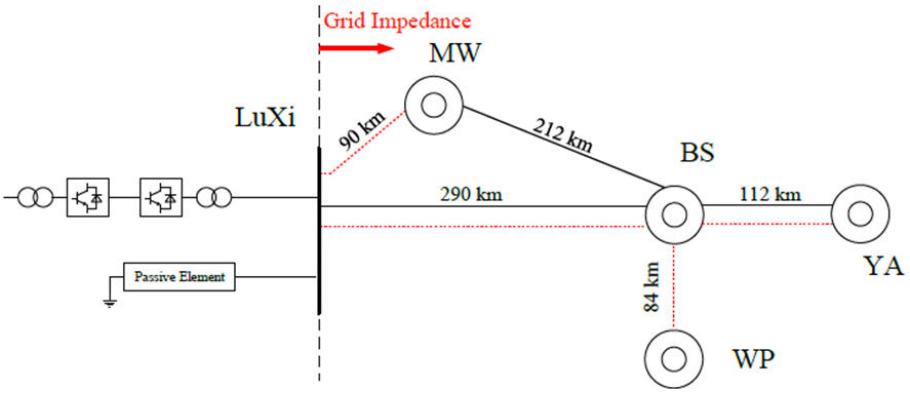

Figure 2.10 Guangxi side AC network of the Luxi HVDC project [54].

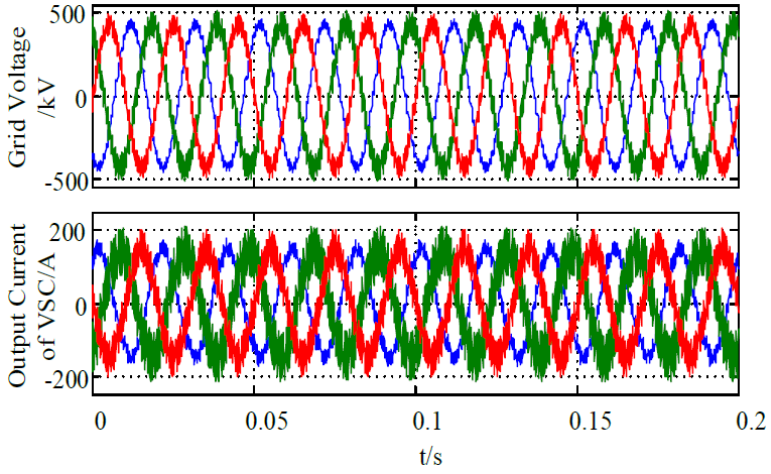

(a)

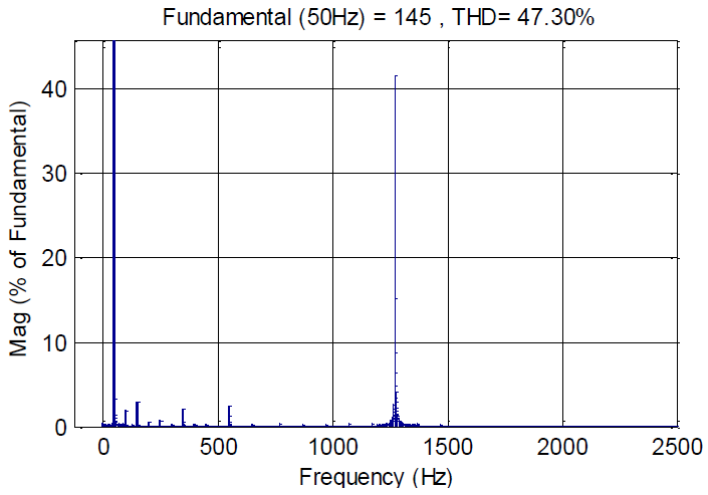

(b)

Figure 2.11 The recorded 1270 Hz resonance in Luxi back-to-back VSC-HVDC in 2017 [54].

In Germany, another high-frequency resonance (around 1100 Hz) between an HVDC converter station and the main AC grid was reported in a recent year at the connection point of an HVDC station [55]. However, the details of the incident including the date and the location are not given in [55]. Figure 2.12 shows the simulation result from the real event. The voltage oscillation at the PCC between HVDC station and AC grid was triggered by the interaction of converter control loops and grid impedance after grid topology change and disconnection of a conventional generation unit.

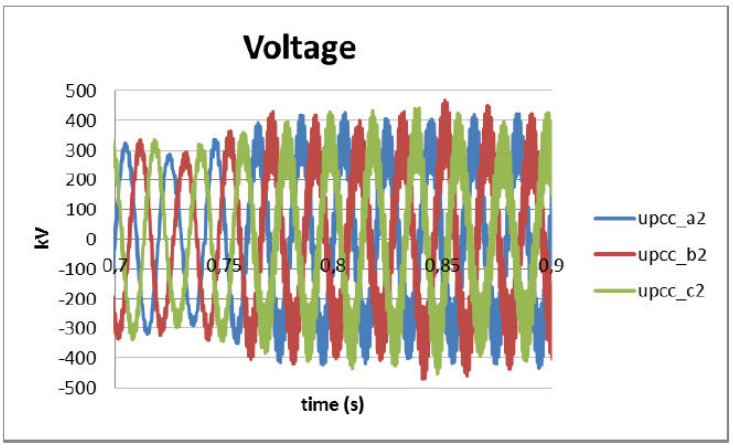

Figure 2.12 Voltage waveform of the 1100 Hz resonance in German North Sea area [55].

2.2 Features of Resonances in Converter-dominated Power Systems

Modern power electronics based power systems are characterized by the multi-timescale control dynamics as illustrated in Figure 2.13. Taking the HVDC connected OWF as example, the speed control of WT is quite slow, the bandwidth of which is far less than 1 Hz, while the DC voltage control and Q & U control of WT usually have the bandwidth of around 10 Hz. The control bandwidth of PLL is usually between several Hz and 100 Hz and its main influence on dynamics is around the fundamental frequency. The fastest dynamic of WT comes from the current control loop which typically has the bandwidth of up to hundreds of Hz. As for the HVDC converters for wind farm integration, the dynamics of the single-loop AC voltage control or a cascaded double-loop voltage and current control are mainly in the frequency range between 1 Hz and several hundreds of Hz.

As illustrated in Figure 2.13, the interaction between converter controls and interaction between converter control and passive grid components introduce wideband resonances into the system. Here both SSR and the resonances for above 50 Hz are generally called harmonic resonances. Due to the most commonly used asymmetrical control in grid-following converters, e.g. the PLL and power loop control, the frequency coupling effect around fundamental frequency is introduced. Moreover, due to the PWM switching and sampling process of converters, another frequecy coupling effect around the switching frequency is introduced. These frequency couplings may induce the sideband resonances of fundamental frequency and switching frequency [56]-[58].

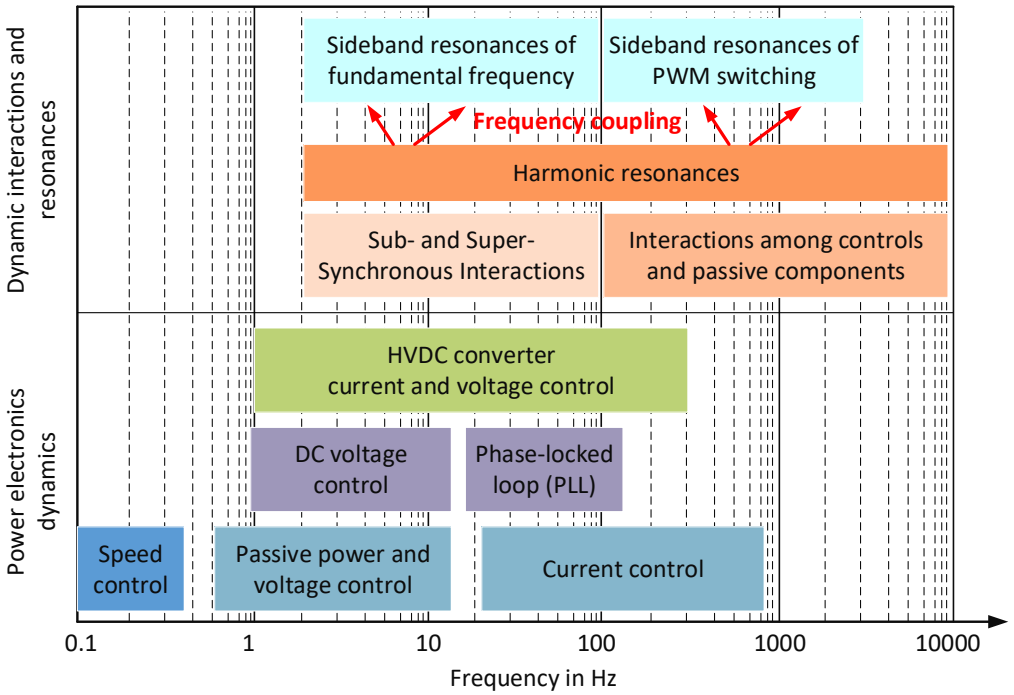

Figure 2.13 Frequency range of different control dynamics and system interactions

As the converter control and its digital delay can introduce negative damping effect into power systems, the interactions among differenct controls and passive grid components may lead to resonance instability. This is one reason for the reported real-world resonance incidents as presented in section 2.1.

2.3 Symmetrical Component Theory

In studies of three-phase AC systems, three-phase signals and impedance network are usually transformed to their symmetrical sequence components, i.e. positive-, negative-

and zero-sequence components, so that each sequence subsystem can be analyzed separately, thus simplifies analysis. The symmetrical components $\underline{U}_1$, $\underline{U}_2$, $\underline{U}_0$ of a three-phase voltage signal $\underline{U}_\mathrm{a}$, $\underline{U}_\mathrm{b}$, $\underline{U}_\mathrm{c}$ at the frequency ω can be computed as follows:

$$\underbrace{\begin{bmatrix} \underline{U}_1 \\ \underline{U}_2 \\ \underline{U}_0 \end{bmatrix}}_{\underline{\boldsymbol{u}}_{120}} = \underbrace{\frac{1}{3}\begin{bmatrix} 1 & \underline{\mathrm{a}} & \underline{\mathrm{a}}^2 \\ 1 & \underline{\mathrm{a}}^2 & \underline{\mathrm{a}} \\ 1 & 1 & 1 \end{bmatrix}}_{\underline{\boldsymbol{T}}_\mathrm{M}} \underbrace{\begin{bmatrix} \underline{U}_\mathrm{a} \\ \underline{U}_\mathrm{b} \\ \underline{U}_\mathrm{c} \end{bmatrix}}_{\underline{\boldsymbol{u}}_{\mathrm{abc}}} \tag{2.1}$$

where the complex number $\underline{\mathrm{a}}$ is $\mathrm{e}^{\mathrm{j}\frac{2\pi}{3}}$, $\underline{\boldsymbol{T}}_\mathrm{M}$ is the transformation matrix and the subscripts 1, 2, 0 denotes the positive-, negative- and zero-sequence components respectively.

Based on the above transformation of three-phase signals, the concept of sequence impedances can be introduced. For example, the three-phase voltages $\underline{\boldsymbol{u}}_{\mathrm{abc}}$ and currents $\underline{\boldsymbol{i}}_{\mathrm{abc}}$ of a shunt component at a specified frequency ω can be formulated as

$$\underbrace{\begin{bmatrix} \underline{U}_\mathrm{a} \\ \underline{U}_\mathrm{b} \\ \underline{U}_\mathrm{c} \end{bmatrix}}_{\underline{\boldsymbol{U}}_{\mathrm{abc}}} = \underbrace{\begin{bmatrix} \underline{Z}_{\mathrm{aa}} & \underline{Z}_{\mathrm{ab}} & \underline{Z}_{\mathrm{ac}} \\ \underline{Z}_{\mathrm{ba}} & \underline{Z}_{\mathrm{bb}} & \underline{Z}_{\mathrm{bc}} \\ \underline{Z}_{\mathrm{ca}} & \underline{Z}_{\mathrm{cb}} & \underline{Z}_{\mathrm{cc}} \end{bmatrix}}_{\underline{\boldsymbol{Z}}_{\mathrm{abc}}} \underbrace{\begin{bmatrix} \underline{I}_\mathrm{a} \\ \underline{I}_\mathrm{b} \\ \underline{I}_\mathrm{c} \end{bmatrix}}_{\underline{\boldsymbol{I}}_{\mathrm{abc}}} \tag{2.2}$$

where $\underline{Z}_{\mathrm{aa}}$, $\underline{Z}_{\mathrm{bb}}$, $\underline{Z}_{\mathrm{cc}}$ represent phase impedances, and $\underline{Z}_{\mathrm{ab}}$, $\underline{Z}_{\mathrm{ac}}$, $\underline{Z}_{\mathrm{bc}}$, $\underline{Z}_{\mathrm{ba}}$, $\underline{Z}_{\mathrm{ca}}$, $\underline{Z}_{\mathrm{cb}}$ represent between-phase impedances, i.e. phase-to-phase mutual impedances, then substituting

$$\begin{aligned} \underline{\boldsymbol{u}}_{\mathrm{abc}} &= \underline{\boldsymbol{T}}_\mathrm{M}^{-1} \cdot \underline{\boldsymbol{u}}_{120} \\ \underline{\boldsymbol{i}}_{\mathrm{abc}} &= \underline{\boldsymbol{T}}_\mathrm{M}^{-1} \cdot \underline{\boldsymbol{i}}_{120} \end{aligned} \tag{2.3}$$

into (2.2) yields

$$\underline{\boldsymbol{u}}_{120} = \underbrace{\underline{\boldsymbol{T}}_\mathrm{M} \cdot \underline{\boldsymbol{Z}}_{\mathrm{abc}} \cdot \underline{\boldsymbol{T}}_\mathrm{M}^{-1}}_{\underline{\boldsymbol{Z}}_{120}} \underline{\boldsymbol{i}}_{120} \tag{2.4}$$

where $\underline{\boldsymbol{Z}}_{120}$ denotes the sequence impedance matrix and it can be represented by

$$\underline{\boldsymbol{Z}}_{120} = \begin{bmatrix} \underline{Z}_{11} & \underline{Z}_{12} & \underline{Z}_{10} \\ \underline{Z}_{21} & \underline{Z}_{22} & \underline{Z}_{20} \\ \underline{Z}_{01} & \underline{Z}_{02} & \underline{Z}_{00} \end{bmatrix} \tag{2.5}$$

with $\underline{Z}_{11}$, $\underline{Z}_{22}$, $\underline{Z}_{00}$ representing the sequence impedances and the off-diagonal terms of the matrix representing the couplings between sequence impedances. Assuming the three-phase impedance network as given in (2.2) is symmetrical, i.e.

$$\underline{Z}_{ab} = \underline{Z}_{ba} \qquad \underline{Z}_{ac} = \underline{Z}_{ca} \qquad \underline{Z}_{bc} = \underline{Z}_{cb} \tag{2.6}$$

then the off-diagonal items of the sequence impedance matrix $\underline{\boldsymbol{Z}}_{120}$ become 0 and $\underline{\boldsymbol{Z}}_{120}$ can be rewritten as

$$\underline{\boldsymbol{Z}}_{120} = \begin{bmatrix} \underline{Z}_{1} & 0 & 0 \\ 0 & \underline{Z}_{2} & 0 \\ 0 & 0 & \underline{Z}_{0} \end{bmatrix} \tag{2.7}$$

Note, that in real-world power systems, some three-phase grid components are not exactly symmetrical due to their phase-to-phase parasitic capacitances, e.g. the three-phase five-leg transformers and the three-phase flat-formation HV cable systems, thus the independent sequence impedances $\underline{Z}_1$, $\underline{Z}_2$ and $\underline{Z}_0$ in (2.7) can not be obtained. However, the asymmetry in passive grid components is generally small and can be neglected in analysis.

In modern power electronic based power systems, converter-interfaced components are usually not three-phase symmetrical due to their asymmetrical converter control, and it is not feasible to transform their three-phase impedance matrix $\underline{\boldsymbol{Z}}_{abc}$ to the independent sequence impedances $\underline{Z}_1$, $\underline{Z}_2$ and $\underline{Z}_0$ as given in (2.7). Section 3.3 presents more details on this point.

2.4 Concept and analysis methods of Resonances

Resonance is an electromagnetic energy exchange phenomenon observed between inductive and capacitive energy storage elements. The series and parallel connection of

abundant inductive and capacitive elements in power systems constitutes many resonance circuits and the resonance frequencies determined by the parameters of inductive and capacitive elements can extend from several Hz to thousands of Hz or even higher.

For traditional power systems with few or no converter-interfaced components, grid components are usually modelled with capacitive and inductive elements, which have linear impedance characteristics. However, with the ever-growing penetration level of renewable energy sources, the constantly increased integration of storage and electric-vehicles as well as the wide utilization of HVDC grid connection of offshore wind farms, modern power systems have gradually been dominated by grid-connected converters, the equivalent impedance network of which are influenced by multiple timescale converter control effects. Since grid-connected converters are highly nonlinear, their impedance responses are typically derived by performing small- or large-signal analysis at chosen operating points.

According to the impedances of all grid components and their connection relationships, the equivalent electrical circuits of a power system can be built, in which the parallel connection of capacitive and inductive elements forms parallel resonance circuit and the series connection of capacitive and inductive elements forms series resonance circuit. The typical illustration of parallel and series resonance circuits are shown in Figure 2.14, in which $\underline{U}_\mathrm{P}$, $\underline{I}_\mathrm{P}$, $\underline{U}_\mathrm{S}$, $\underline{I}_\mathrm{S}$ represents the voltage and currents at the frequency ω. Their respective output impedances $\underline{Z}_\mathrm{P}$ and $\underline{Z}_\mathrm{S}$, as illustrated in Figure 2.14, can be formulated as

$$\underline{Z}_\mathrm{P} = \frac{1}{\mathrm{j}\omega C + \dfrac{1}{\mathrm{j}\omega L} + \dfrac{1}{R}} \qquad \underline{Z}_\mathrm{S} = \frac{1}{\mathrm{j}\omega C} + \mathrm{j}\omega L + R \tag{2.8}$$

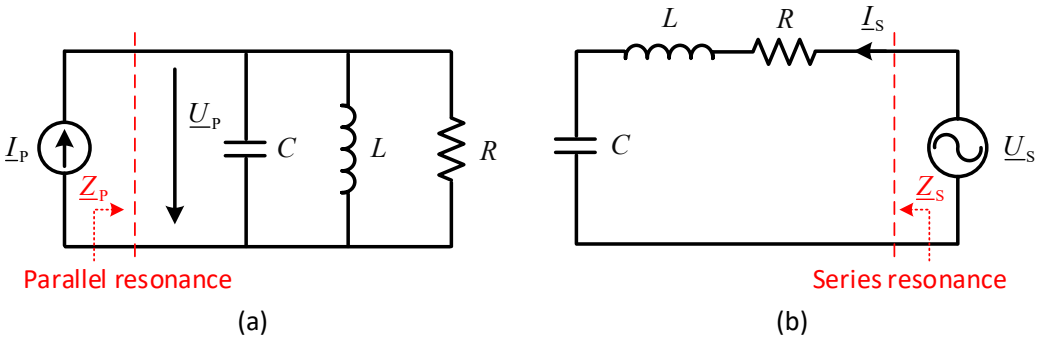

Figure 2.14 Schematic diagram of the parallel and series resonance circuits

For the parallel resonance circuit, the output impedance $\underline{Z}_{\mathrm{P}}$ as illustrated in Figure 2.14 (a) has the maximum magnitude $\left|\underline{Z}_{\mathrm{P,max}}\right|$ of R at the frequency ω_{P} which satisfies

$$\mathrm{j}\omega_{\mathrm{P}}C+\frac{1}{\mathrm{j}\omega_{\mathrm{P}}L}=0 \tag{2.9}$$

where the frequency ω_{P} is defined as the parallel resonance frequency. Even if a small current perturbation $\underline{i}_{\mathrm{P}}$ of this frequency is injected into the circuit, a large voltage response as represented by

$$\underline{U}_{\mathrm{P}}=\left|\underline{Z}_{\mathrm{P,max}}\right|\cdot\underline{I}_{\mathrm{P}} \tag{2.10}$$

will be induced at the same frequency.

For the series resonance circuit, the output impedance $\underline{Z}_{\mathrm{S}}$ as illustrated in Figure 2.14 (b) has the minimum magnitude $\left|\underline{Z}_{\mathrm{S,min}}\right|$ of R at the frequency ω_{S} which satisfies

$$\frac{1}{\mathrm{j}\omega_{\mathrm{S}}C}+\mathrm{j}\omega_{\mathrm{S}}L=0 \tag{2.11}$$

where the frequency ω_{S} in this context is the series resonance frequency. Even if a small harmonic voltage $\underline{U}_{\mathrm{S}}$ of this frequency is imposed on the circuit, a large current response as represented by

$$\underline{I}_{\mathrm{S}}=\underline{U}_{\mathrm{S}}/\left|\underline{Z}_{\mathrm{S,min}}\right| \tag{2.12}$$

will be induced at the same frequency.

For both the parallel and series resonances, the resistance R is also an important factor influencing the harmonic distortion or resonance stability. Its relations with the LC parameters can be described by quality factor, which relates the maximum or peak energy stored in the circuit (the reactance) to the energy dissipated (the resistance) during each cycle of oscillation. Its mathematical expression is

$$Q = \frac{\omega_{\text{res}} L}{R} = \frac{X_{\text{L}}}{R} = \frac{1}{\omega_{\text{res}} CR} = \frac{X_{\text{C}}}{R} = \frac{1}{R}\sqrt{\frac{L}{C}} \tag{2.13}$$

where ω_{res} denotes the general resonance frequency for both the parallel and series resonance circuits as shown in Figure 2.14. For the parallel resonance circuit, the higher the value Q is, the sharper peak can be observed in the impedance amplitude versus frequency curve, while for the series resonance circuit, the higher the value Q is, the sharper vally can be observed in the impedance amplitude versus frequency curve.

In the investigation of resonances in wind-integrated systems, the whole system can be aggregated to a so-called load-source system, i.e. the wind farm subsystem and the grid subsystem here, as illustrated by Figure 2.15 (a). The wind farm is represented by its Norton equivalent circuit and the grid connection is represented by its Thevenin equivalent circuit. Assuming the system is three-phase symmetrical, it can be decomposed into three single-line symmetrical component systems, each of which can be illustrated by Figure 2.15 (b).

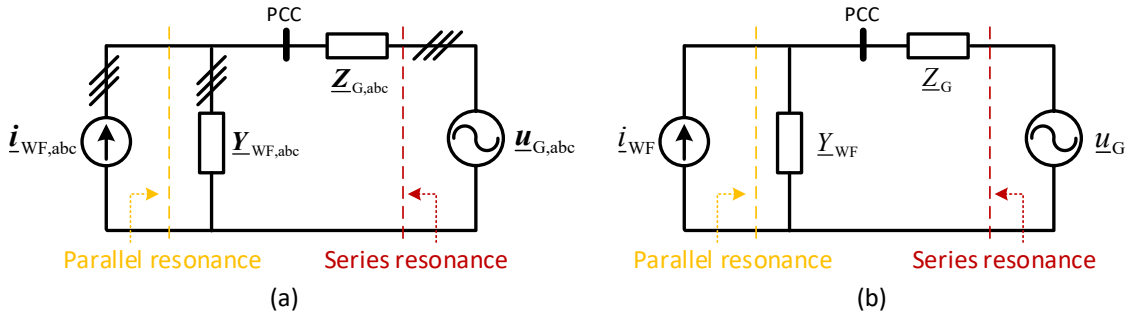

Figure 2.15 Equivalent circuits of a wind-integrated power system.

A comprehensive review of the system stability analysis for power electronics based power systems has been conducted in [58], in which the analytical methods for stability assessment can be mainly categorized to the eigenvalue-based analysis using the state-space model of the system in the time domain and the impedance-based analysis in the frequency domain. The impedance-based frequency domain analysis methods can be furtherly classified into the Nyquist diagram or Bode plot method and the nodal admittance matrix based method. In comparsion to the time-domain methods, the nodal admittance matrix based method is more computationally efficient and is scalable to different sizes of power systems. Additionally, another advantage of the impedance-based method is: when some of the system parameters are unknown, the blackbox impedance models of the grid components with unkonwn parameters can be utilised for analysis, e.g.

it can obtained through measurements. Since the analytical methods in the time-domain are not in the scope of the study, only the impedance-based methods will be furtherly discussed.

When a system is reduced to a load-source system as illustrated in Figure 2.15, resonance analysis can be conducted using the Nyquist diagram or Bode-plot methods. When a complex multi-node system is difficult to be reduced to a load-source system, another impedance-based method based on the nodal admittance matrix, i.e. resonance mode analysis (RMA), can be applied. A comparison of these two methods has been conducted using a case study in [59], and it is found that Bode plots could wrongly predict system stability while Nyquist diagrams are not straightforward for stablity check. In this dissertation, both the Bode plot and RMA methods will be applied taking into account their advantages.

3 Modelling of Power System Components

This chapter presents the analytical impedance modelling of grid components for harmonic resonance analysis. Partial results of this chapter were published in advance in [12], [35]. In the grid integration of DFIG-based OWF with HVDC transmission, system components can include WTs, undersea AC cables, transformers, harmonics filters, HVDC converters, DC cables and an equivalent external grid, as shown in Figure 3.1.

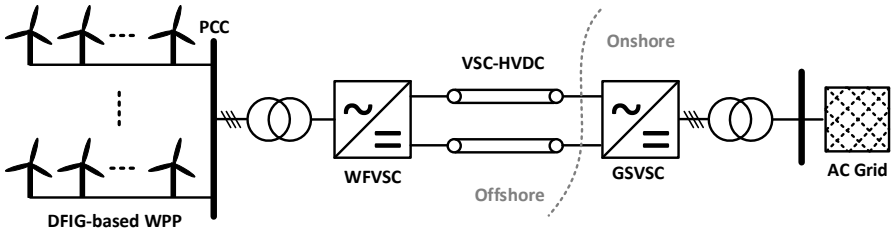

Figure 3.1 Diagram of a DFIG-based OWF with VSC-HVDC connection

In theoretical analysis, modelling three-phase AC grid components using the full three-phase circuits can complicate analysis, thus under the assumption of balanced three-phase systems, they can typically be modelled with the symmetrical components. However, for converter-interfaced components, the positive- and negative-sequence impedance models are mostly coupled due to the asymmetry of converter control [60], [61]. Therefore, the frequency-coupling effect between converter sequence impedances should be carefully modelled.

3.1 Cables

The integration of OWF with HVDC transmission may involve three kinds of submarine cables, they are the medium-voltage (MV) three-phase AC cables, which are used for collecting WTs, the high-voltage AC cables, which are used for interconnecting OWF platforms and HVDC converter station, as well as the high-voltage DC cables used in the HVDC link. Since the MV cables are typically laid in three-core formation, it is reasonable to assume that they are three-phase symmetrical and can be modelled with separate positive-, negative- and zero-sequence components. The HV submarine AC cables are typically laid in flat-formation, since only a short length is used here for interconnecting the OWF platforms and the offshore HVDC station, the asymmetry will be ignored and same models as MV AC cables will be adopted. The modelling of the DC cables is not necessary when assuming a constant DC voltage in the HVDC link. This is

because the AC side output impedance of a HVDC converter is not influenced by the DC side circuits when the DC side dynamic is neglected.

In comparison to overhead lines, one important consideration about cables is the strong capacitance effect. As stated in [62], for voltages above 10 kV, the shunt admittance of cables longer than 200 m and overhead lines longer than 1000 m should not be neglected. In real-world OWFs, the length of the cables connecting two neighboring WTs usually lies between 500 m and 1000 m, thus the shunt admittance should not be ignored by modelling. Then according to the interested frequency range, nominal Pi model or equivalent Pi model can be applied for the study. Figure 3.2 shows the diagram of the widely adopted Pi model for cables, in which the subscripts A and B denote sending and receiving ends, $\underline{Z}_{\text{Series}}$ denotes the equivalent series impedance, $\underline{Y}_{\text{Shunt}}$ denotes the equivalent shunt admittance and $\underline{U}_{\text{A}}$, $\underline{I}_{\text{A}}$, $\underline{U}_{\text{B}}$, $\underline{I}_{\text{B}}$ denotes the terminal currents and voltages for the frequency ω.

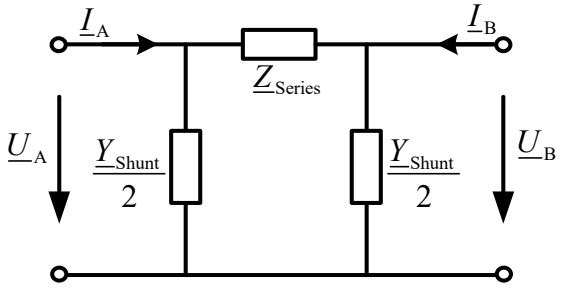

Figure 3.2 Diagram of cable Pi model.

The series impedance $\underline{Z}_{\text{Series}}$ and the shunt admittance $\underline{Y}_{\text{Shunt}}$ in Figure 3.2 can be represented with the parameters of cable resistance, inductance and capacitance. The electrical parameters of cables are mainly influenced by the following two factors: (1) long line effects induced by the distribution of parameter along the cable lenth; (2) the frequency dependency of parameters caused by the skin and proximity effects [62].

When neglecting long-line effects and the frequency dependency of parameters, the equivalent resistance, inductance and capacitance of cables can be obtained by multiplying the unit-length parameters with cable length. That is how the nominal Pi model of cable is defined. Taking the positive sequence component as example, with the lumped parameters R_1, L_1, C_1, the so-called nominal Pi model can be described by

$$\underline{Z}_{\text{Series}} = R_1 + \mathrm{j}\omega L_1,\ \underline{Y}_{\text{Shunt}} = \mathrm{j}\omega C_1 \tag{3.1}$$

The long line effects can be accounted for by including the long line hyperbolic correction factors [62], with consideration of which we also call it as equivalent Pi model, as represented by

$$\underline{Z}_{\text{Series}} = \underline{Z}_0 \sin\left(\underline{\gamma} \cdot Len\right),\ \underline{Y}_{\text{Shunt}} = \frac{1}{\underline{Z}_0} \tanh\frac{\underline{\gamma} \cdot Len}{2} \tag{3.2}$$

where

$$\begin{aligned} \underline{Z}_{\text{unit}} &= R_{\text{unit}} + \mathrm{j}\omega L_{\text{unit}},\ \underline{Y}_{\text{unit}} = \mathrm{j}\omega C_{\text{unit}} / 2 \\ \underline{\gamma} &= \sqrt{\underline{Z}_{\text{unit}} \underline{Y}_{\text{unit}}},\ \underline{Z}_0 = \sqrt{\underline{Z}_{\text{unit}} / \underline{Y}_{\text{unit}}} \end{aligned} \tag{3.3}$$

and R_{unit}, L_{unit}, C_{unit} are the unit-length resistance, inductance and capacitance parameters of the cable, and *Len* is the length of the cable.

Formulating the relationship of the input and output signals of the 4-port network in Figure 3.2, the cable can be represented by a second-order admittance matrix $\underline{\boldsymbol{Y}}_{\text{Cable}}$, as in

$$\begin{bmatrix} \underline{I}_{\text{A}} \\ \underline{I}_{\text{B}} \end{bmatrix} = \underbrace{\begin{bmatrix} 1/\underline{Z}_{\text{Series}} + \underline{Y}_{\text{Shunt}} & -1/\underline{Z}_{\text{Series}} \\ -1/\underline{Z}_{\text{Series}} & 1/\underline{Z}_{\text{Series}} + \underline{Y}_{\text{Shunt}} \end{bmatrix}}_{\underline{\boldsymbol{Y}}_{\text{Cable}}} \begin{bmatrix} \underline{U}_{\text{A}} \\ \underline{U}_{\text{B}} \end{bmatrix} \tag{3.4}$$

Frequency dependency of parameters due to skin and proximity effects is typically accounted for by using frequency dependent correction factors [63]. Although all the electrical parameters of cables are frequency dependent, the most prominent effect is on the series resistance. The representation of series resistance suggested by the National Grid UK is

$$R = R_1\left(0.187 + 0.532\sqrt{h}\right),\ h > 2.35$$

where R_1 is the fundamental frequency resistance, and *h* is harmonic order [64]. The corrected value of resistance *R* can then be applied in (3.1) or (3.2).

For harmonic analysis involving overhead lines, the nominal Pi model is generally considered acceptable for fundamental frequency when the line length is less than 250 km. Since cables generally have much greater capacitance effect than overhead lines, long

line effects should be considered for much shorter cables. However, the cables to be modelled for resonance analysis in the thesis are the quite short MV collector cables and high-voltage AC cables, using nominal Pi model to represent each collector cable section and high-voltage AC cable can give sufficient accuracy.

3.2 Transformer

3.2.1 Impedance modelling

For most harmonic studies, a three-phase two-winding transformer can be sufficiently modelled with the series short-circuit impedance and shunt magnetizing admittance assuming constant resistance and inductance parameters [62]. Two examples are the T model (see Figure 3.3) and Pi model (see Figure 3.4), in which three-phase transformers are composed of three single-phase transformers. The transformer Pi model in Figure 3.4 is an approximation of the transformer T model in Figure 3.3. Through eliminating the transformer internal node in Figure 3.3, the 4-port impedance network in Figure 3.4 can be represented by a second-order admittance matrix, as given in (3.5).

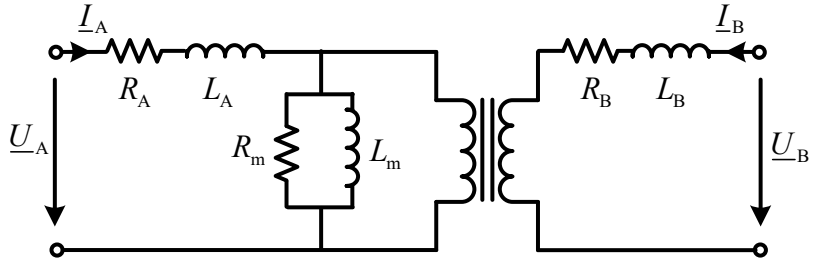

Figure 3.3 Single-line representation of the T model of three-phase transformer

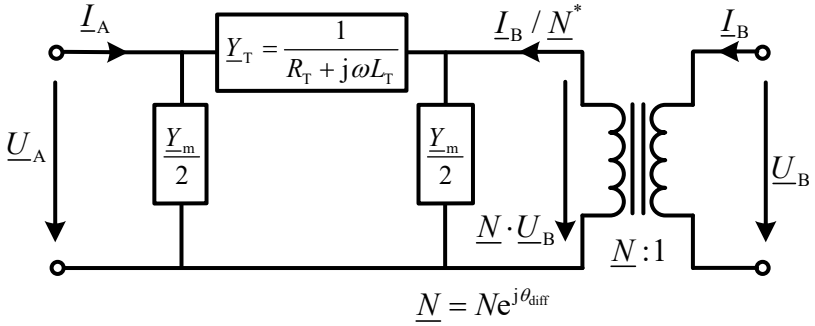

Figure 3.4 Single-line representation of the Pi model of three-phase transformer [65]

$$\begin{bmatrix} \underline{I}_{\mathrm{A}} \\ \underline{I}_{\mathrm{B}} \end{bmatrix} = \underbrace{\begin{bmatrix} \underline{Y}_{\mathrm{T}} + \dfrac{\underline{Y}_{\mathrm{m}}}{2} & -\underline{Y}_{\mathrm{T}} N \mathrm{e}^{\mathrm{j}\theta_{\mathrm{diff}}} \\ -\underline{Y}_{\mathrm{T}} N \mathrm{e}^{-\mathrm{j}\theta_{\mathrm{diff}}} & \left(\underline{Y}_{\mathrm{T}} + \dfrac{\underline{Y}_{\mathrm{m}}}{2}\right) N^2 \end{bmatrix}}_{\underline{\boldsymbol{Y}}_{\mathrm{Tr}}} \begin{bmatrix} \underline{U}_{\mathrm{A}} \\ \underline{U}_{\mathrm{B}} \end{bmatrix} \tag{3.5}$$

where $\underline{Y}_{\mathrm{T}}$ represents short-circuit admittance, $\underline{Y}_{\mathrm{m}}$ represents magnetizing admittance and $\underline{U}_{\mathrm{A}}$, $\underline{I}_{\mathrm{A}}$, $\underline{U}_{\mathrm{B}}$, $\underline{I}_{\mathrm{B}}$ denotes the terminal currents and voltages for the frequency ω. The phase shifting θ_{diff} in (3.5) may cause significant harmonic cancellations when there are multiple harmonic sources in a system, therefore, it is essential to include the effect by harmonic calculations.

Considering that the magnetizing admittance $\underline{Y}_{\mathrm{m}}$ is much smaller than the short-circuit admittance $\underline{Y}_{\mathrm{T}}$ and the connected load or source admitances when a transformer works under full-load operation, it is reasonable to model the transformer with only the short-circuit impedance, as conducted in most harmonic studies. But when a transformer works under open-circuit (during energization period) or light-load conditions, the magnetizing branch is not negligible in comparison to other branches, thus it requires to adequately represent the magnetizing branch. Moreover, by the occurrence of transformer core saturation, the magnetizing admittance can also become comparable to winding admittances due to the nonlinear flux-current characteristic of iron core [66].

In above discussions, it is assumed that transformer windings have constant resistance and inductance parameters, however, the resistance and inductance of the windings are frequency-dependent due to the inter-winding or parasitic capacitances, and this effect becomes significant when the considered frequency is up to serveral kHz, especially for high voltage level transformers [67]. Therefore, a finer transformer model considering stray capacitances is needed for wide-band resonance analysis.

Figure 3.5 shows a detailed electromagnetically coupled model where the primary and secondary windings are represented by multiple cascaded winding sections with concentrated *R*, *L*, *C* parameters [68]. Each winding section is electromagnetically coupled with neigbouring sections of the same and another side windings. The magnetic flux linkings are represented with dashed lines. Transformer capacitances include the winding capacitances C_{WA}, C_{WB} between the winding sections of the same side, the capacitance C_{M} between the primary and secondary windings, and the earth capacitance C_{E} between the winding sections and iron core. Copper losses of primary and secondary

windings are represented by R_A, R_B. Dielectric loss in winding insulation are represented by G_A, G_B. Note that all secondary side parameters are referred to the primary side.

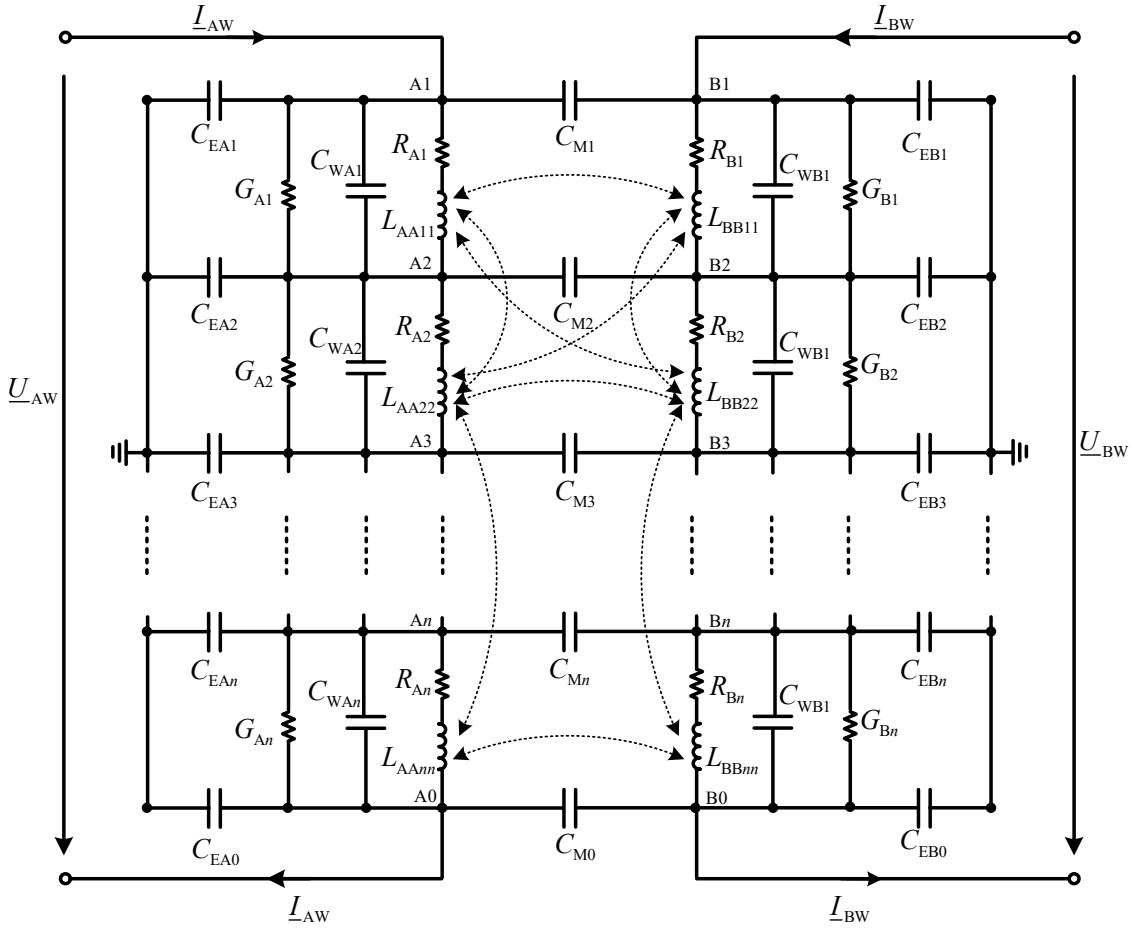

Figure 3.5 Cascade model of a single-phase two-winding transformer [68]

The detailed transformer model in Figure 3.5 is suitable for very high freuqency or transient studies where current and voltage distribution along the windings are investigated. Ref [69] shows, using only one section of the fully electromagnetically cascade model with lumped parameters is sufficient for the frequency analysis up to 20 kHz. Furtherly in [70], the reduced single-section model is analytically equivalent to the one as shown in Figure 3.6, where dielectric losses in windings are not included.

Corresponding parameters in Figure 3.6 are defined as from (3.6) to (3.14). The analytically reduced transformer model is acutally an improvement of the conventional transformer T-model by adding stray capacitances. Throught the transformer turn ratio N, electrical parameters of the secondary side are reflected to the primary side.

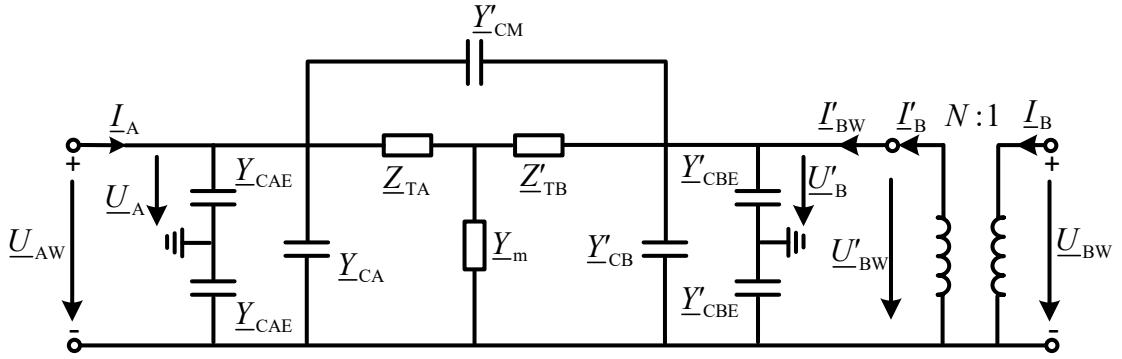

Figure 3.6 Analytically reduced model of a single-phase two-winding transformer [70]

$$\underline{Z}_{\mathrm{TA}} = \frac{1}{\underline{Y}_{\mathrm{TA}}} = R_{\mathrm{A}} + \mathrm{j}\omega L_{\mathrm{A}} \tag{3.6}$$

$$\underline{Z}'_{\mathrm{TB}} = \frac{1}{\underline{Y}'_{\mathrm{TB}}} = R'_{\mathrm{B}} + \mathrm{j}\omega L'_{\mathrm{B}} \tag{3.7}$$

$$\underline{Z}_{\mathrm{T}} = \underline{Z}_{\mathrm{TA}} + \underline{Z}'_{\mathrm{TB}} \tag{3.8}$$

$$\underline{Y}_{\mathrm{m}} = \frac{1}{R_{\mathrm{m}}} + \frac{1}{\mathrm{j}\omega L_{\mathrm{m}}} \tag{3.9}$$

$$\underline{Y}_{\mathrm{CA}} = \mathrm{j}\omega\left(C_{\mathrm{WA}} + C_{\mathrm{M}} - \frac{C_{\mathrm{M}}}{N}\right) = \mathrm{j}\omega C_{\mathrm{A}} \tag{3.10}$$

$$\underline{Y}'_{\mathrm{CB}} = \mathrm{j}\omega\left(\frac{C_{\mathrm{WB}}}{N^2} + \frac{C_{\mathrm{M}}}{N^2} - \frac{C_{\mathrm{M}}}{N}\right) = \mathrm{j}\omega C'_{\mathrm{B}} \tag{3.11}$$

$$\underline{Y}_{\mathrm{CAE}} = \mathrm{j}\omega\frac{C_{\mathrm{EA}}}{2} \tag{3.12}$$

$$\underline{Y}'_{\mathrm{CBE}} = \mathrm{j}\omega\frac{C_{\mathrm{EB}}}{2N^2} \tag{3.13}$$

$$\underline{Y}'_{\mathrm{CM}} = \mathrm{j}\omega\frac{C_{\mathrm{M}}}{N} \tag{3.14}$$

Assuming that $\underline{Y}_{\mathrm{m}}$ is much smaller than $\underline{Y}_{\mathrm{TA}}$ and $\underline{Y}'_{\mathrm{TB}}$, the internal node in Figure 3.6 can be mathematically eliminated and the corresponding nodal matrix equation can be formulated as

$$\begin{bmatrix} \underline{I}_{\mathrm{A}} \\ \underline{I}_{\mathrm{B}} \end{bmatrix} = \begin{bmatrix} \underline{Y}_{\mathrm{CAE}} & 0 \\ 0 & N^2\underline{Y}'_{\mathrm{CBE}} \end{bmatrix} \begin{bmatrix} \underline{U}_{\mathrm{A}} \\ \underline{U}_{\mathrm{B}} \end{bmatrix} + \begin{bmatrix} \underline{Y}_{\mathrm{AAW}} & N\underline{Y}_{\mathrm{ABW}} \\ N\underline{Y}_{\mathrm{BAW}} & N^2\underline{Y}_{\mathrm{BBW}} \end{bmatrix} \begin{bmatrix} \underline{U}_{\mathrm{AW}} \\ \underline{U}_{\mathrm{BW}} \end{bmatrix} \tag{3.15}$$

where

$$\begin{aligned} \underline{Y}_{\mathrm{AAW}} &= \underline{Y}_{\mathrm{T}} + 0.5\underline{Y}_{\mathrm{m}} + \underline{Y}_{\mathrm{CA}} + \underline{Y}'_{\mathrm{CM}} \\ \underline{Y}_{\mathrm{BBW}} &= \underline{Y}_{\mathrm{T}} + 0.5\underline{Y}_{\mathrm{m}} + \underline{Y}'_{\mathrm{CB}} + \underline{Y}'_{\mathrm{CM}} \\ \underline{Y}_{\mathrm{ABW}} &= \underline{Y}_{\mathrm{BAW}} = -\underline{Y}_{\mathrm{T}} - \underline{Y}'_{\mathrm{CM}} \end{aligned} \tag{3.16}$$

The short-circuit impedance $\underline{Z}_{\mathrm{T}}$ in (3.8) can be determined by performing a short-circuit test at the fundamental frequency. The magnetizing shunt admittance consisting the core resistance R_{m} and the magnetizing inductance L_{m} in (3.9) can be determined by an open-circuit test at the fundamental frequency. The capacitances can be obtained either by analytical methods or measurements. Typical values of the lumped parameters in Figure 3.6 can be taken from [71].

According to the type of transformer core, three-phase two-winding transformer can be categorized into three single-phase transformers, three-limb core transformer and five-limb core transformer. To simplify analysis, the first type is adopted to generally represent three-phase transformers. As a result, the electromagnetic coupling among phases in the three-limb or five-limb type will be neglected in the modelling. On this basis, a three-phase transformer model can be obtained by connecting three single-phase transformers as illustrated in Figure 3.6 in a certain manner. Primary winding is connected with primary winding, and secondary winding is connected with secondary winding. Three phases can be connected either in Wye form or in Delta form, and the connection can be in any phase sequence. Moreover, the neutral point of primary windings or secondary windings can be grounded. Figure 3.7 shows an example of three-phase transformer model, where the 4-port networks I, II, III each represent a single-phase two-winding transformer. The Wye-connection of primary windings and Delta-connection of secondary windings leads to the vector group of Yd5, the definition of which and other vector groups can be found in Appendix B.

Taking into account transfomer vector group, the relationship between winding and terminal voltage/current vectors can be described as in (3.17), (3.18) and (3.19), where $\underline{Z}_{\mathrm{MEA}}$ and $\underline{Z}_{\mathrm{MEB}}$ denotes the grounding impedances of primary and secondary sides respectively, $\boldsymbol{E}_3$ denotes the third-order identity matrix, $\mathbf{0}$ denotes the third-order zero matrix. For Delta connection where no neutral point exists or Wye-connection with direct grounding, there is not the second term in (3.18). For non-grounded Wye-connection, grouding impedance should be set to a very high value. The matrices $\boldsymbol{D}_{\mathrm{A}}$ and $\boldsymbol{D}_{\mathrm{B}}$ denotes the winding configuration of the primary and secondary sides, and their values vary with the vector group of the winding connection, which can be found in Appendix B.

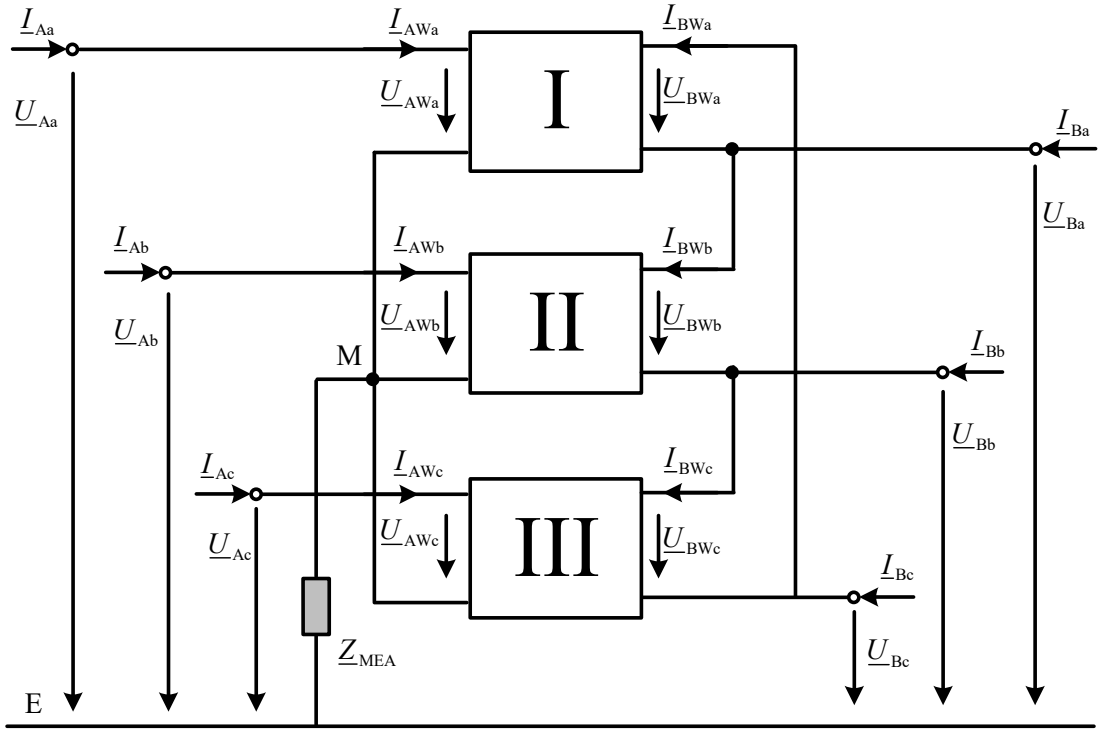

Figure 3.7 Diagram of a three-phase two-winding transformer with the vector group Yd5 [70]

$$\begin{bmatrix} \underline{\boldsymbol{i}}_{\mathrm{A,abc}} \\ \underline{\boldsymbol{i}}_{\mathrm{B,abc}} \end{bmatrix} = \begin{bmatrix} \underline{Y}_{\mathrm{CAE}}\boldsymbol{E}_3 & \boldsymbol{0} \\ \boldsymbol{0} & N^2\underline{Y}'_{\mathrm{CBE}}\boldsymbol{E}_3 \end{bmatrix} \begin{bmatrix} \underline{\boldsymbol{u}}_{\mathrm{A,abc}} \\ \underline{\boldsymbol{u}}_{\mathrm{B,abc}} \end{bmatrix} + \begin{bmatrix} \underline{Y}_{\mathrm{AAW}}\boldsymbol{E}_3 & N\underline{Y}_{\mathrm{ABW}}\boldsymbol{E}_3 \\ N\underline{Y}_{\mathrm{BAW}}\boldsymbol{E}_3 & N^2\underline{Y}_{\mathrm{BBW}}\boldsymbol{E}_3 \end{bmatrix} \begin{bmatrix} \underline{\boldsymbol{u}}_{\mathrm{AW,abc}} \\ \underline{\boldsymbol{u}}_{\mathrm{BW,abc}} \end{bmatrix} \tag{3.17}$$

$$\begin{bmatrix} \underline{\boldsymbol{u}}_{\mathrm{AW,abc}} \\ \underline{\boldsymbol{u}}_{\mathrm{BW,abc}} \end{bmatrix} = \begin{bmatrix} \boldsymbol{D}_{\mathrm{A}} & \boldsymbol{0} \\ \boldsymbol{0} & \boldsymbol{D}_{\mathrm{B}} \end{bmatrix} \begin{bmatrix} \underline{\boldsymbol{u}}_{\mathrm{A,abc}} \\ \underline{\boldsymbol{u}}_{\mathrm{B,abc}} \end{bmatrix} - \begin{bmatrix} \underline{Z}_{\mathrm{MEA}}\boldsymbol{E}_3 & \boldsymbol{0} \\ \boldsymbol{0} & \underline{Z}_{\mathrm{MEB}}\boldsymbol{E}_3 \end{bmatrix} \begin{bmatrix} \underline{\boldsymbol{i}}_{\mathrm{A,abc}} \\ \underline{\boldsymbol{i}}_{\mathrm{B,abc}} \end{bmatrix} \tag{3.18}$$

$$\begin{bmatrix} \underline{\boldsymbol{i}}_{\mathrm{A,abc}} \\ \underline{\boldsymbol{i}}_{\mathrm{B,abc}} \end{bmatrix} = \begin{bmatrix} \boldsymbol{D}_{\mathrm{A}}^{\mathrm{T}} & 0 \\ 0 & \boldsymbol{D}_{\mathrm{B}}^{\mathrm{T}} \end{bmatrix} \begin{bmatrix} \underline{\boldsymbol{i}}_{\mathrm{AW,abc}} \\ \underline{\boldsymbol{i}}_{\mathrm{BW,abc}} \end{bmatrix} \tag{3.19}$$

Combining (3.17), (3.18) and (3.19), the mathmatical representation of the three-phase two-winding transformer model which relates the terminal currents and voltages can be obtained as

$$\begin{bmatrix} \underline{\boldsymbol{i}}_{\mathrm{A,abc}} \\ \underline{\boldsymbol{i}}_{\mathrm{B,abc}} \end{bmatrix} = \underbrace{\underline{\boldsymbol{F}}^{-1}\underline{\boldsymbol{M}}}_{\underline{\boldsymbol{Y}}_{\mathrm{T,abc}}} \begin{bmatrix} \underline{\boldsymbol{u}}_{\mathrm{A,abc}} \\ \underline{\boldsymbol{u}}_{\mathrm{B,abc}} \end{bmatrix} \tag{3.20}$$

where

$$\underline{\boldsymbol{F}} = \begin{bmatrix} \boldsymbol{E}_3 + \underline{Z}_{\mathrm{MEp}} \underline{Y}_{\mathrm{ppW}} \boldsymbol{D}_{\mathrm{up}}^{\mathrm{T}} & N \underline{Z}_{\mathrm{MEs}} \underline{Y}_{\mathrm{psW}} \boldsymbol{D}_{\mathrm{up}}^{\mathrm{T}} \\ N \underline{Z}_{\mathrm{MEp}} \underline{Y}_{\mathrm{spW}} \boldsymbol{D}_{\mathrm{us}}^{\mathrm{T}} & \boldsymbol{E}_3 + N^2 \underline{Z}_{\mathrm{MEs}} \underline{Y}_{\mathrm{ssW}} \boldsymbol{D}_{\mathrm{us}}^{\mathrm{T}} \end{bmatrix}$$
$$\underline{\boldsymbol{M}} = \begin{bmatrix} \boldsymbol{D}_{\mathrm{up}}^{\mathrm{T}} \left(\underline{Y}_{\mathrm{CpE}} \boldsymbol{I} + \underline{Y}_{\mathrm{ppW}} \boldsymbol{D}_{\mathrm{up}} \right) & N \underline{Y}_{\mathrm{psW}} \boldsymbol{D}_{\mathrm{up}}^{\mathrm{T}} \boldsymbol{D}_{\mathrm{us}} \\ N \underline{Y}_{\mathrm{spW}} \boldsymbol{D}_{\mathrm{us}}^{\mathrm{T}} \boldsymbol{D}_{\mathrm{up}} & N^2 \boldsymbol{D}_{\mathrm{us}}^{\mathrm{T}} \left(\underline{Y}'_{\mathrm{CsE}} + \underline{Y}_{\mathrm{ssW}} \boldsymbol{D}_{\mathrm{us}} \right) \end{bmatrix} \tag{3.21}$$

Using the transformation matrix $\underline{\boldsymbol{T}}_{\mathrm{M}}$ as given in (2.1), the phase current and voltage vectors in (3.20) can be transformed to their symmetrical sequence components as follows

$$\underline{\boldsymbol{i}}_{\mathrm{A},120} = \underline{\boldsymbol{T}}_{\mathrm{M}} \underline{\boldsymbol{i}}_{\mathrm{A,abc}} \quad \underline{\boldsymbol{i}}_{\mathrm{B},120} = \underline{\boldsymbol{T}}_{\mathrm{M}} \underline{\boldsymbol{i}}_{\mathrm{B,abc}} \quad \underline{\boldsymbol{u}}_{\mathrm{A},120} = \underline{\boldsymbol{T}}_{\mathrm{M}} \underline{\boldsymbol{u}}_{\mathrm{A,abc}}$$
$$\underline{\boldsymbol{u}}_{\mathrm{B},120} = \underline{\boldsymbol{T}}_{\mathrm{M}} \underline{\boldsymbol{u}}_{\mathrm{B,abc}} \tag{3.22}$$

Furtherly, the phase admittance matrix $\underline{\boldsymbol{Y}}_{\mathrm{T,abc}}$ in (3.20) can be transformed to the sequence admittance matrix $\underline{\boldsymbol{Y}}_{\mathrm{T},120}$ as in

$$\begin{bmatrix} \underline{\boldsymbol{i}}_{\mathrm{A},120} \\ \underline{\boldsymbol{i}}_{\mathrm{B},120} \end{bmatrix} = \underbrace{\begin{bmatrix} \underline{\boldsymbol{T}}_{\mathrm{M}} & \boldsymbol{0} \\ \boldsymbol{0} & \underline{\boldsymbol{T}}_{\mathrm{M}} \end{bmatrix} \underline{\boldsymbol{Y}}_{\mathrm{T,abc}} \begin{bmatrix} \underline{\boldsymbol{T}}_{\mathrm{M}} & \boldsymbol{0} \\ \boldsymbol{0} & \underline{\boldsymbol{T}}_{\mathrm{M}} \end{bmatrix}^{-1}}_{\underline{\boldsymbol{Y}}_{\mathrm{T},120}} \begin{bmatrix} \underline{\boldsymbol{u}}_{\mathrm{A},120} \\ \underline{\boldsymbol{u}}_{\mathrm{B},120} \end{bmatrix} \tag{3.23}$$

Under balanced operating condition, the 6-order admittance matrix $\underline{\boldsymbol{Y}}_{\mathrm{T},120}$ can be furtherly decomposed into three second-order sequence component admittance matrices as in

$$\begin{bmatrix} \underline{I}_{\mathrm{A},1} \\ \underline{I}_{\mathrm{B},1} \end{bmatrix} = \underbrace{\begin{bmatrix} \underline{\boldsymbol{Y}}_{\mathrm{T},120}(1,1) & \underline{\boldsymbol{Y}}_{\mathrm{T},120}(1,4) \\ \underline{\boldsymbol{Y}}_{\mathrm{T},120}(4,1) & \underline{\boldsymbol{Y}}_{\mathrm{T},120}(4,4) \end{bmatrix}}_{\underline{\boldsymbol{Y}}_{\mathrm{T},1}} \begin{bmatrix} \underline{U}_{\mathrm{A},1} \\ \underline{U}_{\mathrm{B},1} \end{bmatrix}$$
$$\begin{bmatrix} \underline{I}_{\mathrm{A},2} \\ \underline{I}_{\mathrm{B},2} \end{bmatrix} = \underbrace{\begin{bmatrix} \underline{\boldsymbol{Y}}_{\mathrm{T},120}(2,2) & \underline{\boldsymbol{Y}}_{\mathrm{T},120}(2,5) \\ \underline{\boldsymbol{Y}}_{\mathrm{T},120}(5,2) & \underline{\boldsymbol{Y}}_{\mathrm{T},120}(5,5) \end{bmatrix}}_{\underline{\boldsymbol{Y}}_{\mathrm{T},2}} \begin{bmatrix} \underline{U}_{\mathrm{A},2} \\ \underline{U}_{\mathrm{B},2} \end{bmatrix} \tag{3.24}$$
$$\begin{bmatrix} \underline{I}_{\mathrm{A},0} \\ \underline{I}_{\mathrm{B},0} \end{bmatrix} = \underbrace{\begin{bmatrix} \underline{\boldsymbol{Y}}_{\mathrm{T},120}(3,3) & \underline{\boldsymbol{Y}}_{\mathrm{T},120}(3,6) \\ \underline{\boldsymbol{Y}}_{\mathrm{T},120}(6,3) & \underline{\boldsymbol{Y}}_{\mathrm{T},120}(6,6) \end{bmatrix}}_{\underline{\boldsymbol{Y}}_{\mathrm{T},0}} \begin{bmatrix} \underline{U}_{\mathrm{A},0} \\ \underline{U}_{\mathrm{B},0} \end{bmatrix}$$

where $\underline{\boldsymbol{Y}}_{\mathrm{T},1}$, $\underline{\boldsymbol{Y}}_{\mathrm{T},2}$ and $\underline{\boldsymbol{Y}}_{\mathrm{T},0}$ represente the postive-, negative- and zero-sequence admittance matrices of a three-phase two-winding transformer, respectively. Through matrix inversion, the corresponding impedance matrices can be obtained as

$$\underline{\boldsymbol{Z}}_{\mathrm{T},1} = \underline{\boldsymbol{Y}}_{\mathrm{T},1}^{-1} \qquad \underline{\boldsymbol{Z}}_{\mathrm{T},2} = \underline{\boldsymbol{Y}}_{\mathrm{T},2}^{-1} \qquad \underline{\boldsymbol{Z}}_{\mathrm{T},0} = \underline{\boldsymbol{Y}}_{\mathrm{T},0}^{-1} \tag{3.25}$$

3.2.2 Simulation Validation

Based on the three-phase two-winding transformer model, a transformer model considering capacitance effect is built in MATLAB/Simulink, as shown in Figure 3.8. Parameters of the transformer are given in Table 3.1. Winding connection vector group of the examplary transformer is Yd5. To validate its impedance characteristic, the transformer is tested in the way of setting the secondary windings as short-circuit, and the primary windings in connection with an equivalent 150 kV grid with the short-circuit capacity of 3 GW and X/R ratio of 10.

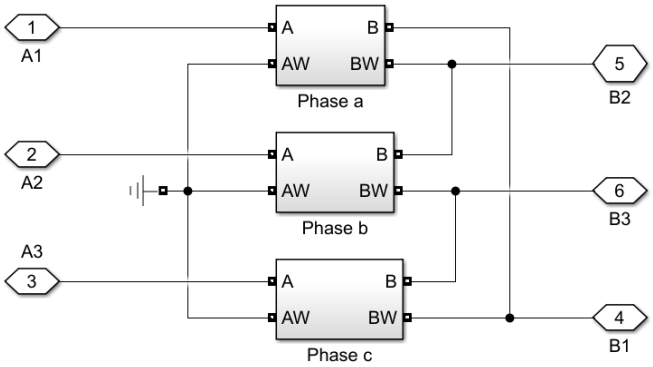

(a) Winding configuration in vector group Yd5

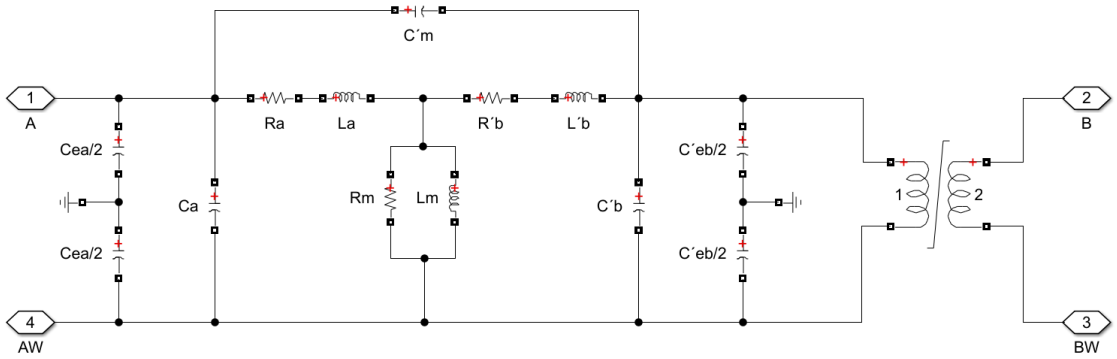

(b) Electrical circuit of a single phase

Figure 3.8 Tranformer model considering capacitance effect in Simulink

Table 3.1 Parameters of the simulated transformer

Rated Power	420 MW
Nominal voltages	150 kV/155 kV
Winding connections	Primary: Yg, secondary: D1
Primary winding parameters (pu)	$L_{\mathrm{A}} = 0.07,\ R_{\mathrm{A}} = 0.07/100$
Secondary winding parameters, reflected to primary side (pu)	$L_{\mathrm{B}} = 0.07,\ R_{\mathrm{B}} = 0.07/100$
Magnetizing branch (pu)	$L_{\mathrm{m}} = 500,\ R_{\mathrm{m}} = 500$
Parasitic capacitances C_{M}, C_{WA}, C_{WB}, C_{EA} or C_{EB}	1 nF or 20 nF

From the test setting, the secondary side phase voltages $\underline{\boldsymbol{u}}_{\mathrm{B,abc}}$ are equal to $\begin{bmatrix}0 & 0 & 0\end{bmatrix}^{\mathrm{T}}$, thus the corresponding symmetrical components $\underline{\boldsymbol{u}}_{\mathrm{B,120}}$ are also equal to $\begin{bmatrix}0 & 0 & 0\end{bmatrix}^{\mathrm{T}}$. After obtaining the primary side voltages $\underline{\boldsymbol{u}}_{\mathrm{A,abc}}$ and currents $\underline{\boldsymbol{i}}_{\mathrm{A,abc}}$ from simulations and transforming them into sequence components $\underline{\boldsymbol{u}}_{\mathrm{A,120}}$ and $\underline{\boldsymbol{i}}_{\mathrm{A,120}}$, the primary side admittances of the matrices $\underline{\boldsymbol{Y}}_{\mathrm{T,1}}$, $\underline{\boldsymbol{Y}}_{\mathrm{T,2}}$, $\underline{\boldsymbol{Y}}_{\mathrm{T,0}}$ in (3.24) can be obtained as in

$$\begin{aligned}
\underline{\boldsymbol{Y}}_{\mathrm{T,1}}(1,1) &= \underline{I}_{\mathrm{A,1}} / \underline{U}_{\mathrm{A,1}} \\
\underline{\boldsymbol{Y}}_{\mathrm{T,2}}(1,1) &= \underline{I}_{\mathrm{A,2}} / \underline{U}_{\mathrm{A,2}} \\
\underline{\boldsymbol{Y}}_{\mathrm{T,0}}(1,1) &= \underline{I}_{\mathrm{A,0}} / \underline{U}_{\mathrm{A,0}}
\end{aligned} \tag{3.26}$$

where $\underline{I}_{\mathrm{A,1}}$, $\underline{I}_{\mathrm{A,2}}$, $\underline{I}_{\mathrm{A,0}}$ denote the symmetrical components of the primary side currents, and $\underline{U}_{\mathrm{A,1}}$, $\underline{U}_{\mathrm{A,2}}$, $\underline{U}_{\mathrm{A,0}}$ denote the symmetrical components of the primary side voltages.

Figure 3.9 shows the frequency scanning of the positive sequence impedance $\underline{\boldsymbol{Z}}_{\mathrm{T,1}}(1,1)$ when all capacitance parameters of the transformer model as illustrated in Figure 3.8 are set to 1 nF or 20 nF. Solid lines represent the analytically derived impedances and the asterisks represent the simulation results. It is observed, that the simulation results in Simulink match well with the analytical models. In the scenario that all capacitance parameters are set to 20 nF, the first internal resonance of the simulated transformer is seen at the frequency down to 2 kHz. In the scenario that all capacitance parameters are set to 1 nF, the transformer shows near-linear inductive characteristic for the whole frequency range and the capacitance effect is only observable at above 3 kHz, which is indicated by the occurrence of nonlinearity in the impedance curve. Note, that the mismatch between the analytical model and the simulation result in the phase plot of Figure 3.9 (a) is induced by the equivalence of the magnetizing branch in the analytical

impedance model. Since the error is smaller than 1°, it is negligible for the tested frequency range.

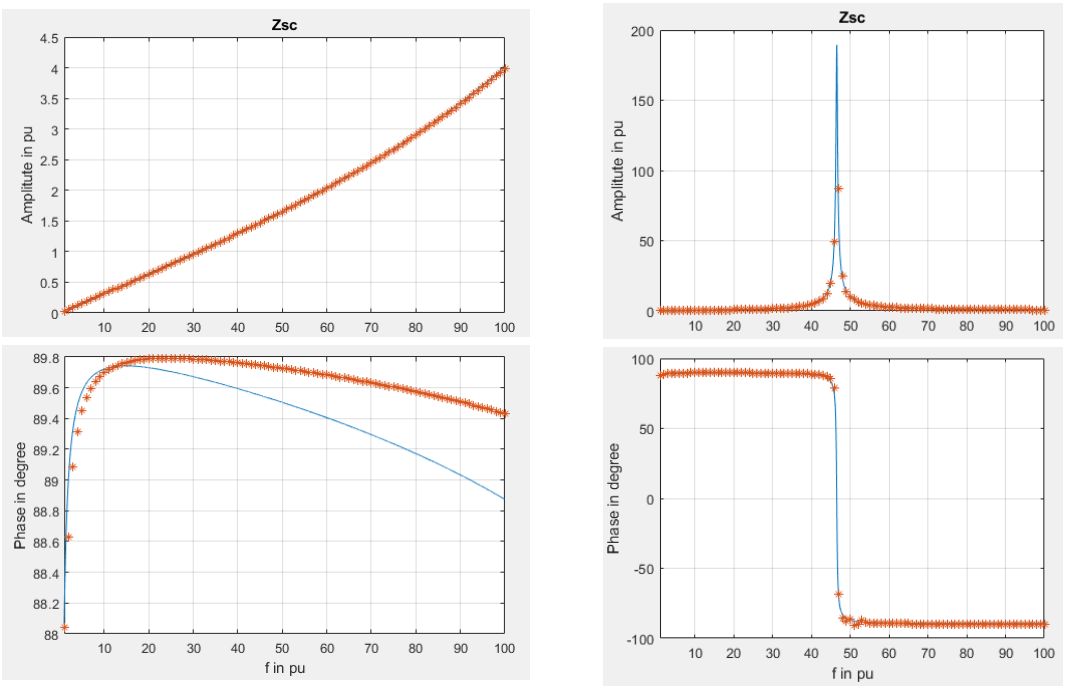

(a) 1 nF (b) 20 nF

Figure 3.9 Validation of the transformer model considering stray capacitance effects.

3.3 DFIG-based Wind Turbine

The DFIG-based WT is typically comprised of an induction machine, rotor side converter (RSC), grid side converter (GSC) and a terminal harmonic filter. Some recent published papers [23]-[26] tried to obtain its accurate impedance model accounting for converter outer loop control, frequency coupling effect or the DC dynamic between the back-to-back converters. Although model accuracy has been largely improved, the impedance modelling regarding differenct control strategies still needs to be furtherly investigated.

Figure 3.10 shows the circuit and control diagram of the investigated DFIG-based WT. Cascased double-loop PI control is applied under synchronous reference frame (SRF) for the GSC and RSC. The RSC controls active power through regulating rotor speed in the d-axis and controls reactive power or AC voltage in the q-axis. The GSC controls DC side voltage. Phase-locked loop is used to synchronize WT terminal voltage with the grid voltage.

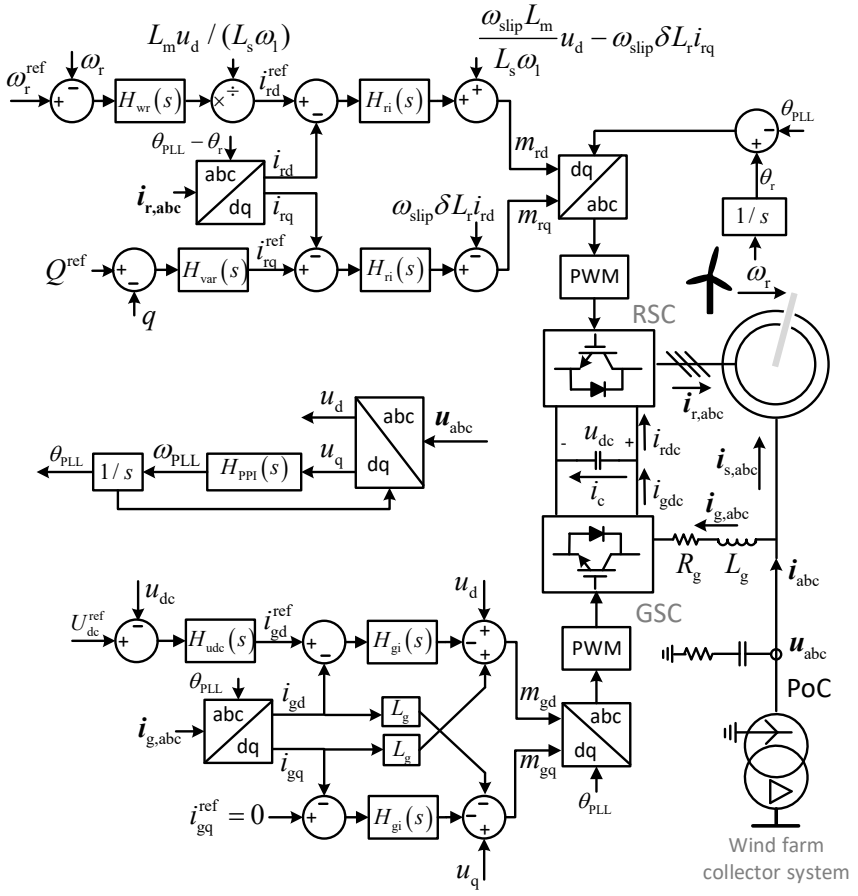

Figure 3.10 Circuit and control diagram of the investigated DFIG-based wind turbine

Generally, the impedance modelling for DFIG-based wind turbine is conducted either in dq frame or using symmetric components in stationary reference frame. In comparison with DQ impedances, symmetric component impedances have clearer physical meaning, and are easier to be validated through simulations or grid measurements. The impedances under different frames can be transformed to each other through frequency shifting and linear matrix transformation. Since the converter control is implemented in SRF, the impedance modelling of the DFIG-based WT will be firstly conducted in dq frame, and then for easier simulation validation and application in resonance analysis, it is transformed to sequence impedances.

According to the current and voltage relationships as illustrated in Figure 3.10 and the Park transformation of different frequency components as derived in Appendix A, the frequency domain representation of the DFIG energy conversion system are easily found to be

$$\begin{aligned}
&\text{GSC Branch} \begin{cases} \Delta \underline{\boldsymbol{i}}_{\text{g,dq}} = \underline{\boldsymbol{Y}}_{\text{gsc}} \Delta \underline{\boldsymbol{u}}_{\text{dq}} - \underline{\boldsymbol{a}}_{2\times 1} \Delta \underline{u}_{\text{dc}} \\ \Delta \underline{i}_{\text{gdc}} = \underline{\boldsymbol{b}}_{1\times 2} \Delta \underline{\boldsymbol{u}}_{\text{dq}} - \underline{Y}_{\text{gdc}} \Delta \underline{u}_{\text{dc}} \end{cases} \\
&\text{RSC Branch} \begin{cases} \Delta \underline{\boldsymbol{i}}_{\text{s,dq}} = \underline{\boldsymbol{Y}}_{\text{rsc}} \Delta \underline{\boldsymbol{u}}_{\text{dq}} + \underline{\boldsymbol{c}}_{2\times 1} \Delta \underline{u}_{\text{dc}} \\ \Delta \underline{i}_{\text{rdc}} = \underline{\boldsymbol{d}}_{1\times 2} \Delta \underline{\boldsymbol{u}}_{\text{dq}} + \underline{Y}_{\text{rdc}} \Delta \underline{u}_{\text{dc}} \end{cases} \\
&\text{DC Link} \qquad sC_{\text{dc}} \Delta \underline{u}_{\text{dc}} = \Delta \underline{i}_{\text{gdc}} - \Delta \underline{i}_{\text{rdc}}
\end{aligned} \tag{3.27}$$

where the symbol Δ denotes small signal perturbation or response, the voltage and current variables in bold type denote the d- and q-axis component vectors, e.g. $\Delta \underline{\boldsymbol{u}}_{\text{dq}}$ denotes $[\Delta \underline{u}_{\text{d}} \; \Delta \underline{u}_{\text{q}}]^{\text{T}}$, the other quantities in bold type are matrices, column or row vectors, and the underlined quantities denote complex values. The basic idea of the dq-frame impedance modelling as given in (3.27) is: when imposing a voltage perturbation $\Delta \underline{\boldsymbol{u}}_{\text{dq}}$ at WT terminal, the GSC and RSC branches will have both AC current responses ($\Delta \underline{\boldsymbol{i}}_{\text{g,dq}}$ and $\Delta \underline{\boldsymbol{i}}_{\text{s,dq}}$) and DC current responses ($\Delta \underline{i}_{\text{gdc}}$ and $\Delta \underline{i}_{\text{rdc}}$), and as well, the DC link will have DC voltage response $\Delta \underline{u}_{\text{dc}}$. Jointly solving the equations in (3.27) gives the relationship between WT terminal voltage and feed-in current, as represented by

$$\Delta \underline{\boldsymbol{i}}_{\text{dq}} = \Delta \underline{\boldsymbol{i}}_{\text{g,dq}} + \Delta \underline{\boldsymbol{i}}_{\text{s,dq}} = \underline{\boldsymbol{Y}}_{\text{wt,dq}} \Delta \underline{\boldsymbol{u}}_{\text{dq}} \tag{3.28}$$

where

$$\underline{\boldsymbol{Y}}_{\text{wt,dq}} = \underline{\boldsymbol{Y}}_{\text{gsc}} + \underline{\boldsymbol{Y}}_{\text{rsc}} + \frac{\left(\underline{\boldsymbol{c}}_{2\times 1} - \underline{\boldsymbol{a}}_{2\times 1}\right)\left(\underline{\boldsymbol{b}}_{1\times 2} - \underline{\boldsymbol{d}}_{1\times 2}\right)}{\underline{Y}_{\text{gdc}} + \underline{Y}_{\text{rdc}} + sC_{\text{dc}}} \tag{3.29}$$

with $\underline{\boldsymbol{Y}}_{\text{wt,dq}}$ denoting WT output admittance, $\underline{\boldsymbol{Y}}_{\text{gsc}}$ and $\underline{\boldsymbol{Y}}_{\text{rsc}}$ denoting the output admittances of the RSC and GSC branches under the assumption of a constant DC voltage, and the other part of the admittance expression interpreting the DC-coupling of the RSC and GSC branches. Details on the derivation of the GSC and RSC models in (3.27) will be presented in sections 3.3.1 and 3.3.2. Transformation of the model in (3.29) to sequence impedances will be presented in section 3.3.3. The derivation will be conducted in per unit system. Base values for both AC and DC side grids are given in Appendix C.

3.3.1 GSC modelling

In the GSC branch, the converter control has two dq frames due to the dynamic of the Phase-locked Loop (PLL): one is the system dq frame (denoted by a superscript s), and

the other is the controller dq frame (denoted by a superscript c), as shown in Figure 3.11 [73]. The system dq frame is defined by the grid voltage and the controller dq frame is defined by the PLL, which estimates the frequency ω_1 and angle $\theta_1(t)$ of the grid voltage to find the position of the system dq frame. In a steady state, the controller dq frame is aligned with the system dq frame. When small-signal perturbations are added to the grid voltage, the controller dq frame is no longer aligned with the system dq frame because of the PLL dynamics. The angle difference between the two dq frames is

$$\Delta\theta(t) = \theta_{\mathrm{PLL}}(t) - \theta_1(t) \tag{3.30}$$

where $\theta_{\mathrm{PLL}}(t)$ denotes the PLL angle.

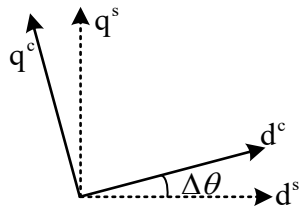

Figure 3.11 Diagram of system and controller dq frames

In order to deal with the nonlinearity in Park's transformation, the transformation matrix

$$\boldsymbol{T}(\theta_{\mathrm{PLL}}(t)) = \frac{2}{3}\begin{bmatrix} \cos\theta_{\mathrm{PLL}}(t) & \cos(\theta_{\mathrm{PLL}}(t)-2\pi/3) & \cos(\theta_{\mathrm{PLL}}(t)+2\pi/3) \\ \sin\theta_{\mathrm{PLL}}(t) & \sin(\theta_{\mathrm{PLL}}(t)-2\pi/3) & \sin(\theta_{\mathrm{PLL}}(t)+2\pi/3) \end{bmatrix} \tag{3.31}$$

can be decomposed into $\boldsymbol{T}(\theta_1(t))$ and $\boldsymbol{T}_{\Delta\theta}(t)$, as given by

$$\boldsymbol{T}\left(\theta_{\mathrm{PLL}}(t)\right) = \underbrace{\begin{bmatrix} \cos\left(\Delta\theta(t)\right) & \sin\left(\Delta\theta(t)\right) \\ -\sin\left(\Delta\theta(t)\right) & \cos\left(\Delta\theta(t)\right) \end{bmatrix}}_{\boldsymbol{T}_{\Delta\theta}(t)} \boldsymbol{T}\left(\theta_1(t)\right) \approx \begin{bmatrix} 1 & \Delta\theta(t) \\ -\Delta\theta(t) & 1 \end{bmatrix} \boldsymbol{T}\left(\theta_1(t)\right) \tag{3.32}$$

where $\boldsymbol{T}(\theta_1(t))$ denotes the Park's transformation from phase domain to the system dq frame, which equals to the rotation of $\mathrm{e}^{-\mathrm{j}\omega_1 t}$, and $\boldsymbol{T}_{\Delta\theta}(t)$ denotes the transformation from the system dq frame to the controller dq frame. Under the assumption of a small $\Delta\theta(t)$, $\cos(\Delta\theta(t))$ can be approximated to $\Delta\theta(t)$ and $\sin(\Delta\theta(t))$ can be approximated to 1.

As the inputs of GSC control, the voltages and currents in the system dq frame need to be transformed to the controller dq frame by multiplying $\boldsymbol{T}_{\Delta\theta}(t)$. To generate the modulation

signals for the power converter, the outputs of the cascaded double-loop PI control need to be transformed back to the system dq frame by multiplying $\boldsymbol{T}_{\Delta\theta}(t)^{-1}$. The frequency domain representation of the involved dq frame rotations for voltages, currents and modulating signals are

$$\underline{\boldsymbol{u}}_{\mathrm{dq}}^{\mathrm{c}} = \underline{\boldsymbol{T}}_{\Delta\theta}\,\underline{\boldsymbol{u}}_{\mathrm{dq}}^{\mathrm{s}} \qquad \underline{\boldsymbol{i}}_{\mathrm{g,dq}}^{\mathrm{c}} = \underline{\boldsymbol{T}}_{\Delta\theta}\,\underline{\boldsymbol{i}}_{\mathrm{g,dq}}^{\mathrm{s}} \qquad \underline{\boldsymbol{m}}_{\mathrm{g,dq}}^{\mathrm{s}} = \underline{\boldsymbol{T}}_{\Delta\theta}^{-1}\,\underline{\boldsymbol{m}}_{\mathrm{g,dq}}^{\mathrm{c}} \tag{3.33}$$

where $\underline{\boldsymbol{T}}_{\Delta\theta}$ is the frequency domain representation for $\boldsymbol{T}_{\Delta\theta}(t)$, $\underline{\boldsymbol{u}}_{\mathrm{dq}}^{\mathrm{c}}$ denotes $\begin{bmatrix}\underline{u}_{\mathrm{d}}^{\mathrm{c}} & \underline{u}_{\mathrm{q}}^{\mathrm{c}}\end{bmatrix}^{\mathrm{T}}$, $\underline{\boldsymbol{u}}_{\mathrm{dq}}^{\mathrm{s}}$ denotes $\begin{bmatrix}\underline{u}_{\mathrm{d}}^{\mathrm{s}} & \underline{u}_{\mathrm{q}}^{\mathrm{s}}\end{bmatrix}^{\mathrm{T}}$ and other quantities follow the same notation. Performing small-signal analysis to the voltage, current and modulating signals in (3.33) yields

$$\begin{aligned}
\Delta\underline{\theta} &= \underline{H}_{\mathrm{PLL}}\Delta\underline{u}_{\mathrm{q}}^{\mathrm{s}} \\
\Delta\underline{\boldsymbol{u}}_{\mathrm{dq}}^{\mathrm{c}} = \underline{\boldsymbol{H}}_{\mathrm{PLL}}^{\mathrm{u}}\Delta\underline{\boldsymbol{u}}_{\mathrm{dq}}^{\mathrm{s}},\ \Delta\underline{\boldsymbol{i}}_{\mathrm{g,dq}}^{\mathrm{c}} &= \underline{\boldsymbol{H}}_{\mathrm{PLL}}^{\mathrm{i}}\Delta\underline{\boldsymbol{u}}_{\mathrm{dq}}^{\mathrm{s}} + \Delta\underline{\boldsymbol{i}}_{\mathrm{g,dq}}^{\mathrm{s}} \\
\Delta\underline{\boldsymbol{m}}_{\mathrm{g,dq}}^{\mathrm{s}} &= \underline{\boldsymbol{H}}_{\mathrm{PLL}}^{\mathrm{m}}\Delta\underline{\boldsymbol{u}}_{\mathrm{dq}}^{\mathrm{s}} + \Delta\underline{\boldsymbol{m}}_{\mathrm{g,dq}}^{\mathrm{c}}
\end{aligned} \tag{3.34}$$

where $\Delta\underline{\theta}$ is the frequency domain representation of $\Delta\theta(t)$ and

$$\begin{aligned}
\underline{H}_{\mathrm{PLL}} &= \frac{\underline{H}_{\mathrm{PPI}}}{\underline{s} + U_{1\mathrm{d}}\underline{H}_{\mathrm{PPI}}} \qquad \underline{\boldsymbol{H}}_{\mathrm{PLL}}^{\mathrm{u}} = \begin{bmatrix} 1 & U_{1\mathrm{q}}\underline{H}_{\mathrm{PPI}} \\ 0 & 1 - U_{1\mathrm{d}}\underline{H}_{\mathrm{PPI}} \end{bmatrix} \\
\underline{\boldsymbol{H}}_{\mathrm{PLL}}^{\mathrm{i}} &= \begin{bmatrix} 0 & I_{\mathrm{g1q}}\underline{H}_{\mathrm{PPI}} \\ 0 & -I_{\mathrm{g1d}}\underline{H}_{\mathrm{PPI}} \end{bmatrix} \quad \underline{\boldsymbol{H}}_{\mathrm{PLL}}^{\mathrm{m}} = \begin{bmatrix} 0 & -M_{\mathrm{g1q}}\underline{H}_{\mathrm{PPI}} \\ 0 & M_{\mathrm{g1d}}\underline{H}_{\mathrm{PPI}} \end{bmatrix}
\end{aligned} \tag{3.35}$$

with $\underline{H}_{\mathrm{PPI}}$ denoting the transfer function of the PI controller in PLL and $U_{1\mathrm{d}}$, $U_{1\mathrm{q}}$, I_{g1d}, I_{g1q}, M_{g1d}, M_{g1q} denoting the steady state values of the corresponding voltage, current and modulation signals. Then performing small-signal analysis to the GSC power-stage circuit and converter control yields

$$\begin{aligned}
\Delta\underline{\boldsymbol{u}}_{\mathrm{dq}}^{\mathrm{s}} &= \underline{\boldsymbol{Z}}_{\mathrm{RL}}\Delta\underline{\boldsymbol{i}}_{\mathrm{g,dq}}^{\mathrm{s}} + \Delta\underline{\boldsymbol{m}}_{\mathrm{g,dq}}^{\mathrm{s}}\underline{G}_{\mathrm{d}}U_{\mathrm{dc0}} + \boldsymbol{m}_{\mathrm{g1}}\underline{G}_{\mathrm{d}}\Delta\underline{u}_{\mathrm{dc}} \\
\Delta\underline{\boldsymbol{m}}_{\mathrm{g,dq}}^{\mathrm{c}} &= -\underline{\boldsymbol{H}}_{\mathrm{gi}}(s)\left(\Delta\underline{\boldsymbol{i}}_{\mathrm{g,dq}}^{\mathrm{ref}} - \Delta\underline{\boldsymbol{i}}_{\mathrm{g,dq}}^{\mathrm{c}}\right) + \boldsymbol{K}_{\mathrm{gd}}\Delta\underline{\boldsymbol{i}}_{\mathrm{g,dq}}^{\mathrm{c}} + \Delta\underline{\boldsymbol{u}}_{\mathrm{dq}}^{\mathrm{c}} \\
\Delta\underline{\boldsymbol{i}}_{\mathrm{g,dq}}^{\mathrm{ref}} &= -\underline{\boldsymbol{h}}_{\mathrm{udc}}\Delta\underline{u}_{\mathrm{dc}}
\end{aligned} \tag{3.36}$$

where U_{dc0} denotes the steady state value of the DC voltage, $\boldsymbol{m}_{g1}$ denotes $[M_{g1d}\ M_{g1q}]^T$, $\underline{H}_d$ denotes the digital control delay for 1.5 times of sampling periods as described by

$$\underline{H}_d = 1/(1+1.5T_s\underline{s}) \tag{3.37}$$

and

$$\begin{aligned} \underline{\boldsymbol{Z}}_{RL} &= \begin{bmatrix} R_g + \underline{s}L_g/\omega_b & -\omega_1 L_g \\ \omega_1 L_g & R_g + \underline{s}L_g/\omega_b \end{bmatrix} \quad \underline{\boldsymbol{H}}_{gi}(s) = \begin{bmatrix} \underline{H}_{gi} & 0 \\ 0 & \underline{H}_{gi} \end{bmatrix} \\ \boldsymbol{K}_{gd} &= \begin{bmatrix} 0 & \omega_1 L_g \\ -\omega_1 L_g & 0 \end{bmatrix} \qquad \underline{\boldsymbol{h}}_{udc} = \begin{bmatrix} \underline{H}_{udc} \\ 0 \end{bmatrix} \end{aligned} \tag{3.38}$$

with $\underline{H}_{gi}$ denoting the transfer function of GSC current PI controller, $\underline{H}_{udc}$ denoting the transfer function of GSC DC voltage PI controller and ω_b is the base angular frequency for the per unit system. Jointly solving the equations in (3.34) and (3.36) yields

$$\Delta\underline{\boldsymbol{i}}^s_{g,dq} = \underline{\boldsymbol{Y}}_{gsc}\Delta\underline{\boldsymbol{u}}^s_{dq} - \underline{\boldsymbol{a}}_{2\times1}\Delta\underline{u}_{dc} \tag{3.39}$$

where the detailed expression of $\underline{\boldsymbol{Y}}_{gsc}$ and $\underline{\boldsymbol{a}}_{2\times1}$ are

$$\begin{aligned} \underline{\boldsymbol{Y}}_{gsc} &= \left[\underline{\boldsymbol{Z}}_{RL} + \left(\underline{\boldsymbol{H}}_{gi} + \boldsymbol{K}_{gd}\right)\underline{H}_d U_{dc0}\right]^{-1} \cdot \\ &\quad \left\{\boldsymbol{E}_2 - \left[\underline{\boldsymbol{H}}^m_{PLL} + \underline{\boldsymbol{H}}^u_{PLL} + \left(\underline{\boldsymbol{H}}_{gi} + \boldsymbol{K}_{gd}\right)\underline{\boldsymbol{H}}^i_{PLL}\right]\underline{H}_d U_{dc0}\right\} \\ \underline{\boldsymbol{a}}_{2\times1} &= \left[\underline{\boldsymbol{Z}}_{RL} + \left(\underline{\boldsymbol{H}}_{gi} + \boldsymbol{K}_{gd}\right)\underline{H}_d U_{dc0}\right]^{-1}\left(\underline{\boldsymbol{H}}_{gi}\underline{\boldsymbol{h}}_{udc}\underline{H}_d U_{dc0} + \boldsymbol{m}_{g1}\underline{H}_d\right) \end{aligned} \tag{3.40}$$

where $\boldsymbol{E}_2$ denotes the second-order identity matrix. Assuming an ideal lossless model for the converter, the time domain per unit representation of the power balance between the AC input and DC output of the GSC can be written as

$$p(t) = i_{gdc}(t)u_{dc}(t) = \mathrm{Re}\left\{\underline{i}^*_{g,dq}(t)\underline{u}_{g,dq}(t)\right\} \tag{3.41}$$

where

$$\underline{i}^*_{g,dq}(t) = i^s_{gd}(t) - \mathrm{j}i^s_{gq}(t) \qquad \underline{u}_{g,dq}(t) = u^s_{gd}(t) + \mathrm{j}u^s_{gq}(t) \tag{3.42}$$

Substituting

$$\underline{\boldsymbol{u}}_{\mathrm{g,dq}} = \underline{\boldsymbol{m}}^{\mathrm{s}}_{\mathrm{g,dq}} \underline{H}_{\mathrm{d}} \tag{3.43}$$

into the frequency domain representation of (3.41), performing small signal analysis to and rewriting the resulted equation can give

$$\Delta \underline{i}_{\mathrm{gdc}} = \underline{H}_{\mathrm{d}} \left(\boldsymbol{m}^{\mathrm{T}}_{\mathrm{g1}} \Delta \underline{\boldsymbol{i}}^{\mathrm{s}}_{\mathrm{g,dq}} + \boldsymbol{i}^{\mathrm{T}}_{\mathrm{g1}} \Delta \underline{\boldsymbol{m}}^{\mathrm{s}}_{\mathrm{g,dq}} \right) \tag{3.44}$$

where $\boldsymbol{i}^{\mathrm{T}}_{\mathrm{g1}}$ denotes $[I_{\mathrm{g1d}}\ I_{\mathrm{g1q}}]$. Furtherly substituting the modulating signals in (3.34) and (3.36) as well as the AC current signal in (3.39) into (3.44) yields

$$\Delta \underline{i}_{\mathrm{gdc}} = \underline{\boldsymbol{b}}_{\mathrm{1\times 2}} \Delta \underline{\boldsymbol{u}}^{\mathrm{s}}_{\mathrm{dq}} - \underline{Y}_{\mathrm{gdc}} \Delta \underline{u}_{\mathrm{dc}} \tag{3.45}$$

where the detailed expressions of $\underline{\boldsymbol{b}}_{1\times 2}$ and $\underline{Y}_{\mathrm{gdc}}$ are

$$\begin{aligned} \underline{\boldsymbol{b}}_{\mathrm{1\times 2}} &= \underline{H}_{\mathrm{d}} \left[\boldsymbol{m}^{\mathrm{T}}_{\mathrm{g1}} + \boldsymbol{i}^{\mathrm{T}}_{\mathrm{g1}} \left(\underline{\boldsymbol{H}}_{\mathrm{gi}} + \boldsymbol{K}_{\mathrm{gd}} \right) \right] \underline{\boldsymbol{Y}}_{\mathrm{gsc}} + \underline{H}_{\mathrm{d}} \boldsymbol{i}^{\mathrm{T}}_{\mathrm{g1}} \left[\underline{\boldsymbol{H}}^{\mathrm{m}}_{\mathrm{PLL}} + \left(\underline{\boldsymbol{H}}_{\mathrm{gi}} + \boldsymbol{K}_{\mathrm{gd}} \right) \underline{\boldsymbol{H}}^{\mathrm{i}}_{\mathrm{PLL}} + \underline{\boldsymbol{H}}^{\mathrm{u}}_{\mathrm{PLL}} \right] \\ \underline{Y}_{\mathrm{gdc}} &= \underline{H}_{\mathrm{d}} \left\{ -\boldsymbol{i}^{\mathrm{T}}_{\mathrm{g1}} \underline{\boldsymbol{H}}_{\mathrm{gi}} \underline{\boldsymbol{h}}_{\mathrm{udc}} + \left[\boldsymbol{m}^{\mathrm{T}}_{\mathrm{g1}} + \boldsymbol{i}^{\mathrm{T}}_{\mathrm{g1}} \left(\underline{\boldsymbol{H}}_{\mathrm{gi}} + \boldsymbol{K}_{\mathrm{gd}} \right) \right] \underline{\boldsymbol{a}}_{\mathrm{2\times 1}} \right\} \end{aligned} \tag{3.46}$$

Finally, the equations in (3.39) and (3.45) can represent the admittance model of the GSC branch.

3.3.2 RSC and DFIG machine modelling

Figure 3.12 shows the induction machine model in the system dq frame, in which all the rotor side quantities are reflected to the stator side and the variables $\underline{u}_{\mathrm{s}}(t)$, $\underline{i}_{\mathrm{s}}(t)$, $\underline{\psi}_{\mathrm{s}}(t)$, $\underline{u}_{\mathrm{r}}(t)$, $\underline{i}_{\mathrm{r}}(t)$ and $\underline{\psi}_{\mathrm{r}}(t)$ denote the space vectors composed of d- and q-axis components, e.g.

$$\underline{i}_{\mathrm{s}}(t) = i_{\mathrm{sd}}(t) + \mathrm{j} i_{\mathrm{sq}}(t)\,. \tag{3.47}$$

Note, that the stator voltage $\underline{u}_{\mathrm{s}}(t)$ is also the WT terminal voltage $\underline{u}(t)$.

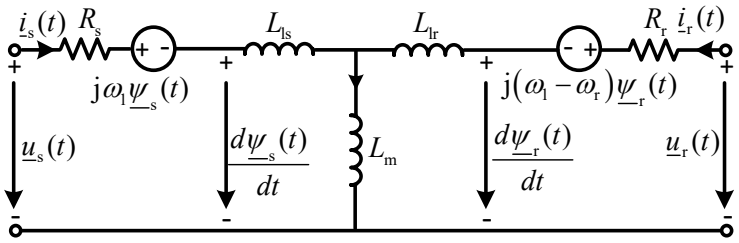

Figure 3.12 The induction machine model under synchronous frame [30]

According to the relationships between the rotor and stator voltages and the rotor and stator currents as illustrated in Figure 3.12, the d- and q-component flux and voltage equations of the induction machine can be formulated as

$$\text{Voltage equations}\begin{cases} u_d(t)=R_s i_{sd}(t)+\dfrac{d\psi_{sd}(t)}{dt}-\omega_l\psi_{sq}(t) \\ u_q(t)=R_s i_{sq}(t)+\dfrac{d\psi_{sq}(t)}{dt}+\omega_l\psi_{sd}(t) \\ u_{rd}(t)=R_r i_{rd}(t)+\dfrac{d\psi_{rd}(t)}{dt}-(\omega_l-\omega_r)\psi_{rq}(t) \\ u_{rq}(t)=R_r i_{rq}(t)+\dfrac{d\psi_{rq}(t)}{dt}+(\omega_l-\omega_r)\psi_{rd}(t) \end{cases} \tag{3.48}$$

$$\text{Flux equations}\begin{cases} \psi_{sd}(t)=(L_{ls}+L_m)i_{sd}(t)+L_m i_{rd}(t)=L_s i_{sd}(t)+L_m i_{rd}(t) \\ \psi_{sq}(t)=(L_{ls}+L_m)i_{sq}(t)+L_m i_{rq}(t)=L_s i_{sq}(t)+L_m i_{rq}(t) \\ \psi_{rd}(t)=(L_{lr}+L_m)i_{rd}(t)+L_m i_{sd}(t)=L_r i_{rd}(t)+L_m i_{sd}(t) \\ \psi_{rq}(t)=(L_{lr}+L_m)i_{rq}(t)+L_m i_{sq}(t)=L_r i_{rq}(t)+L_m i_{sq}(t) \end{cases} \tag{3.49}$$

where ω_r denotes the rotor speed. Performing Laplace transformation and small-signal analysis to (3.48) and (3.49), and then jointly solving them lead to

$$\begin{aligned} \Delta\underline{\boldsymbol{u}}^s_{dq} &= \underbrace{\begin{bmatrix} R_s+\underline{s}L_s & -\omega_l L_s \\ \omega_l L_s & R_s+\underline{s}L_s \end{bmatrix}}_{\underline{\boldsymbol{z}}_{ss}}\Delta\underline{\boldsymbol{i}}^s_{s,dq}+\underbrace{\begin{bmatrix} \underline{s}L_m & -\omega_l L_m \\ \omega_l L_m & \underline{s}L_m \end{bmatrix}}_{\underline{\boldsymbol{z}}_{sr}}\Delta\underline{\boldsymbol{i}}^s_{r,dq} \\ \Delta\underline{\boldsymbol{u}}^s_{r,dq} &= \underbrace{\begin{bmatrix} \underline{s}L_m & -\omega_{slip} L_m \\ \omega_{slip} L_m & \underline{s}L_m \end{bmatrix}}_{\underline{\boldsymbol{z}}_{rs}}\Delta\underline{\boldsymbol{i}}^s_{s,dq}+\underbrace{\begin{bmatrix} R_r+\underline{s}L_r & -\omega_{slip} L_r \\ \omega_{slip} L_r & R_r+\underline{s}L_r \end{bmatrix}}_{\underline{\boldsymbol{z}}_{rr}}\Delta\underline{\boldsymbol{i}}^s_{r,dq} \end{aligned} \tag{3.50}$$

where

$$L_s = L_{ls} + L_m \qquad L_r = L_{lr} + L_m \qquad \omega_{slip} = \omega_l - \omega_r \tag{3.51}$$

with ω_{slip} denoting the slip speed.

In comparison with the Park's transformation of GSC control, the angle needed for the Park transformation in RSC control involves not only $\theta_{PLL}(t)$, but also the angle of the rotor speed $\theta_r(t)$. Therefore, the Park's transformation in RSC control can be decomposed into

$$\boldsymbol{T}\left(\theta_{PLL}(t) - \theta_r(t)\right) \approx \underbrace{\begin{bmatrix} 1 & \Delta\theta(t) - \Delta\theta_r(t) \\ -\left(\Delta\theta(t) - \Delta\theta_r(t)\right) & 1 \end{bmatrix}}_{\boldsymbol{T}_{\Delta\theta r}(t)} \boldsymbol{T}\left(\theta_l(t) - \theta_{r1}(t)\right) \tag{3.52}$$

where $\theta_{r1}(t)$ denotes the steady state rotor speed angle, $\Delta\theta_r(t)$ is equal to $\theta_r(t)$ - $\theta_{r1}(t)$, $\boldsymbol{T}(\theta_l(t)$-$\theta_{r1}(t))$ denotes the Park's transformation from three-phase signal to the system dq frame and $\boldsymbol{T}_{\Delta\theta r}(t)$ denotes the transformation from the system dq frame to the controller dq frame. Since the frequency domain representation of $\Delta\theta(t)$ as denoted by $\Delta\underline{\theta}$ is already obtained in (3.34), only the frequency domain representation of $\Delta\theta_r(t)$, as denoted by $\Delta\underline{\theta}_r$, is needed to get the frequency domain representation of $\boldsymbol{T}_{\Delta\theta r}(t)$, as denoted by $\underline{\boldsymbol{T}}_{\Delta\theta r}$. For the induction machine of the wind turbine, the time domain motion, electromagnetic torque and stator voltage equations can be written as

$$\begin{aligned} J\frac{d\omega_r}{dt} &= T_m(t) - T_e(t) \\ T_e(t) &= \left(\psi_{sq}(t) i_{rd}(t) - \psi_{sd}(t) i_{rq}(t)\right) L_m / L_s \approx \psi_{sq}(t) i_{rd}(t) L_m / L_s \\ u_d(t) &= R_s i_{sd}(t) + \frac{d\psi_{sd}(t)}{dt} - \omega_l \psi_{sq}(t) \approx -\omega_l \psi_{sq}(t) \end{aligned} \tag{3.53}$$

where $T_m(t)$ and $T_e(t)$ represent the mechanical and electromagnetic torques and J is the turbine moment of inertia [30]. Performing small-signal analysis to the equations in (3.53) and jointly solving them in frequency domain yield

$$\Delta\underline{\omega}_r = \underbrace{\frac{U_d L_m}{\omega_l L_s J \underline{s}}}_{\underline{H}_{wr}} \Delta\underline{i}_{rd} \qquad \Delta\underline{\theta}_r = \underbrace{\frac{U_d L_m}{\omega_l L_s J \underline{s}^2}}_{\underline{H}_{wtr}} \Delta\underline{i}_{rd} \tag{3.54}$$

where $\underline{H}_{\mathrm{wr}}$ and $\underline{H}_{\mathrm{wr}}$ are the transfer functions from $\Delta\underline{i}_{\mathrm{rd}}$ to $\Delta\underline{\omega}_{\mathrm{r}}$ and $\Delta\underline{\theta}_{\mathrm{r}}$. Furtherly performing small-signal analysis to the dq-frame rotations involved in the RSC control as represented by

$$\underline{\boldsymbol{i}}^{\mathrm{c}}_{\mathrm{r,dq}} = \underline{\boldsymbol{T}}_{\Delta\theta\mathrm{r}}\,\underline{\boldsymbol{i}}^{\mathrm{s}}_{\mathrm{r,dq}} \qquad \underline{\boldsymbol{m}}^{\mathrm{s}}_{\mathrm{r}} = \underline{\boldsymbol{T}}^{-1}_{\Delta\theta\mathrm{r}}\,\underline{\boldsymbol{m}}^{\mathrm{c}}_{\mathrm{r}} \tag{3.55}$$

yields

$$\begin{aligned}\Delta\underline{\boldsymbol{i}}^{\mathrm{c}}_{\mathrm{r,dq}} &= \underline{\boldsymbol{H}}^{\mathrm{ri}}_{\mathrm{PLL}}\Delta\underline{\boldsymbol{u}}^{\mathrm{s}}_{\mathrm{dq}} + \underline{\boldsymbol{H}}^{\mathrm{i}}_{\mathrm{wtr}}\Delta\underline{\boldsymbol{i}}^{\mathrm{s}}_{\mathrm{r,dq}}\\ \Delta\underline{\boldsymbol{m}}^{\mathrm{s}}_{\mathrm{r,dq}} &= \underline{\boldsymbol{H}}^{\mathrm{rm}}_{\mathrm{PLL}}\Delta\underline{\boldsymbol{u}}^{\mathrm{s}}_{\mathrm{dq}} + \underline{\boldsymbol{H}}^{\mathrm{m}}_{\mathrm{wtr}}\Delta\underline{\boldsymbol{i}}^{\mathrm{s}}_{\mathrm{r,dq}} + \Delta\underline{\boldsymbol{m}}^{\mathrm{c}}_{\mathrm{r,dq}}\end{aligned} \tag{3.56}$$

where

$$\begin{aligned}\underline{\boldsymbol{H}}^{\mathrm{ri}}_{\mathrm{PLL}} &= \begin{bmatrix}0 & I_{\mathrm{r1q}}\underline{H}_{\mathrm{PLL}}\\ 0 & -I_{\mathrm{r1d}}\underline{H}_{\mathrm{PLL}}\end{bmatrix} \qquad \underline{\boldsymbol{H}}^{\mathrm{i}}_{\mathrm{wtr}} = \begin{bmatrix}1-\underline{H}_{\mathrm{wtr}}I_{\mathrm{r1q}} & 0\\ \underline{H}_{\mathrm{wtr}}I_{\mathrm{r1d}} & 1\end{bmatrix}\\ \underline{\boldsymbol{H}}^{\mathrm{rm}}_{\mathrm{PLL}} &= \begin{bmatrix}0 & -M_{\mathrm{r1q}}\underline{H}_{\mathrm{PLL}}\\ 0 & M_{\mathrm{r1d}}\underline{H}_{\mathrm{PLL}}\end{bmatrix} \qquad \underline{\boldsymbol{H}}^{\mathrm{m}}_{\mathrm{wtr}} = \begin{bmatrix}\underline{H}_{\mathrm{wtr}}M_{\mathrm{r1q}} & 0\\ -\underline{H}_{\mathrm{wtr}}M_{\mathrm{r1d}} & 0\end{bmatrix}\end{aligned} \tag{3.57}$$

with I_{r1d}, I_{r1q}, M_{r1d}, M_{r1q} denoting the steady state values of the corresponding current and modulation signals. For the RSC control, the small-signal representation can be written as

$$\begin{aligned}\Delta\underline{\boldsymbol{u}}^{\mathrm{s}}_{\mathrm{r}} &= \Delta\underline{\boldsymbol{m}}^{\mathrm{s}}_{\mathrm{r,dq}}\underline{H}_{\mathrm{d}}U_{\mathrm{dc0}} + \boldsymbol{m}_{\mathrm{r1}}\underline{H}_{\mathrm{d}}\Delta\underline{u}_{\mathrm{dc}}\\ \Delta\underline{\boldsymbol{m}}^{\mathrm{c}}_{\mathrm{r,dq}} &= \underline{\boldsymbol{H}}_{\mathrm{ri}}\left(\Delta\underline{\boldsymbol{i}}^{\mathrm{ref}}_{\mathrm{r,dq}} - \Delta\underline{\boldsymbol{i}}^{\mathrm{c}}_{\mathrm{r,dq}}\right) + \boldsymbol{K}_{\mathrm{rd}}\Delta\underline{\boldsymbol{i}}^{\mathrm{c}}_{\mathrm{r,dq}} + \boldsymbol{K}_{\mathrm{us}}\Delta\underline{\boldsymbol{u}}^{\mathrm{c}}_{\mathrm{s,dq}}\\ \Delta\underline{\boldsymbol{i}}^{\mathrm{ref}}_{\mathrm{r,dq}} &= \underline{\boldsymbol{H}}_{\mathrm{pq1}}\Delta\underline{\boldsymbol{i}}^{\mathrm{c}}_{\mathrm{r,dq}} + \underline{\boldsymbol{H}}_{\mathrm{var1}}\Delta\underline{\boldsymbol{u}}^{\mathrm{c}}_{\mathrm{s,dq}} + \underline{\boldsymbol{H}}_{\mathrm{var2}}\Delta\underline{\boldsymbol{i}}^{\mathrm{c}}_{\mathrm{s,dq}}\end{aligned} \tag{3.58}$$

where $\boldsymbol{m}_{\mathrm{r1}}$ denotes $[M_{\mathrm{r1d}}\ \ M_{\mathrm{r1q}}]^{\mathrm{T}}$ and

$$\begin{aligned}&\underline{\boldsymbol{H}}_{\mathrm{ri}} = \underline{H}_{\mathrm{ri}}\begin{bmatrix}1 & 0\\ 0 & 1\end{bmatrix} \qquad \boldsymbol{K}_{\mathrm{rd}} = \omega_{\mathrm{slip}}L_{\mathrm{r}}\delta\begin{bmatrix}0 & -1\\ 1 & 0\end{bmatrix} \qquad \boldsymbol{K}_{\mathrm{us}} = \begin{bmatrix}\dfrac{\omega_{\mathrm{slip}}L_{\mathrm{m}}}{\omega_{1}L_{\mathrm{s}}} & 0\\ 0 & 0\end{bmatrix}\\ &\underline{\boldsymbol{H}}_{\mathrm{pq1}} = \frac{\underline{H}_{\mathrm{wr}}}{\mathrm{J}\underline{s}}\begin{bmatrix}1 & 0\\ 0 & 0\end{bmatrix} \qquad \underline{\boldsymbol{H}}_{\mathrm{var1}} = \underline{H}_{\mathrm{var}}\begin{bmatrix}0 & 0\\ I_{\mathrm{s1q}} & -I_{\mathrm{s1d}}\end{bmatrix} \qquad \underline{\boldsymbol{H}}_{\mathrm{var2}} = \underline{H}_{\mathrm{var}}\begin{bmatrix}0 & 0\\ -U_{\mathrm{s1q}} & U_{\mathrm{s1d}}\end{bmatrix}\end{aligned} \tag{3.59}$$

with $\underline{H}_{\mathrm{ri}}$, $\underline{H}_{\mathrm{wr}}$ and $\underline{H}_{\mathrm{var}}$ denoting the transfer functions of RSC current PI controller, rotor speed PI controller and reactive power PI controller respectively, and δ denoting the magnetic flux leakage coefficient of the induction machine as formulated in

$$\delta = 1 - L_{\mathrm{m}}^{\ 2} / \left(L_{\mathrm{s}} L_{\mathrm{r}} \right). \tag{3.60}$$

Jointly solving the equations in (3.50), (3.56) and (3.58) yields

$$\Delta \underline{\boldsymbol{i}}_{\mathrm{s,dq}}^{\mathrm{s}} = \underbrace{\underline{\boldsymbol{A}}^{-1} \cdot \left\{ \underline{H}_{\mathrm{d}} U_{\mathrm{dc0}} \underline{\boldsymbol{B}} - \underline{\boldsymbol{Z}}_{\mathrm{rr}} \underline{\boldsymbol{Z}}_{\mathrm{sr}}^{-1} \right\}}_{\underline{\boldsymbol{Y}}_{\mathrm{rsc}}} \Delta \underline{\boldsymbol{u}}_{\mathrm{s,dq}}^{\mathrm{s}} + \underbrace{\underline{\boldsymbol{A}}^{-1} \boldsymbol{m}_{\mathrm{r1}} \underline{H}_{\mathrm{d}}}_{\underline{\boldsymbol{c}}_{2\times 1}} \Delta \underline{u}_{\mathrm{dc}} \tag{3.61}$$

where the detailed expressions of $\underline{\boldsymbol{A}}$ and $\underline{\boldsymbol{B}}$ are

$$\begin{aligned} \underline{\boldsymbol{A}} &= \underline{H}_{\mathrm{d}} U_{\mathrm{dc0}} \left[\underline{\boldsymbol{H}}_{\mathrm{wtr}}^{\mathrm{m}} - \left(\underline{\boldsymbol{H}}_{\mathrm{ri}} - \boldsymbol{K}_{\mathrm{rd}} - \underline{\boldsymbol{H}}_{\mathrm{ri}} \underline{\boldsymbol{H}}_{\mathrm{pq1}} \right) \underline{\boldsymbol{H}}_{\mathrm{wtr}}^{\mathrm{i}} \right] \underline{\boldsymbol{Z}}_{\mathrm{sr}}^{-1} \underline{\boldsymbol{Z}}_{\mathrm{ss}} \\ &\quad - \underline{H}_{\mathrm{d}} U_{\mathrm{dc0}} \underline{\boldsymbol{H}}_{\mathrm{ri}} \underline{\boldsymbol{H}}_{\mathrm{var2}} + \underline{\boldsymbol{Z}}_{\mathrm{rs}} - \underline{\boldsymbol{Z}}_{\mathrm{rr}} \underline{\boldsymbol{Z}}_{\mathrm{sr}}^{-1} \underline{\boldsymbol{Z}}_{\mathrm{ss}} \\ \underline{\boldsymbol{B}} &= \underline{\boldsymbol{H}}_{\mathrm{PLL}}^{\mathrm{rm}} - \left(\underline{\boldsymbol{H}}_{\mathrm{ri}} - \boldsymbol{K}_{\mathrm{rd}} - \underline{\boldsymbol{H}}_{\mathrm{ri}} \underline{\boldsymbol{H}}_{\mathrm{pq1}} \right) \underline{\boldsymbol{H}}_{\mathrm{PLL}}^{\mathrm{ri}} + \left(\boldsymbol{K}_{\mathrm{us}} + \underline{\boldsymbol{H}}_{\mathrm{ri}} \underline{\boldsymbol{H}}_{\mathrm{var1}} \right) \underline{\boldsymbol{H}}_{\mathrm{PLL}}^{\mathrm{u}} \\ &\quad + \underline{\boldsymbol{H}}_{\mathrm{ri}} \underline{\boldsymbol{H}}_{\mathrm{var2}} \underline{\boldsymbol{H}}_{\mathrm{PLL}}^{\mathrm{si}} + \left(\underline{\boldsymbol{H}}_{\mathrm{wtr}}^{\mathrm{m}} - \left(\underline{\boldsymbol{H}}_{\mathrm{ri}} - \boldsymbol{K}_{\mathrm{rd}} - \underline{\boldsymbol{H}}_{\mathrm{ri}} \underline{\boldsymbol{H}}_{\mathrm{wt}} \right) \right) \underline{\boldsymbol{H}}_{\mathrm{wtr}}^{\mathrm{i}} \underline{\boldsymbol{Z}}_{\mathrm{sr}}^{-1} \end{aligned} \tag{3.62}$$

For the power balance between the AC input and DC output of the RSC, the frequency domain small-signal representation can be written as

$$\Delta \underline{i}_{\mathrm{rdc}} = \underline{H}_{\mathrm{d}} \left(\boldsymbol{m}_{\mathrm{r1}}^{\mathrm{T}} \Delta \underline{\boldsymbol{i}}_{\mathrm{r,dq}}^{\mathrm{s}} + \boldsymbol{i}_{\mathrm{r1}}^{\mathrm{T}} \Delta \underline{\boldsymbol{m}}_{\mathrm{r,dq}}^{\mathrm{s}} \right) \tag{3.63}$$

where $\boldsymbol{i}_{\mathrm{r1}}^{\mathrm{T}}$ denotes [I_{r1d} I_{r1q}]. Jointly solving (3.56)-(3.63) yields

$$\Delta \underline{i}_{\mathrm{rdc}} = \underline{\boldsymbol{d}}_{1\times 2} \Delta \underline{\boldsymbol{u}}_{\mathrm{s,dq}}^{\mathrm{s}} + \underline{Y}_{\mathrm{rdc}} \Delta \underline{u}_{\mathrm{dc}} \tag{3.64}$$

where the detailed expressions of $\underline{\boldsymbol{d}}_{1\times 2}$ and $\underline{Y}_{\mathrm{rdc}}$ are

$$\begin{aligned}\underline{\boldsymbol{d}}_{1\times 2} = {} & \underline{H}_{\mathrm{d}}\left[\boldsymbol{m}_{\mathrm{r1}}^{\mathrm{T}} + \boldsymbol{i}_{\mathrm{r1}}^{\mathrm{T}}\underline{\boldsymbol{H}}_{\mathrm{wtr}}^{\mathrm{m}} - \boldsymbol{i}_{\mathrm{r1}}^{\mathrm{T}}\left(\underline{\boldsymbol{H}}_{\mathrm{ri}} - \boldsymbol{K}_{\mathrm{rd}} - \underline{\boldsymbol{H}}_{\mathrm{ri}}\underline{\boldsymbol{H}}_{\mathrm{pq1}}\right)\underline{\boldsymbol{H}}_{\mathrm{wtr}}^{\mathrm{i}}\right]\cdot\left(\underline{\boldsymbol{Z}}_{\mathrm{sr}}^{-1} - \underline{\boldsymbol{Z}}_{\mathrm{sr}}^{-1}\underline{\boldsymbol{Z}}_{\mathrm{ss}}\underline{\boldsymbol{Y}}_{\mathrm{rsc}}\right) \\ & - \underline{H}_{\mathrm{d}}\boldsymbol{i}_{\mathrm{r1}}^{\mathrm{T}}\left(\underline{\boldsymbol{H}}_{\mathrm{ri}} - \boldsymbol{K}_{\mathrm{rd}} - \underline{\boldsymbol{H}}_{\mathrm{ri}}\underline{\boldsymbol{H}}_{\mathrm{pq1}}\right)\underline{\boldsymbol{H}}_{\mathrm{PLL}}^{\mathrm{ri}} + \underline{H}_{\mathrm{d}}\boldsymbol{i}_{\mathrm{r1}}^{\mathrm{T}}\underline{\boldsymbol{H}}_{\mathrm{PLL}}^{\mathrm{rm}} + \underline{H}_{\mathrm{d}}\boldsymbol{i}_{\mathrm{r1}}^{\mathrm{T}}\left(\underline{\boldsymbol{K}}_{\mathrm{us}} + \underline{\boldsymbol{H}}_{\mathrm{ri}}\underline{\boldsymbol{H}}_{\mathrm{var1}}\right)\underline{\boldsymbol{H}}_{\mathrm{PLL}}^{\mathrm{u}} \\ & + \underline{H}_{\mathrm{d}}\boldsymbol{i}_{\mathrm{r1}}^{\mathrm{T}}\underline{\boldsymbol{H}}_{\mathrm{ri}}\underline{\boldsymbol{H}}_{\mathrm{var2}}\underline{\boldsymbol{H}}_{\mathrm{PLL}}^{\mathrm{si}} + \underline{H}_{\mathrm{d}}\boldsymbol{i}_{\mathrm{r1}}^{\mathrm{T}}\underline{\boldsymbol{H}}_{\mathrm{ri}}\underline{\boldsymbol{H}}_{\mathrm{var2}}\underline{\boldsymbol{Y}}_{\mathrm{rsc}}\end{aligned} \tag{3.65}$$

$$\begin{aligned}\underline{Y}_{\mathrm{rdc}} = {} & -\underline{H}_{\mathrm{d}}\left[\boldsymbol{m}_{\mathrm{r1}}^{\mathrm{T}} + \boldsymbol{i}_{\mathrm{r1}}^{\mathrm{T}}\underline{\boldsymbol{H}}_{\mathrm{wtr}}^{\mathrm{m}} - \boldsymbol{i}_{\mathrm{r1}}^{\mathrm{T}}\left(\underline{\boldsymbol{H}}_{\mathrm{ri}} - \boldsymbol{K}_{\mathrm{rd}} - \underline{\boldsymbol{H}}_{\mathrm{ri}}\underline{\boldsymbol{H}}_{\mathrm{pq1}}\right)\underline{\boldsymbol{H}}_{\mathrm{wtr}}^{\mathrm{i}}\right]\underline{\boldsymbol{Z}}_{\mathrm{sr}}^{-1}\underline{\boldsymbol{Z}}_{\mathrm{ss}}\underline{\boldsymbol{c}}_{2\times 1} \\ & + \underline{H}_{\mathrm{d}}\boldsymbol{i}_{\mathrm{r1}}^{\mathrm{T}}\underline{\boldsymbol{H}}_{\mathrm{ri}}\underline{\boldsymbol{H}}_{\mathrm{var2}}\underline{\boldsymbol{c}}_{2\times 1}\end{aligned}$$

Finally, the equations in (3.61) and (3.64) can represent the admittance model of the RSC and the induction machine branch.

3.3.3 Derivation of WT Sequence Impedances

For the convenience of model validation and grid-level resonance analysis using the symmetric componets, the developed dq admittance model as given in (3.29) is furtherly transformed to sequence impedances in this section. After adding small-signal perturbations to the fundamendal frequency component ω_1 in grid voltage $\boldsymbol{u}_{\mathrm{abc}}(t)$, the phase-a voltage can be written as

$$u_{\mathrm{a}}(t) = U_1\cos\left(\omega_1 t\right) + U_{\mathrm{p}}\cos\left(\omega_{\mathrm{p}} t + \phi_{\mathrm{up}}\right) + U_{\mathrm{n}}\cos\left(\omega_{\mathrm{n}} t + \phi_{\mathrm{un}}\right) \tag{3.66}$$

where ω_{p} denotes the positive sequence component of a perturbation and ω_{n} denotes the coupled frequency component of ω_{p} and satisfies

$$\omega_{\mathrm{n}} = \begin{cases} 2\omega_1 - \omega_{\mathrm{p}}, & \omega_{\mathrm{p}} < 2\omega_1 \\ \omega_{\mathrm{p}} - 2\omega_1, & \omega_{\mathrm{p}} \geq 2\omega_1 \end{cases}. \tag{3.67}$$

Note, that ω_{p} and ω_{n} would be symmetrical about ω_1 and have the same phase sequence if allowing ω_{n} to be a negative value. However, ω_{n} is treated as a positive value here, thus to satisfy the mathematical equivalency, the phase sequence of ω_{n} is changed to negative sequence when ω_{p} is larger than $2\omega_1$.

After substituting the trigonometric functions in (3.66) with complex exponential functions, the frequency domain representation of the phase-a voltage can be written as

$$\underline{U}_{\mathrm{a}}(\omega)=\begin{cases}U_{1}, & \omega=\pm\omega_{1}\\ \underline{U}_{\mathrm{p}}, & \omega=\pm\omega_{\mathrm{p}}\\ \underline{U}_{\mathrm{n}}, & \omega=\pm\omega_{\mathrm{n}}\end{cases} \tag{3.68}$$

where

$$\underline{U}_{\mathrm{p}}=(U_{\mathrm{p}}/2)\mathrm{e}^{\pm\mathrm{j}\phi_{\mathrm{up}}} \tag{3.69}$$

and others follow the same notation. Then performing Park's transformation to (3.68), the voltage components in system dq frame can be written as

$$\underline{U}_{\mathrm{d}}=\begin{cases}U_{1}, & \omega_{\mathrm{dq}}=0\\ \underline{U}_{\mathrm{p}}, & \omega_{\mathrm{dq}}=\pm(\omega_{\mathrm{p}}-\omega_{1})\\ \underline{U}_{\mathrm{n}}, & \omega_{\mathrm{dq}}=\pm(\omega_{\mathrm{n}}+\omega_{1})\end{cases}\qquad \underline{U}_{\mathrm{q}}=\begin{cases}0, & \omega_{\mathrm{dq}}=0\\ \mp\mathrm{j}\underline{U}_{\mathrm{p}}, & \omega_{\mathrm{dq}}=\pm(\omega_{\mathrm{p}}-\omega_{1})\\ \pm\mathrm{j}\underline{U}_{\mathrm{n}}, & \omega_{\mathrm{dq}}=\pm(\omega_{\mathrm{n}}+\omega_{1})\end{cases} \tag{3.70}$$

Combining (3.68) and (3.70), the relationship between the dq components and sequence components can be solved as

$$\begin{bmatrix}\underline{U}_{\mathrm{d}}(\omega_{\mathrm{dq}})\\ \underline{U}_{\mathrm{q}}(\omega_{\mathrm{dq}})\end{bmatrix}=\underbrace{\begin{bmatrix}1 & 1\\ -\mathrm{j} & \mathrm{j}\end{bmatrix}}_{\underline{\boldsymbol{T}}_{\mathrm{Z}}}\begin{bmatrix}\underline{U}_{\mathrm{p}}(\omega_{\mathrm{p}})\\ \underline{U}_{\mathrm{n}}(\omega_{\mathrm{n}})\end{bmatrix} \tag{3.71}$$

where the transformation matrix $\underline{\boldsymbol{T}}_{\mathrm{Z}}$ also applies to other voltage and current signals.

Replacing $\underline{s}$ with $\mathrm{j}\omega_{\mathrm{dq}}$ in the WT admittance equation in (3.28) gives

$$\begin{bmatrix}\underline{U}_{\mathrm{d}}(\omega_{\mathrm{dq}})\\ \underline{U}_{\mathrm{q}}(\omega_{\mathrm{dq}})\end{bmatrix}=\underbrace{\begin{bmatrix}\underline{Z}_{\mathrm{dd}}(\omega_{\mathrm{dq}}) & \underline{Z}_{\mathrm{dq}}(\omega_{\mathrm{dq}})\\ \underline{Z}_{\mathrm{qd}}(\omega_{\mathrm{dq}}) & \underline{Z}_{\mathrm{qq}}(\omega_{\mathrm{dq}})\end{bmatrix}}_{\underline{\boldsymbol{Z}}_{\mathrm{wt,dq}}(\omega_{\mathrm{dq}})=\underline{\boldsymbol{Y}}_{\mathrm{wt,dq}}^{-1}(\omega_{\mathrm{dq}})}\begin{bmatrix}\underline{I}_{\mathrm{wtd}}(\omega_{\mathrm{dq}})\\ \underline{I}_{\mathrm{wtq}}(\omega_{\mathrm{dq}})\end{bmatrix} \tag{3.72}$$

where $\underline{\boldsymbol{Z}}_{\mathrm{wt,dq}}(\underline{s})$ denotes the dq-frame impedance of the WT.

Then substituting the voltages and currents in (3.72) with the corresponding sequence components as obtained according to (3.71) yields

$$\begin{aligned}
\begin{bmatrix} \underline{U}_{\mathrm{p}}(\omega_{\mathrm{p}}) \\ \underline{U}_{\mathrm{n}}(\omega_{\mathrm{n}}) \end{bmatrix} &= \underbrace{\boldsymbol{T}_{\mathrm{Z}}^{-1} \begin{bmatrix} \underline{Z}_{\mathrm{dd}}(\omega_{\mathrm{dq}}) & \underline{Z}_{\mathrm{dq}}(\omega_{\mathrm{dq}}) \\ \underline{Z}_{\mathrm{qd}}(\omega_{\mathrm{dq}}) & \underline{Z}_{\mathrm{qq}}(\omega_{\mathrm{dq}}) \end{bmatrix} \boldsymbol{T}_{\mathrm{Z}}}_{\underline{\boldsymbol{Z}}_{\mathrm{wt,pn}}^{\mathrm{M}}(\omega_{\mathrm{dq}})} \begin{bmatrix} \underline{I}_{\mathrm{p}}(\omega_{\mathrm{p}}) \\ \underline{I}_{\mathrm{n}}(\omega_{\mathrm{n}}) \end{bmatrix} \\
&\Updownarrow \text{ for } \underline{s}=\mathrm{j}\omega_{\mathrm{dq}} \\
\begin{bmatrix} \underline{U}_{\mathrm{p}}(\underline{s}+\mathrm{j}\omega_{\mathrm{l}}) \\ \underline{U}_{\mathrm{n}}(\underline{s}-\mathrm{j}\omega_{\mathrm{l}}) \end{bmatrix} &= \underbrace{\boldsymbol{T}_{\mathrm{Z}}^{-1} \begin{bmatrix} \underline{Z}_{\mathrm{dd}}(\underline{s}) & \underline{Z}_{\mathrm{dq}}(\underline{s}) \\ \underline{Z}_{\mathrm{qd}}(\underline{s}) & \underline{Z}_{\mathrm{qq}}(\underline{s}) \end{bmatrix} \boldsymbol{T}_{\mathrm{Z}}}_{\underline{\boldsymbol{Z}}_{\mathrm{wt,pn}}^{\mathrm{M}}(\underline{s})} \begin{bmatrix} \underline{I}_{\mathrm{p}}(\underline{s}+\mathrm{j}\omega_{\mathrm{l}}) \\ \underline{I}_{\mathrm{n}}(\underline{s}-\mathrm{j}\omega_{\mathrm{l}}) \end{bmatrix}
\end{aligned} \tag{3.73}$$

where

$$\underline{\boldsymbol{Z}}_{\mathrm{wt,pn}}^{\mathrm{M}}(\underline{s}) = \begin{bmatrix} \underline{Z}_{\mathrm{pp}}^{\mathrm{M}}(\underline{s}) & \underline{Z}_{\mathrm{pn}}^{\mathrm{M}}(\underline{s}) \\ \underline{Z}_{\mathrm{np}}^{\mathrm{M}}(\underline{s}) & \underline{Z}_{\mathrm{nn}}^{\mathrm{M}}(\underline{s}) \end{bmatrix} \tag{3.74}$$

denotes the modified sequence impedances as defined in [28]. By shifting the frequency of ω_{l} for the voltage, current and impedance terms in (3.73), i.e. substituting $\underline{s}$ with $\underline{s}-\mathrm{j}\omega_{\mathrm{l}}$ for the positive sequence and its coupling terms, and substituting $\underline{s}$ with $\underline{s}+\mathrm{j}\omega_{\mathrm{l}}$ for the negative sequence and its coupling terms, the real sequence impedance $\underline{\boldsymbol{Z}}_{\mathrm{wt,pn}}(\underline{s})$ can be derived, which satisfies

$$\begin{bmatrix} \underline{U}_{\mathrm{p}}(\underline{s}) \\ \underline{U}_{\mathrm{n}}(\underline{s}) \end{bmatrix} = \underbrace{\begin{bmatrix} \underline{Z}_{\mathrm{pp}}^{\mathrm{M}}(\underline{s}-\mathrm{j}\omega_{\mathrm{l}}) & \underline{Z}_{\mathrm{pn}}^{\mathrm{M}}(\underline{s}+\mathrm{j}\omega_{\mathrm{l}}) \\ \underline{Z}_{\mathrm{np}}^{\mathrm{M}}(\underline{s}-\mathrm{j}\omega_{\mathrm{l}}) & \underline{Z}_{\mathrm{nn}}^{\mathrm{M}}(\underline{s}+\mathrm{j}\omega_{\mathrm{l}}) \end{bmatrix}}_{\underline{\boldsymbol{Z}}_{\mathrm{wt,pn}}(s)} \begin{bmatrix} \underline{I}_{\mathrm{p}}(\underline{s}) \\ \underline{I}_{\mathrm{n}}(\underline{s}) \end{bmatrix} \tag{3.75}$$

where the off-diagonal elements of $\underline{\boldsymbol{Z}}_{\mathrm{wt,pn}}(\underline{s})$ are not equal to zero and they are induced by the asymmetrical PLL control and the asymmetrical outer loop PI control of WT converters. The sequence impedance coupling in (3.75) reflects the relationship between the voltage and current of different frequencies. To be specific, when there is a positive-sequence current / voltage perturbation with the frequency ω_{p} larger than $2\omega_{\mathrm{l}}$, a negative sequence voltage / current response ω_{n} will be induced, but when ω_{p} is smaller than $2\omega_{\mathrm{l}}$, the coupled frequency component ω_{n} has the same phase sequence as ω_{p}.

3.3.4 Simulation validation

The analytically derived models are validated through simulations using the detailed wind turbine model in Simulink. Involved parameters of the DFIG system can be found in the Apendix D.

Current injections are implemented in simulations to measure the WT impedance responses. For each positive sequence perturbation ω_p, there is another perturbation ω_n which satisfies (3.67) and has a phase sequence dependent on the relationship between ω_p and $2\omega_1$, as described in section 3.3.3. These two perturbations will be injected into the simulated WT in two separate simulations, from which two set of frequency components can be extracted from the current and voltage signals, they are $\underline{U}_{p1}$, $\underline{I}_{p1}$, $\underline{U}_{n1}$, $\underline{I}_{n1}$ and $\underline{U}_{p2}$, $\underline{I}_{p2}$, $\underline{U}_{n2}$, $\underline{I}_{n2}$.

Since the two injections are linearly independent, the following equation can be obtained to find the sequence impedances [28], [74]:

$$\begin{bmatrix} \underline{Z}_{pp} & \underline{Z}_{pn} \\ \underline{Z}_{np} & \underline{Z}_{nn} \end{bmatrix} \begin{bmatrix} \underline{I}_{p1} & \underline{I}_{p2} \\ \underline{I}_{n1} & \underline{I}_{n2} \end{bmatrix} = \begin{bmatrix} \underline{U}_{p1} & \underline{U}_{p2} \\ \underline{U}_{n1} & \underline{U}_{n2} \end{bmatrix} \tag{3.76}$$

where the impedances $\underline{Z}_{pp}$, $\underline{Z}_{pn}$, $\underline{Z}_{np}$ and $\underline{Z}_{nn}$ have the following interpretations: (a) $\underline{Z}_{pp}$ measures the positive sequence voltage response at ω_p induced by the positive sequence current perturbation at ω_p; (b) Z_{pn} measures the positive sequence voltage response at ω_p induced by the negative (if ω_p is greater than $2\omega_1$) or positive (if ω_p is less than $2\omega_1$) sequence current perturbation at ω_n; (c) Z_{np} measures the negative (if ω_p is greater than $2\omega_1$) or positive (if ω_p is less than $2\omega_1$) sequence voltage response at ω_n induced by the positive sequence current perturbation at ω_p; (d) Z_{nn} measures the voltage response at ω_n induced by the current perturbation at ω_n.

Performing the simulations point by point as stated above for the considered frequency range, the wide-band impedance responses of the simulated WT can be obtained. Figure 3.13 shows the comparison of the analytical model with the simulation impedance responses of the studied DFIG-based WT, solid lines represent the analytical model and

circles represent the simulation results, as observed, both magnitude and angle of the analytical impedances are in good agreement with the simulation results.

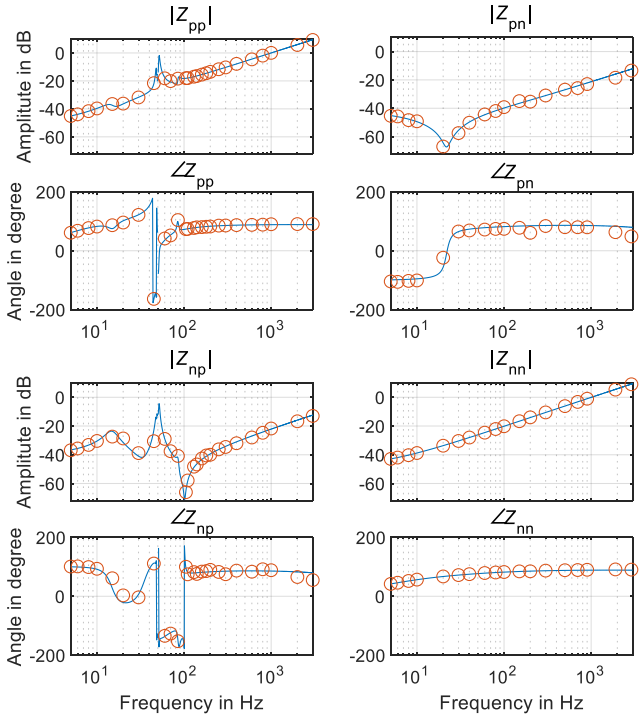

Figure 3.13 Analytical model and simulation impedance responses of the DFIG-based WT.

3.4 HVDC Converter

This section presents the impedance modelling of two-level VSC based HVDC transmission system. The harmonic linearization approach in [75] is adopted in the derivation of converter output impedance for certain operating points. Although there are several types of HVDC converters such as two-level VSC, three-level VSC and modular multilevel converter (MMC), the method for deriving the two-level VSC impedance can also be applied to the three-level VSC and MMC if making some simplifications, and their impedance responses are usually similar as they can be configured with the same or similar converter level control. The main difference of their impedance responses lies on the dynamics of the circulating current control and modular level control that are only applied in MMC, and the affected frequencies are typically not above 100 Hz [19], [76]. More details on the impedance modelling and the impedance characteristics of three-level VSC or MMC can be found in [76]-[78].

3.4.1 Impedance Modelling

In the HVDC grid integration of OWF, the HVDC transmission system is typically comprised of a wind farm side VSC converter (WFVSC) station, a grid side VSC converter (GSVSC) station and the HVDC link. When GSVSC is connected to a strong onshore grid, a constant DC voltage can be maintained on the HVDC link through the control of GSVSC, and it is reasonable to treat the DC side circuits, GSVSC as well as the connected onshore grid as an ideal DC voltage source. On this assumption, the impedance modelling of the HVDC system looking from OWF into WFVSC can be simplified to the impedance modelling of the WFVSC from the AC side.

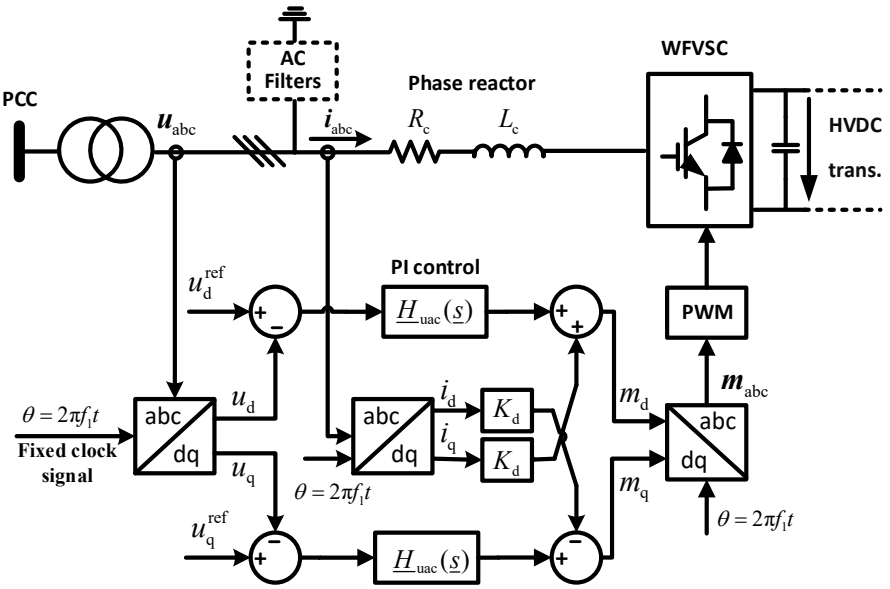

Figure 3.14 Circuit and Control diagram of wind farm side HVDC converter

Figure 3.14 shows the electrical circuit and control of the WFVSC. R_c and L_c represents converter reactor. AC filters in shunt branch are a group of high-pass damped filters for compensating switching harmonics of the WFVSC. Next to PCC is a coupling transformer that is usually arranged with a winding connection of Wye grounded / Delta to block tripplen harmonics produced by the converter. The WFVSC is controlled as a slack bus to maintain a strong offshore network for wind power integration. The control system mainly comprises measurement and filtering blocks, coordinate transformation blocks, AC voltage regulators, and PWM block. Instead of implementing the widely adopted cascaded double-loop PI control, i.e. outer loop voltage control and inner loop current control, AC voltage is regulated by a single loop PI controller to achieve better dynamic performance [79], [80]. A fixed clock signal is used to generate the phase angle

needed for the coordinate transformations, thus regulating the frequency of the AC voltage. Under natural reference frame, the AC side circuit of the WFVSC can be represented by

$$\boldsymbol{u}_{\mathrm{abc}}(t)-\boldsymbol{m}_{\mathrm{abc}}(t)u_{\mathrm{dc}}(t)=R_{\mathrm{c}}\boldsymbol{i}_{\mathrm{abc}}(t)+L_{\mathrm{c}}\frac{d}{dt}\boldsymbol{i}_{\mathrm{abc}}(t) \tag{3.77}$$

where $\boldsymbol{m}_{\mathrm{abc}}(t)$ denotes the three-phase modulating signal vector and $\boldsymbol{u}_{\mathrm{abc}}(t)$ and $\boldsymbol{i}_{\mathrm{abc}}(t)$ denote the three-phase voltage and current vectors, e.g. $\boldsymbol{u}_{\mathrm{abc}}(t)$ represents $\begin{bmatrix}u_{\mathrm{a}}(t) & u_{\mathrm{b}}(t) & u_{\mathrm{c}}(t)\end{bmatrix}^{\mathrm{T}}$. After replacing the three-phase signals with the dq-frame space vectors, the power stage equation of the converter in (3.77) can be rewritten as

$$\underline{u}_{\mathrm{dq}}(t)-\underline{m}_{\mathrm{dq}}(t)u_{\mathrm{dc}}(t)-\mathrm{j}\omega_{1}L_{\mathrm{c}}\underline{i}_{\mathrm{dq}}(t)=R_{\mathrm{c}}\underline{i}_{\mathrm{dq}}(t)+L_{\mathrm{c}}\frac{d}{dt}\underline{i}_{\mathrm{dq}}(t) \tag{3.78}$$

where

$$\begin{gathered}\underline{u}_{\mathrm{dq}}(t)=u_{\mathrm{d}}(t)+\mathrm{j}u_{\mathrm{q}}(t)\quad \underline{i}_{\mathrm{dq}}(t)=i_{\mathrm{d}}(t)+\mathrm{j}i_{\mathrm{q}}(t)\\ \underline{m}_{\mathrm{dq}}(t)=m_{\mathrm{d}}(t)+\mathrm{j}m_{\mathrm{q}}(t)\end{gathered} \tag{3.79}$$

and ω_1 denotes the fundamental frequency. Neglecting the DC side dynamic of the HVDC link and taking into account the digital control delay of the converter, the decomposed d- and q-component small-signal representation of (3.78) can be written as

$$\underbrace{\begin{bmatrix}\Delta\underline{u}_{\mathrm{d}}\\ \Delta\underline{u}_{\mathrm{q}}\end{bmatrix}}_{\Delta\underline{\boldsymbol{u}}_{\mathrm{dq}}}=\underbrace{\begin{bmatrix}\Delta\underline{m}_{\mathrm{d}}\\ \Delta\underline{m}_{\mathrm{q}}\end{bmatrix}}_{\Delta\underline{\boldsymbol{m}}_{\mathrm{dq}}}\underline{H}_{\mathrm{d}}U_{\mathrm{dc0}}+\underbrace{\begin{bmatrix}R_{\mathrm{c}}+\underline{s}L_{\mathrm{c}} & -\omega_{1}L_{\mathrm{c}}\\ \omega_{1}L_{\mathrm{c}} & R_{\mathrm{c}}+\underline{s}L_{\mathrm{c}}\end{bmatrix}}_{\underline{\boldsymbol{Z}}_{\mathrm{RL}}(\underline{s})}\underbrace{\begin{bmatrix}\Delta\underline{i}_{\mathrm{d}}\\ \Delta\underline{i}_{\mathrm{q}}\end{bmatrix}}_{\Delta\underline{\boldsymbol{i}}_{\mathrm{dq}}} \tag{3.80}$$

where U_{dc0} is the steady-state value of the converter DC voltage, and $\underline{H}_{\mathrm{d}}$ denotes the converter control delay for 1.5 times of the sampling period, as formulated in (3.37).

Since the system is coupled between the d- and q-axis under SRF, a feedforward compensation is introduced into the control loop for decoupling. According to the control block diagram in Figure 3.14, the dq-frame modulating signals can be described as

$$\underline{m}_{\mathrm{dq}}(t)=\underline{H}_{\mathrm{uac}}(\underline{u}_{\mathrm{dq}}^{\mathrm{ref}}-\underline{u}_{\mathrm{dq}}(t))-\mathrm{j}K_{\mathrm{d}}\underline{i}_{\mathrm{dq}}(t) \tag{3.81}$$

where $\underline{u}_{\mathrm{dq}}^{\mathrm{ref}}$ denotes the reference voltage space vector, $\underline{H}_{\mathrm{uac}}$ representes the transfer function of converter AC voltage PI controller, and the decoupling parameter K_{d} is set to L_{c}. The mathematical models of the converter as given by (3.78) and (3.81) can also be illustrated by the block diagram as shown in Figure 3.15.

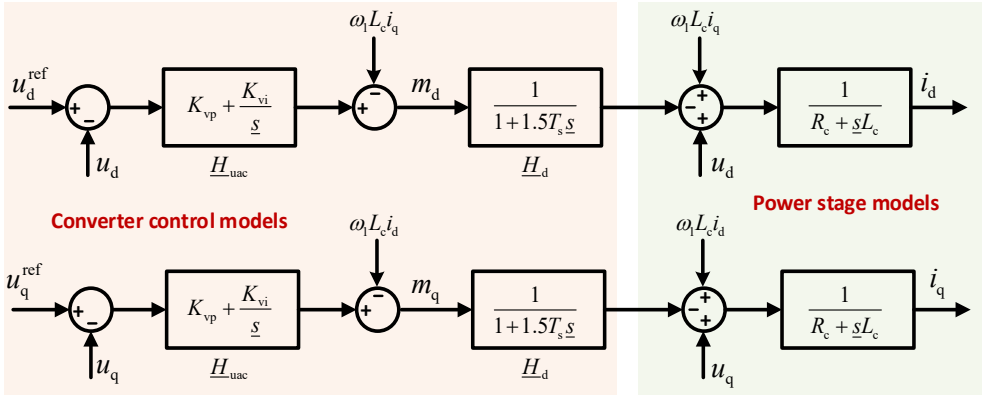

Figure 3.15 Block diagram of the dq-frame model of the converter

Performing small-signal analysis to (3.81) and rearranging it yields the frequency-domain representation

$$\begin{bmatrix}\Delta\underline{m}_{\mathrm{d}}\\ \Delta\underline{m}_{\mathrm{q}}\end{bmatrix}=-\underbrace{\begin{bmatrix}\underline{H}_{\mathrm{uac}} & 0\\ 0 & \underline{H}_{\mathrm{uac}}\end{bmatrix}}_{\boldsymbol{H}_{\mathrm{uac}}}\begin{bmatrix}\Delta\underline{u}_{\mathrm{d}}\\ \Delta\underline{u}_{\mathrm{q}}\end{bmatrix}+\underbrace{\begin{bmatrix}0 & -K_{\mathrm{d}}\\ K_{\mathrm{d}} & 0\end{bmatrix}}_{\boldsymbol{K}_{\mathrm{dd}}}\begin{bmatrix}\Delta\underline{i}_{\mathrm{d}}\\ \Delta\underline{i}_{\mathrm{q}}\end{bmatrix} \tag{3.82}$$

Finally substituting (3.82) into (3.80) yields

$$\Delta\underline{\boldsymbol{u}}_{\mathrm{dq}}=\underbrace{\left(\boldsymbol{E}_2+\underline{H}_{\mathrm{d}}U_{\mathrm{dc0}}\boldsymbol{H}_{\mathrm{vac}}\right)^{-1}\left(\underline{H}_{\mathrm{d}}U_{\mathrm{dc0}}\boldsymbol{K}_{\mathrm{dd}}+\underline{\boldsymbol{Z}}_{\mathrm{RL}}\right)}_{\underline{\boldsymbol{Z}}_{\mathrm{vsc,dq}}(\underline{s})}\Delta\underline{\boldsymbol{i}}_{\mathrm{dq}} \tag{3.83}$$

where $\boldsymbol{E_2}$ is a seconde-order identity matrix, $\underline{\boldsymbol{Z}}_{\mathrm{vsc,dq}}(\underline{s})$ represents the dq-frame impdedance of the HVDC converter and can be expressed in the following form

$$\underline{\boldsymbol{Z}}_{\mathrm{vsc,dq}}(\underline{s})=\begin{bmatrix}\underline{Z}_{\mathrm{dd}}(\underline{s}) & \underline{Z}_{\mathrm{dq}}(\underline{s})\\ \underline{Z}_{\mathrm{qd}}(\underline{s}) & \underline{Z}_{\mathrm{qq}}(\underline{s})\end{bmatrix}. \tag{3.84}$$

For the convenience of model validation and grid-level resonance analysis using phase or sequence-component signals, the developed dq-domain impedance matrix is furtherly transformed into sequence impedances. Performing both linearization transformation using $\underline{\boldsymbol{T}}_{\mathrm{Z}}$ and frequency shifting as described in section 3.3.3 can give

$$\underline{\boldsymbol{Z}}_{\mathrm{vsc,pn}}(\underline{s}) = \underline{\boldsymbol{T}}_{\mathrm{Z}}^{-1}\begin{bmatrix} \underline{Z}_{\mathrm{dd}}(\underline{s}-\mathrm{j}\omega_1) & \underline{Z}_{\mathrm{dq}}(\underline{s}+\mathrm{j}\omega_1) \\ \underline{Z}_{\mathrm{qd}}(\underline{s}-\mathrm{j}\omega_1) & \underline{Z}_{\mathrm{qq}}(\underline{s}+\mathrm{j}\omega_1) \end{bmatrix}\underline{\boldsymbol{T}}_{\mathrm{Z}} \tag{3.85}$$

where $\underline{\boldsymbol{T}}_{\mathrm{Z}}$ is a constant-value matrix, as given in (3.71). Since the d-axis and q-axis controls are fully symmetrical in the adopted single-loop PI control structure, $\underline{\boldsymbol{Z}}_{\mathrm{vsc,pn}}$ is frequency decoupled [28], which means, when injecting a positive-sequence voltage perturbation $\underline{U}_{\mathrm{p}}$ with frequency ω_{p}, only a positive-sequence current response with the same frequency will be induced.

If the dq controls are asymmetrical, e.g. setting different PI parameters for d- and q-axis controllers or adopting different d- and q-axis control structure, the resulting $\underline{\boldsymbol{Z}}_{\mathrm{vsc,pn}}$ will be frequency coupled, i.e. when injecting a positive-sequence voltage perturbation $\underline{U}_{\mathrm{p}}$ with the frequency ω_{p}, not only a positive-sequence current response $\underline{I}_{\mathrm{p}}$ of the same frequency will be induced, but also a coupled frequency component $\underline{I}_{\mathrm{n}}$ with a frequency satisfying (3.67) and the phase sequence as described in Section 3.3.3 will be induced.

3.4.2 Simulation Validation

The analytically derived models are validated through simulations in MATLAB / Simulink. Involved parameters of the HVDC system are given in Appendix D. To measure the converter impedance responses, the current injection approach as discussed in [28], [74] is applied in simulations. For each positive sequence perturbation ω_{p}, there is another perturbation ω_{n} which satisfies (3.67) and its phase sequence is dependent on the relationship between ω_{p} and $2\omega_1$, as described in section 3.3.3. These two perturbations are injected into the simulated HVDC converter in two separate simulations, from which two set of frequency components can be extracted from the current and voltage signals, they are $\underline{U}_{\mathrm{p1}}$, $\underline{I}_{\mathrm{p1}}$, $\underline{U}_{\mathrm{n1}}$, $\underline{I}_{\mathrm{n1}}$ and $\underline{U}_{\mathrm{p2}}$, $\underline{I}_{\mathrm{p2}}$, $\underline{U}_{\mathrm{n2}}$, $\underline{I}_{\mathrm{n2}}$. Since

the two injections are linearly independent, the sequence impedances of the HVDC converter can be solved as in (3.76).

Figure 3.16 shows the impedance responses of the simulated HVDC converter, solid lines represent analytical models and circles show numerical simulation results. It can be observed, both magnitude and phase of the analytical impedances are in good agreement with the simulation results in Simulink. In this case, $\underline{Z}_{\mathrm{pn}}$ and $\underline{Z}_{\mathrm{np}}$ are equal to zero for the whole investigated frequency range, which indicates that there is no frequency coupling effect.

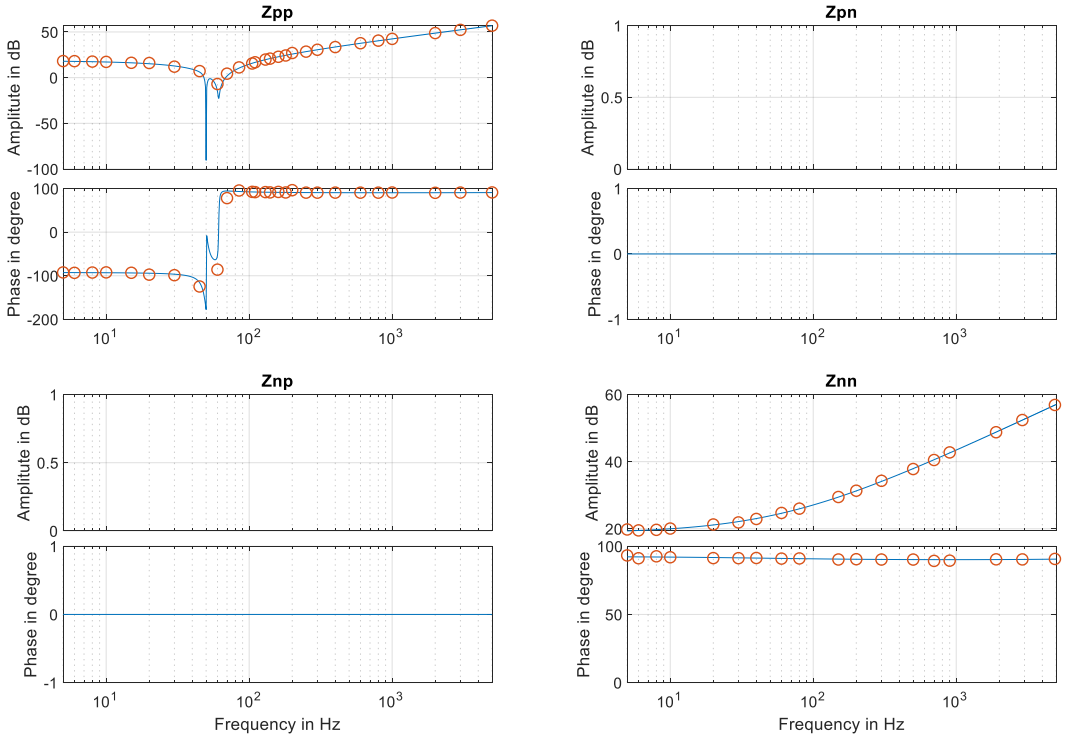

Figure 3.16 Analytical model and simulation impedance responses of the HVDC converter.

To see the frequency coupling effect, the d- and q-axis AC voltage regulators can be configurated with different parameters, here setting the matrix $\underline{\boldsymbol{H}}_{\mathrm{uac}}(\underline{s})$ in (3.82) and (3.83) as

$$\underline{\boldsymbol{H}}_{\mathrm{uac}}(\underline{s}) = \begin{bmatrix} 0.3 + 60/\underline{s} & 0 \\ 0 & 0.001 + 5/\underline{s} \end{bmatrix} \tag{3.86}$$

As well, the decoupling term in (3.82) is set as

$$\boldsymbol{K}_{\mathrm{dd}} = \begin{bmatrix} 0 & -K_{\mathrm{d}} \\ 0 & 0 \end{bmatrix}. \tag{3.87}$$

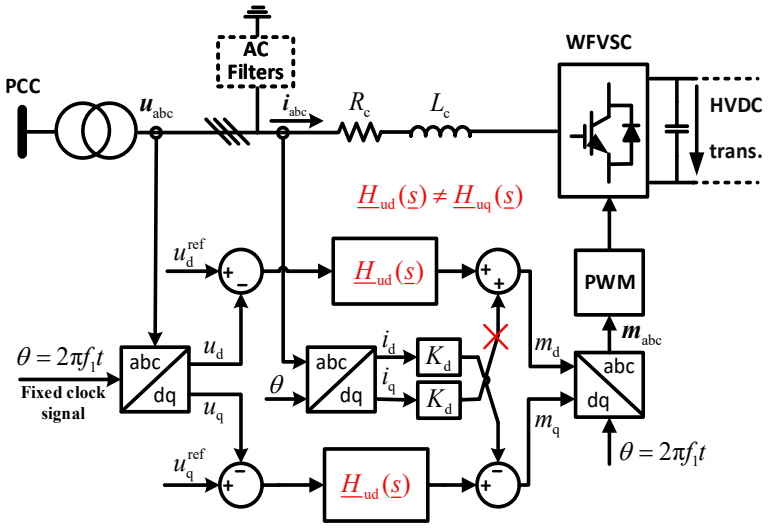

Figure 3.17 Modified WFVSC controller for showing frequency coupling effect

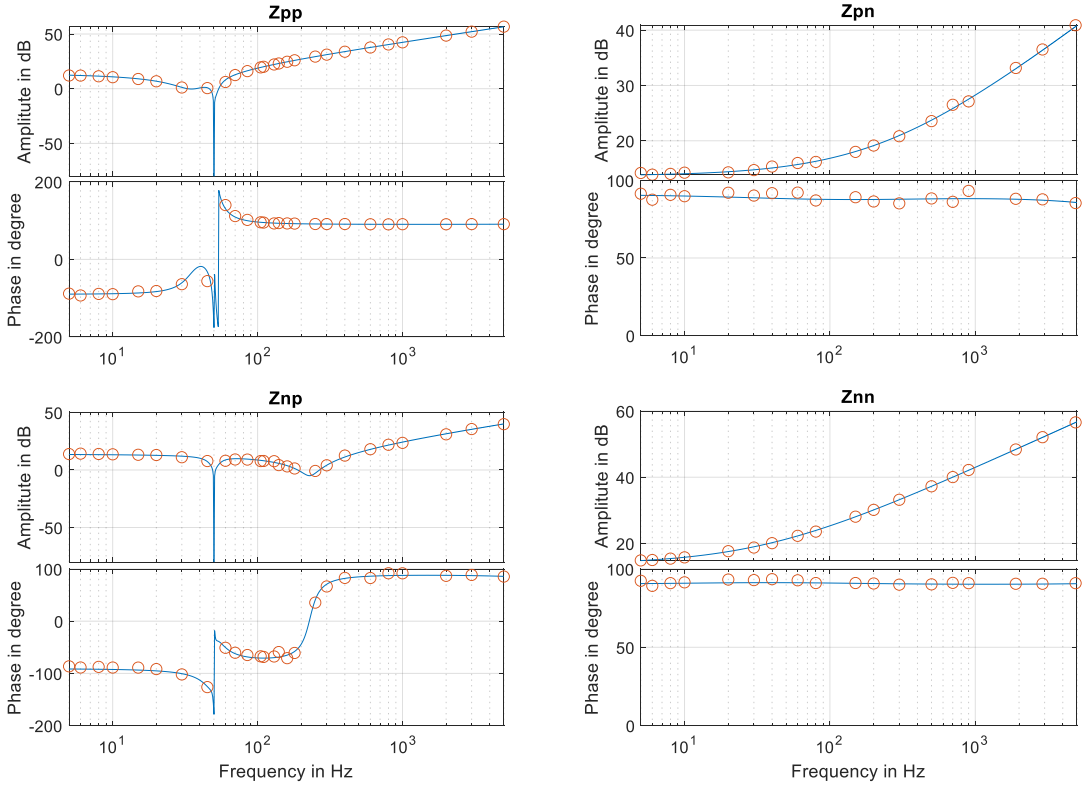

Figure 3.18 Impedance responses of the HVDC converter by asymmetrical control.

Then the revised controller of the HVDC converter can be illustrated by Figure 3.17. After updating the changes to both the analytical impedance model in (3.83) and the simulation models in Simulink, the frequency coupling effect can be observed both in theoretical analysis and in simulation results, as shown in Figure 3.18.

4 Modelling of Wind Farm Collector System

In OWFs, WTs are typically collected through medium-voltage (MV) AC grids. Several typical configurations of WT collector systems are string topology, star topology and circular topology [81]-[83]. In this chapter, the commonly used string topology is taken as example to show the aggregated modelling of WT collector systems. Present practices in the aggregated modelling of wind farm MV collector system [31] [32] will be presented and their suitability for wideband resonance analysis will be analyzed through comparing with the detailed analytical model that is derived on the basis of the basic circuit theory. The results of this chapter were published in advance in [35].

Illustration of the aggregated single-machine model for wind farm collector system is given in Figure 4.1. Figure 4.2 shows the typical configuration of an OWF with radially distributed MV collector systems. Each MV main bus connects *M* arrays of WTs, and in the *m* array, N_m WTs are collected through N_m sections of collecting cables.

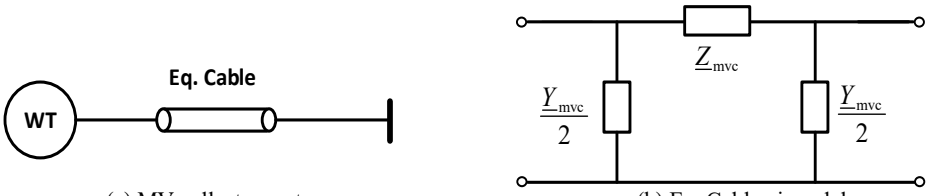

(a) MV collector system (b) Eq. Cable pi model

Figure 4.1 Aggregated single-machine model of MV collector system

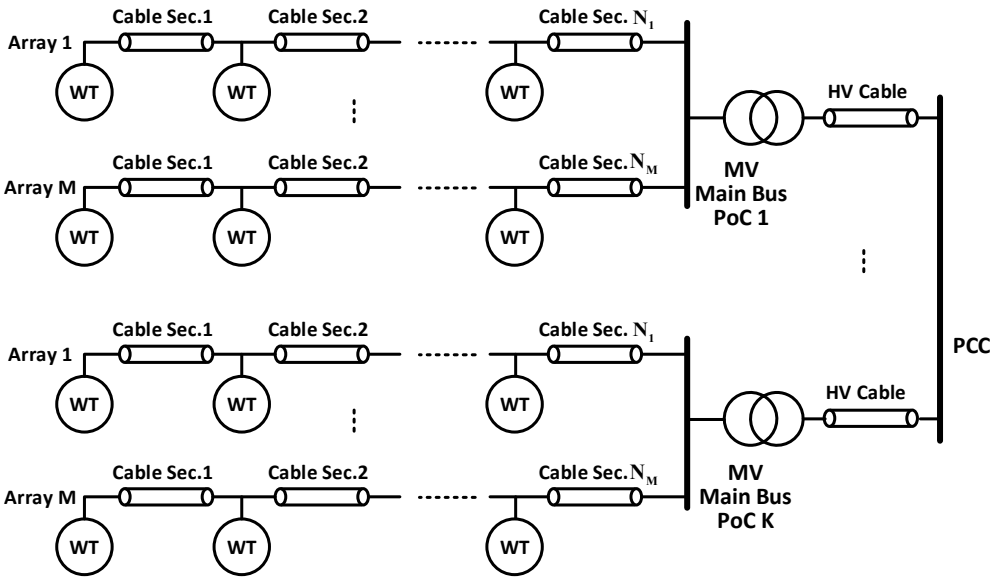

Figure 4.2 Typical radially distributed OWF configuration

Specifically in the test grid, each MV collector system is set to have 40 WTs, which are distributed in 6 wind arrays. The cable settings of the MV collector system are shown in Figure 4.3, in which the parameters of the cables are estimated from ABB user's guide for submarine systems [84], as presented in Table 4.1.

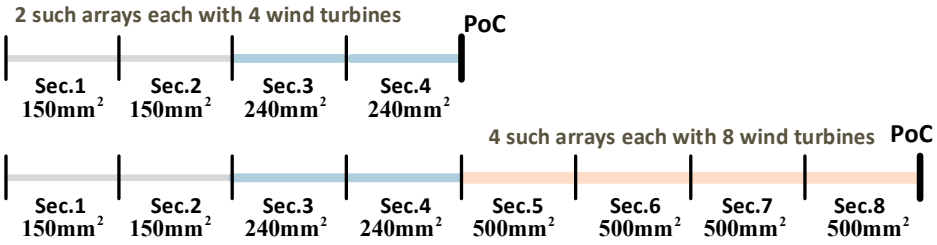

Figure 4.3 Cable settings of each medium-voltage collector system

Table 4.1 Parameters of collector cables

Cable Type	Cross section	Length	Electrical Parameters
1	150 mm^2	1 km	$R = 0.16\ \Omega$/km, $L = 0.41$ mH/km, $C = 0.21\ \mu$F/km
2	240 mm^2	1 km	$R = 0.098\ \Omega$/km, $L = 0.38$ mH/km, $C = 0.24\ \mu$F/km
3	500 mm^2	1 km	$R = 0.05\ \Omega$/km, $L = 0.34$ mH/km, $C = 0.32\ \mu$F/km

4.1 Power loss based aggregation model

Assuming each WT injects the same amount of current $\underline{I}_{\mathrm{WT}}$, the total current contributed from the radial m can be written as

$$\underline{I}_m = \sum_{n=1}^{N_m} \underline{I}_{m,n} = N_m \underline{I}_{\mathrm{WT}},\ m = 1,2,\ldots,M,\ n = 1,2,\ldots,N \tag{4.1}$$

where the subscripts m, n represent the n^{th} WT in array m and $\underline{I}_{m,n}$ denotes the injected current of the corresponding WT. For each cable section, the nominal Pi model with lumped parameters is adopted. If defining the equivalent series impedance of all the cable sections in the array m as $\underline{Z}_m$, the power loss in the array m can be formulated as

$$\underline{I}_m^2 \underline{Z}_m = \sum_{n=1}^{N_m} \left(n \frac{\underline{I}_{m,n}}{N_m} \right)^2 \underline{Z}_{m,n} \tag{4.2}$$

where

$$\underline{Z}_{m,n} = R_{m,n} + \mathrm{j}\omega L_{m,n} \tag{4.3}$$

denotes the series impedance of the cable section which connects the n^{th} and the $(n + 1)^{\text{th}}$ WTs in the array m with $R_{m,n}$ and $L_{m,n}$ denoting the resistance and inductance of the corresponding cable section. Combining (4.1) and (4.2), $\underline{Z}_m$ is solved as

$$\underline{Z}_m = \frac{1}{N_m^2}\sum_{n=1}^{N_m} n^2 \underline{Z}_{m,n} \tag{4.4}$$

Combining the current and power loss expressions as given in (4.5), (4.6), the equivalent series impedance $\underline{Z}_{\text{mvc}}$ for all the cable sections of a MV collector system can be deduced as in (4.7). The lumped resistance R_{mv} and inductance $\underline{L}_{\text{mv}}$ parameters could be furtherly solved from (4.8).

$$\underline{I}_{\text{mv}} = \sum_{m=1}^{M} \underline{I}_m = \sum_{m=1}^{M} N_m \underline{I}_{\text{WT}},\ m = 1,2,\ldots,M \tag{4.5}$$

$$\underline{I}_{\text{mv}}^2 \underline{Z}_{\text{mvc}} = \sum_{m=1}^{M} \underline{I}_m^2 \underline{Z}_m \tag{4.6}$$

$$\underline{Z}_{\text{mvc}} = \sum_{m=1}^{M} \underline{I}_m^2 \underline{Z}_m \Big/ \underline{I}_{\text{mv}}^2 = \sum_{m=1}^{M} N_m^2 \underline{Z}_m \Big/ \left(\sum_{m=1}^{M} N_m\right)^2 \tag{4.7}$$

$$\underline{Z}_{\text{mvc}}(\omega_1) = R_{\text{mvc}} + \mathrm{j}\omega_1 L_{\text{mvc}} \tag{4.8}$$

For the aggregation of the shunt admittance of the distributed cables, the capacitances of all the cable sections can be simply added together. So the accumulated capacitance C_{mv} and the resulted shunt admittance Y_{mv} of a MV collector system can be represented by

$$C_{\text{mvc}} = \sum_{m=1}^{M}\sum_{n=1}^{N} C_{m,n} \tag{4.9}$$

$$\underline{Y}_{\text{mvc}} = \mathrm{j}\omega C_{\text{mvc}} \tag{4.10}$$

As for the aggregation of WTs, all the WTs of a MV collector system can be assumed in direct parallel connection due to negligible series impedances of the collecting cables compared to WT impedances. Furtherly assuming all the WTs are under the same

operating point, the equivalent impedance of the WTs taking into account the terminal filters and step-up transformers can be formulated as

$$\underline{\boldsymbol{Z}}_{\mathrm{wt,agg}} = \left((\underline{\boldsymbol{Z}}_{\mathrm{wt}}^{-1} + 1/\underline{Z}_{\mathrm{F}}\boldsymbol{E}_2)^{-1} + \underline{Z}_{\mathrm{T}}\boldsymbol{E}_2 \right) / N_{\mathrm{wt}} \tag{4.11}$$

where $\boldsymbol{E}_2$ represents the second-order identity matrix, $\underline{\boldsymbol{Z}}_{\mathrm{wt}}$ is the abbreviation for $\underline{\boldsymbol{Z}}_{\mathrm{wt,pn}}$, $\underline{Z}_{\mathrm{F}}$ represents the impedance of WT terminal filter, $\underline{Z}_{\mathrm{T}}$ represents the impedance of WT step-up transformer and N_{wt} denotes the total number of WTs.

Finally, the output impedance of the aggregated MV collector system as illustrated in Figure 4.1 can be derived as

$$\underline{\boldsymbol{Z}}_{\mathrm{mv}} = \left(\left((\underline{\boldsymbol{Z}}_{\mathrm{wt,agg}}^{-1} + 0.5\underline{Y}_{\mathrm{mvc}}\boldsymbol{E}_2)^{-1} + \underline{Z}_{\mathrm{mvc}}\boldsymbol{E}_2 \right)^{-1} + 0.5\underline{Y}_{\mathrm{mvc}}\boldsymbol{E}_2 \right)^{-1} \tag{4.12}$$

4.2 Voltage drop based aggregation model

Considering the same MV collector system as presented in Figure 4.2, the voltage drop of the m^{th} wind array can be represented by

$$\underline{I}_m \underline{Z}_m = \sum_{n=1}^{N_m} n \underline{I}_{m,n} \underline{Z}_{m,n} = \sum_{n=1}^{N_m} n \frac{\underline{I}_m}{N_m} \underline{Z}_{m,n} \tag{4.13}$$

where $\underline{Z}_m$ denotes the equivalent impedance of that array. According to the current relationship as given in (4.13), $\underline{Z}_m$ can be solved as

$$\underline{Z}_m = \frac{1}{N_m} \sum_{n=1}^{N_m} n \underline{Z}_{m,n} \tag{4.14}$$

Furtherly according to the parallel circuit theory, the equivalent series impedance of all the cables of a MV collector system can be represented by

$$\underline{Z}_{\mathrm{mvc}} = \frac{1}{\sum_{m=1}^{M} \frac{1}{\underline{Z}_m}} \tag{4.15}$$

For the aggregation of the shunt admittance of the distributed cables, the equations in (4.9) and (4.10) still apply. The equivalent impedance of all the WTs can be derived as in (4.11) and the equivalent output impedance of the MV collector system can be deduced as in (4.12).

4.3 Detailed Model and Comparative Accuracy Analysis

Figure 4.4 shows the equivalent circuit of the m^{th} wind array of a MV collector system. Neglecting the voltage differences among WT terminals, all WTs can be modelled with the same output impedance, thus the output admittance of the wind array can be derived as in (4.16). The output impedance of the wind array $\underline{\boldsymbol{Z}}_{\text{m,str}}$ as well as the output impedance of the complete MV collector system $\underline{\boldsymbol{Z}}_{\text{mv}}$ can be derived as in (4.17) and (4.18) respectively.

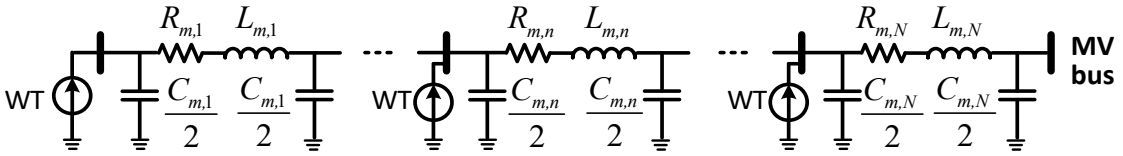

Figure 4.4 Equivalent circuit of the m^{th} wind array

$$
\begin{aligned}
\underline{\boldsymbol{Y}}_{1,\text{sec}} &= \left(\underline{Z}_{m,1}\boldsymbol{E}_2 + \left(0.5\underline{Y}_{m,1}\boldsymbol{E}_2 + \underline{\boldsymbol{Z}}_{\text{wt}}^{-1}\right)^{-1}\right)^{-1} + 0.5\underline{Y}_{m,1}\boldsymbol{E}_2 \\
\underline{\boldsymbol{Y}}_{2,\text{secs}} &= \left(\underline{Z}_{m,2}\boldsymbol{E}_2 + \left(0.5\underline{Y}_{m,2}\boldsymbol{E}_2 + \underline{\boldsymbol{Z}}_{\text{wt}}^{-1} + \underline{\boldsymbol{Y}}_{1\text{sec}}\right)^{-1}\right)^{-1} + 0.5\underline{Y}_{m,2}\boldsymbol{E}_2 \\
&\cdots \\
\underline{\boldsymbol{Y}}_{N,\text{secs}} &= \left(\underline{Z}_{m,N}\boldsymbol{E}_2 + \left(0.5\underline{Y}_{m,N}\boldsymbol{E}_2 + \underline{\boldsymbol{Z}}_{\text{wt}}^{-1} + \underline{\boldsymbol{Y}}_{N-1,\text{secs}}\right)^{-1}\right)^{-1} + 0.5\underline{Y}_{m,N}\boldsymbol{E}_2
\end{aligned}
\tag{4.16}
$$

$$
\underline{\boldsymbol{Z}}_{m,\text{str}} = \underline{\boldsymbol{Y}}_{N,\text{secs}}^{-1} \tag{4.17}
$$

$$
\underline{\boldsymbol{Z}}_{\text{mv}} = \begin{bmatrix} \underline{Z}_{\text{pp}} & \underline{Z}_{\text{pn}} \\ \underline{Z}_{\text{np}} & \underline{Z}_{\text{nn}} \end{bmatrix} = \left(\sum\nolimits_{m=1}^{M} \underline{\boldsymbol{Z}}_{m,\text{str}}^{-1}\right)^{-1} \tag{4.18}
$$

The detailed model derived in (4.16)-(4.18) is then used to check the accuracies of the aggregated single-machine models. The frequency scanning of the aggregated models and the detailed impedance model is shown in Figure 4.5. For the detailed impedance model,

an extra scenario without considering cable capacitances is shown for comparison. For space reason, only the positive sequence impedance $\underline{Z}_{pp}$ and the coupling term $\underline{Z}_{pn}$ of the impedance matrix $\underline{\boldsymbol{Z}}_{mv}$ in (4.18) are presented. Same observations can be seen for the other impedance terms. For this specific MV collector system, neglecting the cable capacitances introduces large error at the frequencies starting from 200 Hz, while the power loss and voltage drop based aggregation models show acceptable accuracy at the frequencies between 5 Hz and 3 kHz.

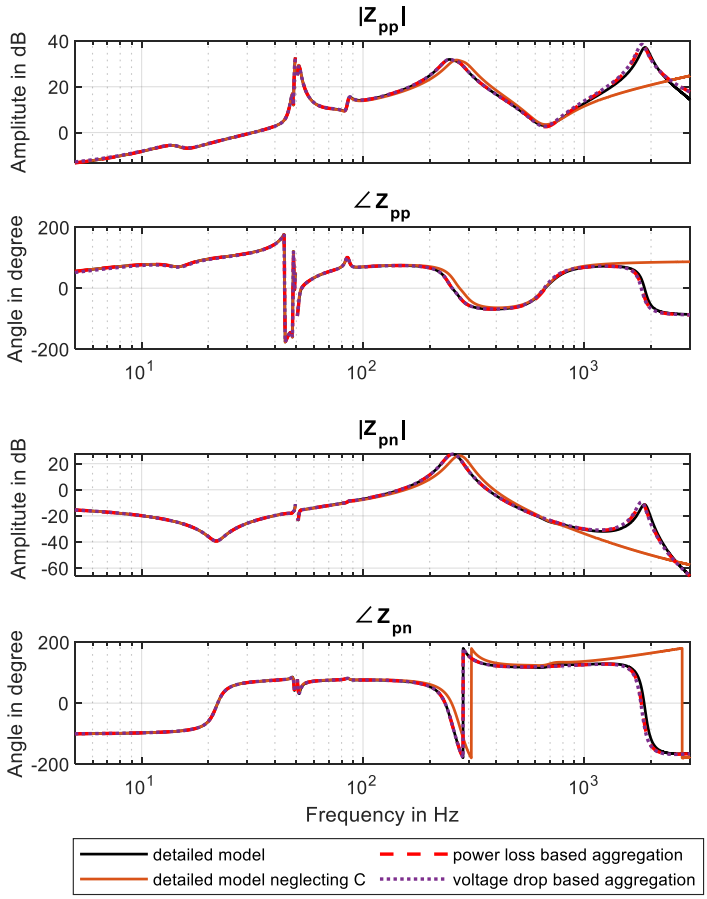

Figure 4.5 Comparison of different impedance models for the tested MV collector system

4.4 Simulation Validation

To furtherly show the suitability of the above analytically derived aggregation models for wide-band resonance analysis, simulations for checking whether the aggregated single-machine model can properly represent the impedance responses of the detailed MV collector system are conducted. To measure the impedance responses of the simulated

MV collector system, the series voltage injection approach as discussed in [28] is applied in simulations. In each simulation, the measured object is connected to an infinite bus.

To handle the enormous computation burden of tens of DFIG-based WTs in MATLAB/Simulink, the model validation of the aggregated MV collector system is divided into two steps. In the first step simulations, the impedance reponses of an 8-WT array and a 4-WT array are measured respectively, in which each WT is represented by the detailed DFIG model and each cable subsection is represented by the distributed parameters cable model from Simulink library. In the second step simulations, the impedance reponses of the MV collector system with each wind array represented by a single-machine model are measured. Figure 15 shows the good match of the analytical models with the simulation results.

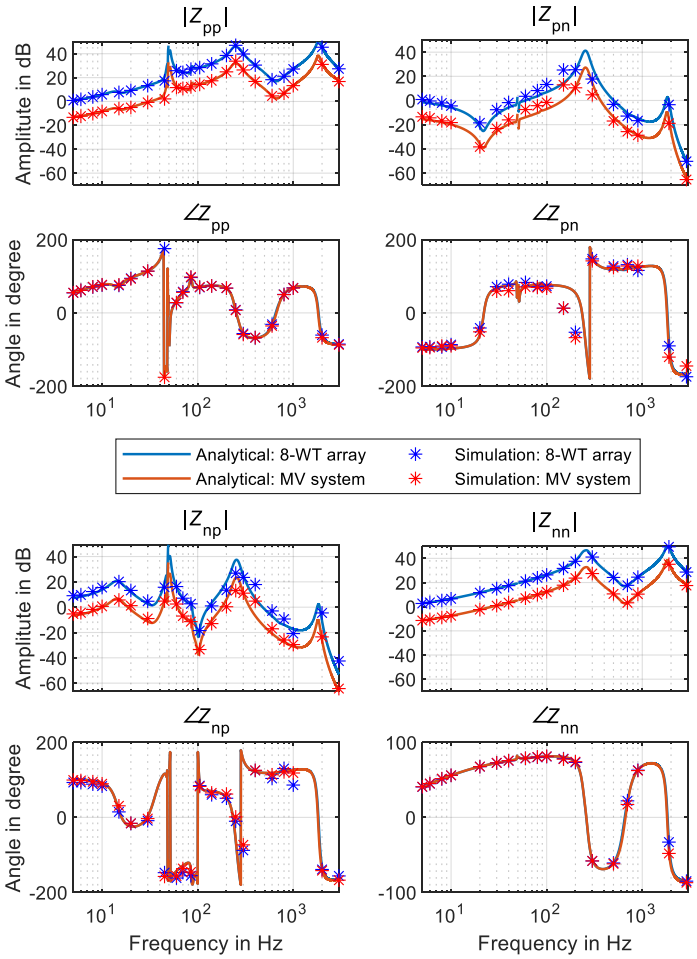

Figure 4.6 Stepwise simulation validation of the tested MV collector system.

5 Resonance Analysis

This chapter adopts the RMA and Bode plot methods to characterize the resonances in a DFIG-based OWF with HVDC connection. Sideband resonances of both the fundamental frequencey and the PWM switching frequency are analyzed. Moreover, the sources of the main resonance modes in the test system are evaluated through bus participation factor analysis. Partial results of this chapter were published in advance in [10], [35].

Figure 5.1 gives the single-line diagram of the investigated OWF integration system, which attempts to simulate a German Northsea application: the 400 MW Bard OWF and BorWin1 HVDC Transmission. The left side MV collector systems comprise 12 arrays of WTs. The total number of WTs is 80. In the middle, there are two wind farm platforms that step up grid voltage from 33 kV (MV) to 155 kV (HV). The collected wind power at each OWF platform is then fed into the right-side HVDC converter through a short length of 155 kV AC submarine cables. This offshore system is considered to be isolated from the main onshore grid by assuming a constant DC voltage in the HVDC link.

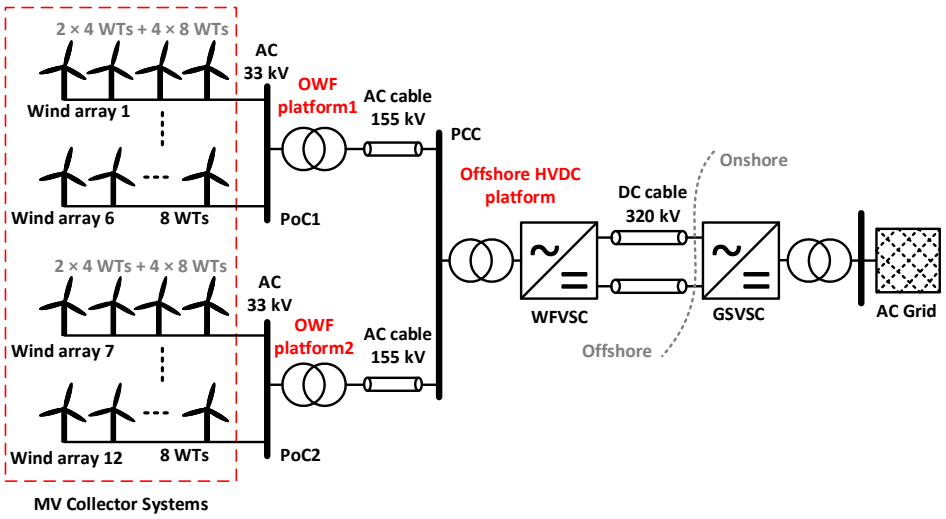

Figure 5.1 Diagram of the investigated OWF integration system

Aggregated modelling of wind farm collector systems are adopted to reduce system complexity. Based on the aggregation, a 2-machine 8-bus grid model is obtained, as shown in Figure 5.2. For the HVDC transmission system, the high-voltage DC cables, grid side VSC converter (GSVSC) as well as the main onshore grid are not shown since they have negligible influence on the dynamic of the investigated offshore grid when a constant DC voltage is ensured in the HVDC link. In the wind farm side VSC converter

(WFVSC) station, the installed high-pass damped filters are used for mitigating switching harmonics. Detailed paramters of the grid model are available in Appendix D.

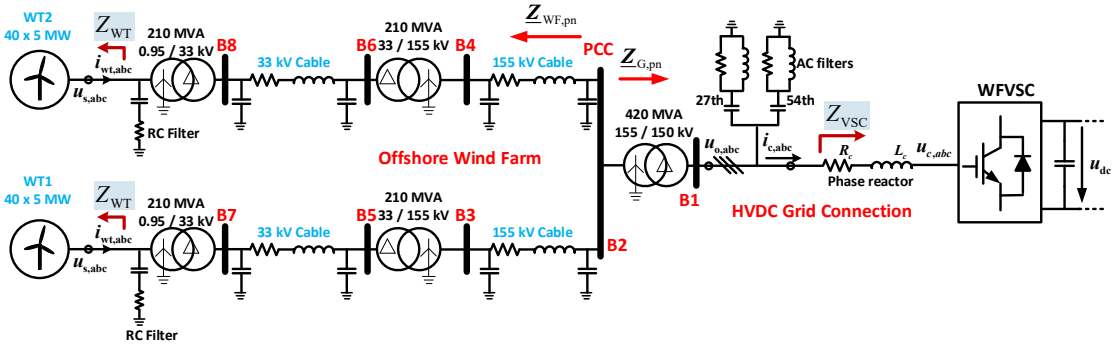

Figure 5.2 Aggregated 8-bus representation of the investigated HVDC connected OWF.

5.1 Frequency-Coupled Resonance Analysis

In section 3.3, it has been shown that the DFIG-based WT has the frequency-coupling feature. In order to evaluate the impact of frequency-coupling on the risk of resonances, this sections adopts the impedance-based method to evaluate the resonance stability of the OWF-HVDC system at their PCC point, which requires to derive the output impedances of the OWF and the HVDC grid connection, e.g. their sequence impedances $\underline{\boldsymbol{Z}}_{\mathrm{WF,pn}}$ and $\underline{\boldsymbol{Z}}_{\mathrm{G,pn}}$, as illustrated in Figure 5.2. Note, that the PWM switching and sampling process as an extra source of frequency-coupling is not included in the derived impedance models, it will be analyzed in a separate section.

Grid component models and aggregated models of WT collecting systems as derived in Chapters 3 and 4 are directly applied in this chapter's resonance analysis. All cables are represented with nominal Pi models regarding their length up to a few km. Transformer capacitance effect is neglected by setting all capacitance parameters to zero.

Taking into account the AC filters and the coupling transformer of the WFVSC, the positive- and negative-sequence impedances of the HVDC grid connection can be derived as

$$\begin{aligned}\underline{Z}_{\mathrm{G,p}}(\underline{s}) &= 1/(1/\underline{Z}_{\mathrm{vsc,p}}(\underline{s}) + 1/\underline{Z}_{\mathrm{filters}}(\underline{s})) + \underline{Z}_{\mathrm{ctr}}(\underline{s}) \\ \underline{Z}_{\mathrm{G,n}}(\underline{s}) &= 1/(1/\underline{Z}_{\mathrm{vsc,n}}(\underline{s}) + 1/\underline{Z}_{\mathrm{filters}}(\underline{s})) + \underline{Z}_{\mathrm{ctr}}(\underline{s})\end{aligned} \tag{5.1}$$

where $\underline{Z}_{\text{filters}}(\underline{s})$ denotes the overall impedance of the 27th and 54th high-pass damped filters, $\underline{Z}_{\text{vsc,p}}(\underline{s})$ and $\underline{Z}_{\text{vsc,n}}(\underline{s})$ denote the positive- and negative sequence impedances of the VSC converter, and $\underline{Z}_{\text{ctr}}(\underline{s})$ denotes the short circuit impedance of the coupling transformer. Since there is no frequency-coupling, i.e. sequence impedance coupling, in the HVDC grid connection, its sequence impedance matrix $\underline{\boldsymbol{Z}}_{\text{G,pn}}$ can be written as

$$\underline{\boldsymbol{Z}}_{\text{G,pn}} = \begin{bmatrix} \underline{Z}_{\text{G,p}} & 0 \\ 0 & \underline{Z}_{\text{G,n}} \end{bmatrix} \tag{5.2}$$

Assuming the two HV branches of the OWF are identical, the equivalent output impedance of the OWF looking from PCC can be formulated as

$$\underline{\boldsymbol{Z}}_{\text{WF,pn}}(\underline{s}) = \frac{1}{2}\left(\left((\underline{\boldsymbol{Z}}_{\text{mv}} + \underline{\boldsymbol{Z}}_{\text{T}})^{-1} + 0.5\underline{\boldsymbol{Y}}_{\text{hvc}}\right)^{-1} + \underline{\boldsymbol{Z}}_{\text{hvc}}\right)^{-1} + 0.5\underline{\boldsymbol{Y}}_{\text{hvc}}\Bigg)^{-1} \tag{5.3}$$

where

$$\underline{\boldsymbol{Z}}_{\text{T}} = \begin{bmatrix} \underline{Z}_{\text{T}} & 0 \\ 0 & \underline{Z}_{\text{T}} \end{bmatrix} \qquad \underline{\boldsymbol{Z}}_{\text{hvc}} = \begin{bmatrix} \underline{Z}_{\text{hvc}} & 0 \\ 0 & \underline{Z}_{\text{hvc}} \end{bmatrix} \qquad \underline{\boldsymbol{Y}}_{\text{hvc}} = \begin{bmatrix} \underline{Y}_{\text{hvc}} & 0 \\ 0 & \underline{Y}_{\text{hvc}} \end{bmatrix} \tag{5.4}$$

with $\underline{Z}_{\text{T}}$ denoting the short circuit impedance of the 33 / 155 kV wind farm transformer, $\underline{Z}_{\text{hvc}}$ and $\underline{Y}_{\text{hvc}}$ denoting the series impedance and shunt admittance of the 155 kV cables. The nonzero off-diagonal elements of the sequence impedance matrix $\underline{\boldsymbol{Z}}_{\text{WF,pn}}(\underline{s})$ as defined in

$$\underline{\boldsymbol{Z}}_{\text{WF,pn}}(\underline{s}) = \begin{bmatrix} \underline{Z}_{\text{WF,pp}}(\underline{s}) & \underline{Z}_{\text{WF,pn}}(\underline{s}) \\ \underline{Z}_{\text{WF,np}}(\underline{s}) & \underline{Z}_{\text{WF,nn}}(\underline{s}) \end{bmatrix} \tag{5.5}$$

make the DFIG-based OWF with HVDC grid connection a MIMO system. The root causes of the coupling between the positive and negative sequence impedances of the OWF are the PLL and asymmetrical d- and q-axis control structures in the DFIG energy conversion systems. For the better understanding of the impedance coupling in (5.5), the sequence equivalents of the investigated MIMO system in case of a shunt current perturbation are presented in Figure 5.3 (a). Given a positive sequence current perturbation $\underline{I}_{\text{p}}$ at the frequency ω_{p}, the system will have both the positive sequence

responses $\underline{U}_{\mathrm{PCC,p}}$, $\underline{I}_{\mathrm{WF,p}}$, $\underline{I}_{\mathrm{G,p}}$ at the same frequency and the negative sequence responses $\underline{U}_{\mathrm{PCC,n}}$, $\underline{I}_{\mathrm{WF,n}}$ at the frequency $\omega_{\mathrm{p}}-2\omega_{\mathrm{l}}$. Note that for ω_{p} smaller than $2\omega_{\mathrm{l}}$, the negative sequence responses at the frequency $\omega_{\mathrm{p}}-2\omega_{\mathrm{l}}$ actually correspond to the positive sequence responses $\underline{U}^{*}_{\mathrm{PCC,n}}$, $\underline{I}^{*}_{\mathrm{WF,n}}$ at the frequency $2\omega_{\mathrm{l}}-\omega_{\mathrm{p}}$, where the superscript * denotes the conjugation operation. If neglecting the frequency coupling, the independent sequence subsystems can be obtained, as illustrated by Figure 5.15 (b).

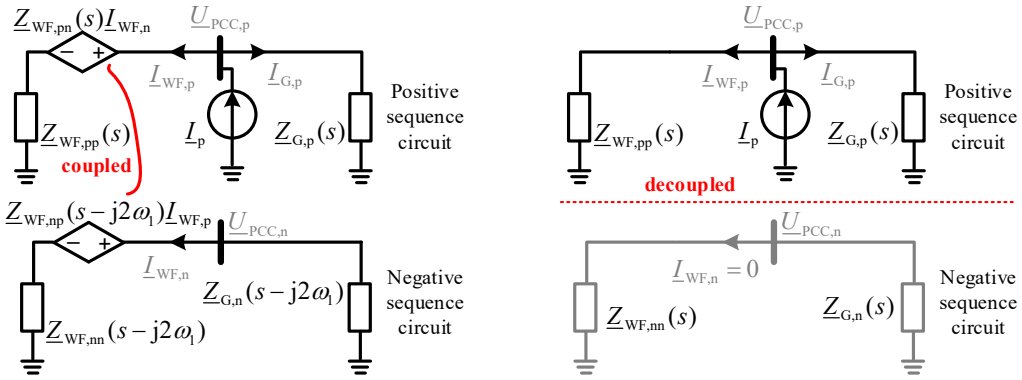

Figure 5.3 Sequence equivalents of the HVDC-connected OWF.

In terms of the positive sequence current perturbation $\underline{I}_{\mathrm{p}}$, the sequence equivalents of the HVDC-connected OWF as given in Figure 5.3 (a) can be formulated as

$$\begin{aligned}
\underline{U}_{\mathrm{PCC,p}} &= \underline{Z}_{\mathrm{WF,pp}}(\underline{s})\underline{I}_{\mathrm{WF,p}} + \underline{Z}_{\mathrm{WF,pn}}(\underline{s})\underline{I}_{\mathrm{WF,n}} \\
\underline{U}_{\mathrm{PCC,p}} &= \underline{I}_{\mathrm{G,p}}\underline{Z}_{\mathrm{G,p}}(\underline{s}) \\
\underline{U}_{\mathrm{PCC,n}} &= \underline{Z}_{\mathrm{WF,nn}}(\underline{s}-\mathrm{j}2\omega_{\mathrm{l}})\underline{I}_{\mathrm{WF,n}} + \underline{Z}_{\mathrm{WF,np}}(\underline{s}-\mathrm{j}2\omega_{\mathrm{l}})\underline{I}_{\mathrm{WF,p}} \\
\underline{U}_{\mathrm{PCC,n}} &= -\underline{I}_{\mathrm{WF,n}}\underline{Z}_{\mathrm{G,p}}(\underline{s}-\mathrm{j}2\omega_{\mathrm{l}})
\end{aligned} \tag{5.6}$$

Jointly solving the equations in (5.6) yields the equivalent SISO sequence impedances of the wind farm, as given in

$$\begin{aligned}
\underline{Z}_{\mathrm{WF,p}}(\underline{s}) &= \underline{U}_{\mathrm{PCC,p}} / \underline{I}_{\mathrm{WF,p}} = \underline{Z}_{\mathrm{WF,pp}}(\underline{s}) - \frac{\underline{Z}_{\mathrm{WF,pn}}(\underline{s})\underline{Z}_{\mathrm{WF,np}}(\underline{s}-\mathrm{j}2\omega_{\mathrm{l}})}{\underline{Z}_{\mathrm{WF,nn}}(\underline{s}-\mathrm{j}2\omega_{\mathrm{l}}) + \underline{Z}_{\mathrm{G,n}}(\underline{s}-\mathrm{j}2\omega_{\mathrm{l}})} \\
\underline{Z}_{\mathrm{WF,n}}(\underline{s}-\mathrm{j}2\omega_{\mathrm{l}}) &= \underline{U}_{\mathrm{PCC,n}} / \underline{I}_{\mathrm{WF,n}} = \underline{Z}_{\mathrm{WF,nn}}(\underline{s}-\mathrm{j}2\omega_{\mathrm{l}}) - \frac{\underline{Z}_{\mathrm{WF,pn}}(\underline{s})\underline{Z}_{\mathrm{WF,np}}(\underline{s}-\mathrm{j}2\omega_{\mathrm{l}})}{\underline{Z}_{\mathrm{WF,pp}}(\underline{s}) + \underline{Z}_{\mathrm{G,p}}(\underline{s})}
\end{aligned} \tag{5.7}$$

where $\underline{Z}_{\mathrm{WF,p}}(\underline{s})$ denotes the equivalent SISO positive sequence impedance, $\underline{Z}_{\mathrm{WF,n}}(\underline{s}-\mathrm{j}2\omega_1)$ denotes the equivalent SISO negative sequence impedance with the frequency shifting of $2\omega_1$, and the last terms in the equations of $\underline{Z}_{\mathrm{WF,p}}(\underline{s})$ and $\underline{Z}_{\mathrm{WF,n}}(\underline{s}-\mathrm{j}2\omega_1)$ interpret the frequency couplings. These frequency couplings are not only determined by the off-diagonal elements of the wind farm impedance $\underline{\boldsymbol{Z}}_{\mathrm{WF,pn}}(\underline{s})$, but also determined by the diagonal elements of $\underline{\boldsymbol{Z}}_{\mathrm{WF,pn}}(\underline{s})$ as well as the grid impedances $\underline{Z}_{\mathrm{G,p}}(\underline{s})$ and $\underline{Z}_{\mathrm{G,n}}(\underline{s})$, thus they are actually related to all the grid components of the system. The strength of the frequency couplings can be evaluated by the proximity of the real sequence impedances to the equivalent SISO sequence impedances, i.e. the proximity of $\underline{Z}_{\mathrm{WF,pp}}(\underline{s})$ to $\underline{Z}_{\mathrm{WF,p}}(\underline{s})$ and the proximity of $\underline{Z}_{\mathrm{WF,nn}}(\underline{s})$ to $\underline{Z}_{\mathrm{WF,n}}(\underline{s})$.

For the identification of the resonances in the frequency-coupled MIMO system, the PCC nodal impedances of the equivalent SISO sequence systems as formulated in (5.8) will be used. In comparison to using the loop gain or the impedance ratio of the OWF and HVDC connection for stability analysis, the PCC nodal impedances can intuitively show the natural features of resonances, i.e. frequency and damping. From the frequency scanning of $\underline{Z}_{\mathrm{PCC,p}}(\underline{s})$ and $\underline{Z}_{\mathrm{PCC,n}}(\underline{s})$, the resonances of the system can be found by the peaks of the magnitude versus frequency plots, and the damping of the resonances can be determined by the angle variations around the resonance frequencies in the angle versus frequency plots. If the phase variation around a resonance frequency is greater than 180°, i.e. a resonance with negative damping, the resonance is unstable [10]. Otherwise, the resonance may amplify the harmonic distortion at the resonance frequency and the amplification degree is proportional to the impedance magnitude.

$$\underline{Z}_{\mathrm{PCC,p}}(\underline{s})=\frac{\underline{Z}_{\mathrm{WF,p}}(\underline{s})\underline{Z}_{\mathrm{G,p}}(\underline{s})}{\underline{Z}_{\mathrm{WF,p}}(\underline{s})+\underline{Z}_{\mathrm{G,p}}(\underline{s})} \qquad \underline{Z}_{\mathrm{PCC,n}}(\underline{s})=\frac{\underline{Z}_{\mathrm{WF,n}}(\underline{s})\underline{Z}_{\mathrm{G,n}}(\underline{s})}{\underline{Z}_{\mathrm{WF,n}}(\underline{s})+\underline{Z}_{\mathrm{G,n}}(\underline{s})} \tag{5.8}$$

Since the frequency-coupling in DFIG-based OWF is introduced by the asymmetrical PLL and power loop control, it mainly has influence on the low-frequency impedance responses, typically for frequencies no larger than 100 Hz [23], [25]. Here the proportional coefficient K_{rp} of the RSC current controller $\underline{H}_{\mathrm{ri}}(\underline{s})$, which is sensitive to the low-frequency impedance responses of DFIG-based WT [15], is chosen for evaluating the frequency-coupling effect.

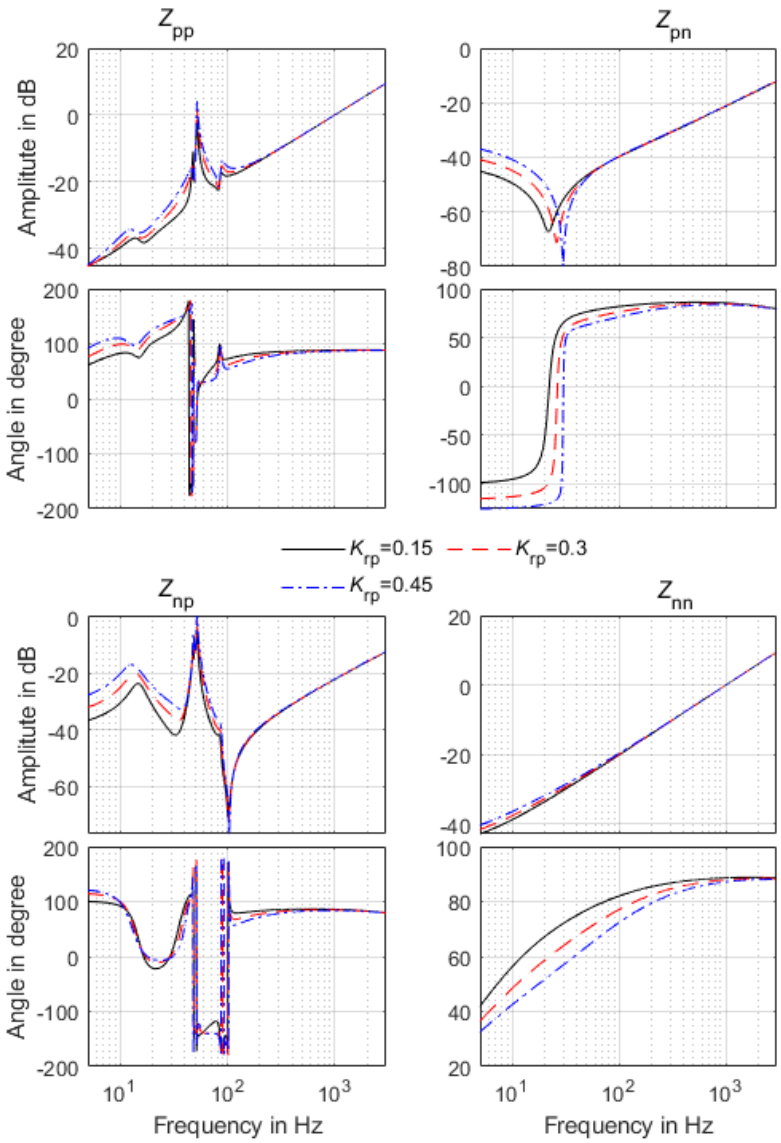

Figure 5.4 Impact of K_{rp} on the output impedances of the simulated DFIG-based WT.

Figure 5.4 shows the impedance responses of the simulated DFIG system under different K_{rp}. It is observed, as K_{rp} increases, the angles of the positive sequence impedance $\underline{Z}_{pp}$ and the coupling impedances $\underline{Z}_{pn}$ and $\underline{Z}_{np}$ will increase to be above 90º or decrease to be below -90º in the subsynchronous frequency area, which indicates negative resistances at the corresponding frequencies. For the scenarios setting K_{rp} to 0.15 and 0.45, the impact of K_{rp} on the frequency coupling of the investigated DFIG-based OWF is shown in Figure 5.5. To reflect the resonance points of the studied MIMO system, the positive sequence impedance of the connected HVDC system, $\underline{Z}_{G,p}$, is also shown in Figure 5.5. Through comparing $\underline{Z}_{WF,p}$ with $\underline{Z}_{WF,pp}$, it can be observed the frequency coupling mainly exists in the frequency range less than 100 Hz, and the strength or the degree of the frequency coupling in the scenario setting K_{rp} to 0.45 is greater than that in the scenario setting

K_{rp} to 0.15. At the frequencies above 100 Hz, the frequency coupling is not observable, thus can be neglected. Since the impact of the frequency coupling on the negative sequence impedance of the investigated OWF is negligible, it is not shown here.

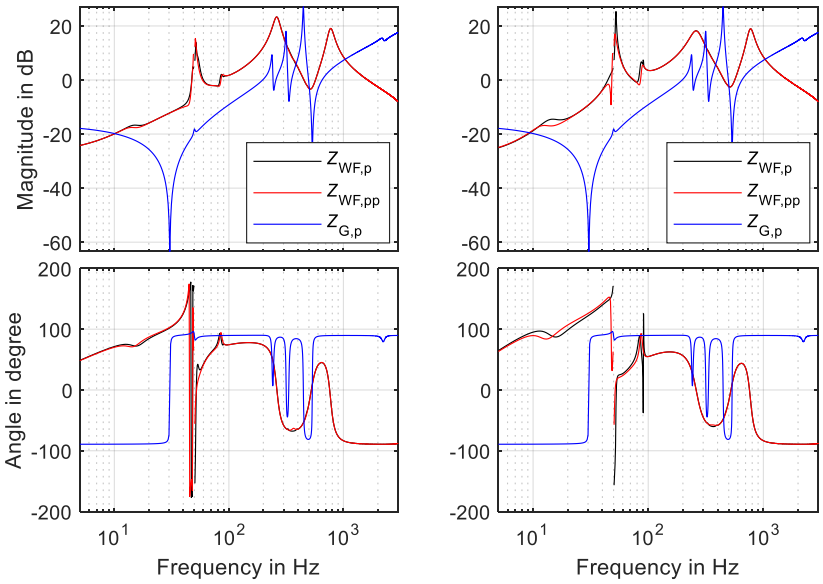

(a) K_{rp} = 0.15 (b) K_{rp} = 0.45

Figure 5.5 Positive sequence impedances of the OWF and HVDC grid connection.

In Figure 5.5, it can also be observed, that there are several resonance points determined by the cross-points of the magnitudes of $\underline{Z}_{WF,p}$ / $\underline{Z}_{WF,pp}$ and $\underline{Z}_{G,p}$ and the variation of K_{rp} mainly influences the SSR resonance mode. To better show the impact of the frequency coupling on the SSR, the PCC nodal impedances of the equivalent SISO positive sequence system as well as the corresponding impedances neglecting the frequency coupling are shown in Figure 5.6.

In Figure 5.6 (a), the frequency coupling is included. For the scenarios setting K_{rp} to 0.45 and 0.5, the resonance peaks at the frequencies around 10 Hz and 90 Hz in the magnitude plots indicate strong frequency coupling and the negative real part values of the PCC nodal impedances at the SSR frequencies indicate SSR instability [10]. As for the PCC nodal impedances neglecting the frequency coupling (by making $\underline{Z}_{WF,p}$ equal to $\underline{Z}_{WF,pp}$), the SSR mode is stable when setting K_{rp} to 0.45, which is indicated by the positive real part value of the impedance at the SSR frequency, as shown in Figure 5.6 (b). Thus, for the scenario setting K_{rp} to 0.45, neglecting the frequency coupling leads to a wrong stability assessment result.

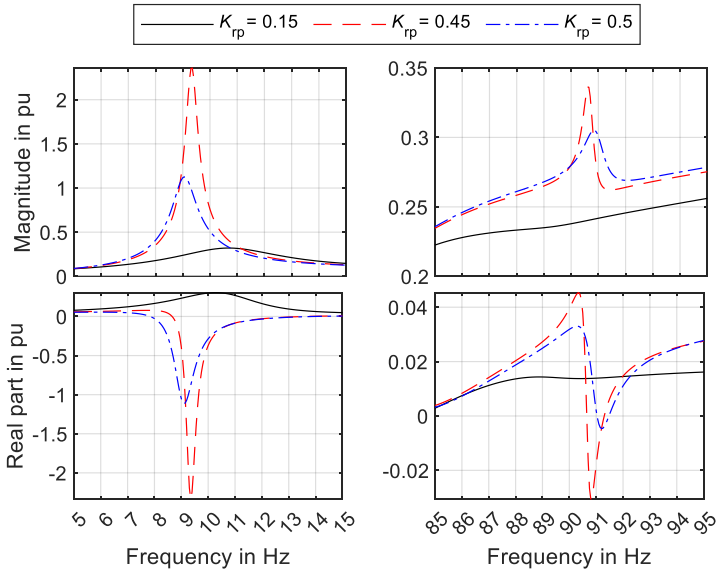

(a) including frequency coupling

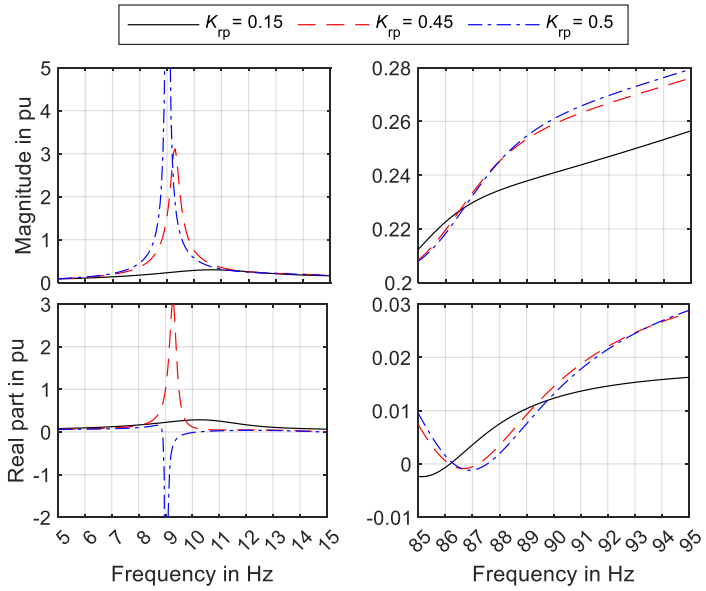

(b) neglecting frequency coupling

Figure 5.6 Impact of K_{rp} on the PCC nodal impedances for the SSR mode.

Figure 5.7 shows the simulation results in case of control parameter variation, when K_{rp} is varied from 0.15 to 0.45 at 10 s, the system becomes unstable due to the formation of the strong PCC current oscillation, which verifies the theoretical analysis on the SSR stability assessment. The frequency and damping of the SSR actually vary continuously with the growth of the resonance due to the strong nonlinearities in the converter control induced by the large current oscillation [11], [85].

In practical operating conditions, the HVDC connected DFIG-based OWF may also have such SSR instability risks when wind speed is quite low or the OWF receives a lowering power generation command from its superior level control center [10], [11]. Therefore, including frequency-coupling in the assessment of resonance stability plays an important role for critical stable operating conditions and can help system operators to take proper preventive corrections.

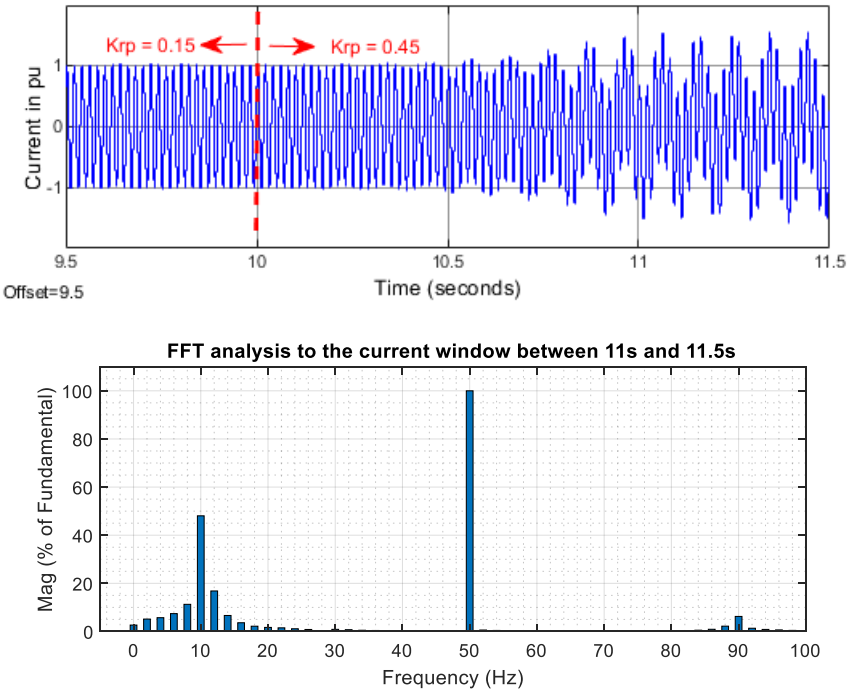

Figure 5.7 PCC current waveform and FFT analysis under variation of K_{rp}.

5.2 Sideband Resonances of Switching Frequencies

The PWM switching and sampling process of voltage-source converters (VSCs) is actually a modulation process that adds images, which can be explained as the sideband harmonics of the modulated frequency [57]. For the present sampling and PWM switching techniques, the sampling angular frequency ω_s is either equal to the switching angular frequency ω_{sw} (single update) or 2 times of ω_{sw} (double update). For the latter one, both the switching process and the sampling process produce their own sideband harmonics, thus multiple sideband harmonics will be introduced in converter output signals. However, since the harmonic components beyond the switching frequency ω_{sw} are typically well attenuated by converter terminal filters and control signal filters, no

matter the digital control system is sampled and updated once or twice for each switching cycle, the harmonic spectrum of the converter output signal will be nearly the same.

In this work, the type of double update in each switching cycle is adopted, i.e. converters are configured with ω_s equal to $2\omega_{sw}$. Assuming the PWM reference contains only the fundamental component ω_1, the harmonic spectrum of the converter ouput voltage can be illustrated by Figure 5.8 (a). The frequencies of the switching harmonics can be described by (5.9) [86]. After adding a small-signal perturbation in the PWM reference, which can either be a positive sequence perturbation with the frequency ω_p or a negative sequence perturbation with the frequency ω_n, the harmonic spectrum of the converter ouput voltage can be illustrated by Figure 5.8 (b), (c) , as discussed in [56].

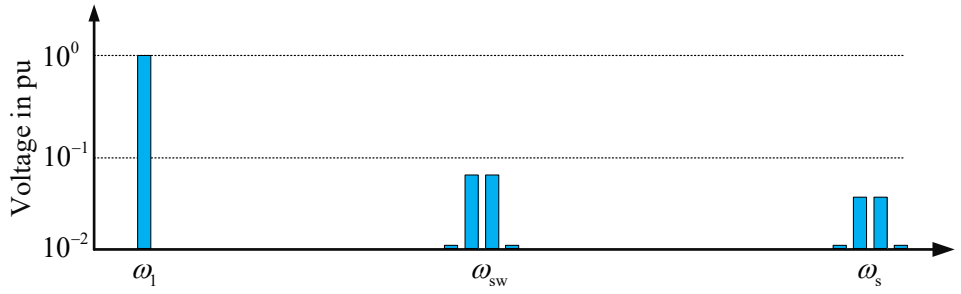

(a) PWM reference contains only ω_1

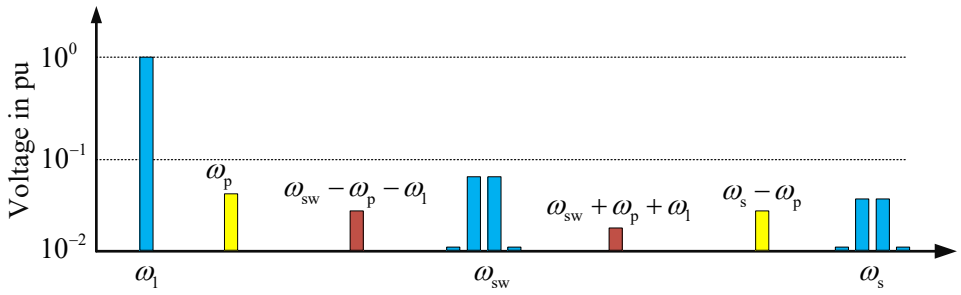

(b) PWM reference contains ω_1 and ω_p

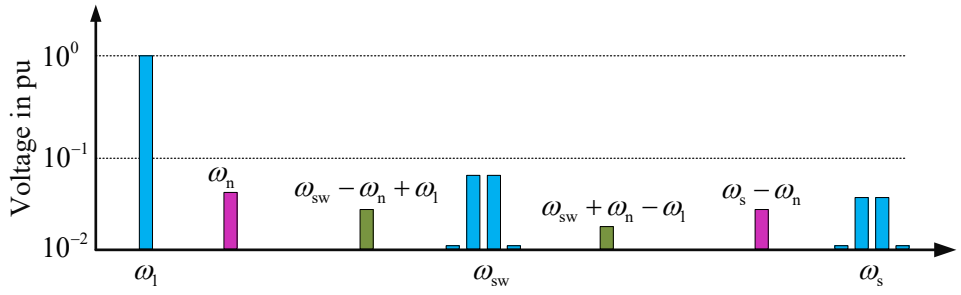

(c) PWM reference contains ω_1 and ω_n

Figure 5.8 Schematic diagram of the harmonic spectrum of converter ouput voltage.

$$k\omega_{sw} \pm n\omega_1 \begin{cases} k = 1,3,5 \ldots, \text{n=0,2,4, ...} \\ k = 2,4,6 \ldots, \text{n=1,3,5, ...} \end{cases} \tag{5.9}$$

Taking into account the attenuation of the frequency components beyond the switching frequency or the so-called Nyquist frequency, the main sideband component of the positive sequence perturbation ω_p is $\omega_{sw} - \omega_p - \omega_1$, which is in the negative sequence, while the main sideband component of the negative sequence perturbation ω_n is $\omega_{sw} - \omega_n + \omega_1$, which is in the positive sequence. In the further discussions, only the main sideband components $\omega_{sw} - \omega_p - \omega_1$ for ω_p and $\omega_{sw} - \omega_n + \omega_1$ for ω_n will be considered.

Then simulations using the detailed model of the HVDC converter as shown in Figure 5.2 are conducted to verify the above theoretical analysis. The DC side of the converter is connected to an DC voltage source and the AC side of the converter is connected to a three-phase resistive load, as shown in Figure 5.9.

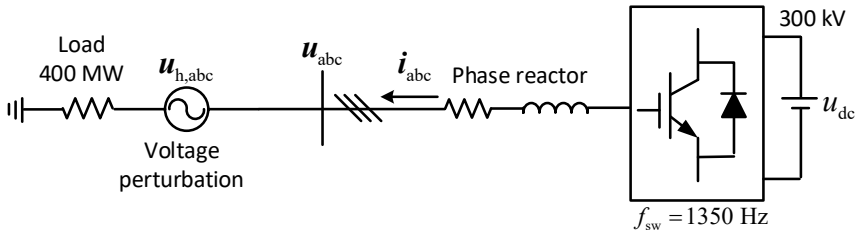

Figure 5.9 A simple test grid for checking the sideband harmonics of VSC converters

Under the condition of no voltage perturbation, a positive- or a negative-sequence voltage perturbation $\boldsymbol{u}_{h,abc}$, the harmonic spectrums of the voltage $\boldsymbol{u}_{abc}$ are shown in Figure 5.10, respectively. The observed sideband harmonics validate the theoretical analysis as illustrated in Figure 5.8. Note that the imposed voltage perturbations are set to be sufficient large to observe the sideband harmonic phenomena. Even though the sideband harmonics of the imposed voltage perturbations are very small, the resulting sideband resonances can have great impact on system stablity, as reported in [56], [57].

In [56], [57], the frequency-coupling induced by PWM switching and sampling process is incorporated in the impedance modelling of VSC converters, which helps correctly evaluating system stability taking into account the sideband resonances of switching frequency. However, the derived converter impedance model is quite complicated, particularly for a system comprising multiple converters with different switching

frequencies, for instance, a HVDC connected OWF. Therefore, this work tries to analyse the sideband resonances of switching frequencies using the relevant simple impedance models as presented in chapters 3 and 4. The high risk resonance conditions can be identified by simplying checking if there are two or more resonances matching the frequencies of the sideband harmonics of each switching frequency as illustrated in Figure 5.8 (b), (c).

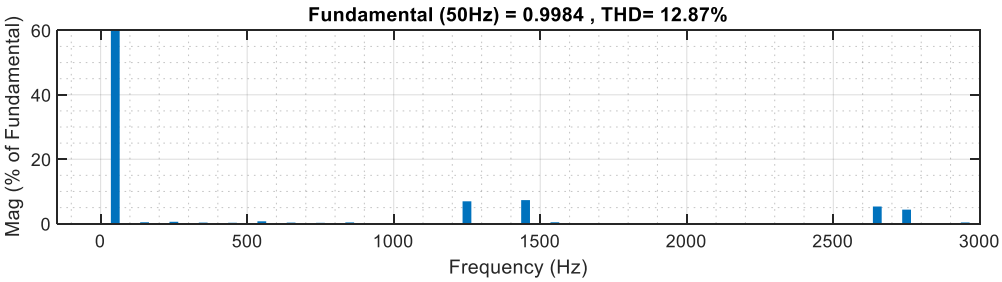

(a) imposing no perturbation

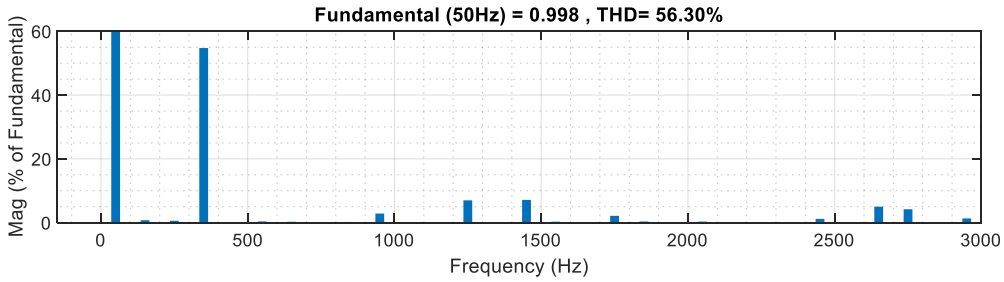

(b) with a positive sequence voltage perturbation

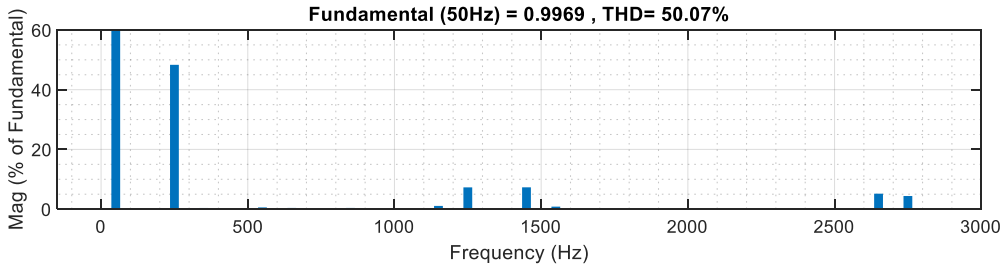

(c) with a negative sequence voltage perturbation

Figure 5.10 Harmonic spectrums of the voltage signal $\boldsymbol{u}_{\text{abc}}$ from simulations

When neglecting the sideband harmonics beyond switching frequency, the rules for identifying risky resonances can be formulated as in Table 5.1, in which ε denotes the threshold of the angular frequency differences, e.g. it can be set to $0.1\omega_1$.

To validate the risk criterions as listed in Table 5.1, the test grid in Figure 5.2 is modified by replacing the HVDC converter with an AC grid, and both the short circuit ratio (SCR) and the X/R of the AC grid are set to 10, as illustrated in Figure 5.11. In order to better

observe the switching harmonics, WT terminal filters are switched off. Frequency scanning of the PCC nodal impedances, i.e. positive sequence impedance $\underline{Z}_{PCC,p}$ and negative sequence impedance $\underline{Z}_{PCC,n}$, under different SCR are shown in Figure 5.12. In the case of setting SCR to 20, the 973 Hz resonance mode satisfies the risk criterion 1 in Table 5.1, and its simulation validation is shown in Figure 5.13.

Table 5.1 Identification of the risky sideband resonances of each switching frequency

Resonance modes	Risk criterion	Risk criterion 1	Risk criterion 2
ω_{p1}, ω_{p2}, ... ω_{pk} in positive sequence system	$\lvert\omega_{pi}+\omega_{pj}+\omega_{1}-\omega_{sw}\rvert \le \varepsilon$ $i, j = 1,2, \dots, k$	$\lvert 2\omega_{pi}+\omega_{1}-\omega_{sw}\rvert \le \varepsilon$ $i = 1,2, \dots, k$	$\lvert\omega_{pi}+\omega_{pj}+\omega_{1}-\omega_{sw}\rvert \le \varepsilon$ $i, j = 1,2, \dots, k$ and $i \neq j$
ω_{n1}, ω_{n2}, ... ω_{nm} in negative sequence system	$\lvert\omega_{ni}+\omega_{nj}-\omega_{1}-\omega_{sw}\rvert \le \varepsilon$ $i, j = 1,2, \dots, k$	$\lvert 2\omega_{ni}+\omega_{1}-\omega_{sw}\rvert \le \varepsilon$ $i = 1,2, \dots, k$	$\lvert\omega_{ni}+\omega_{nj}-\omega_{1}-\omega_{sw}\rvert \le \varepsilon$ $i, j = 1,2, \dots, k$ and $i \neq j$

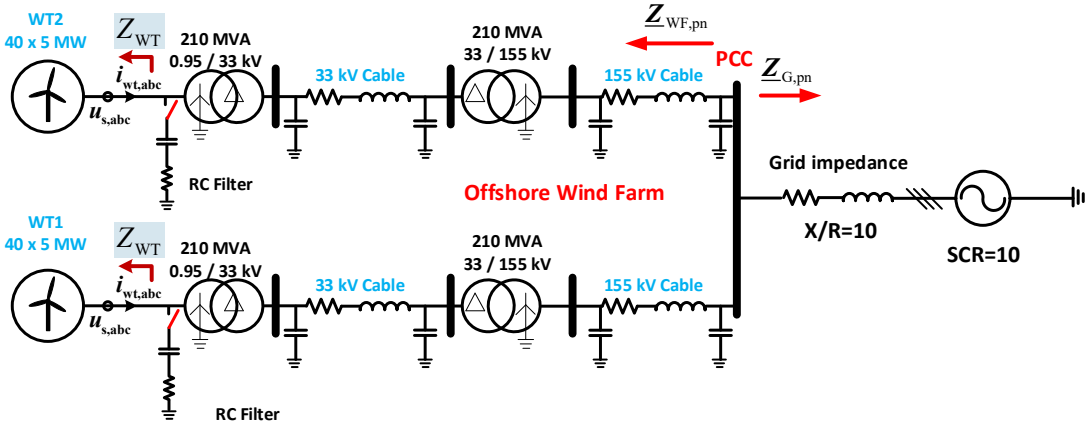

Figure 5.11 Test grid for the validation of sideband resonances

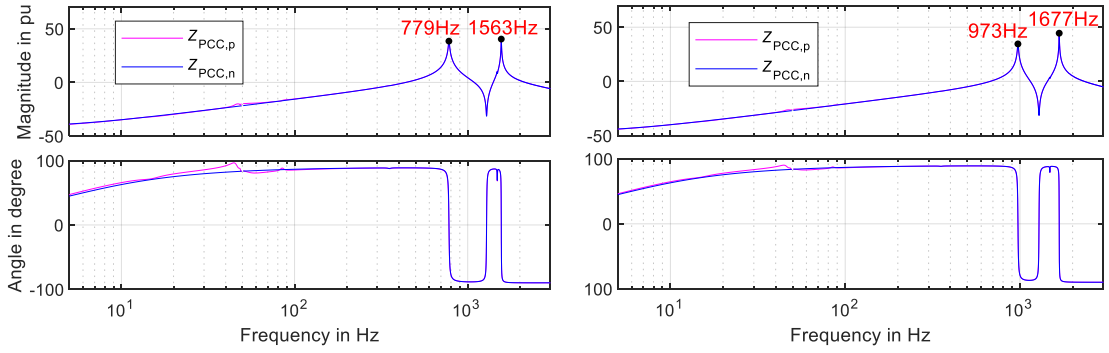

(a) SCR=10 (b) SCR=20

Figure 5.12 PCC nodal impedances under variation of grid SCR.

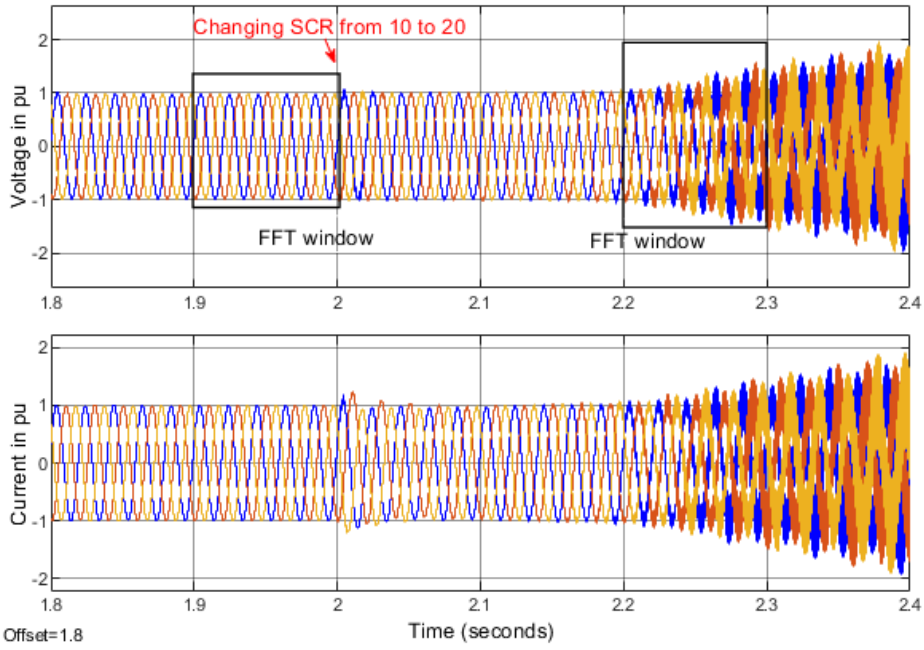

(a)

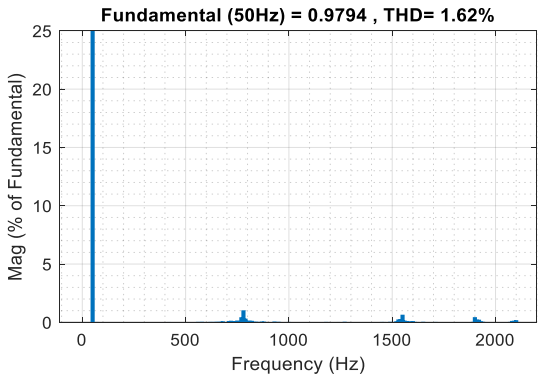

(b)

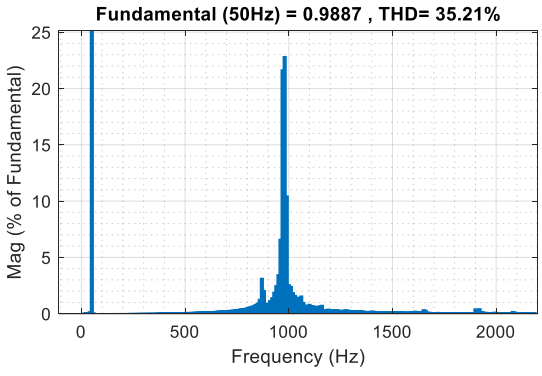

(c)

Figure 5.13 PCC waveforms and FFT analysis under the variation of grid SCR

Keeping the SCR of the test grid as 10 but changing the switching frequencies of WTs from 2 to 2.4 kHz for both the GSCs and RSCs, then the two resonance modes of 779 Hz and 1563 Hz in Figure 5.12 (a) satisfy the risk criterion 2 in Table 5.1. The simulation validation of these sideband resonances is shown in Figure 5.14.

From the above two examplary case studies, it can be concluded, that the sideband resonances of PWM switching frequency plays an important role in the assessment of system stability and neglecting them may lead to optimistic risk assessment for resonances.

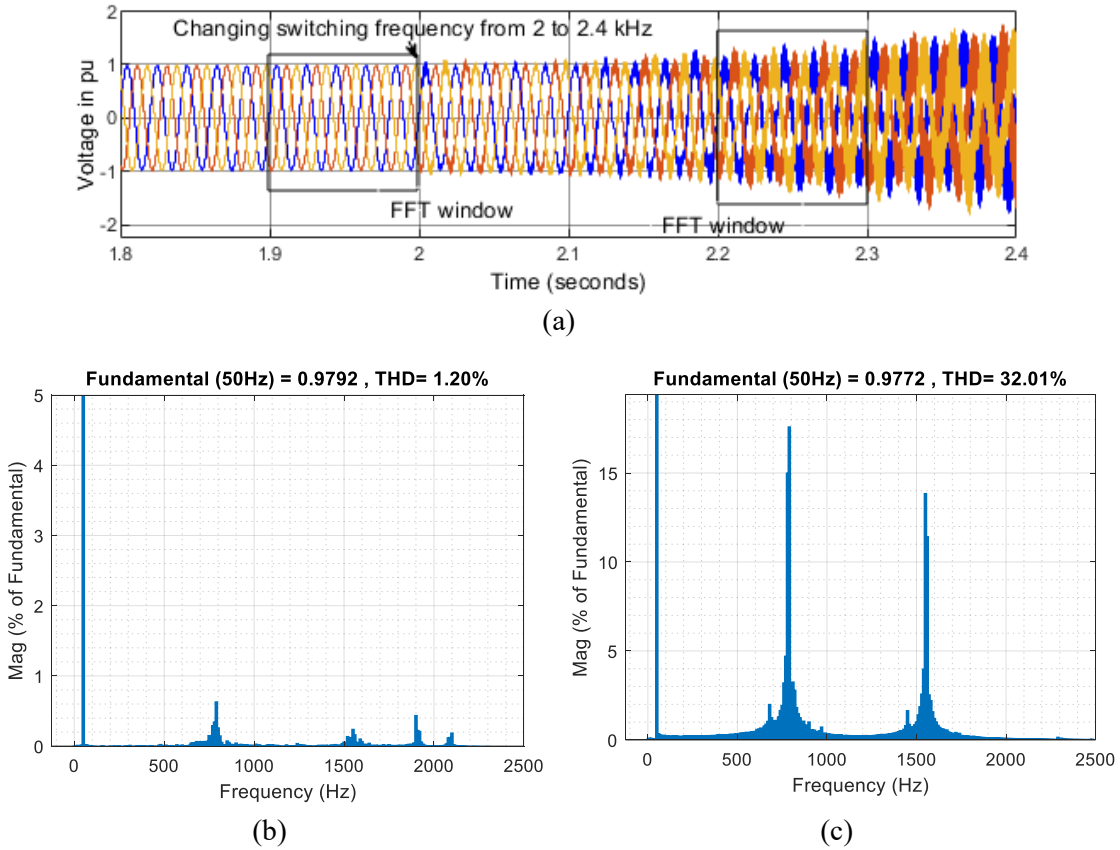

Figure 5.14 PCC voltage and FFT analysis as the PWM switching frequency varies

5.3 Resonance Mode Analysis Neglecting Frequency-Coupling

Neglecting the coupling between positive and negative sequence impedances may not be effective for quantitative stability analysis, but it is useful for identifying the resonance points of a system and analyzing their risk qualitatively [34]. Generally, as long as the resonances do not make the system enter into critical stable states, the frequency coupling effect can be neglected for the simplicity of resonance analysis [35].

Without losing generality, this section focuses on the resonances in positive-sequence component system. According to the grid component connections as illustrated in Figure 5.2, an 8-by-8 nodal admittance matrix that relates the voltages and currents of the buses from B1 to B8 can be built, as represented in (5.10). As known, a square matrix has an inverse if and only if its determinant is non zero. Here each diagonal term of $\underline{\boldsymbol{Y}}_{\mathrm{NN}}$ includes the admittances of at least one shunt component and most of the off-diagonal terms of $\underline{\boldsymbol{Y}}_{\mathrm{NN}}$ are zero as each of the buses is only connected to 3 other buses at most, which tends

to make the matrix a non-singular matrix. On this basis, inversing the nodal admittance matrix $\underline{\boldsymbol{Y}}_{\mathrm{NN}}$ gives the nodal impedance matrix $\underline{\boldsymbol{Z}}_{\mathrm{NN}}$ as in (5.11).

$$\begin{bmatrix} \underline{I}_{\mathrm{B1}} \\ \underline{I}_{\mathrm{B2}} \\ \vdots \\ \underline{I}_{\mathrm{B8}} \end{bmatrix} = \underbrace{\begin{bmatrix} \underline{Y}_{11} & \underline{Y}_{12} & \cdots & \underline{Y}_{18} \\ \underline{Y}_{21} & \underline{Y}_{22} & \ddots & \underline{Y}_{28} \\ \vdots & \ddots & \ddots & \vdots \\ \underline{Y}_{81} & \underline{Y}_{82} & \cdots & \underline{Y}_{88} \end{bmatrix}}_{\underline{\boldsymbol{Y}}_{\mathrm{NN}}(s)} \begin{bmatrix} \underline{U}_{\mathrm{B1}} \\ \underline{U}_{\mathrm{B2}} \\ \vdots \\ \underline{U}_{\mathrm{B8}} \end{bmatrix} \tag{5.10}$$

$$\underline{\boldsymbol{Z}}_{\mathrm{NN}}(\underline{s}) = \underline{\boldsymbol{Y}}_{\mathrm{NN}}(\underline{s})^{-1} = \begin{bmatrix} \underline{Z}_{11} & \underline{Z}_{12} & \cdots & \underline{Z}_{18} \\ \underline{Z}_{21} & \underline{Z}_{22} & \ddots & \underline{Z}_{28} \\ \vdots & \ddots & \ddots & \vdots \\ \underline{Z}_{81} & \underline{Z}_{82} & \cdots & \underline{Z}_{88} \end{bmatrix} \tag{5.11}$$

Due to the physical connections of system buses, the parallel connected electrical circuits represented by the driving point impedances from $\underline{Z}_{11}$ to $\underline{Z}_{88}$ are coupled with each other, thus two or more driving point impedances will contain similar information of one resonance mode, which is not favor of the identificaiton of resonance frequency and harmonic amplificaiton effect [12]. To handle this problem, the nodal impedance matrix $\underline{\boldsymbol{Z}}_{\mathrm{NN}}$ is transformed into a diagonal impedance matrix $\underline{\boldsymbol{Z}}_{\mathrm{M}}$ through the following matrix manipulation

$$\underline{\boldsymbol{Z}}_{\mathrm{M}}(\underline{s}) = \underline{\boldsymbol{T}}_{\mathrm{N}}^{-1}\underline{\boldsymbol{Z}}_{\mathrm{NN}}(\underline{s})\underline{\boldsymbol{T}}_{\mathrm{N}} = \begin{bmatrix} \underline{Z}_{\mathrm{m1}} & 0 & \cdots & 0 \\ 0 & \underline{Z}_{\mathrm{m2}} & \ddots & 0 \\ \vdots & \ddots & \ddots & \vdots \\ 0 & 0 & \cdots & \underline{Z}_{\mathrm{m8}} \end{bmatrix} \tag{5.12}$$

where $\underline{\boldsymbol{T}}_{\mathrm{N}}$ is the right eigenvector matrix of $\underline{\boldsymbol{Z}}_{\mathrm{NN}}$. Through the transformation from $\underline{\boldsymbol{Z}}_{\mathrm{NN}}$ to $\underline{\boldsymbol{Z}}_{\mathrm{M}}$, the physically coupled electrical circuits under nodal coordinate system are transformed to independent electrical circuits under modal coordinate system. Then performing frequency scanning to the frequency-dependent modal impedances will give the resonance information of the system. This is the basis idea of the resonance mode analysis (RMA) [38].

Figure 5.15 shows the frequency scanning of the modal impedances from $\underline{Z}_{\mathrm{m1}}$ to $\underline{Z}_{\mathrm{m8}}$. Curve peaks in the magnitude plot indicate resonances. Harmonic amplification level is

indicated by the magnitude of the curve peak, and the frequency where the curve peak appears is resonance frequency. Note that the occurrence of negative damping for a resonance mode can not be identified using the conventional RMA by only analyzing the magnitudes of modal impedances, instead it can be identified by a larger than 180° angle variation around the resonance frequency in the phase plot [10]. For the resonance modes with positive damping, a larger peak value in the magnitude plot means greater harmonic amplification effect for the resonance frequency.

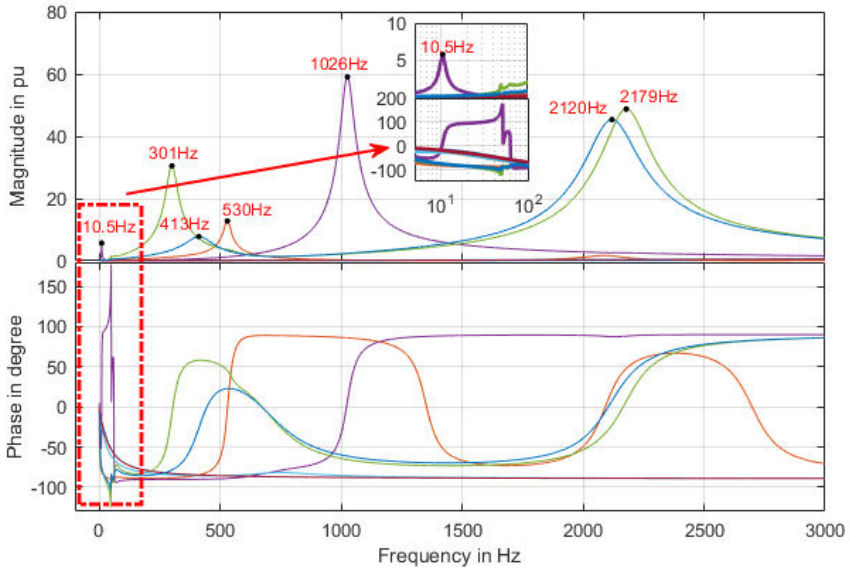

Figure 5.15 Frequency scanning of the modal impedances in the positive sequence subsystem

Figure 5.16 shows the results of FFT analysis to the PCC current and voltage waveforms in simulations, the dominated harmonics are the typical low-order odd harmonics, the switching sideband harmonics of WT and HVDC converters, as well as the harmonic components at or around resonance frequencies (see Figure 5.15). A subsynchronous frequency component within 50 Hz and its mirrored frequency component between 50 Hz and 100 Hz exist due to the interactions of the OWF and the HVDC at the resonance frequency of 10.5 Hz. Most other harmonic currents are far smaller than 0.2% of the fundamental value. Distortions of individual harmonic orders and total harmonic distortions (THD) of PCC current and voltage satisfy the harmonic distortion requirements as stipulated in [5].

Using the RMA method, not only dominating resonances could be obtained, but also the most influential buses (resonance sources) could be identified, which are given by the participation factors (PF) obtained through eigenvalue decomposition [38], as shown in Table 5.2. For the 10.5 Hz resonance mode, the buses B1, B2, B3 and B4 in 155 kV high-

voltage side contributes mostly to the formed LC resonance circuit, but as the source of negative damping at SSR frequencies [11], the buses B7 and B8 where DFIG-based WTs are located have larger impact on the risk of this SSR mode. For the 301 Hz, 413 Hz, 2120 Hz and the 2179 Hz resonance modes, the buses B5, B6, B7 and B8 in two MV collector systems have the largest PFs, thus are the main resonance sources. For the 530 Hz and 1026 Hz resonance modes, the buses B2, B3 and B4 where 155 kV AC cables are located play an important role, besides, the switching harmonic filters of HVDC converter at bus B1 also participate the 530 Hz resonance.

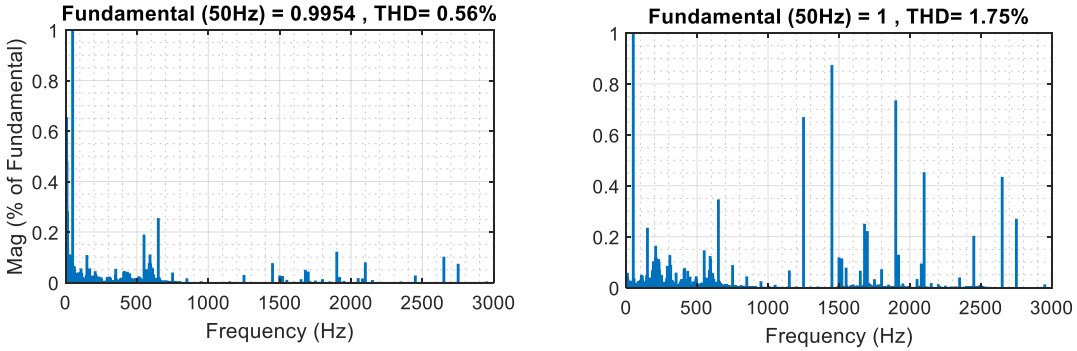

(a) Current frequency spectrum (b) Voltage frequency spectrum

Figure 5.16 FFT analysis to the current and voltage of the 155 kV PCC bus

Table 5.2 Bus participation factor analysis

Modal Resonances		**f_{res} in Hz**	**10.5**	**301**	**413**	**530**	**1026**	**2120**	**2179**
		$\|Z_m\|$ in pu	5.7	31	7.8	12.8	59	45	49
Participation Factor (PF) in %	HV buses	B1	**25**	3	5	**14**	0	0	0
		B2	**15**	10	9	**16**	**31**	0	0
		B3	**15**	11	9	**15**	**31**	0	1
		B4	**15**	11	9	**15**	**31**	0	1
	MV buses	B5	8	**16**	**17**	9	3	**27**	**26**
		B6	8	**16**	**17**	9	3	**27**	**26**
		B7	7	**17**	**18**	11	2	**23**	**23**
		B8	7	**17**	**18**	11	2	**23**	**23**

Note that the PFs in Table 5.2 are only valid for the operating condition that all WTs are in-service and generate full power. For other grid configurations or wind farm operating conditions, the dominating resonance modes and their bus PFs should be recalculated.

6 Damping Strategies

For hamonic filtering and resonance damping, there are a variety of choices. They are passive filter [87], [88], active power filter (APF) [89], [90], active damper [91]-[46], and active damping in converter-interfaced component [94]-[98].

Passive filter has gained its popularity by the simple structure and easy implementation. It can be designed for filtering harmonics of a certain frequency or a frequency band, e.g. single-tuned passive filter, low- or high-pass filter, and C-type filter. Moreover, passive filter may more or less influence the dynamics of a system at fundamental frequency, and cause extra power loss, thus get limited applications, so does passive damper.

As converter-interfaced components can be flexibly controlled, some active damping functionalities have been introduced into wind generation units and they are typically realized by adding an extra control loop or adding a filter in existing control loops [94]-[98]. If defining low frequency (LF) range as below 100 Hz, middle frequency (MF) range as between 100 Hz and 1000 Hz, and (HF) range as above 1000 Hz, then for large-scale DFIG generation unit, the relatively low switching frequencies of its GSC and RSC constrain their damping application in LF and MF bands. Similar to WT converters, active damping can be provided by HVDC converter through adding an extra control loop or adding a filter in existing control loops [18], [80]. Note that HVDC converter usually has a switching frequency down to 1 kHz, its damping application is also constrained to LF and MF ranges.

To cover the resonance damping in HF range, adding an extra converter-interfaced component with higher switching frequency, e.g. 5 kHz, can be an effective option. In [89], Resistive-Active Power Filter (R-APF) is proposed for harmonic termination of a 6.6 kV radial power distribution line, in which a series transformer is used for stepping dow grid voltage. This design is afterwards revised by replacing the transformer with a capacitor, which largely reduces the overall size and production cost [90]. However, these R-APF filters are only designed for attenuating LF and MF harmonics of certain harmonic orders. In [91]-[93], L-filtered and LC-filtered active dampers are proposed for adaptively damping HF resonances, but they are designed for LV applications.

In the following sections, several damping possibilities suited for the application of HVDC connected DFIG-OWF will be presented, and a coordinated damping strategy covering the frequencies from several Hz to a few kHz will be proposed. Partial results of this chapter were published in advance in [10], [46].

6.1 Damping Control in DFIG-based WT

Resonances can be damped by reshaping converter output impedance in a passive or active way. For DFIG-based WT, passive damping is typically realized by adding a series or parallel resistor in the GSC or RSC AC side circuit. Considering the high power loss and low flexibility, the passive damping methods are deemed as impractical in field applications. In contrast, active damping can be achieved through the control of GSC or RSC in different forms, which convert the power of unexpected frequency into fundamental power instead of consuming it. For example, changing the bandwidth of converter current control loop or PLL has been proved effective in mitigating resonances [94]. However, such method will influence the overall performance of WT. Using active control to emulate a resistance is more effective in resonance damping, thus in this section, it is presented as a representative active damping method.

Since the damping control through RSC is usually more effective than through GSC [15], the converter control to emulate a series resistor in RSC ac side circuit will be elaborated here. Figure 6.1 shows the location of the emulated resistance and the implemented active control. The additional control paths denoted as $\underline{Z}_{\mathrm{rd}}$ are added to both the d- and q-axis of RSC current control loop. Expression of the series virtual impedance $\underline{Z}_{\mathrm{rd}}$ is

$$\underline{Z}_{\mathrm{rd}}(\underline{s}) = R \underbrace{\frac{\underline{s}}{\underline{s}+\omega_{\mathrm{c1}}} \frac{\omega_{\mathrm{c2}}}{\underline{s}+\omega_{\mathrm{c2}}}}_{\underline{H}_{\mathrm{f}}(\underline{s})} \tag{6.1}$$

where R is the desired damping, $\underline{H}_{\mathrm{f}}(\underline{s})$ represents the series connection of a high-pass filter and a low-pass filter, which together function as a band-pass filter. Considering the Park transformation from the dq-frame to the three-phase signal, ω_{c1} denotes the cutoff frequency around fundamental frequency, and ω_{c2} denotes the cutoff frequency for switching noise rejection.

The desired virtual resistance in (6.1) has RSC terminal current as input and RSC voltage response as output. According to the frequency shifting of inverse Park transformation (see Table 6.1), for the positive-sequence signals under stationary reference frame, the added paths mainly emulate a resistance R for the frequencies between $\omega_{\mathrm{c1}}+\omega_{\mathrm{1}}$ and

$\omega_{c2}+\omega_1$ and for the frequencies below $\omega_1-\omega_{c1}$, with ω_1 denoting the nominal angular frequency of the system.

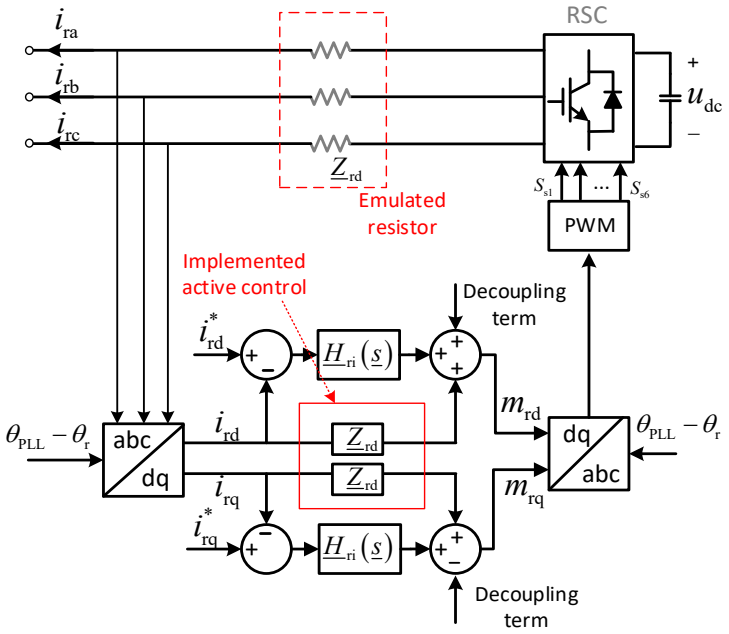

Figure 6.1 Damping control implemented in the RSC of DFIG-based WT

Table 6.1 Frequency shifting in the inverse Park transformation neglecting PLL dynamics

$\underline{U}_d(\omega)$, $\underline{U}_q(\omega)$	$\boldsymbol{T}^{-1}(\theta)$	$\underline{U}_a(\omega)$, $\underline{U}_b(\omega)$, $\underline{U}_c(\omega)$	**Phase Sequence**
dc	$\pm\omega_1$	$\pm\omega_1$	Positive
$\pm(\omega_p-\omega_1)$	$\pm\omega_1$	$\pm\omega_p$	Positive
	$\mp\omega_1$	$\pm(\omega_p-2\omega_1)$	Negative
$\pm(\omega_n+\omega_1)$	$\mp\omega_1$	$\pm\omega_n$	Negative
	$\pm\omega_1$	$\pm(\omega_n+2\omega_1)$	Positive

Figure 6.2 shows the frequency scanning of the emulated impedance $\underline{Z}_{rd}(\underline{s}-\mathrm{j}\omega_1)$ in the positive-sequence system, in which R denotes the emulated resistance, f_{c1} and f_{c2} correspond to the angular frequencies ω_{c1} and ω_{c2} as given in (6.1). Three sets of R, f_{c1} and f_{c2} parameters are adopted for comparison. For the parameter setting of R equal to 0.06 pu, f_{c1} equal to 10 Hz and f_{c2} equal to 300 Hz, the voltage response to the current input is greatly attenuated at fundamental frequency, thus the added path will not influence the fundamental power flow of the system. At SSR frequencies, the virtual

impedance nearly maintains the gain of R and shows strong resistive feature as its phase angle tends to be zero degree. At supersynchronous frequencies up to the cutoff frequency f_{c2} or ω_{c2}, the gain of the virtual impedance that is mainly determined by R does not change much and the phase angle varies from 50° and -50°, which shows certain level of resistive feature. Increasing R from 0.06 to 0.1 clearly enlarges the gain but has no influence on the phase angle, while increasing f_{c2} from 300 Hz to 800 Hz clearly strengthens the damping capability for the frequencies above 50 Hz (more resistive) but weakens the SSR damping capability (less resistive) as well as the switching noise rejection capability (larger gain for the frequencies from around 200 Hz to a few kHz).

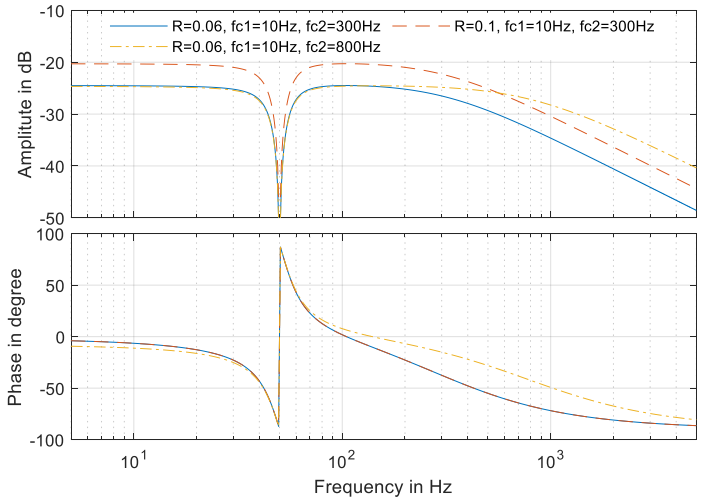

Figure 6.2 Frequency scanning of the emulated impedance in the positive-sequence system.

According to the above analysis, the virtual impedance with the parameter setting R equal to 0.06 pu, f_{c1} equal to 10 Hz and f_{c2} equal to 300 Hz is selected and implemented in the simulated DFIG-based WT as described in Section 3.3 (see Appendix D for WT parameters). Figure 6.3 shows the frequency scanning of the analytical impedances of the DFIG-based WT with active damping (red line) and without active damping (blue line) as well as the impedance responses from simulations in Simulink (circles). The nominal operating point is assumed for the WT. It can be oberserved that including the active damping effectively reshapes WT output impedance. The most influencing impact is moving the impedance phase angle down by some degrees at SSR frequencies, e.g. from 90° or above to be less than 90°, which means the addition of some positive resistances to the negative or low resistive WT at SSR frequencies. Simulation results validate the control effect of the virtual impedance in reshaping the WT output impedance.

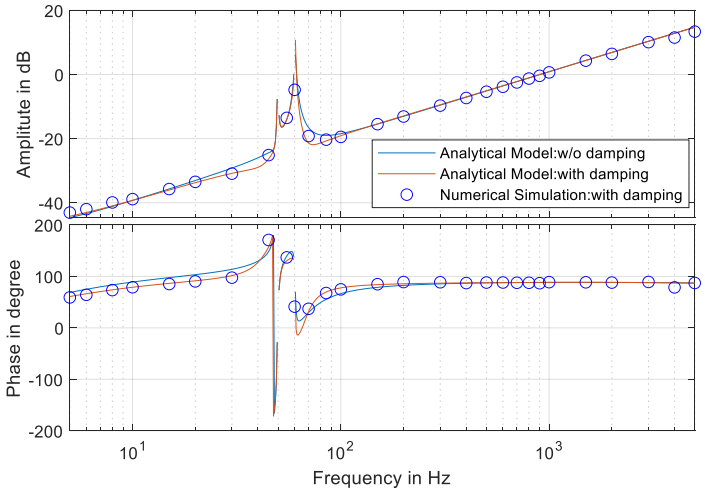

Figure 6.3 Impact of the damping control on the positive sequence impedance of the WT

As demonstrated in [10], the induction generator effect (IGE) of a DFIG-based WT tends to induce SSR issue as WT is switched from supersynchronous operation mode (with rotor speed ω_r greater than nominal angular speed ω_l) to subsynchronous operation mode (with ω_r smaller than ω_l). As shown in Figure 6.4, the phase angle of WT's output impedance in the positive sequence system is greatly changed by the variation of rotor speed at SSR frequencies, and when ω_r is equal to 0.8 pu (red dashed line), the phase angle is larger than 90° for a wide range of the SSR frequencies, which indicates negative resistance or damping for corresponding frequencies in WT's output impedance.

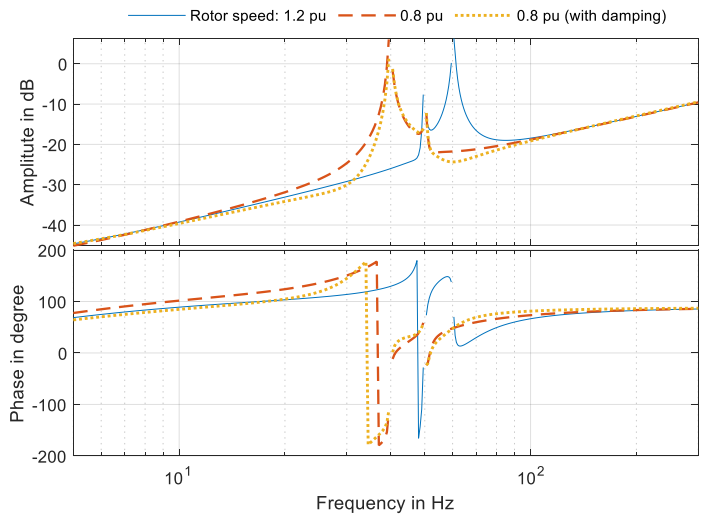

Figure 6.4 Impact of rotor speed and active damping on the output impedance of WT

Also, it can be observed from Figure 6.4, after adding the active damping, the phase angle of the WT output impedance in the scenario that ω_r is equal to 0.8 pu is almost changed to be the same as the phase angle in the scenario that ω_r is equal to 1.2 pu for the sub-synchronous frequency range, which tends to increase the stability of the system.

6.2 Damping Control in HVDC Converter

As introduced in [94], varying the bandwidth of the inner or outer control loops or PLL of a converter-interfaced component can change its output impedance response, thus providing some damping capability for a certain frequency range. However, the control-loop bandwidth is limited by the switching frequency of the converter, and in case it is required to decrease control bandwidth for reshaping converter output impedance, system performance will also be decreased. Alternatively, the active damping through adding an extended control path is preferred. In the literature, a variety of damping schemes has been proposed, either implemented in dq frame or directly in the stationary reference frame [18], [36]. In this work, the damping scheme from [18] is adopted, as shown in Figure 6.5.

The AC voltage regulated by the HVDC converter is connected to the extended control path as shown in Figure 6.5 (b), which is equivalent to a high-pass filter as represented by

$$\underline{H}_{ad}(\underline{s}) = K_{ad} \frac{\underline{s}}{\underline{s} + \omega_{ad}} \tag{6.2}$$

where K_{ad} and ω_{ad} are the gain and the cutoff frequency of the high-pass filter, respectively. The output of the extented control path is subtracted from the reference voltage obtained from PI controller of the AC voltage for modulation, so that all frequency components between $\omega_1 - \omega_{ad}$ and $\omega_1 + \omega_{ad}$ are filtered out by the added active damping. Through setting the cutoff frequency ω_{ad} of the equivalent high-pass filter, it can be assured that fundamental power flow will not be influenced. The gain K_{ad} can be tuned according to the available capacity of the HVDC converter.

After adding the active damping, the small-signal modulation ratio and the terminal current-voltage relationship of the simulated HVDC converter as given in (3.82) and (3.83) are changed to

$$\underbrace{\begin{bmatrix}\Delta\underline{m}_{\mathrm{d}}\\ \Delta\underline{m}_{\mathrm{q}}\end{bmatrix}}_{\Delta\underline{\boldsymbol{m}}_{\mathrm{dq}}}=-\underbrace{\begin{bmatrix}\underline{H}_{\mathrm{uac}} & 0\\ 0 & \underline{H}_{\mathrm{uac}}\end{bmatrix}}_{\underline{\boldsymbol{H}}_{\mathrm{vac}}(s)}\underbrace{\begin{bmatrix}\Delta\underline{u}_{\mathrm{d}}\\ \Delta\underline{u}_{\mathrm{q}}\end{bmatrix}}_{\Delta\underline{\boldsymbol{u}}_{\mathrm{dq}}}+\underbrace{\begin{bmatrix}0 & -K_{\mathrm{d}}\\ K_{\mathrm{d}} & 0\end{bmatrix}}_{\boldsymbol{K}_{\mathrm{pp}}}\begin{bmatrix}\Delta\underline{i}_{\mathrm{d}}\\ \Delta\underline{i}_{\mathrm{q}}\end{bmatrix}-\underbrace{\begin{bmatrix}\underline{H}_{\mathrm{ad}} & 0\\ 0 & \underline{H}_{\mathrm{ad}}\end{bmatrix}}_{\underline{\boldsymbol{H}}_{\mathrm{ad}}(s)}\begin{bmatrix}\Delta\underline{u}_{\mathrm{d}}\\ \Delta\underline{u}_{\mathrm{q}}\end{bmatrix} \tag{6.3}$$

$$\Delta\underline{\boldsymbol{u}}_{\mathrm{dq}}=\underbrace{\left(\boldsymbol{E}_2+\underline{H}_{\mathrm{d}}U_{\mathrm{dc0}}\underline{\boldsymbol{H}}_{\mathrm{uac}}+\underline{H}_{\mathrm{d}}U_{\mathrm{dc0}}\underline{\boldsymbol{H}}_{\mathrm{ad}}\right)^{-1}\left(\underline{H}_{\mathrm{d}}U_{\mathrm{dc0}}\boldsymbol{K}_{\mathrm{pp}}+\underline{\boldsymbol{Z}}_{\mathrm{RL}}\right)}_{\underline{\boldsymbol{Z}}_{\mathrm{vscad,dq}}}\Delta\underline{\boldsymbol{i}}_{\mathrm{dq}} \tag{6.4}$$

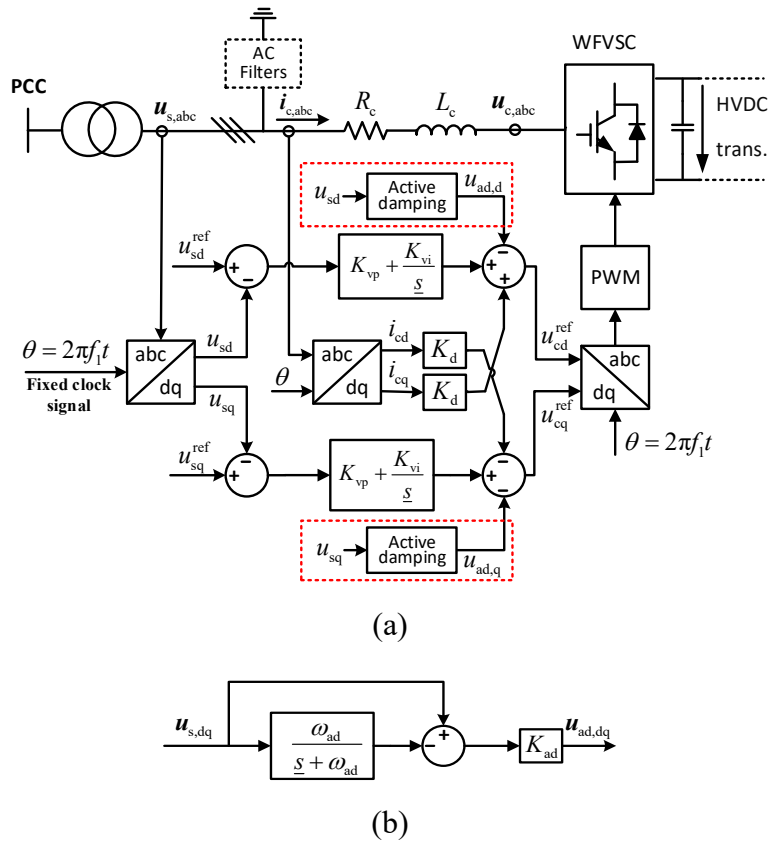

Figure 6.5 Diagram of an active damping scheme implemented in HVDC converter

Then applying the transformation from dq-frame to symmetrical components as described in section 3.3.3, the sequence impedance $\underline{\boldsymbol{Z}}_{\mathrm{vscad,pn}}$ of the simulated HVDC converter taking into account the damping control can be obtained. The effectiveness of the damping strategy will be validated both theoretically and through simulations in the case studies in Section 7.4 .

6.3 LC-filtered MV-level Active Damper

The active damping of HF resonances requires a converter with sufficient switching frequency. This is the biggest obstacle for DFIG-based WT or HVDC converter to provide the service of HF resonance damping. Thus, the idea of placing one or several extra active dampers in the MV collecting cable system will be explored. The design of such an active damper will be briefly elaborated.

In comparison to traditional R-APF [89], the required active damper in the HVDC-connected OWF is not intended to damp SSR or low-order harmonic resonances that can be mitigated by WT or HVDC converter, but to detect and damp HF resonances. Therefore, the active damper should have a high switching frequency, e.g. 5 kHz, and its power capacity should be kept low to reduce switching loss and asset investment. Based on these needs, an LC-filtered MV-level active damper is proposed here. Figure 6.6 shows the single-line diagram of the proposed active damper. Main parameters of the active damper are listed in Table 6.2.

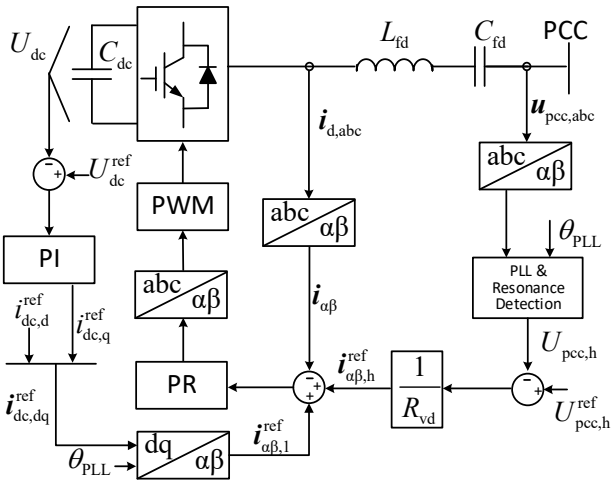

Figure 6.6 Control bock diagram of the active damper

Table 6.2 Main parameters of the proposed active damper

PCC voltage	33 kV
LC filter	L_{fd} =2.7 mL, C_{fd} = 10 μF
DC side capacitor	C_{dc} =4700 μF , U_{dc} = 10 kV
Switching frequency	10 kHz
DC voltage PI controller	K_{pv} =10, K_{iv} =0.01
PR controller	K_{pc} =5, K_{rc} =1
Emulated resistance	R_{vd} = 0.1 Ω

PCC voltage	33 kV
LC filter	L_{fd}=2.7 mL, C_{fd} = 10 μF
DC side capacitor	C_{dc}=4700 μF , U_{dc} = 10 kV
Reference distortion level	$U_{\mathrm{pcc,h}}^{\mathrm{ref}}$ =1%

The active damper consists of an LC filter, a VSC converter and a DC side capacitor. The capacitor C_{fd} of the LC filter undertakes a large part of the PCC voltage $\boldsymbol{u}_{\mathrm{pcc,abc}}$, so less voltage is imposed on the converter. DC voltage regulation of the active damper involves an outer loop PI controller and an inner loop PR controller. Their purpose is to keep a constant DC-link voltage U_{dc} across the DC side capacitor C_{dc}. Note that PCC voltage is aligned with the d-axis through Park transformation. Since $\boldsymbol{u}_{\mathrm{pcc,abc}}$ mainly drops on filter capacitor C_{fd}, and the capacitor's voltage is approximately in phase with the PCC voltage, the current flowing through LC filter is approximately orthogonal to the PCC voltage and the active current command is aligned along the orthogonal q-axis. That is the reason why the output of the DC voltage PI controller is set as the active current command $i_{\mathrm{dc,q}}^{\mathrm{ref}}$ along the q-axis to follow. Furtherly, the reactive current command $i_{\mathrm{dc,d}}^{\mathrm{ref}}$ of the converter is along the d-axis and is set to zero. Note that it does not follow the convention, that active current reference is in d-axis and reactive current reference is in q-axis. For more details on the control structure, refer to [93].

The PLL & Resonance Detection block in Figure 6.6 is realized by cascading multiple Pre-filtered Adaptive Notch Filter (P-ANF) based Frequency-Locked Loops (FLL), as shown in Figure 6.7. The first P-ANF-based FLL is used to extract the fundamental frequency component from the PCC voltage, and the followings are used to extract resonance components, i.e. the dominated harmonic components of the PCC voltage signal. The realization of each P-ANF-based FLL is given in Figure 6.8.

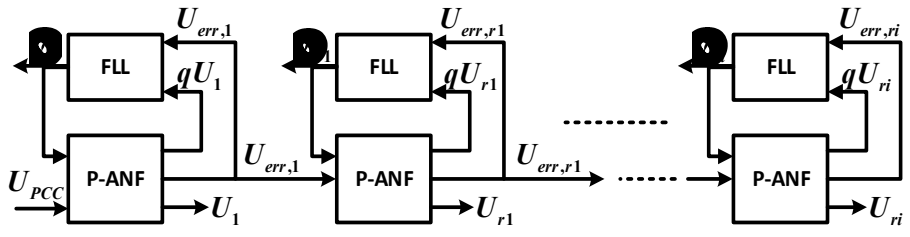

Figure 6.7 Cascaded structure with multiple P-ANF-based FLLs

To make the active damper emulate the effect of a resistor at the detected resonance frequency, the harmonic component of the PCC voltage for resonance frequency is firstly

subtracted from the specified reference distortion level $U_{\mathrm{pcc,h}}^{\mathrm{ref}}$, then is divided by a chosen virtual resistance R_{vd}, and afterwards fed to the quasi Proportional Resonant (PR) controller as a reference current command for tracking. The reference voltage distortion level $U_{\mathrm{pcc,h}}^{\mathrm{ref}}$ at the detected resonance frequency can be configured regarding the requirements on allowed harmonic distortion limits that is recommented in relevant standards [5], [6]. The virtual resistance R_{vd} should be tuned according to the available power rating of the active damper.

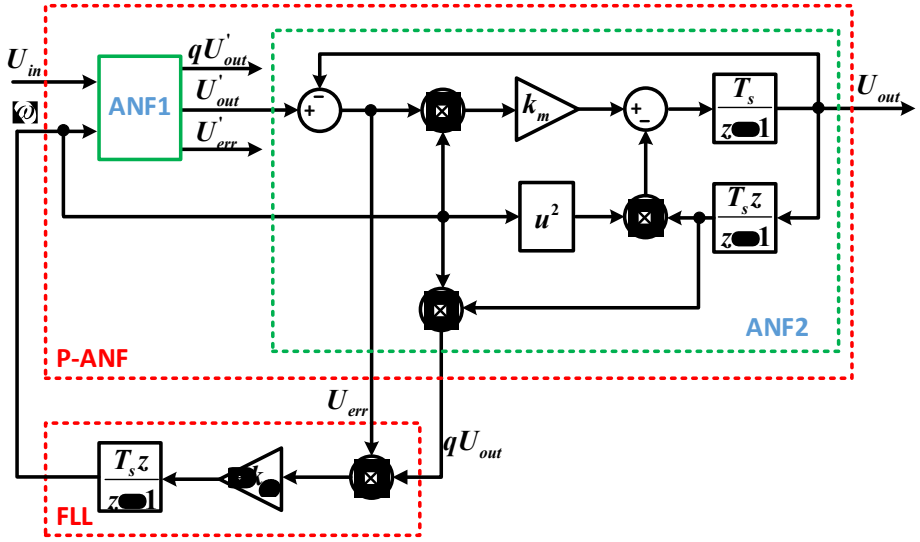

Figure 6.8 Block diagram of the P-ANF-based FLL

The effectiveness of the MV active damper described here will be validated through the case studies in Section 7.4 .

6.4 A Coordinated Resonance Damping Strategy

According to the resonance analysis presented in Chapter 6, resonances in DFIG-based OWF with HVDC connection can occur in any of the frequency bands as illustrated in Figure 6.9. This point will be furtherly validated by the case studies to be presented in Chapter 7. As a result, a wideband resonance damping strategy is needed considering the various operating conditions and grid topologies of the investigated system.

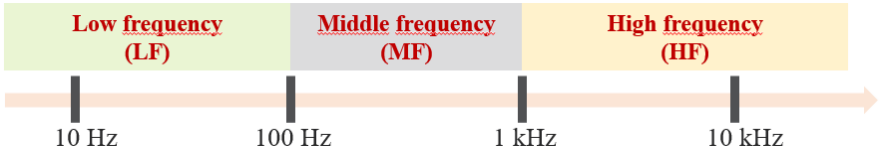

Figure 6.9 Definition of the frequency bands over a wide frequency range

LF and MF resonances could be damped by the active controls of WT or HVDC converters [14], [23]. Since the switching frequencies of high power rating WT and HVDC converters are usually not greater than 2 kHz, their capability of controlling HF resonances are limited, so extra active damper with higher switching frequency could be used to address the HF resonance issue [24]. The resonance detection capability of the active damper in [24] makes it suitable for handling the enormous variation of resonance frequency resulted from the change of operating condition or grid topology.

Considering that active control in DFIG converters for damping LF and MF resonances may involves the configuration of dozens of WTs, it is less attractive than the active control in HVDC converter. Therefore, the active damping from HVDC converter in coordination with active damper can be a feasible solution for mitigating the resonances ranging from several Hz to a few kHz. Figure 6.10 shows the diagram of the coordinated damping strategy that can be applied in HVDC connected DFIG-based OWF. The damping control from HVDC converter is in charge of the LF and MF resonance damping. The LC-filtered active dampers located in MV main buses adaptively damp the detected HF resonances to get the acceptable voltage distortions at PCC. The effectiveness of this coordinated damping scheme will be validated through the case studies in Section 7.4.

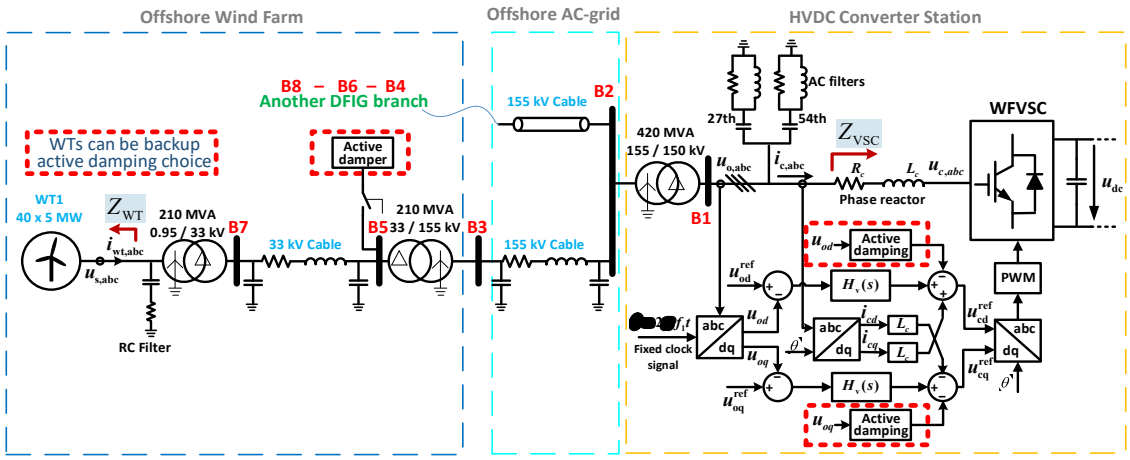

Figure 6.10 Schematic diagram of the coordinated damping strategy

Note that the damping control from a converter-interfaced grid component is always restricted to its available power capacity. Under some critical resonance conditions, the damping capability of a grid component can be used up, thus requires the complementary damping control from other converter-interfaced grid components. As for the active damping of LF and MF resonances, DFIG-based WTs can provide complementary damping control when HVDC converter control approaches saturation, which means WTs can be configured with damping control as backup damping solution. As for the damping of HF resonances, an alternative or a complementary solution would be installing extra passive dampers.

To furtherly improve system stability and prevent extra asset investment and operating power loss, there is still the necessity of investigation on other damping solutions based on existing grid components. The selection of the damping strategies will depend on the overall evaluation of the performance and the cost.

7 Case Studies

In this chapter, the RMA method is adopted to analyze the impacts of modelling deepness, wind farm operating condition and switching states of grid components on the resonances of HVDC connected DFIG-based OWF as given in Figure 5.2. Moreover, the effectiveness of the proposed damping stratedy in attenuating the identified resonances is analyzed and validated through simulations in MATLAB/Simulink. Partial results of this chapter were published in advance in [10].

7.1 Impact of Modelling Deepness on Resonances

About which modelling deepness is suited for power electronic-based grid components in grid integration studies, a lot of studies have been conducted [24], [28], [99], [100]. Several important influencing factors are the category of study (frequency stability, small-signal stability, or transient stablity), the studied frequency range (LF, MF or HF), or the size of the studied system (microgrid, a relatively isolated local grid, or a bulk power system). For the wideband resonance analysis of the HVDC connected OWF, the analytical modelling of the converter-interfaced grid components as derived in Sections 3.3 and 3.4 are suitable for identifying the potential resonances of the investigated system, thus the impact of their modelling deepness on resonance analysis will not be furtherly discussed in this work.

On the contrary, studies on how the modelling deepness of power transformers influence resonance analysis have not been sufficiently reported up to date. For the resonance analysis in Chapter 5, all the parasitic capacitance parameters of the transformers are set to zero. Here the impact of the parasitic capacitances in transformers, particularly for those in the 155 kV HV grid levels, will be investigated. The MV and HV transformers T1, T2 and T3 in Figure 5.2 are modelled accounting for the winding capacitances C_{M}, C_{Wp}, C_{Ws}, C_{Ep} and C_{Es} as 0 nF, 1 nF and 10 nF respectively. For all the LV transformers, the capacitance parameters C_{M}, C_{Wp}, C_{Ws}, C_{Ep} and C_{Es} are still set to zero. After updating the transformer models, new modal impedances of the positive sequence system can be obtained and the frequency scanning of the updated modal impedances is shown in Figure 7.1.

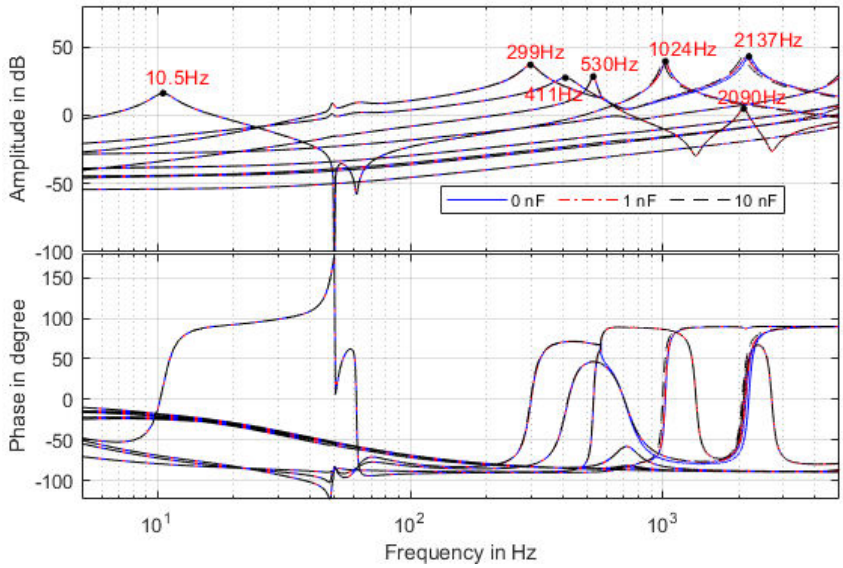

Figure 7.1 Modal impedances under the variation of transformer winding capacitances

It is observed that setting transformer winding capacitances in a continuously increased way, i.e. setting C_{M}, C_{Wp}, C_{Ws}, C_{Ep}, C_{Es} to 0 nF, 1 nF and 10 nF for the transformers T1, T2 and T3 respectively, does not change the modal impdances of the system much. Slight influences are observed in the impedance curves for the frequency range of above 1 kHz. The zoom-in display of the most influenced 1024 Hz and 2137 Hz modal impedances are shown in Figure 7.2. As seen, the 10 nF capacitance parameter setting has certain impact on these resonance modes, however, such high capacitance value is actually much larger than the real-world capacitance of the transformers under normal operations [71]. Since the 1 nF scenario is more likely to exist in the HV windings of real-world transformers and the impact of the 1 nF setting is hard to observe for the frequencies up to 5 kHz, it is reasonable to neglect the transformer capacitance effect in this thesis.

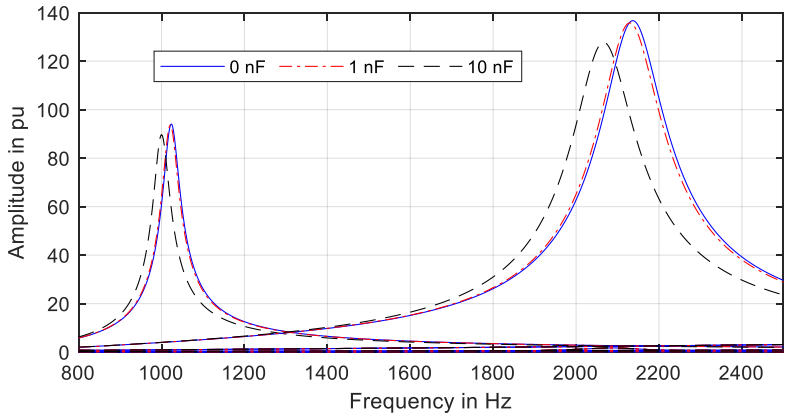

Figure 7.2 Zoomed-in display of Figure 7.1 for the frequency range between 800 and 2500 Hz

After neglecting the capcaticance effect of transformers, the necessity of modelling the excitation branch and the connection groups of primary and secondary windings will be furtherly investigated. As observed in Figure 7.3, modelling the transformers T1, T2 and T3 with their short-cirtuit impedances leads to the less damping of the resonance modes for 1024 Hz and 2137 Hz in comparison to the results using the extended T model as described in Section 3.2, which indicates that, including the excitation branch and winding connection group of a three-phase transformer in the impedance modelling has slight influence on its resistive characteristic, i.e. the damping capability, but there is no observable influence on the inductive characteristic as the resonance frequencies stay unchanged.

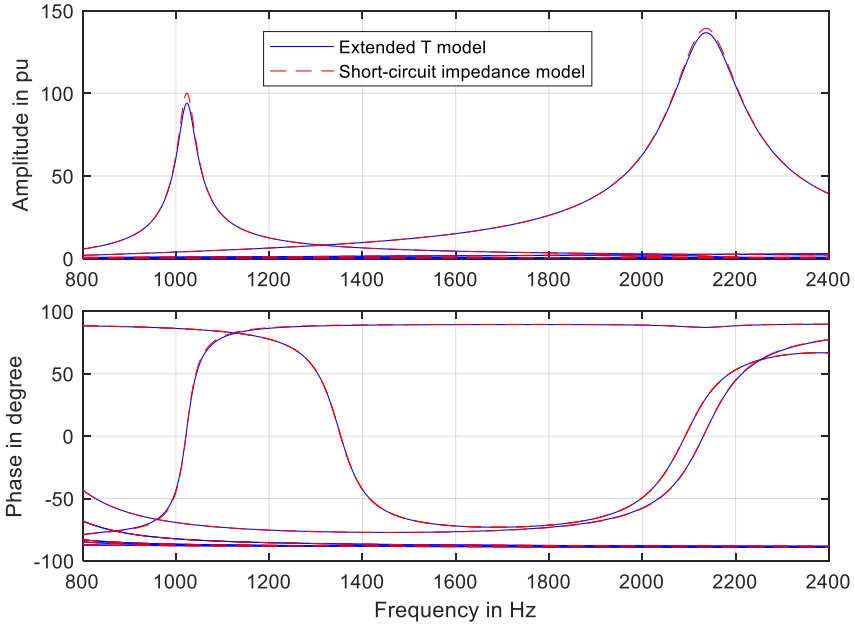

Figure 7.3 Modal impedances regarding different transformer models

To sum up, the modelling deepness of transformers has certain impact on the HF resonances of the investigated system. An extended transformer T model contributes to more accurate results of resonance analysis than directly using the short-circuit impedance model. Under nominal operating conditions, neglecting the capacitance effect can not only simplify analyses but also maintain sufficient accuracy. About the modelling deepness of other grid components and wind farm collector systems, there is always the contradiction between simplicity and accuracy, it is important to choose the right model for a specific study.

7.2 Impact of Generator Rotor Speed on Resonances

Under noncritical wind conditions, WT usually works under the maximum power point tracking (MPPT) mode. The variation of wind speed to a lower value may cause WT output power decreases, and as follows, rotor speed will be regulated down from its nominal value (1.2 pu). This behavior is included in the detailed DFIG model by following

$$\omega_{\mathrm{r}}^{\mathrm{ref}} = -0.67\,P^2 + 1.42\,P + 0.51 \tag{7.1}$$

where $\omega_{\mathrm{r}}^{\mathrm{ref}}$ denotes the reference value for the rotor speed controller to track, P is the acitve power generated by the WT [29]. The speed reference $\omega_{\mathrm{r}}^{\mathrm{ref}}$ slowly tracks changes in power P with a time constant of approximately 5 seconds.

In order to qualitatively evalutate the impact of rotor speed on the risk of resonances, it is reasonable to neglect the frequency-coupling effect of the OWF for simplification. Figure 7.4 shows the impact of rotor speed on the positive-sequence modal impedances of the system given in Figure 5.2. Here only the frequency range of the SSR mode is displayed as the variation of rotor speed has no observable impact on other resonance modes.

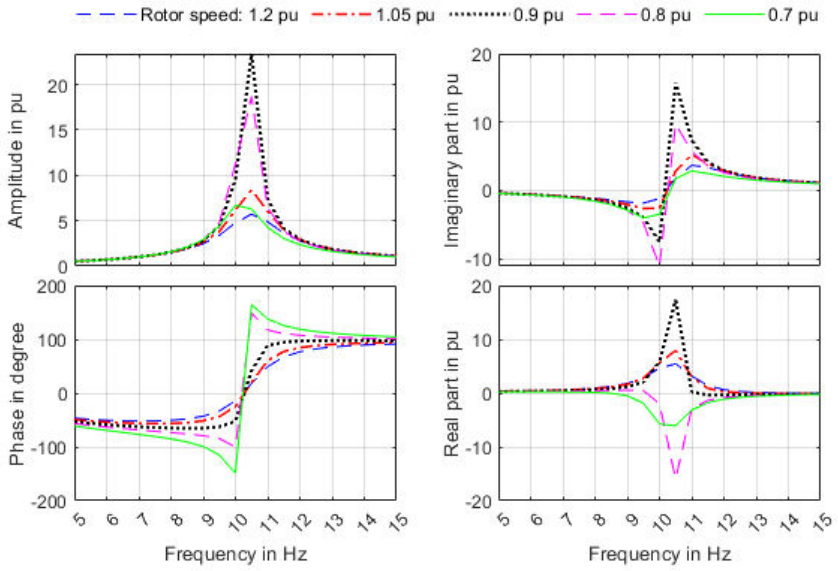

Figure 7.4 Impact of rotor speed ω_{r} on system modal impedances

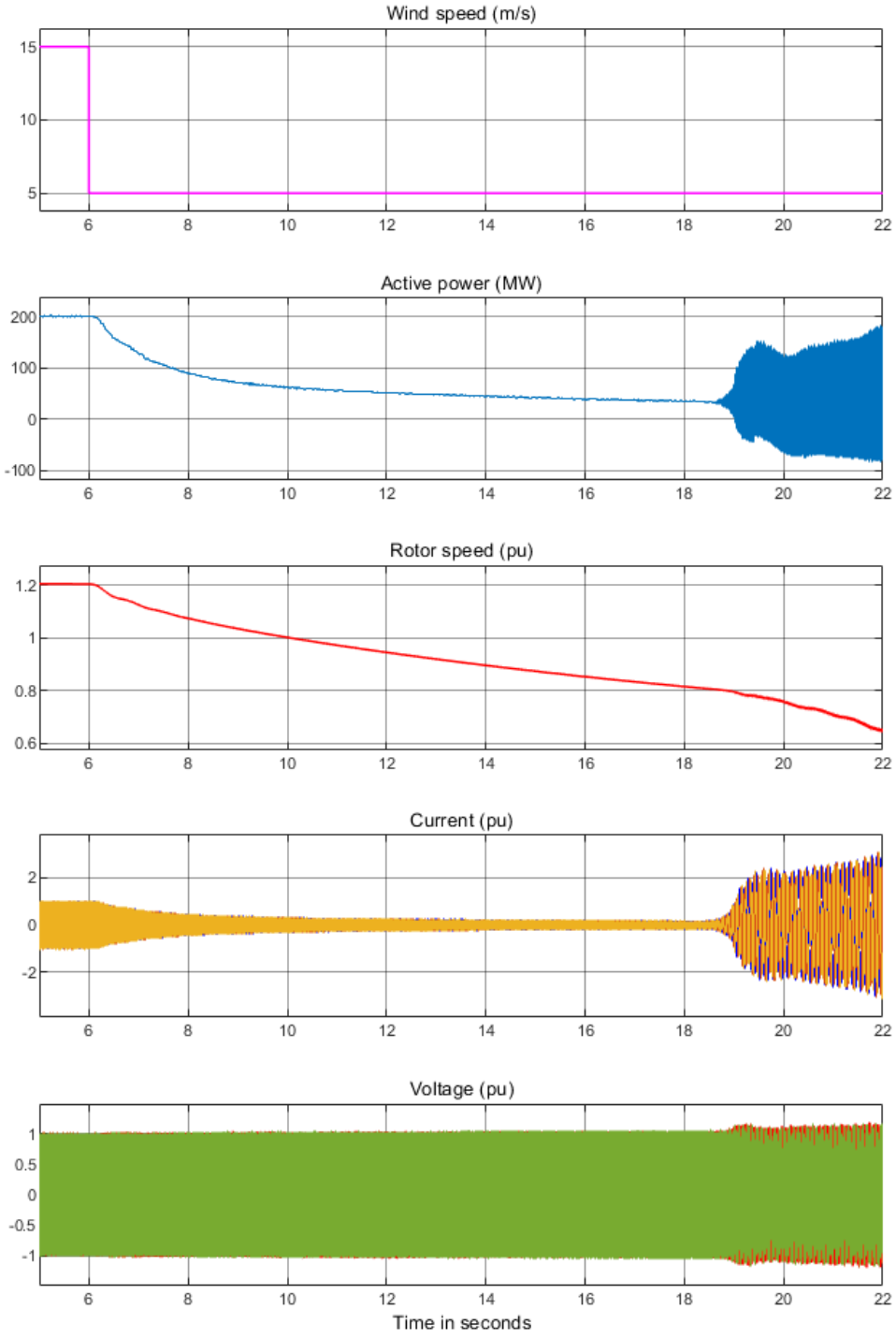

Figure 7.5 Simulation outputs of one MV collector system following wind speed variation

As observed from Figure 7.4, when the rotor speed continously decreases, the total resistance of the system changes from a positive value to a negative value for the SSR resonance mode. This is because of the extra negative resistance induced in the WTs, which endangers SSR stability. Specifically, the SSR instability occurs when the rotor

speed is regulated down to 0.8 pu or an even lower value. The phase variation larger than 180º around the SSR frequency also indicates the negative damping of the SSR resonance mode.

In order to validate this analytical result, simulation models are built up in MATLAB/Simulink, where the DFIG system is taken from the standard simulation model [29], only parameter changes and minor modification of the control structure are made. In time-domain simulation, wind speed is varied from 15 m/s to 5 m/s at t=6 s. The variation of wind speed, power output, rotor speed, voltage and current waveforms of a MV collector system are shown in Figure 7.5. Diverging power, voltage and current oscillations are observed when the rotor speed drops to be around 0.8 pu.

Furtherly, FFT analysis is conducted to the PCC voltage of the OWF and HVDC system, i.e. the voltage of the 155 kV AC bus B2. Figure 7.6 shows the FFT analysis results. A large SSR frequency component is observed at the starting stage of the diverging oscillation. Besides, a mirror frequency component around 90 Hz that is induced by the frequency coupling about the fundament frequency can be clearly observed in the frequency spectrum.

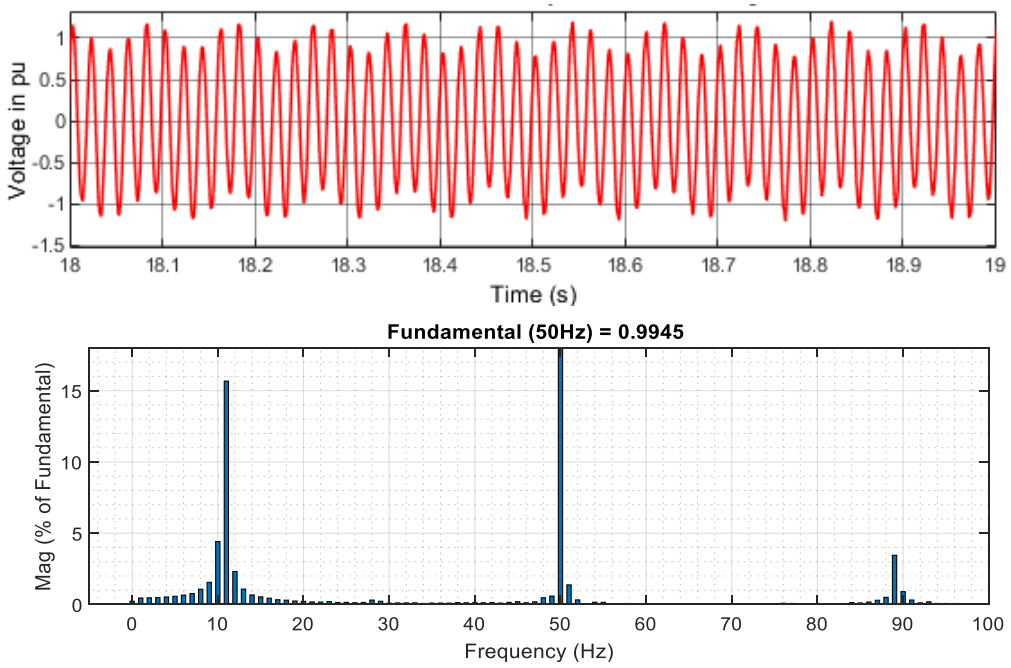

Figure 7.6 FFT analysis of the PCC voltage for the starting stage of the oscillation

In real operating conditions of a wind farm, apart from the variation of wind speed, its output power could also be changed when the wind farm receives a lowering power

generation command from its superior level control center, then as a consequence, the rotor speeds of DFIG-based WTs might be regulated down and risk SSR stability.

7.3 Impact of Grid Topology Change on Resonances

In real life wind farms, grid topology can be greatly changed during the startup, shutdown and normal operation process. In this section, the change of the switching states of HV breaker, MV collector breaker as well as the WT breaker will be considered, as illustrated in Figure 7.7. Their impact on resonances will be addressed separately.

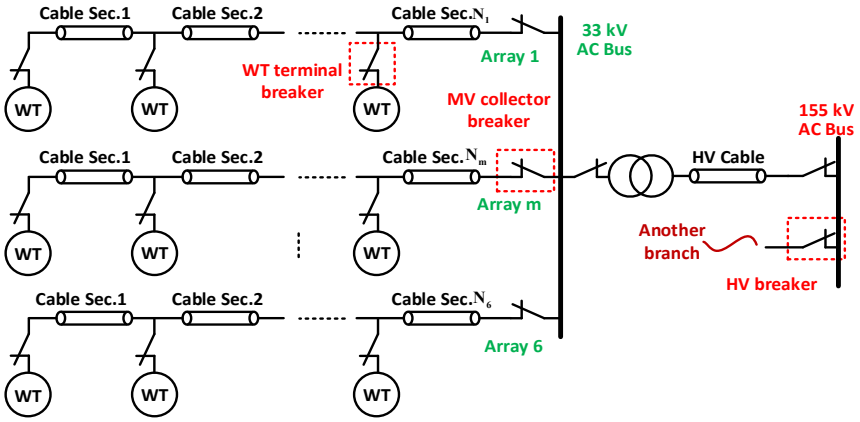

Figure 7.7 Different possibilities of grid topology change in OWF

7.3.1 Switching State of HV breaker

If a three-phase short-circuit fault occurs on one of the two HV feeders, the action of the protection device as well as the opening of the HV breaker will change the 8-bus system to a 5-bus system, as shown in **Figure 7.8**.

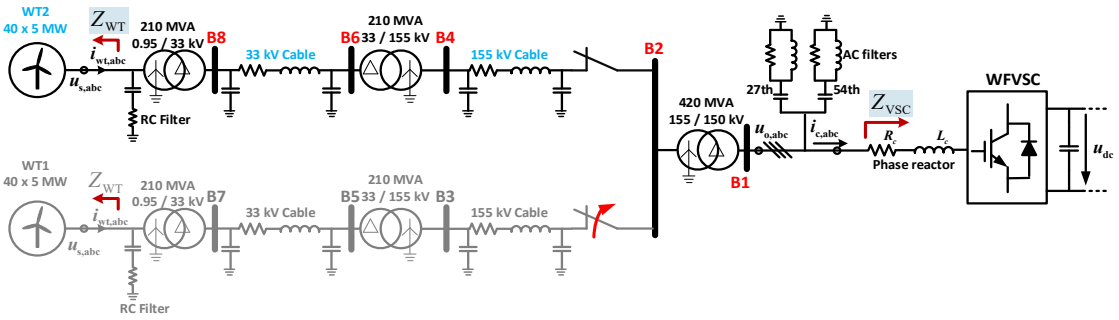

Figure 7.8 Diagram of the grid topology change due to the opening of a HV breaker

Figure 7.9 shows the resulting modal impedances of the system after the grid topology change. Solid lines represent the positive sequence impedances and dashed lines represent the negative sequence impedances. In compasion to the resonances before the grid topology change, as shown in Figure 5.15, the frequencies of the dominated resonance modes have been more or less shifted away, which ranges from a few Hertz to several hundred Hertz. The most influencing one is the change from 2137 Hz to 2756 Hz, which matches the 2750 Hz switching harmonic of the HVDC converter.

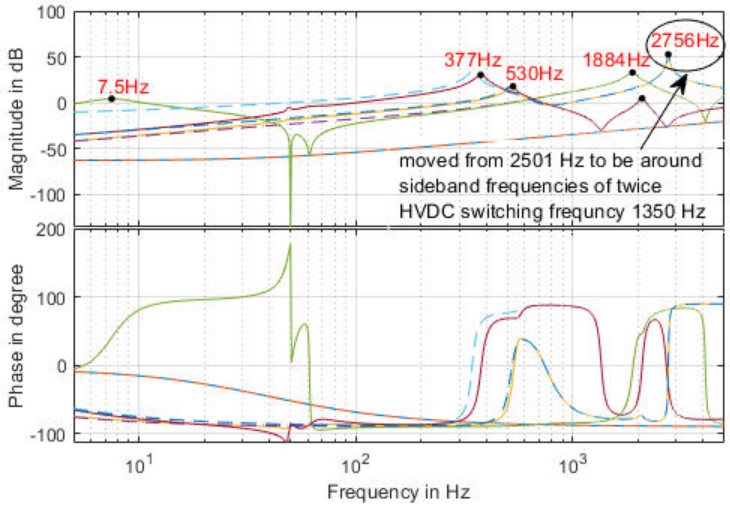

Figure 7.9 Modal impedances of the system after one HV branch is disconnected from grid.

The stimulation of this resonance frequency is verified by a time-domain simulation. As shown in Figure 7.10, after an HV feeder is disconnected at 8 s, large high-frequency ripples appear in the PCC voltage waveform, and the FFT analysis results as shown in Figure 7.11 confirm the high 2750 Hz harmonic distortion induced by the resonance.

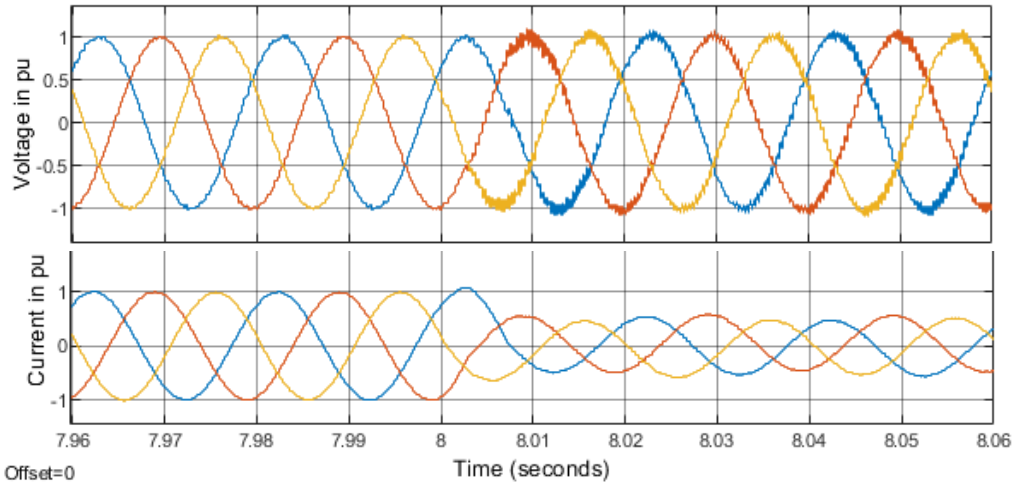

Figure 7.10 PCC voltage and current waveforms as one HV branch is disconnected from grid

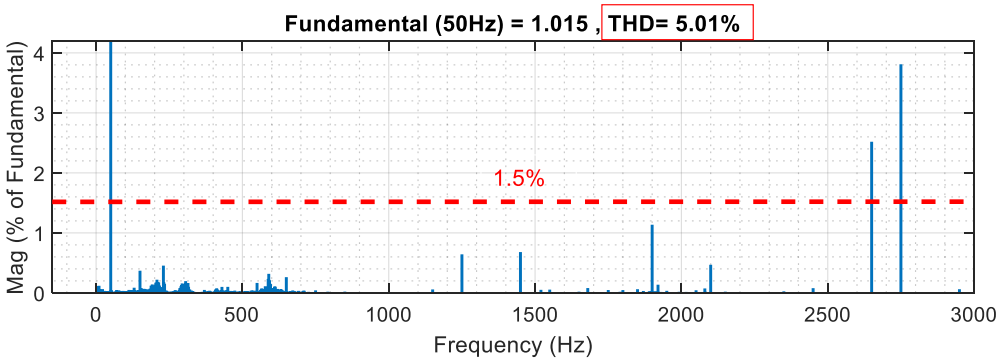

Figure 7.11 FFT analysis to the waveform of PCC voltage

According to the harmonic distortion limits as recommended in [5], the 2750 Hz harmonic distortion of the PCC voltage violates the 1.5% limit that is expressed in percentange of the fundamental component value, and the total harmonic distortion (THD) of the PCC voltage violates the 2.5% limit.

7.3.2 Switching State of MV Collector Breaker

The change of wind array switching state can happen when the OWF is started or stopped, or when a lower generation control order is received from its superior level control center. The impact on the resonances of the positive sequence system is shown in Figure 7.12. The following three scenarios regarding the switching states of wind array breakers in each MV collector system are considered: (1) all 6 wind arrays are connected to the grid; (2) 3 wind arrays are connected to the grid; (3) only 1 wind array is connected to the grid.

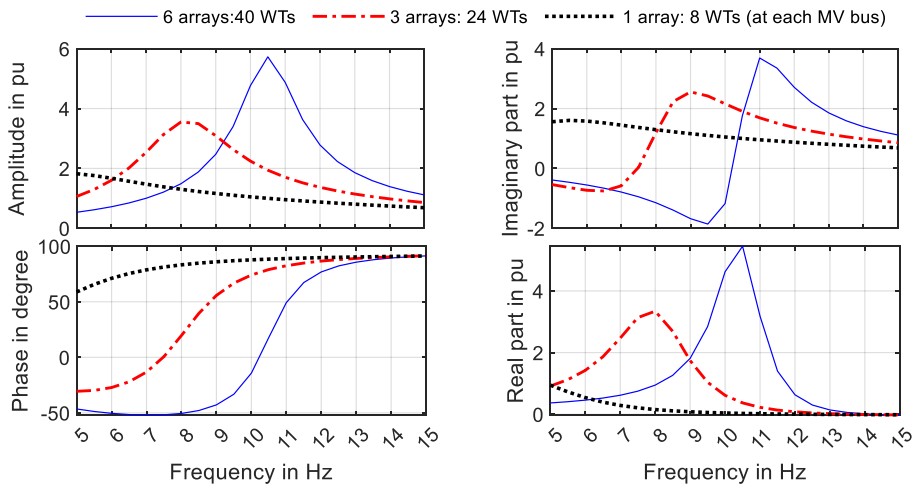

(a) At SSR frequencies

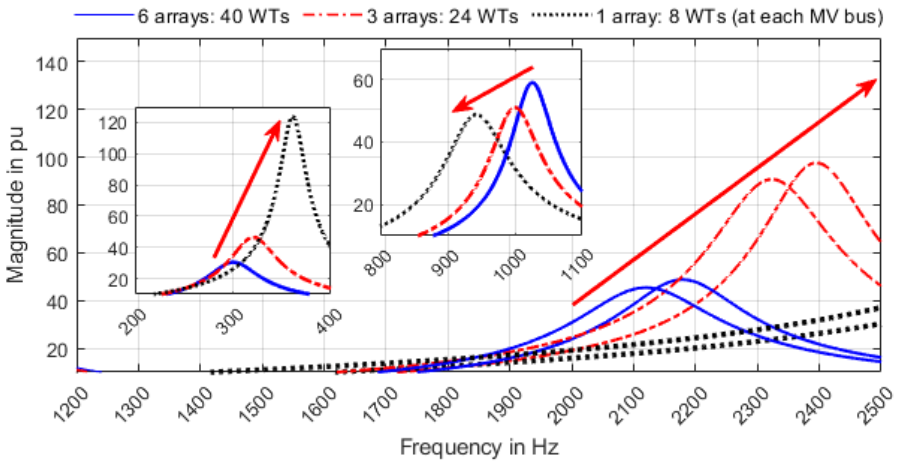

(b) At frequencies above 200 Hz

Figure 7.12 Modal impedances regarding the number of grid-connected wind arrays

As shown in Figure 7.12 (a), for different scenarios, the angle variations around the SSR frequency are all far less than 180°, which means the SSR stability is not at risk. Moreover, for all scenarios, the amplitudes of the modal impedances in the SSR frequency range are relatively small, which means the harmonic amplification effect of the SSR mode is not much influenced by the number of grid-connected wind arrays.

For the frequency range above 200 Hz, as negative damping has not been observed for the dominated resonance modes, only the amplitude plot of the modal impedances is shown in Figure 7.12 (b), which is sufficient for evaluating the harmonic amplification effects of the resonances. The arrows in Figure 7.12 (b) indicate the change of the resonances as less wind arrays are connected to the grid, as observed, the two resonance modes at above 2 kHz move from 2 kHz toward 3 kHz, the resonance mode at around 1 kHz moves from 1100 Hz toward 900 Hz, and the resonance mode at around 300 Hz moves from 300 Hz toward 400 Hz. The most dangerous resonance in these scenarios is the one around 350 Hz, which occurs as the number of grid-connected wind arrays is reduced to one.

Stimulation of the resonance at around 350 Hz is validated by time-domain simulation. The results are shown in Figure 7.13. As observed, after switching off 5 of the 6 wind arrays from each MV collector system at 4 s in the simulation, the waveform of the PCC voltage becomes slightly distorted, and the FFT analysis confirms the harmonic amplification effect of the around 350 Hz resonance mode. According to the harmonic distortion limits as recommended in [5], the 350 Hz harmonic component in the time window of 4.1 s and 4.2 s violates the 1.5% limit, and the THD of the PCC voltage in the same time window violates the 2.5% limit.

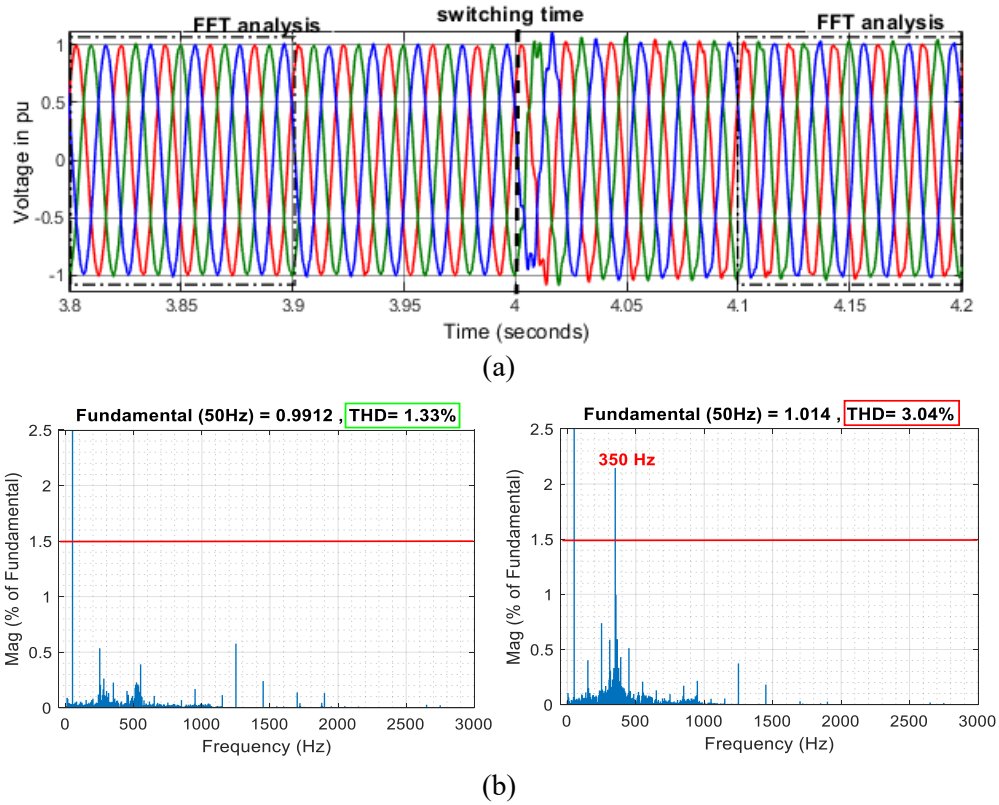

Figure 7.13 Simulation results regarding the variation of grid-connected wind arrays

7.3.3 Switching State of Wind Turbine Breaker

Wind turbines can be disconnected from grids due to maintenance, fault or wind curtailment reasons. By quite low or high wind speed conditions, all WTs can be cut off from grids. The disconnection of WT can be operated through opening the high or low voltage side breakers of their 950 V / 33 kV step-up transformers or the breakers in RSC and GSC branches, as illustrated in Figure 7.14.

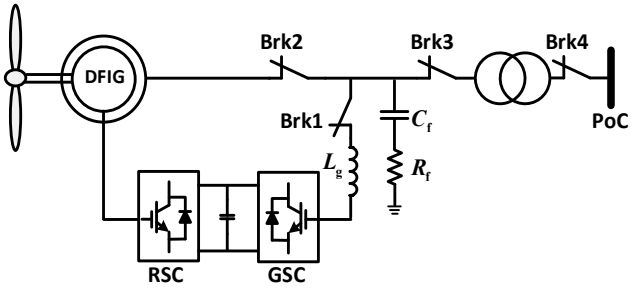

Figure 7.14 Single line circuit of DFIG-based WT with breakers included

Opening the transformer low-voltage side breaker has almost the same effect as opening transformer high-voltage side breaker, as the transformer shunt impedance of the excitation branch is far bigger than its series impedances in the primary and secondary windings, and there is almost no current flowing into a transformer once one side is in open circuit condition.

Note that the grid connection states of WTs do not change the grid connection states of collector cables. The impact of the number of grid-connected WTs on the dominating resonance modes of the positive sequece system is shown in Figure 7.15. Different scenarios regarding the switching states of transformer breakers or GSC and RSC branch breakers are presented in Figure 7.15 (a) and Figure 7.15 (b) separately. Since all the considered scenarios do not have much impact on the SSR resonance mode, this frequency range is not displayed.

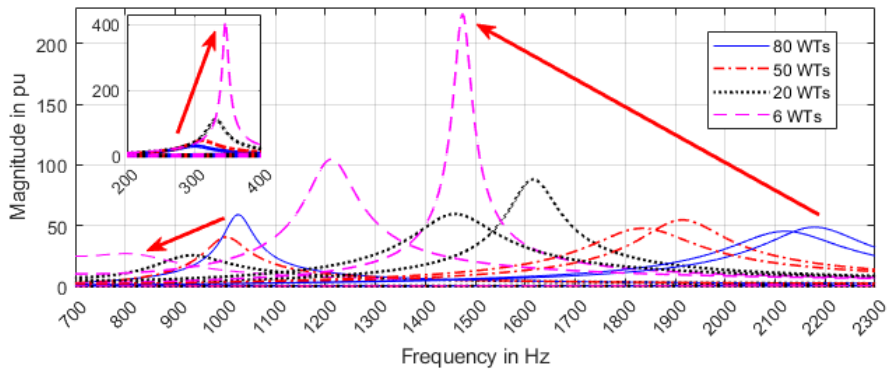

(a) opening transformer breaker

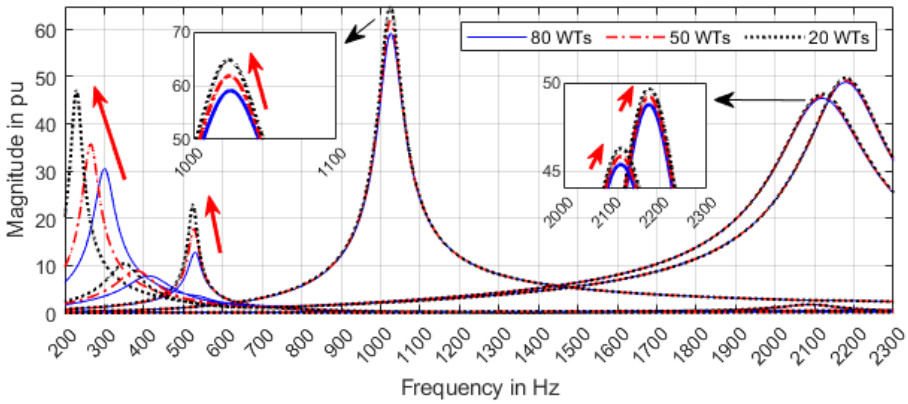

(b) opening GSC and RSC branch breakers

Figure 7.15 Modal impedances under the variation of in-service WTs.

As observed in Figure 7.15 (a), when WTs are disconnected from the grid by opening one side of the transformer breakers, a poor-damped resonance at around 350 Hz as indicated

by the sharp curve peak is introduced by the critical condition that there is only 6 grid-connected WTs. Moreover, as the number of grid-connected WTs decreases, two HF resonance modes move from above 2 kHz toward 1 kHz, and their resonance frequencies can match the switching sideband frequencies of WT converters or HVDC converter. In this specific case, when only 6 WTs are connected to the grid, a sharp resonance peak is observed between 1400 Hz and 1500 Hz, which matches the switching sideband frequency of the HVDC converter.

For the case that WTs are disconnected from the grid by opening GSC and RSC branch breakers, as shown in Figure 7.15 (b), the reduction of grid-connected WTs has negative impact on all the MF and HF resonance modes regarding the harmonic amplification effect, as indicated by the peak values of the modal impedances. However, only the resonance modes around 300 Hz and 500 Hz can induce slightly increased harmonic distortions. Specifically, when there is only 20 grid-connected WTs in the sytem, the typical 5^{th} and 11^{th} harmonics can be slightly magnified.

Stimulations of the 350 Hz and 1450 Hz resonances as identified in Figure 7.15 (a) are then validated through time-domain simulation. As shown in Figure 7.16, after disconnecting 74 of the 80 WTs from the grid through opening transformer high-voltage side breakers at 4 s, large harmonic distortions are observed in the PCC voltage waveform, and the FFT analysis for the time window between 4.05 s and 4.15 s shows, both the 350 Hz and 1450 Hz harmonic components of the PCC voltage violate the 1.5% distortion limit as recommended in [5].

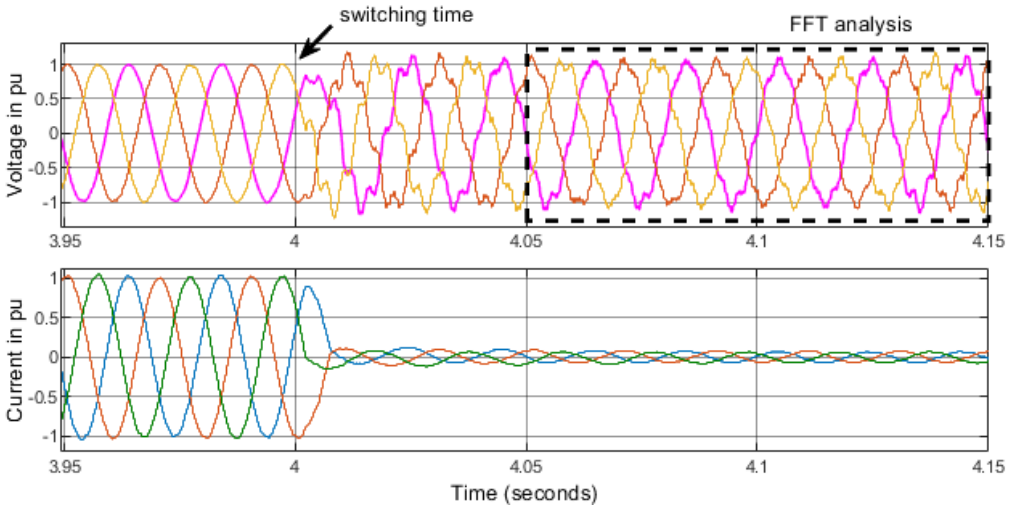

(a)

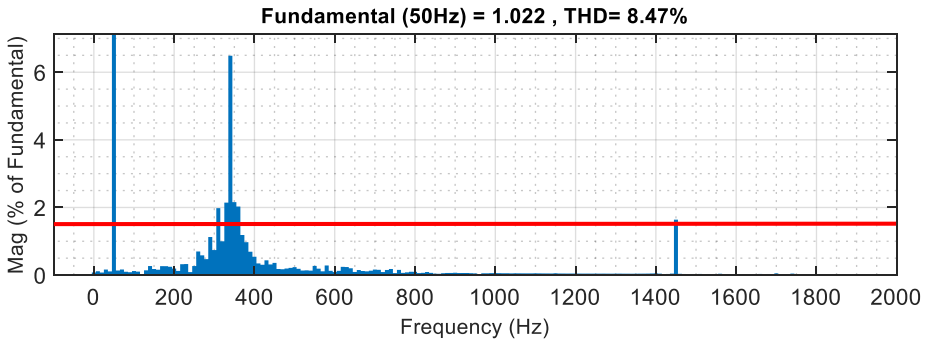

(b)

Figure 7.16 Simulation results regarding the variation of grid-connected WTs

7.4 Damping Effectiveness

To show the effectiveness of the active damping control implemented in DFIG-based WT (see Section 6.1), the SSR issue identified in Section 7.2 is chosen for the validation here. As observed in Figure 7.17, when the rotor speed of WT ω_r is switched from 1.2 pu to 0.8 pu, the overall damping of the SSR mode in the system becomes negative, which can be indicated by the phase variation of 180° at the resonance peak in the amplitude plot. After adding the active damping control in WT, system stablity can be recovered again through the increased damping.

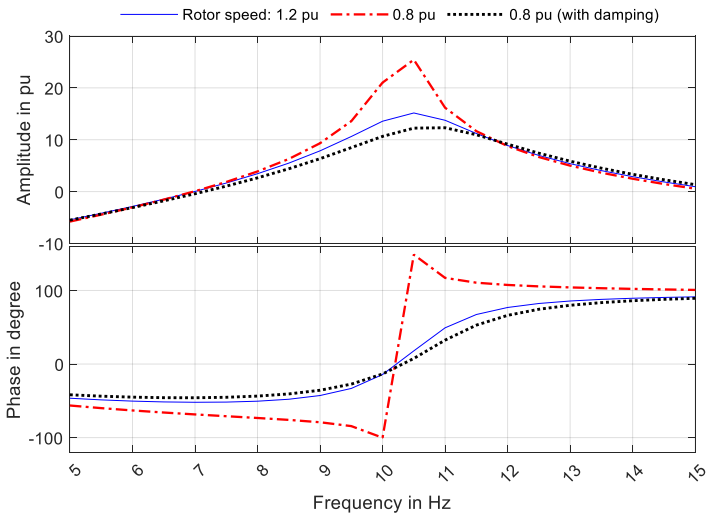

Figure 7.17 Impact of rotor speed and active damping on the SSR resonance mode

Furtherly, the above theoretical analysis is validated by simulations in Simulink, as shown in Figure 7.18. After varying the wind speed from 15 m/s to 5 m/s at 6 s, the rotor speed

of the aggregated WT continuously decreases, and a diverging current oscillation is observed when the rotor speed drops to be around 0.8 pu. Through activating the active damping at the instant of 20 s, the strong current oscillation has been attenuated in about several hundred milliseconds, which validates the functionality of the damping control of the DFIG-based WT.

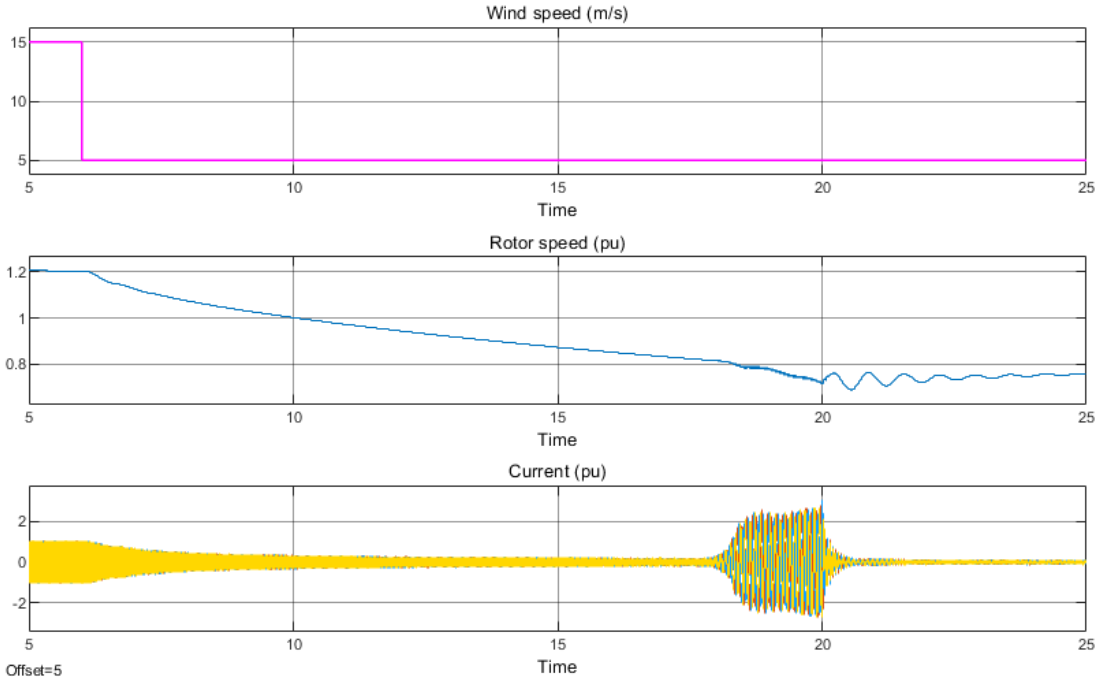

Figure 7.18 Simulation validation on the effectiveness of the active damping in WT

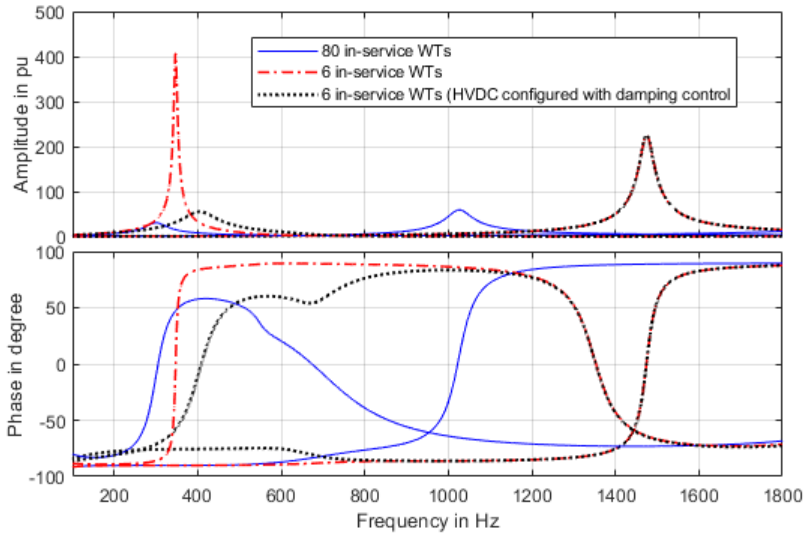

Figure 7.19 Impact of the active damping in HVDC converter on modal impedances

About the effectiveness of the active damping in HVDC converter as described in Section 6.2, the resonance case as given in Section 7.3.3 is selected for validation. After performing RMA analysis to the test system with and without HVDC damping control, the critical modal impedances influenced by the active damping are obtained, as shown in Figure 7.19, it is observed after tripping 74 out of 80 WTs from the test grid, a very sharp resonance peak is appearing at around 350 Hz, and the resonance peak is effectively attenuated due to the added active damping. Simulation results in Figure 7.20 validate the theoretical analysis in Figure 7.19. In Figure 7.20 (a), the tripping of WTs occurs at 4 s and the damping control in HVDC converter is activated at 4.2 s. Figure 7.20 (b) and (c) shows the FFT analysis to the waveform of the PCC voltage.

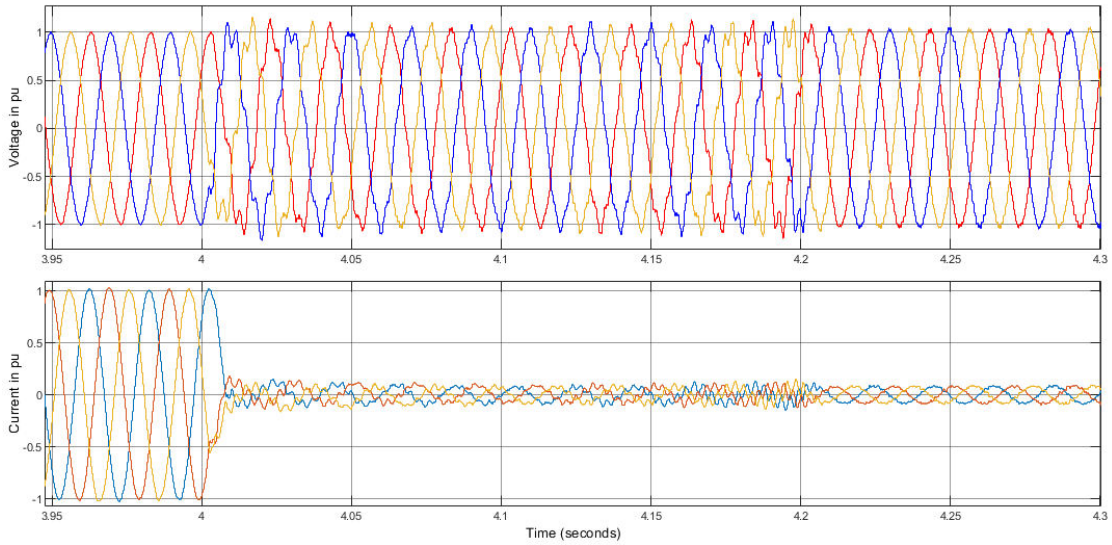

(a) Waveforms of the PCC voltage and current

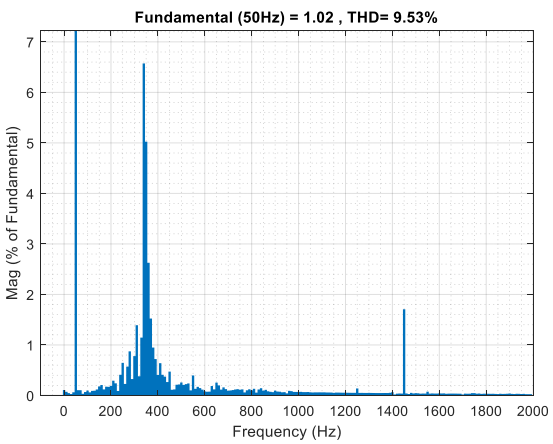

(b) FFT for the time window of 4.1 - 4.2 s

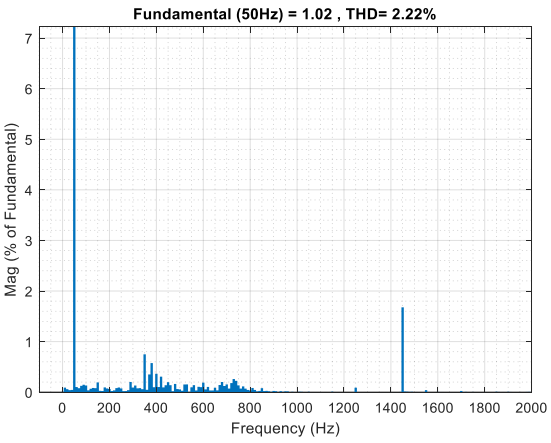

(c) FFT for the time window of 4.2 - 4.3 s

Figure 7.20 Simulation results regarding the tripping of WTs and activation of damping contol.

From Figure 7.19, it can also be observed, that there is a HF resonance peak at around 1450 Hz and the added damping control in HVDC converter has not clearly changed the impedance curve around that resonance mode, therefore, the added damping control in the HVDC converter has a negligible attenuation effect on the 1450 Hz resonance. This is also reflected in the simulation result in Figure 7.20, the larger than 1.5% voltage distortion at 1450 Hz still exists after the activation of the damping control in HVDC converter. The damping of such HF resonance will be discussed furtherly.

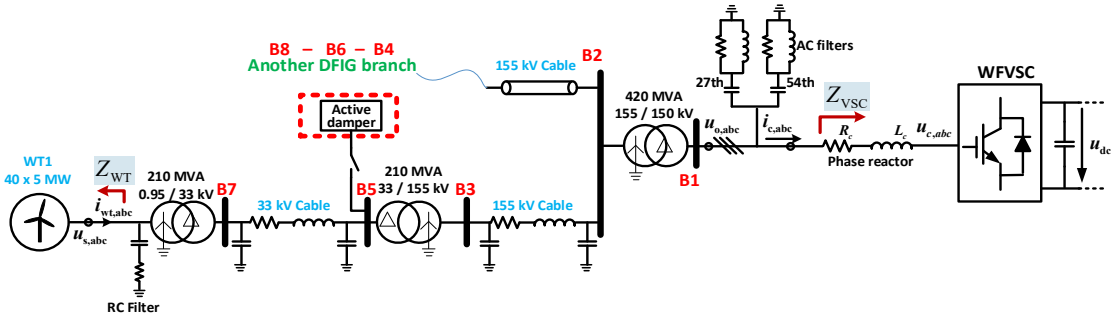

Figure 7.21 Placement of active dampers in the investigated grid

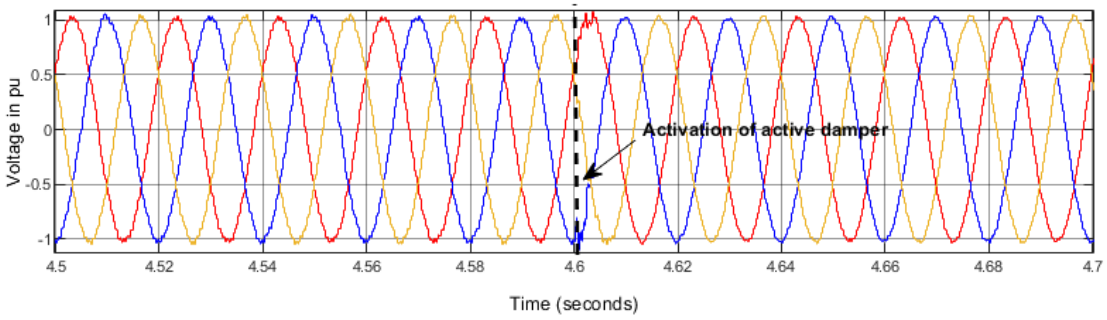

(a) Waveform of the PCC voltage

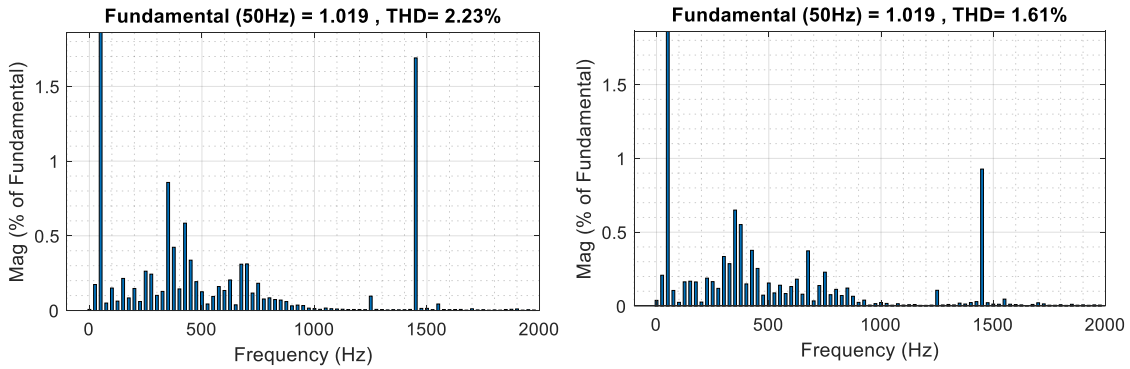

(b) FFT for the time window of 4.5 - 4.6 s (c) FFT for the time window of 4.6 - 4.7 s

Figure 7.22 Simulation results regarding the damping effect of active dampers

Placing extra active dampers in the investigated system as shown in Figure 7.21 and setting the threshold distortion for activating the active dampers to 1 % of the fundamental voltage, the remaining 1450 Hz harmonic component in Figure 7.20 (b) should be detected and trigger the operation of the active dampers. The effectiveness of the resonance damping is presented in Figure 7.22, as observed, the 1.7% level of 1450 Hz harmonic voltage in Figure 7.22 (b) is reduced to the level of 1 % in Figure 7.22 (c). Actually, in this case study, the damping effect of the active dampers has not been fully presented as the HF harmonic distortion to be mitigated is relatively small. Another case study on the damping effect of the LC-filtered MV-level active damper can be fournd in [46].

Note that the parallel operation of mulitiple LC-filtered MV active dampers can contribute to greater damping capability, and the harmonic sharing can be achieved through droop control [101]. The parallel operation of multiple MV active dampers can be adopted when larger damping capacity is required. Besides, replacing the two-level VSC converter with Modular Multiplelevel Converter (MMC) in the active damper can help reduce the required switching frequency, thus reduce switching power loss and increase its efficiency. Moreover, to accurately mitigate the harmonic distortions at resonance frequencies, the digital control delay introduced by sampling, control computation and PWM switching should also be carefully considered [102].

As a conclusion to the damping of wideband resonances, the coordination of the LC-filtered active dampers, the HVDC active damping as well as the WT damping control can limit the harmonic distortions of a wind-integrated power system with HVDC grid connection to a certain level and improve system stability.

8 Conclusions and Future Work

8.1 Conclusions

As the penetration level of offshore wind power continuously increases and the VSC-HVDC technology has been widely applied in offshore wind power integration, massive harmonics are injected into offshore grids and the control interactions among multiple converter-interfaced grid components bring wide-band resonance issues into grids. A critical one is the SSR instability that may occur in HVDC connected OWF employing DFIG-based WTs. To keep low harmonic distortion and stable operation of DFIG-based OWF with HVDC connection, a comprehensive resonance study on the clarification of their mechanisms, the assessment of their risks and the development of damping strategies has been conducted.

The dissertation started with an overview of the real-world resonance incidents, which were categorized into 3 classes: (1) incidents in wind-integrated AC grid; (2) incidents in wind-integrated HVDC grid; (3) incidents in HVDC connected AC grid. Then the new features as well as the analysis methods of the resonances in converter-dominated power systems were presented.

As follows, the analytical impedance modelling of power system components, including both passive grid components (cables and transformers) and converter-interfaced components (WT and HVDC converter), was conducted. Suitable sequence impedance models were built for the resonance analysis covering the frequency range from several Hz to a few kHz. Specifically, the frequency coupling effect corresponding to the fundamental frequency was included in the impedance modelling of DFIG-based WT, and the transformer capacitance effect was included in its impedance modelling.

Following grid component modelling, the aggregated modelling of wind farm MV collector systems was investigated regarding the accuracies of different aggregating approaches. Through stepwise simulation verifications, the equivalent power loss based aggregation model of a large-scale DFIG-based OWF was validated to be feasible for wide frequency range of resonance analysis.

The resonances in the DFIG-based OWF with HVDC connection were firstly investigated using the PCC nodal impedances of the equivalent SISO sequence systems. Including the frequency coupling of fundamental frequency in the resonance analysis was found crucial by the assessment of SSR stability when a SSR resonance mode is approaching critically-

damped stable state. When a SSR resonance mode maintains sufficient damping regarding possible operating conditions and grid configurations, the frequency coupling effect can be neglected for simplicity. As for the frequency coupling corresponding to PWM switching frequency, the induced sideband resonances were proved to be crucial for the risk assessment of the resonances ranging from hundreds of Hz to Nyquist frequency.

The nodal-admittace matrix based RMA approach was then adopted to address the resonance issues related to power quality (mainly refer to large harmonic distortions) and harmonic stability. The locations where resonances can be most easily excited were identified through bus participation factor analysis. The impact of modelling deepness, the variation of wind farm operating condition as well as the grid topology change on the resonance frequency, harmonic amplification level and the occurrence of negative damping were analyzed.

Considering the identified wide frequency range of resonances, the following active damping methods have been studied: (1) active damping in DFIG-based WT and HVDC converter designed for the LF and MF resonance damping; (2) the LC-filtered MV-level active damper designed for HF resonance damping. The coordination of HVDC converter damping control and active damper with high-switching frequency was suggested to be used in mitigating the wide-band resonances. In case of insufficient damping capability, active damping from DFIG-WTs can also be considered as a backup damping option.

All the theoretical analysis in this dissertation, including analytical impedance modelling, resonance analysis as well as the active damping strategies, are validated through simulations in MATLAB/Simulink.

8.2 Future Work

In this work, the analytical impedance models of converter-interfaced grid components are derived based on small-signal harmonic linearization, which will become invalid by the occurrence of large-signal perturbations. For example, by the growing of SSR, harmonic voltage distortion may reach up to tens of percentage of the fundamental component value, and the SSR frequency will undergo continuous variation, under this condition, the large-signal based impedance modelling and resonance analysis can capture the resonance frequency more accurately and quantatively determine harmonic

distortion level, which can be considered as a further research topic, especially for transient studies.

Moreover, the interconnection of multiple OWFs and HVDC links in today's offshore grids are making their control and operation more complicated, which in combination with the dynamics of onshore grids will introduce new power quality and stability issues, thus requires ongoing comprehensive resonance studies on today's power eletronics based power systesms. Besides, more efforts on the small-signal and large-signal resonance analysis regarding grid-forming control are expected.

About resonance damping, with the development of wide band-gap semiconductors, and the help of MMC structure, medium and high voltage active dampers will gain much attraction in the future. However, installing active dampers will result into extra asset investments and operating power losses, it is expected the damping of all wide-band resonances can be achieved through using existing converter-interfaced grid components. For example, implementing flexible modulating strategies in WT converters to let standby WTs work as active dampers that are configured with higher switching frequency than normal operation mode, the feasibility of which can be explored as a further research topic.

9 List of references

[1] WindEurope, “Offshore Wind in Europe - Key treads and statistics 2019,” published in February 2020, available at: https://windeurope.org/about-wind/statistics/offshore/european-offshore-wind-industry-key-trends-statistics-2019/.

[2] X. Liu, “Control of voltage source converter based high voltage direct current transmission systems for grid code compliance,” Ph.D. dissertation, University of Magdeburg, Magdeburg, 2016.

[3] SGRI Participates in Construction of Zhang-Bei DC Grid Pilot Project. Available at: http://www.cepri.com.cn/release/details_66_745.html.

[4] J. Shair, X. Xie, L. Wang, W. Liu, J. He, H. Liu, “Overview of emerging subsynchronous oscillations in practical wind power systems,” *Renewable and Sustainable Energy Reviews*, Elsevier, vol. 99(C), pages 159-168, 2019.

[5] IEEE Recommended Practice and Requirements for Harmonic Control in Electric Power Systems, in *IEEE Std 519-2014 (Revision of IEEE Std 519-1992)* , vol., no., pp.1-29, 11 June 2014.

[6] IEC/TR 61000-3-6 2008, Electromagnetic compatibility (EMC) - Part 3: Limits - Section 6: Assessment of emission limits for distorting loads in MV and HV power systems.

[7] C. Buchhagen, C. Rauscher, A. Menze, and J. Jung, “BorWin1 – first experiences with harmonic interactions in converter dominated grids,” in *Proceedings of International ETG Congress 2015*, 2015, pp. 1–7.

[8] C. Buchhagen, M. Greve, A. Menze, and J. Jung, “Harmonic stability - practical experience of a TSO,” in *Proceedings of the 15th Wind Integration Workshop*, 2016, pp. 1–6.

[9] M. Brendel and G. Traufetter, “Knall auf hoher See,” *Der Spiegel*, no. 35, pp. 71–72, Aug. 2014.

[10] Y. Zhang, C. Klabunde and M. Wolter, “Study of Resonance Issues between DFIG-based OWF and HVDC Transmission,” *Electr. Power Sys. Res*., vol. 190, Jan. 2021, Art. no. 106767, accepted for publication.

[11] X. Xie, X. Zhang, H. Liu, H. Liu, Y. Li and C. Zhang, “Characteristic Analysis of Subsynchronous Resonance in Practical Wind Farms Connected to Series-Compensated Transmissions,” in *IEEE Transactions on Energy Conversion*, vol. 32, no. 3, pp. 1117-1126, Sept. 2017.

[12] Y. Zhang, C. Klabunde and M. Wolter, "Harmonic Resonance Analysis for DFIG-based Offshore Wind Farm with VSC-HVDC Connection," *2019 IEEE Milan PowerTech*, Milan, Italy, 2019, pp. 1-6.

[13] M. Quester, V. Yellisetti, F. Loku and R. Puffer, "Assessing the Impact of Offshore Wind Farm Grid Configuration on Harmonic Stability," *2019 IEEE Milan PowerTech*, Milan, Italy, 2019, pp. 1-6.

[14] H. Jiang, J. You, H. Liu, W. Ning and L. Wu, "Impedance characteristics of DFIGs considering the impacts of DFIG numbers and locations and its application on SSR analysis," *2017 IEEE Power & Energy Society General Meeting*, Chicago, IL, 2017, pp. 1-8.

[15] Z. Miao, "Impedance-Model-Based SSR Analysis for Type 3 Wind Generator and Series-Compensated Network," *IEEE Trans. Energy Convers.*, vol. 27, no. 4, pp. 984–991, Dec. 2012.

[16] Y. Song, X. Wang and F. Blaabjerg, "Impedance-Based High-Frequency Resonance Analysis of DFIG System in Weak Grids," in *IEEE Transactions on Power Electronics*, vol. 32, no. 5, pp. 3536-3548, May 2017.

[17] Y. Song, E. Ebrahimzadeh and F. Blaabjerg, "Analysis of High-Frequency Resonance in DFIG-Based Offshore Wind Farm via Long Transmission Cable," in *IEEE Transactions on Energy Conversion*, vol. 33, no. 3, pp. 1036-1046, Sept. 2018.

[18] M. Amin, and M. Molinas, "Understanding the Origin of Oscillatory Phenomena Observed Between Wind Farms and HVdc Systems," *IEEE Journal of Emerging and Selected Topics in Power Electronics*, vol. 5, no. 1, pp.378–392, Mar. 2017.

[19] J. Lyu, X. Zhang, X. Cai and M. Molinas, "Harmonic State-Space Based Small-Signal Impedance Modeling of a Modular Multilevel Converter With Consideration of Internal Harmonic Dynamics," in *IEEE Transactions on Power Electronics*, vol. 34, no. 3, pp. 2134-2148, March 2019, doi: 10.1109/TPEL.2018.2842682.

[20] H. Zong, J. Lyu, C. Zhang, X. Cai, M. Molinas and F. Rao, "MIMO impedance based stability analysis of DFIG-based wind farm with MMC-HVDC in modifed sequence domain," *8th Renewable Power Generation Conference (RPG 2019)*, Shanghai, China, 2019, pp. 1-7, doi: 10.1049/cp.2019.0652.

[21] H. Zong, C. Zhang, J. Lyu, X. Cai, M. Molinas and F. Rao, "Generalized MIMO Sequence Impedance Modeling and Stability Analysis of MMC-HVDC With Wind Farm Considering Frequency Couplings," in *IEEE Access*, vol. 8, pp. 55602-55618, 2020, doi: 10.1109/ACCESS.2020.2981177.

[22] I. Vieto and J. Sun, "Sequence Impedance Modeling and Analysis of Type-III Wind Turbines," in *IEEE Transactions on Energy Conversion*, vol. 33, no. 2, pp. 537-545, June 2018

[23] Y. Xu, H. Nian, T. Wang, L. Chen and T. Zheng, "Frequency Coupling Characteristic Modeling and Stability Analysis of Doubly Fed Induction Generator," in *IEEE Transactions on Energy Conversion*, vol. 33, no. 3, pp. 1475-1486, Sept. 2018.

[24] H. Nian, Y. Xu, L. Chen and M. Zhu, "Modeling and Analysis of DC-Link Dynamics in DFIG System With an Indicator Function," in *IEEE Access*, vol. 7, pp. 125401-125412, 2019.

[25] C. Zhang, X. Cai, M. Molinas and A. Rygg, "Frequency-domain modelling and stability analysis of a DFIG-based wind energy conversion system under non-compensated AC grids: impedance modelling effects and consequences on stability," in *IET Power Electronics*, vol. 12, no. 4, pp. 907-914, 10 4 2019.

[26] X. Chen, Z. Liu, "Impedance Modeling and Stability Analysis of the Converters in a Double-Fed Induction Generator (DFIG)-Based System," *Energies*, MDPI, Open Access Journal, vol. 12(13), pages 1-23, June 2019.

[27] K. Sun, W. Yao, J. Fang, X. Ai, J. Wen and S. Cheng, "Impedance Modeling and Stability Analysis of Grid-Connected DFIG-based Wind Farm with a VSC-HVDC," in *IEEE Journal of Emerging and Selected Topics in Power Electronics*, Feb. 2019.

[28] A. Rygg, M. Molinas, C. Zhang and X. Cai, "A Modified Sequence-Domain Impedance Definition and Its Equivalence to the dq-Domain Impedance Definition for the Stability Analysis of AC Power Electronic Systems," in *IEEE Journal of Emerging and Selected Topics in Power Electronics*, vol. 4, no. 4, pp. 1383-1396, Dec. 2016.

[29] N. W. Miller, J. J. Sanchez-Gasca, W. W. Price and R. W. Delmerico, "Dynamic modeling of GE 1.5 and 3.6 MW wind turbine-generators for stability simulations," *2003 IEEE Power Engineering Society General Meeting* (IEEE Cat. No.03CH37491), Toronto, Ont., 2003, pp. 1977-1983 Vol. 3.

[30] B. Wu, Y. Lang, N. Zargari and S. Kouro, *Power Conversion and Control of Wind Energy Systems.* John Wiley & Sons, 2011.

[31] E. Muljadi et al., "Equivalencing the collector system of a large wind power plant," *2006 IEEE Power Engineering Society General Meeting*, Montreal, Que., 2006, pp. 9 pp.-.

[32] Ł. H. Kocewiak, "Harmonics in Large Offshore Wind Farms," PhD Thesis, Dept. Energy Technol., Aalborg University, Aalborg, Denmark, 2012.

[33] H. Zong, J. Lyu, X. Cai, C. Zhang, M. Molinas, F. Rao, "Accurate aggregated modelling of wind farm systems in modified sequence domain for stability analysis," *Electric Power Systems Research*, Volume 175, 2019.

[34] L. Chen, H. Nian and Y. Xu, "Impedance Aggregation Method of Multiple Wind Turbines and Accuracy Analysis," *Energies*, 2019, 12, 2035.

[35] Y. Zhang, C. Klabunde and M. Wolter, "Frequency-Coupled Impedance Modeling and Resonance Analysis of DFIG-Based Offshore Wind Farm With HVDC Connection," in *IEEE Access*, vol. 8, pp. 147880-147894, 2020, doi: 10.1109/ACCESS.2020.3015614.

[36] J. Lyu, X. Cai and M. Molinas, "Frequency Domain Stability Analysis of MMC-Based HVDC for Wind Farm Integration," in *IEEE Journal of Emerging and Selected Topics in Power Electronics*, vol. 4, no. 1, pp. 141-151, March 2016.

[37] Z. Li, H. Hu, L. Tang, Y. Wang, T. Zang and Z. He, "Quantitative Severity Assessment and Sensitivity Analysis Under Uncertainty for Harmonic Resonance Amplification in Power Systems," in *IEEE Transactions on Power Delivery*.

[38] Wilsun Xu, Zhenyu Huang, Yu Cui and Haizhen Wang, "Harmonic resonance mode analysis," in *IEEE Transactions on Power Delivery*, vol. 20, no. 2, pp. 1182-1190, April 2005.

[39] E. Ebrahimzadeh, F. Blaabjerg, X. Wang and C. L. Bak, "Harmonic instability source identification in large wind farms," *2017 IEEE Power & Energy Society General Meeting*, Chicago, IL, 2017, pp. 1-5.

[40] Dehong Xu, Frede Blaabjerg, Wenjie Chen and Nan Zhu, "Resonant Control of DFIG Under Grid Voltage Harmonics Distortion," in *Advanced Control of Doubly Fed Induction Generator for Wind Power Systems* , IEEE, 2018, pp.195-235.

[41] S. Zhang, S. Jiang, X. Lu, B. Ge and F. Z. Peng, "Resonance Issues and Damping Techniques for Grid-Connected Inverters With Long Transmission Cable," in *IEEE Transactions on Power Electronics*, vol. 29, no. 1, pp. 110-120, Jan. 2014.

[42] J. Lyu, X. Cai and M. Molinas, "Optimal Design of Controller Parameters for Improving the Stability of MMC-HVDC for Wind Farm Integration," in *IEEE Journal of Emerging and Selected Topics in Power Electronics*, vol. 6, no. 1, pp. 40-53, March 2018.

[43] A. W. Korai and I. Erlich, "Mitigation of harmonic instability in offshore wind farms using supplementary signals in the HVDC control," *2017 IEEE Power & Energy Society General Meeting*, Chicago, IL, 2017, pp. 1-5.

[44] X. Wang, R. Beres, F. Blaabjerg and P. C. Loh, "Passivity-based design of passive damping for LCL-filtered voltage source converters," *2015 IEEE Energy Conversion Congress and Exposition (ECCE)*, Montreal, QC, 2015, pp. 3718-3725.

[45] R. N. Beres, X. Wang, M. Liserre, F. Blaabjerg and C. L. Bak, "A Review of Passive Power Filters for Three-Phase Grid-Connected Voltage-Source Converters," in *IEEE Journal of Emerging and Selected Topics in Power Electronics*, vol. 4, no. 1, pp. 54-69, March 2016, doi: 10.1109/JESTPE.2015.2507203.

[46] Y. Zhang, C. Klabunde, M. Wolter, "Harmonic Filtering in DFIG-based Offshore Wind Farm through Resonance Damping," *IEEE ISGT Europe 2019*, Bucharest, 2019, pp. 1-5.

[47] J. Adams, C. Carter and S. Huang, "ERCOT experience with Sub-synchronous Control Interaction and proposed remediation," PES T&D 2012, Orlando, FL, 2012, pp. 1-5, doi: 10.1109/TDC.2012.6281678.

[48] Y. Chi et al., "Overview of mechanism and mitigation measures on multi-frequency oscillation caused by large-scale integration of wind power," in *CSEE Journal of Power and Energy Systems*, vol. 5, no. 4, pp. 433-443, Dec. 2019.

[49] H. Liu et al., "Subsynchronous Interaction Between Direct-Drive PMSG Based Wind Farms and Weak AC Networks," in *IEEE Transactions on Power Systems*, vol. 32, no. 6, pp. 4708-4720, Nov. 2017, doi: 10.1109/TPWRS.2017.2682197.

[50] J. Rose et al., "Wind Energy Systems Sub-Synchronous Oscillations: Events and Modeling", *IEEE Power & Energy Society Tech. Rep. PES-TR80*, Jul. 2020.

[51] Y. Zhao, B. Zheng, Z. He, et al, "The control mode and operating performance of nanhui VSC-HVDC demonstration project," Southern Power System Technology, 2012, 6(6): 6-10 (in Chinese).

[52] C. Yin, X. Xie, H. Liu, et al, "Analysis and Control of the Oscillation Phenomenon in VSC-HVDC Transmission System," Power System Technology, 2018 (4): 1117-1123, doi:10.13335/j.1000-3673.pst.2017.2606 (in Chinese).

[53] L. Jing, P. Dong, and S. Gang, "Subsynchronous oscillation and its mitigation of MMC-based HVDC with large doubly-fed induction generator-based wind farm integration," Proc. CSEE, vol. 35, no. 19, pp. 4852–4860, Oct. 2015.

[54] C. Zou et al., "Analysis of Resonance Between a VSC-HVDC Converter and the AC Grid," in *IEEE Transactions on Power Electronics*, vol. 33, no. 12, pp. 10157-10168, Dec. 2018, doi: 10.1109/TPEL.2018.2809705.

[55] M. Ndreko, C. Petino and W. Winter, "High Penetration of Inverter Based Generation in the Power System: A Discussion on Stability Challenges and a Roadmap for R&D," in Proceedings of the 4th International Hybrid Power Systems Workshop, Crete, 2019, pp. 1-7.

[56] D. Yang, X. Wang, and F. Blaabjerg, "Sideband harmonic instability of paralleled inverters with asynchronous carriers," *IEEE Trans. Power Electron*., vol. 33, no. 6, pp. 4571–4577, Jun. 2018.

[57] L. Harnefors, R. Finger, X. Wang, H. Bai, and F. Blaabjerg, "VSC input-admittance modeling and analysis above the Nyquist frequency for passivity-based stability assessment," *IEEE Trans. Ind. Electron*., vol. 64, no. 8, pp. 6362–6370, Aug. 2017.

[58] X. Wang and F. Blaabjerg, "Harmonic Stability in Power Electronic-Based Power Systems: Concept, Modeling, and Analysis," in *IEEE Transactions on Smart Grid*, vol. 10, no. 3, pp. 2858-2870, May 2019, doi: 10.1109/TSG.2018.2812712.

[59] L. Fan and Z. Miao, "Admittance-Based Stability Analysis: Bode Plots, Nyquist Diagrams or Eigenvalue Analysis?," in *IEEE Transactions on Power Systems*, vol. 35, no. 4, pp. 3312-3315, July 2020, doi: 10.1109/TPWRS.2020.2996014.

[60] M. Cespedes and J. Sun, "Impedance modeling and analysis of grid connected voltage-source converters," *IEEE Trans. Power Electron.*, vol. 29, no. 3, pp. 1254–1261, Mar. 2014.

[61] M. K. Bakhshizadeh, X. Wang, F. Blaabjerg, J. Hjerrild, L. Kocewiak, C. L. Bak, and B. Hesselbaek, "Couplings in phase domain impedance modeling of grid-connected converters," IEEE Trans. Power Electron., vol. 31, no. 10, pp. 6792–6796, Oct. 2016.

[62] W. Xu, "Component Modeling Issues for Power Quality Assessment, " in *IEEE Power Engineering Review*, vol. 21, no. 11, pp. 12-17, Nov. 2001.

[63] "Modeling and simulation of the propagation of harmonics in electric power networks. I. Concepts, models, and simulation techniques," in *IEEE Transactions on Power Delivery*, vol. 11, no. 1, pp. 452-465, Jan. 1996.

[64] N.R. Watson J. Arrillaga. *Power System Harmonics*. John Wiley & Sons, 2 edition, 2003.

[65] Zimmerman, Ray D. and Carlos E. Murillo-S. "Matpower 6.0b1 User's Manual." (2016).

[66] G. Singh, S. McGuinness, C. Miller, M. Stephens and M. McGranaghan, "Effects of PV transformer energization on power quality," *2018 18th International Conference on Harmonics and Quality of Power (ICHQP)*, Ljubljana, 2018, pp. 1-6.

[67] W. L. A. Neves, H. W. Dommel and Wilsun Xu, "Practical distribution transformer models for harmonic studies," in *IEEE Transactions on Power Delivery*, vol. 10, no. 2, pp. 906-912, April 1995.

[68] K. Ragavan and L. Satish, "An efficient method to compute transfer function of a transformer from its equivalent circuit," in *IEEE Transactions on Power Delivery*, vol. 20, no. 2, pp. 780-788, April 2005.

[69] CIGRE WG 33.02, "Guidelines for Representation of Network Elements when Calculating Transients," 1990.

[70] C. Amornvipas, "Harmonic Studies and Resonance Analyses in Electrical Power Systems," Ph.D. dissertation, Institute of Electric Power Systems, Eng., Univ. Hannover, Shaker Verlag, 2009.

[71] J. C. Das, *Power System Analysis: Short-Circuit Load Flow and Harmonics*. New York: Marcel Dekker Inc., 2002.

[72] Y. Shen, J. Ma, L. Wang and A. G. Phadke, "Study on DFIG Dissipation Energy Model and Low-Frequency Oscillation Mechanism Considering the Effect of PLL," in *IEEE Transactions on Power Electronics*, vol. 35, no. 4, pp. 3348-3364, April 2020.

[73] B. Wen, D. Boroyevich, R. Burgos, P. Mattavelli and Z. Shen, "Analysis of D-Q Small-Signal Impedance of Grid-Tied Inverters," in *IEEE Transactions on Power Electronics*, vol. 31, no. 1, pp. 675-687, Jan. 2016.

[74] G. Francis, R. Burgos, D. Boroyevich, F. Wang and K. Karimi, "An algorithm and implementation system for measuring impedance in the D-Q domain," *2011 IEEE Energy Conversion Congress and Exposition*, Phoenix, AZ, 2011, pp. 3221-3228.

[75] J. Sun, "Small-Signal Methods for AC Distributed Power Systems–A Review," in *IEEE Transactions on Power Electronics*, vol. 24, no. 11, pp. 2545-2554, Nov. 2009.

[76] H. Wu, X. Wang, Ł. Kocewiak and L. Harnefors, "AC Impedance Modeling of Modular Multilevel Converters and Two-Level Voltage-Source Converters: Similarities and Differences," *2018 IEEE 19th Workshop on Control and Modeling for Power Electronics* (COMPEL), Padua, 2018, pp. 1-8.

[77] J. Sun and H. Liu, "Sequence Impedance Modeling of Modular Multilevel Converters," in *IEEE Journal of Emerging and Selected Topics in Power Electronics*, vol. 5, no. 4, pp. 1427-1443, Dec. 2017.

[78] J. Sun and H. Liu, "Impedance modeling and analysis of modular multilevel converters," 2016 IEEE 17th Workshop on Control and Modeling for Power Electronics (COMPEL), Trondheim, 2016, pp. 1-9.

[79] X. Liu and A. Lindemann, "Control of VSC-HVDC Connected Offshore Windfarms for Providing Synthetic Inertia," in *IEEE Journal of Emerging and Selected Topics in Power Electronics*, vol. 6, no. 3, pp. 1407-1417, Sept. 2018.

[80] J. Lyu, X. Cai and M. Molinas, "Optimal Design of Controller Parameters for Improving the Stability of MMC-HVDC for Wind Farm Integration," in *IEEE Journal of Emerging and Selected Topics in Power Electronics*, vol. 6, no. 1, pp. 40-53, March 2018.

[81] H. J. Bahirat, B. A. Mork and H. K. Høidalen, "Comparison of wind farm topologies for offshore applications," *2012 IEEE Power and Energy Society General Meeting*, San Diego, CA, 2012, pp. 1-8.

[82] Kocewiak, L. H., Hjerrild, J., & Bak, C. L. (2010). Wind Farm Structures' Impact on Harmonic Emission and Grid Interaction. Paper presented at The European Wind Energy Conference & Exhibition, EWEC 2010, Warszawa, Poland.

[83] S. Dutta and T. J. Overbye, "A clustering based wind farm collector system cable layout design," *2011 IEEE Power and Energy Conference* at Illinois, Champaign, IL, 2011, pp. 1-6.

[84] ABB, "XLPE Submarine Cable Systems, Attachment to XLPE Land Cable Systems - User's Guide," volume Rev 5, 2007.

[85] S. Shah et al., "Large-Signal Impedance-Based Modeling and Mitigation of Resonance of Converter-Grid Systems," in *IEEE Transactions on Sustainable Energy*, vol. 10, no. 3, pp. 1439-1449, July 2019.

[86] H. Mouton, B. McGrath, D. G. Holmes, R. H. Wilkinson, "One-dimensional spectral analysis of complex PWM waveforms using superposition," *IEEE Trans. Power Electron.*, vol. 29, no. 12, pp. 6762-6778, Dec., 2014.

[87] Yao Xiao, Jie Zhao and Shijie Mao, "Theory for the design of C-type filter," 2004 *11th International Conference on Harmonics and Quality of Power* (IEEE Cat. No.04EX951), Lake Placid, NY, USA, 2004, pp. 11-15.

[88] H. Brantsæter, Ł. H. Kocewiak, A. Rygg and E. Tedeschi, "Passive Filter Design and Offshore Wind Turbine Modelling for System Level Harmonic Studies," *Energy Procedia*, vol. 80, pp. 401-410, 2015, doi: 10.1016/j.egypro.2015.11.444.

[89] H. Akagi, H. Fujita, and K. Wada, "A shunt active filter based on voltage detection for harmonic termination of a radial power distribution line," *IEEE Trans. Ind. Appl.*, vol. 35, no. 3, pp. 638–645, May/Jun. 1999.

[90] R. Inzunza and H. Akagi, "A 6.6-kV transformerless shunt hybrid active filter for installation on a power distribution system," *IEEE Trans. Power Electron.*, vol. 20, no. 4, pp. 893-900, Jul. 2005.

[91] X. Wang, F. Blaabjerg, and M. Liserre, "An active damper to suppress multiple resonances with unknown frequencies," in *Proc. Appl. Power Electron. Conf. Expo.*, 2014, pp. 2184–2194.

[92] X. Wang, F. Blaabjerg, M. Liserre, Z. Chen, J. He and Y. Li, "An active damper for stabilizing power electronics-based AC systems," 28th IEEE APEC Conference, Long Beach, CA, 2013, pp. 1131-1138.

[93] X. Wang, Y. Pang, P. C. Loh, and F. Blaabjerg, "A series-LC-filtered active damper with grid disturbance rejection for AC power electronics based power systems," *IEEE Trans. Power Electron.*, vol. 30, no. 8, pp. 4037–4041, Aug. 2015.

[94] I. Vieto and J. Sun, "Damping of subsynchronous resonance involving Type-III wind turbines," *2015 IEEE 16th Workshop on Control and Modeling for Power Electronics (COMPEL)*, Vancouver, BC, 2015, pp. 1-8.

[95] Y. Song, F. Blaabjerg, X. Wang, "Analysis and Active Damping of Multiple High Frequency Resonances in DFIG System," *IEEE Trans. Energy Convers.*, vol. 32, no. 1, pp. 369–381, March 2017.

[96] Y. Song, X. Wang, F. Blaabjerg, "High Frequency Resonance Damping of DFIG based Wind Power System under Weak Network," *IEEE Trans. Power Electron.*, vol. 32, no. 3, pp. 1927-1940, March 2017.

[97] X. Wang, Y. Li, F. Blaabjerg, and P. C. Loh, "Virtual-impedance-based control for voltage-source and current-source converters," *IEEE Trans. Power Electron.*, vol. 30, no. 12, pp. 7019–7037, Dec. 2015.

[98] Ł. H. Kocewiak, B. L. Ø. Kramer, O. Holmstrøm, K. H. Jensen and L. Shuai, "Resonance damping in array cable systems by wind turbine active filtering in large offshore wind power plants," in *IET Renewable Power Generation*, vol. 11, no. 7, pp. 1069-1077, 7 6 2017.

[99] G. De Carne et al., "Which Deepness Class Is Suited for Modeling Power Electronics?: A Guide for Choosing the Right Model for Grid-Integration Studies," in *IEEE Industrial Electronics Magazine*, vol. 13, no. 2, pp. 41-55, June 2019.

[100] H. Liu and X. Xie, "Comparative Studies on the Impedance Models of VSC-Based Renewable Generators for SSI Stability Analysis," in *IEEE Transactions on Energy Conversion*, vol. 34, no. 3, pp. 1442-1453, Sept. 2019.

[101] X. Wang, F. Blaabjerg and Z. Chen, "Autonomous Control of Inverter-Interfaced Distributed Generation Units for Harmonic Current Filtering and Resonance Damping in an Islanded Microgrid," in *IEEE Transactions on Industry Applications*, vol. 50, no. 1, pp. 452-461, Jan.-Feb. 2014.

[102] H. Tian, Y. W. Li, and P. Wang, "Hybrid AC/DC system harmonics control through grid interfacing converters with low switching frequency," *IEEE Trans. Ind. Electron*., vol. 65, no. 3, pp. 2256-2267, Mar. 2018.

A Park Transformation: from three-phase (abc) signal to dq-frame

In time domain, a three-phase voltage vector $\boldsymbol{u}_{\mathrm{abc}}(t)$ containing the fundamental frequency component ω_{l}, a positive sequence perturbation with frequency ω_{p} and a negative sequence perturbation with frequency ω_{n} can be written as

$$\underbrace{\begin{bmatrix} u_{\mathrm{a}}(t) \\ u_{\mathrm{b}}(t) \\ u_{\mathrm{c}}(t) \end{bmatrix}}_{\boldsymbol{u}_{\mathrm{abc}}(t)} = \underbrace{\begin{bmatrix} U_{\mathrm{l}}\cos\left(\omega_{\mathrm{l}}t\right) \\ U_{\mathrm{l}}\cos\left(\omega_{\mathrm{l}}t-\frac{2\pi}{3}\right) \\ U_{\mathrm{l}}\cos\left(\omega_{\mathrm{l}}t+\frac{2\pi}{3}\right) \end{bmatrix}}_{\boldsymbol{u}_{\mathrm{abc,l}}(t)} + \underbrace{\begin{bmatrix} U_{\mathrm{p}}\cos\left(\omega_{\mathrm{p}}t+\phi_{\mathrm{p}}\right) \\ U_{\mathrm{p}}\cos\left(\omega_{\mathrm{p}}t+\phi_{\mathrm{p}}-\frac{2\pi}{3}\right) \\ U_{\mathrm{p}}\cos\left(\omega_{\mathrm{p}}t+\phi_{\mathrm{p}}+\frac{2\pi}{3}\right) \end{bmatrix}}_{\boldsymbol{u}_{\mathrm{abc,p}}(t)} + \underbrace{\begin{bmatrix} U_{\mathrm{n}}\cos\left(\omega_{\mathrm{p}}t+\phi_{\mathrm{n}}\right) \\ U_{\mathrm{n}}\cos\left(\omega_{\mathrm{p}}t+\phi_{\mathrm{n}}-\frac{2\pi}{3}\right) \\ U_{\mathrm{n}}\cos\left(\omega_{\mathrm{p}}t+\phi_{\mathrm{n}}+\frac{2\pi}{3}\right) \end{bmatrix}}_{\boldsymbol{u}_{\mathrm{abc,n}}(t)}$$

where $\boldsymbol{u}_{\mathrm{abc,1}}(t)$, $\boldsymbol{u}_{\mathrm{abc,p}}(t)$ and $\boldsymbol{u}_{\mathrm{abc,n}}(t)$ denotes three-phase vectors of the frequency component ω_{l}, ω_{p} and ω_{n}, respectively.

Implementing the following Park transformation to the three-phase voltages $\boldsymbol{u}_{\mathrm{abc}}(t)$ yields

$$\underbrace{\begin{bmatrix} u_{\mathrm{d}}(t) \\ u_{\mathrm{q}}(t) \end{bmatrix}}_{\boldsymbol{u}_{\mathrm{dq}}(t)} = \underbrace{\frac{2}{3}\begin{bmatrix} \cos\left(\omega_{\mathrm{l}}t\right) & \cos(\omega_{\mathrm{l}}t-\frac{2\pi}{3}) & \cos(\omega_{\mathrm{l}}t+\frac{2\pi}{3}) \\ -\sin\left(\omega_{\mathrm{l}}t\right) & -\sin(\omega_{\mathrm{l}}t-\frac{2\pi}{3}) & -\sin(\omega_{\mathrm{l}}t+\frac{2\pi}{3}) \end{bmatrix}}_{\boldsymbol{T}(\omega_{\mathrm{l}}t)} \boldsymbol{u}_{\mathrm{abc}}(t)$$

$$= \boldsymbol{T}(\omega_{\mathrm{l}}t)\boldsymbol{u}_{\mathrm{abc,l}}(t) + \boldsymbol{T}(\omega_{\mathrm{l}}t)\boldsymbol{u}_{\mathrm{abc,p}}(t) + \boldsymbol{T}(\omega_{\mathrm{l}}t)\boldsymbol{u}_{\mathrm{abc,n}}(t)$$

$$= \underbrace{\begin{bmatrix} u_{\mathrm{d,l}}(t) \\ u_{\mathrm{q,l}}(t) \end{bmatrix}}_{\boldsymbol{u}_{\mathrm{dq,l}}(t)} + \underbrace{\begin{bmatrix} u_{\mathrm{d,p}}(t) \\ u_{\mathrm{q,p}}(t) \end{bmatrix}}_{\boldsymbol{u}_{\mathrm{dq,p}}(t)} + \underbrace{\begin{bmatrix} u_{\mathrm{d,p}}(t) \\ u_{\mathrm{q,p}}(t) \end{bmatrix}}_{\boldsymbol{u}_{\mathrm{dq,n}}(t)}$$

where $\boldsymbol{T}(\omega_{\mathrm{l}}t)$ is the Park transformation matrix with the d-axis aligns with the fundamental frequency component of phase-a at t=0. Since $\boldsymbol{T}(\omega_{\mathrm{l}}t)$ transforms the three-phase voltages to the synchronous reference frame (SRF), in which the d- and q-axis

rotates with the fundamental frequency ω_1, all the variables in the above equation with the subscripts p and q denote the values under SRF.

Based on the transformation between trigonometric functions and their complex exponential expressions, the d-axis component of the three-phase perturbation can be calculated as

$$u_{\mathrm{d,p}}(t)=\frac{2}{3}\begin{bmatrix}\cos(\omega_1 t) & \cos\left(\omega_1 t-\frac{2\pi}{3}\right) & \cos\left(\omega_1 t+\frac{2\pi}{3}\right)\end{bmatrix}\begin{bmatrix}U_{\mathrm{p}}\cos\left(\omega_{\mathrm{p}}t+\phi_{\mathrm{p}}\right)\\ U_{\mathrm{p}}\cos\left(\omega_{\mathrm{p}}t+\phi_{\mathrm{p}}-\frac{2\pi}{3}\right)\\ U_{\mathrm{p}}\cos\left(\omega_{\mathrm{p}}t+\phi_{\mathrm{p}}+\frac{2\pi}{3}\right)\end{bmatrix}$$

$$=\frac{2}{3}U_{\mathrm{p}}\begin{pmatrix}\cos(\omega_1 t)\cos\left(\omega_{\mathrm{p}}t+\phi_{\mathrm{p}}\right)\\ +\cos\left(\omega_1 t-\frac{2\pi}{3}\right)\cos\left(\omega_{\mathrm{p}}t+\phi_{\mathrm{p}}-\frac{2\pi}{3}\right)\\ +\cos\left(\omega_1 t+\frac{2\pi}{3}\right)\cos\left(\omega_{\mathrm{p}}t+\phi_{\mathrm{p}}+\frac{2\pi}{3}\right)\end{pmatrix}$$

$$=\frac{1}{6}U_{\mathrm{p}}\begin{pmatrix}\left(\mathrm{e}^{\mathrm{j}\omega_1 t}+\mathrm{e}^{-\mathrm{j}\omega_1 t}\right)\left(\mathrm{e}^{\mathrm{j}\left(\omega_{\mathrm{p}}t+\phi_{\mathrm{p}}\right)}+\mathrm{e}^{-\mathrm{j}\left(\omega_{\mathrm{p}}t+\phi_{\mathrm{p}}\right)}\right)\\ +\left(\mathrm{e}^{\mathrm{j}\left(\omega_1 t-\frac{2\pi}{3}\right)}+\mathrm{e}^{-\mathrm{j}\left(\omega_1 t-\frac{2\pi}{3}\right)}\right)\left(\mathrm{e}^{\mathrm{j}\left(\omega_{\mathrm{p}}t+\phi_{\mathrm{p}}-\frac{2\pi}{3}\right)}+\mathrm{e}^{-\mathrm{j}\left(\omega_{\mathrm{p}}t+\phi_{\mathrm{p}}-\frac{2\pi}{3}\right)}\right)\\ +\left(\mathrm{e}^{\mathrm{j}\left(\omega_1 t+\frac{2\pi}{3}\right)}+\mathrm{e}^{-\mathrm{j}\left(\omega_1 t+\frac{2\pi}{3}\right)}\right)\left(\mathrm{e}^{\mathrm{j}\left(\omega_{\mathrm{p}}t+\phi_{\mathrm{p}}+\frac{2\pi}{3}\right)}+\mathrm{e}^{-\mathrm{j}\left(\omega_{\mathrm{p}}t+\phi_{\mathrm{p}}+\frac{2\pi}{3}\right)}\right)\end{pmatrix}$$

$$=\frac{1}{6}U_{\mathrm{p}}\begin{pmatrix}\mathrm{e}^{\mathrm{j}\left(\left(\omega_1+\omega_{\mathrm{p}}\right)t+\phi_{\mathrm{p}}\right)}+\mathrm{e}^{-\mathrm{j}\left(\left(\omega_1+\omega_{\mathrm{p}}\right)t+\phi_{\mathrm{p}}\right)}+\mathrm{e}^{\mathrm{j}\left(\left(\omega_1-\omega_{\mathrm{p}}\right)t-\phi_{\mathrm{p}}\right)}+\mathrm{e}^{-\mathrm{j}\left(\left(\omega_1-\omega_{\mathrm{p}}\right)t-\phi_{\mathrm{p}}\right)}\\ +\mathrm{e}^{\mathrm{j}\left(\left(\omega_1+\omega_{\mathrm{p}}\right)t+\phi_{\mathrm{p}}-\frac{4\pi}{3}\right)}+\mathrm{e}^{-\mathrm{j}\left(\left(\omega_1+\omega_{\mathrm{p}}\right)t+\phi_{\mathrm{p}}-\frac{4\pi}{3}\right)}+\mathrm{e}^{\mathrm{j}\left(\left(\omega_1-\omega_{\mathrm{p}}\right)t-\phi_{\mathrm{p}}\right)}+\mathrm{e}^{-\mathrm{j}\left(\left(\omega_1-\omega_{\mathrm{p}}\right)t-\phi_{\mathrm{p}}\right)}\\ +\mathrm{e}^{\mathrm{j}\left(\left(\omega_1+\omega_{\mathrm{p}}\right)t+\phi_{\mathrm{p}}+\frac{4\pi}{3}\right)}+\mathrm{e}^{-\mathrm{j}\left(\left(\omega_1+\omega_{\mathrm{p}}\right)t+\phi_{\mathrm{p}}+\frac{4\pi}{3}\right)}+\mathrm{e}^{\mathrm{j}\left(\left(\omega_1-\omega_{\mathrm{p}}\right)t-\phi_{\mathrm{p}}\right)}+\mathrm{e}^{-\mathrm{j}\left(\left(\omega_1-\omega_{\mathrm{p}}\right)t-\phi_{\mathrm{p}}\right)}\end{pmatrix}$$

$$=\frac{1}{6}U_{\mathrm{p}}\begin{pmatrix}6\cos\left(\left(\omega_1-\omega_{\mathrm{p}}\right)t-\phi_{\mathrm{p}}\right)\\ +2\cos\left(\left(\omega_1+\omega_{\mathrm{p}}\right)t+\phi_{\mathrm{p}}\right)\left(\cos(0)+\cos\left(-\frac{\pi}{3}\right)+\cos\left(\frac{\pi}{3}\right)\right)\end{pmatrix}$$

$$=U_{\mathrm{p}}\cos\left(\left(\omega_{\mathrm{p}}-\omega_1\right)t+\phi_{\mathrm{p}}\right)$$

Similarly, the q-axis component of the perturbation ω_p can be derived as

$$u_{\mathrm{q,p}}(t)=\frac{2}{3}\left[-\sin(\omega_\mathrm{l}t)\quad -\sin\left(\omega_\mathrm{l}t-\frac{2\pi}{3}\right)\quad -\sin\left(\omega_\mathrm{l}t+\frac{2\pi}{3}\right)\right]\begin{bmatrix}U_\mathrm{p}\cos\left(\omega_\mathrm{p}t+\phi_\mathrm{p}\right)\\ U_\mathrm{p}\cos\left(\omega_\mathrm{p}t+\phi_\mathrm{p}-\frac{2\pi}{3}\right)\\ U_\mathrm{p}\cos\left(\omega_\mathrm{p}t+\phi_\mathrm{p}+\frac{2\pi}{3}\right)\end{bmatrix}$$

$$=U_\mathrm{p}\sin\left(\left(\omega_\mathrm{p}-\omega_\mathrm{l}\right)t+\phi_\mathrm{p}\right)$$

According to the derivation of $u_{\mathrm{d,p}}(t)$, the d- and q-terms of the frequency component ω_l and ω_n can also be derived, which in combination with the frequency component ω_p can be written as

$$\underline{U}_{\mathrm{dq,l}}(t)=\underbrace{U_\mathrm{l}}_{u_{\mathrm{d,l}}}+\mathrm{j}\underbrace{0}_{u_{\mathrm{q,l}}}$$

$$\underline{U}_{\mathrm{dq,p}}(t)=\underbrace{U_\mathrm{p}\cos\left(\left(\omega_\mathrm{p}-\omega_\mathrm{l}\right)t+\phi_\mathrm{p}\right)}_{u_{\mathrm{d,p}}(t)}+\mathrm{j}\underbrace{U_\mathrm{p}\cos\left(\left(\omega_\mathrm{p}-\omega_\mathrm{l}\right)t+\phi_\mathrm{p}\right)}_{u_{\mathrm{q,p}}(t)}$$

$$\underline{U}_{\mathrm{dq,n}}(t)=\underbrace{-U_\mathrm{n}\cos\left(\left(\omega_\mathrm{n}+\omega_\mathrm{l}\right)t+\phi_\mathrm{n}\right)}_{u_{\mathrm{d,n}}(t)}+\mathrm{j}\underbrace{U_\mathrm{n}\sin\left(\left(\omega_\mathrm{n}+\omega_\mathrm{l}\right)t+\phi_\mathrm{n}\right)}_{u_{\mathrm{q,n}}(t)}$$

Finally, the frequency-domain representation of $u_\mathrm{d}(t)$ and $u_\mathrm{q}(t)$ can be written as

$$\underline{U}_\mathrm{d}(\omega)=\begin{cases}U_\mathrm{l},\ \omega=0\\ \dfrac{U_\mathrm{p}}{2}\mathrm{e}^{\pm\mathrm{j}\phi_\mathrm{p}},\ \omega=\pm(\omega_\mathrm{p}-\omega_\mathrm{l})\\ \dfrac{U_\mathrm{n}}{2}\mathrm{e}^{\pm\mathrm{j}\phi_\mathrm{n}},\ \omega=\pm(\omega_\mathrm{n}+\omega_\mathrm{l})\end{cases}\qquad \underline{U}_\mathrm{q}(\omega)=\begin{cases}0,\ \omega=0\\ \mp\mathrm{j}\dfrac{U_\mathrm{p}}{2}\mathrm{e}^{\pm\mathrm{j}\phi_\mathrm{p}},\ \omega=\pm(\omega_\mathrm{p}-\omega_\mathrm{l})\\ \pm\mathrm{j}\dfrac{U_\mathrm{n}}{2}\mathrm{e}^{\pm\mathrm{j}\phi_\mathrm{n}},\ \omega=\pm(\omega_\mathrm{n}+\omega_\mathrm{l})\end{cases}$$

where $\underline{U}_\mathrm{d}(\omega)$ and $\underline{U}_\mathrm{q}(\omega)$ are the dq-frame (SRF) expressions of the three-phase signal with ω denoting dq-frame frequency.

B Winding Connections of Three-phase Transformer

Vector Group	Phase Shift (degrees)	Winding 1	Winding 2	Connection Matrices $\boldsymbol{D}_A^T$	Connection Matrices $\boldsymbol{D}_B^T$	Delta Terminls to Network ABC
Yy0	0	Y	Y	$\begin{bmatrix}1&0&0\\0&1&0\\0&0&1\end{bmatrix}$	$\begin{bmatrix}1&0&0\\0&1&0\\0&0&1\end{bmatrix}$	--
Dy1	-30	D11	Y	$\begin{bmatrix}1&0&-1\\-1&1&0\\0&-1&1\end{bmatrix}$	$\begin{bmatrix}1&0&0\\0&1&0\\0&0&1\end{bmatrix}$	abc
Dy5	-150	D11	Y	$\begin{bmatrix}1&-1&0\\0&1&-1\\-1&0&1\end{bmatrix}$	$\begin{bmatrix}-1&0&0\\0&-1&0\\0&0&-1\end{bmatrix}$	cab
Yd5	-150	Y	D1	$\begin{bmatrix}1&0&0\\0&1&0\\0&0&1\end{bmatrix}$	$\begin{bmatrix}-1&0&1\\1&-1&0\\0&1&-1\end{bmatrix}$	bca
Dy7	+150	D1	Y	$\begin{bmatrix}1&0&-1\\-1&1&0\\0&-1&1\end{bmatrix}$	$\begin{bmatrix}-1&0&0\\0&-1&0\\0&0&-1\end{bmatrix}$	bca
Yd11	+30	Y	D11	$\begin{bmatrix}1&0&0\\0&1&0\\0&0&1\end{bmatrix}$	$\begin{bmatrix}1&0&-1\\-1&1&0\\0&-1&1\end{bmatrix}$	abc
Dy11	+30	D1	Y	$\begin{bmatrix}1&-1&0\\0&1&-1\\-1&0&1\end{bmatrix}$	$\begin{bmatrix}1&0&0\\0&1&0\\0&0&1\end{bmatrix}$	abc

Examples for phase shifting:
Yd5: The secondary winding (d) is lagging primary winding (Y) by 150 degrees.
Dy11: The secondary winding (y) is leading primary winding (D) by 30 degrees.

C Base System for Per Unit Representation

The following base system is chosen for converting the absolute values of AC-grid or its component into Per Unit quantities.

- Base power: S_b = Norminal three-phase power of AC-grid or its component
- Base voltage: U_b = Norminal peak phase voltage at the AC side = $\sqrt{\frac{2}{3}}U_{LL,rms}$, where $U_{LL,rms}$ denotes line-to-line Root Mean Square (RMS) voltage
- Base current: I_b = Norminal peak phase current = $\frac{2}{3}\frac{S_b}{U_b}$
- Base impedance: $Z_b = \frac{U_b}{I_b}$
- Base frequency: ω_b = Nominal angular frequency of the power system
- Base inductance: $L_b = \frac{Z_b}{\omega_b}$
- Base capacitance: $C_b = \frac{1}{Z_b \omega_b}$

In order to achieve a power invariant transformation, the base DC-side power is the same as the base AC-side power, which gives

$$S_b = 3 \cdot U_{phase} \cdot I_{phase} = \frac{3}{2} \cdot U_b \cdot I_b = U_{dcb} \cdot I_{dcb}$$

In view of the definition of the modulation index, the base voltage for DC-side voltage is defined as

$$U_{dcb} = 2\sqrt{\frac{2}{3}}U_{LL,rms} = 2U_{peak,ph} = 2U_b$$

so that 1 pu AC voltage can be obtained with 1 pu DC voltage under unity modulation index. Then by the power balance equation as above, DC-side base current is defined as

$$I_{dcb} = \frac{S_b}{U_{dcb}} = \frac{S_b}{2U_b} = \frac{3}{4}I_b$$

Then DC-side base impedance, inductance and capacitance are defined as

$$Z_{\mathrm{dcb}} = \frac{U_{\mathrm{dcb}}}{I_{\mathrm{dcb}}} = 2U_{\mathrm{b}} \Big/ \left(\frac{3}{4} I_{\mathrm{b}} \right) = \frac{8}{3} Z_{\mathrm{b}}$$

$$L_{\mathrm{dcb}} = \frac{8}{3} L_{\mathrm{b}}$$

$$C_{\mathrm{dcb}} = \frac{8}{3} C_{\mathrm{b}} .$$

D Parameters of the Test System

Grid components	Parameter discription and values	
Single or Aggregated DFIG-based Wind Turbine (s) (including step-up transformer and terminal filter)	Aggregated WT Number	N_{wt} (quantity)
	Rated Voltage / Power	950 V / $5 \cdot N_{wt}$ MW
	DFIG generator (pu)	$R_s = 0.023,\ L_{\sigma s} = 0.18,\ R_r = 0.016,\ L_{\sigma r} = 0.16,\ L_m = 2.9$
	GSC side reactor (pu)	$R_p = 0.003,\ L_p = 0.3$
	Current controllers	GSC: $K_{gp} = 0.83,\ K_{gi} = 5,$ RSC: $K_{rp} = 0.15,\ K_{ri} = 2$
	DC bus votage regulator	$K_{dcp} = 8,\ K_{dci} = 400$
	DC bus parameters	capacitor $30000 \cdot N_{wt}$ μF , nominal voltage 1900 V
	Speed regulator	$K_{sp} = 3,\ K_{si} = 0.6$
	Q regulator	$K_{qp} = 0.03,\ K_{qi} = 1$
	Terminal filter	$600 \cdot N_{wt}$ kvar , Q=50 (power quality)
	Step-up transformer	$5.5 \cdot N_{wt}$ MVA, 0.95 /33 kV, $u_k = 5\%,\ u_r = 0.17\%,$ $R_m = 500$ (pu), $L_m = \text{inf},$ capacitance effect neglected
	Sampling technique	Asymmetrical regular (double edge)
	Switching frequency	2 kHz
	PLL	$K_{pp} = 16,\ K_{pi} = 50$
Aggregated MV cables	MV1 / MV2	$R = 0.034\ \Omega, L = 0.191$ mH, $C = 10.52$ μF (these parameters vary as MV collector grid topology changes)
HV cables	HV Cable 1 or Cable 2	Length: 4 km, with parameters $R = 0.089\ \Omega/\text{km}, L = 0.36$ mH/km, $C = 0.23$ μF/km
Transformers	T1 (secondary winding parameters are reflected to primary winding side)	420 MVA, 155 / 150 kV Primary winding (pu): $L_A = 7\%,\ R_A = 0.15\%$ Secondary winding (pu): $L_B = 7\%,\ R_B = 0.15\%$ Magnetizing branch (pu) : $L_m = 500,\ R_m = 500$ Parasitic capacitances $C_M,\ C_{WA},\ C_{WB},\ C_{EA}$ or C_{EB} : 0 nF
	T2 and T3 (secondary winding parameters are reflected to primary winding side)	210 MVA, 33 / 155 kV Primary winding (pu): $L_A = 6\%,\ R_B = 0.25\%$ Secondary winding (pu): $L_A = 6\%,\ R_B = 0.25\%$ Magnetizing branch (pu) : $L_m = 500,\ R_m = 500$ Parasitic capacitances $C_M,\ C_{WA},\ C_{WB},\ C_{EA}$ or C_{EB} : 0 nF
HVDC Converter station (including AC filters)	Rated voltage / Power	± 150 kV / 400 MW
	Phase reactors (pu)	$R_c = 0.15/100,\ L_c = 0.15$
	Voltage regulator	$K_{vp} = 0.1,\ K_{vi} = 15$
	Switching frequency	1350 Hz
	Sampling technique	Asymmetrical regular (double edge)
	Switching filters	27th high-pass damped filter: 30 Mvar, Q=15 54th high-pass damped filter: 10 Mvar, Q=15

Res Electricae Magdeburgenses

MAgdeburger FOrum zur Elektrotechnik

MAFO-01 Orths, A.: *Multikriterielle, optimale Planung von Verteilungsnetzen im liberalisierten Energiemarkt unter Verwendung von spieltheoretischen Verfahren*, 2003. ISBN 3-929757-57-5.

MAFO-02 Purmann, M.: *Optimierung des Betriebsverhaltens von PEM-Brennstoffzellen unter Berücksichtigung von elektrischem und Gesamtwirkungsgrad bei unterschiedlichen Lastanforderungen und Betriebsparametern*, 2004. ISBN 3-929757-63-X.

MAFO-03 Al-Hamid, M.: *Extraktion von höheren Moden in TEM-Wellenleitern*, 2004. ISBN 3-929757-64-8.

MAFO-04 Haase, H., J. Nitsch, and T. Steinmetz: *Transmission-Line Super Theory – A new Approach to an Effective Calculation of Electromagnetic Interference*, 2004. ISBN 3-929757-67-2.

MAFO-05 Bachry, A.: *Power Quality Studies in Distribution Systems Involving Spectral Decomposition*, 2004. ISBN 3-929757-68-0.

MAFO-06 Styczynski, Z. A.: *Power Network and Renewables – A Scientific Report*, 2004. ISBN 3-929757-69-9.

MAFO-07 Blume, E.: *Numerische Analyse der Kopplung linearer Antennen innerhalb eines Resonators*, 2004. ISBN 3-929757-71-0.

MAFO-08 Handschin, E. and Z. A. Styczynski: *Power System Application of the Modern Battery Storage*, 2004. ISBN 3-929757-75-3.

MAFO-09 Haase, H.: *Full-Wave Field Interactions of Nonuniform Transmission Lines*, 2005. ISBN 3-929757-78-8.

MAFO-10 Nitsch, D.: *Die Wirkung eingekoppelter ultrabreitbandiger elektromagnetischer Impulse auf komplexe elektronische Systeme*, 2005. ISBN 3-929757-79-6.

MAFO-11 Hadzi-Kostova, B.: *Protection Concepts in Distribution Networks with Decentralized Energy Resources*, 2005. ISBN 3-929757-84-2.

MAFO-12 Steinmetz, T.: *Ungleichförmige und zufällig geführte Mehrfachleitungen in komplexen technischen Systemen*, 2006. Nummerierung geändert, ISBN 3-929757-98-2.

MAFO-13 Styczynski, Z. and J. Haubrock: *Influence of Distributed and Renewable Generation on Power System Security – Proceedings of the CRIS Workshop 2006*, 2006. ISBN 3-929757-99-0.

MAFO-14 Heideck, G.: *Ein autonomes Brennstoffzellensystem: Optimierungsansätze*, 2006. ISBN 3-929757-94-X.

MAFO-15 Styczynski, Z. und H.-D. Musikowski: *Dresdener Kreis Elektroenergieversorgung 7*, 2006. ISBN 3-929757-85-0.

MAFO-16 Gronwald, F.: *Antenna Theory in Resonating Systems derived from Fundamental Electromagnetism*, 2007. ISBN 3-929757-93-1.

MAFO-17 Krauthäuser, H.G.: *Grundlagen und Anwendungen von Modenverwirbelungskammern*, 2007. ISBN 978-3-929757-43-9.

MAFO-18 Dzienis, C.: *Ersatzmodelle nichtlinearer Lasten in elektrischen Verteilungsnetzen*, 2007. ISBN 978-3-929757-07-1.

MAFO-19 Styczynski, Z. and J. Haubrock: *Renewable and Dispersed Power Generation in Power Systems*, 2007. ISBN 978-3-929757-44-6.

MAFO-20 Haubrock, J.: *Parametrierung elektrischer Äquivalentschaltbilder von PEM-Brennstoffzellen*, 2008. ISBN 978-3-940961-02-0.

MAFO-21 Angelov, A. N.: *Rechnergestütztes Lernen im Bereich der Regenerativen Energien (Ausgewählte Aspekte)*, 2008. ISBN 978-3-940961-03-7.

MAFO-22 Komarnicki, P.: *Anwendung hochgenauer, synchroner Messungen zur Verbesserung des Betriebs von Verteilungsnetzen*, 2008. ISBN 978-3-940961-04-4.

MAFO-23 Roggatz, C.: *Trainingssimulator für die Führung von elektrischen Systemen mit dezentralen Energieeinspeisungen – Trainingsszenarien und Umsetzung*, 2008. ISBN 978-3-940961-05-1.

MAFO-24 Rudion, K.: *Aggregated Modelling of Wind Farms*, 2008. ISBN 978-3-940961-14-3.

MAFO-25 Ganjavi, M. R.: *Protection System Coordination Using Expert System*, 2008. ISBN 978-3-940961-15-0.

MAFO-26 Bofinger, S.: *Energieversorgungsnetze mit einem hohen Anteil an photovoltaischer Solarenergie: Standortbestimmung, Solarstromprognose, Netzintegration*, 2008. ISBN 978-3-940961-25-9.

MAFO-27 Styczynski, Z. and P. Komarnicki: *Distributed and Renewable Power Generation*, 2008. ISBN 978-3-940961-26-6.

MAFO-28 Kochetov, S. V.: *Time- and Frequency-Domain Modeling of Passive Interconnection Structures in Field and Circuit Analysis*, 2008. ISBN 978-3-940961-27-3.

MAFO-29 Magdowski, M.: *Entwicklung und Validierung eines Werkzeugs zur Berechnung der elektromagnetischen Einkopplung von stochastischen Feldern in Leitungsstrukturen*, 2008. ISBN 978-3-940961-28-0.

MAFO-30 Sonnemann, F.: *Elektromagnetische Effekte an elektrischen Zündmitteln (EED) mit angeschlossener Zündkreiselektronik (ZKE) bei impulsförmiger, breitbandiger Bestrahlung*, 2009. ISBN 978-3-940961-32-7.

MAFO-31 Smieja, T.: *Multikriterielle Planung interregionaler Elektrizitätsnetze im liberalisierten Energiemarkt*, 2009. ISBN 978-3-940961-35-8.

MAFO-32 Heyde, C. O.: *Dynamic Voltage Security Assessment for On-Line Control Room Application*, 2010. ISBN 978-3-940961-40-2.

MAFO-33 Styczynski, Z. A. and N. I. Voropai (Editors): *Renewable Energy Systems Fundamentals, Technologies, Techniques and Economics*, 2010. ISBN 978-3-940961-42-6.

MAFO-34 Styczynski, Z. A. и N. I. Voropai (Editors): Renewable Energy Systems Fundamentals, Technologies, Techniques and Economics (Russian Version), 2010. ISBN 978-3-940961-44-0.

MAFO-35 Styczynski, Z. A. and A. Lindemann (Editors): *Integration of Renewable Energies into the Grid / Proceedings of the Power & Energy Student Summit 2010*, 2010. ISBN 978-3-940961-47-1.

MAFO-36 Styczynski, Z. A. und H.-D. Musikowski (Editors): *Dresdener Kreis Elektroenergieversorgung 11*, 2010. ISBN 978-3-940961-51-8.

MAFO-37 Gurbiel, M. A.: *Definition and Testing of a Digital Interface of a Power Substation*, 2011. ISBN 978-3-940961-54-9.

MAFO-38 Lombardi, P.: *Multi Criteria Optimization of an Autonomous Virtual Power Plant*, 2011. ISBN 978-3-940961-55-6.

MAFO-39 Powalko, M.: *Beobachtbarkeit eines elektrischen Verteilungsnetzes – Ein Beitrag zum Smart Grid*, 2011. ISBN 978-3-940961-62-4.

MAFO-40 Styczynski, Z. A., K. Rudion, and C. Nguyen-Mau (Editorial Board): *Power System Dynamic Security Assessment*, 2011. ISBN 978-3-940961-61-7.

MAFO-41 Käbisch, M: *Optimale Dimensionierung und Betriebsführung einer brennstoffzellenbasierten Auxiliary Power Unit im Fahrzeug*, 2011. ISBN 978-3-940961-67-9.

MAFO-42 Styczynski, Z. A. und N. I. Voropai (Editors): *Special Issue Grant 220 Russian Federation SSmart Grid for Efficient Energy Power System for the Future", Proceedings Volume I*, 2012. ISBN 978-3-940961-74-7.

MAFO-43 Styczynski, Z. A., P. Komarnicki und A. Naumann (Editors): *Abschlussbericht Harz.ErneuerbareEnergien-mobility*, 2012. ISBN 978-3-940961-71-6.

MAFO-44 Heuer, M.: *Diagnosetool für stationär betriebene PEM-Brennstoffzellensysteme*, 2012. ISBN 978-3-940961-77-8.

MAFO-45 Stötzer, M.: *Demand Side Integration in elektrischen Verteilnetzen – Potenzialanalyse und Bewertung*, 2012. ISBN 978-3-940961-78-5.

MAFO-46 Magdowski, M.: *Vergleich der Einkopplung deterministischer und statistischer elektromagnetischer Felder in Leitungen*, 2012. ISBN 978-3-940961-75-4.

MAFO-47 Naumann, A.: *Leitwarte im Smart Grid*, 2012. ISBN 978-3-940961-81-5.

MAFO-48 Rudion, K.: *Offshore Power System Planning – Selected Aspects*, 2012. ISBN 978-3-940961-82-2.

MAFO-49 Nguyen-Mau, C.: *Electric Power System Stability Enhancement by Voltage Source Converter based High Voltage Direct Current Technology*, 2012. ISBN 978-3-940961-84-6.

MAFO-50 Guo, H.: *Measurement-Based Load Modeling for Smart Grid Planning*, 2012. ISBN 978-3-940961-86-0.

MAFO-51 Styczynski, Z. A.: *Proceedings No. 2 in the Scope of Mega Grant Baikal*, 2013. ISBN 978-3-940961-95-2.

MAFO-52 Styczynski, Z. A.: *Proceedings No. 3 in the Scope of Mega Grant Baikal*, 2013. ISBN 978-3-940961-98-3.

MAFO-53 Wenge, C.: *Optimaler Betrieb von mobilen Speichern im Smart Grid. -Mobilitätsleitwarte-*, 2013. ISBN 978-3-944722-01-6.

MAFO-54 Röhrig, C.: *Smart Distribution Planung unter Berücksichtigung von residualen Lasten*, 2014. ISBN 978-3-944722-06-1.

MAFO-55 Middelstädt, F.: *Research of SEM Poles of Complex Wire Structures*, 2014. ISBN 978-3-944722-07-8.

MAFO-56 Styczynski, Z. A. (Editor): *Power Network and Renewables – A Scientific Report – 15 Years Research*, 2014. ISBN 978-3-944722-08-5.

MAFO-57 Solonina, N. N., V. S. Stepanov, and K. V. Suslov: *Information technology in intelligent power networks*, 2014. ISBN 978-3-944722-13-9.

MAFO-58 Krebs, R.: *Fundamentals of Power System Protection*, 2014. ISBN 978-3-944722-15-3.

MAFO-59 Moskalenko, N.: *Optimal Dynamic Energy Management System in Smart Homes*, 2014. ISBN 978-3-944722-16-0.

MAFO-60 Hauer, I.: *Optimale Last- und Erzeugungsanpassung bei kritischen Netzzuständen – Algorithmen und deren Bewertung*, 2014. ISBN 978-3-944722-18-4.

MAFO-61 Richter, M.: *Dresdner Kreis Elektroenergieversorgung 15, Begleitband zum Workshop 2014*, 2014. ISBN 978-3-944722-21-4.

MAFO-62 Styczynski, Z. A., A. Richter und P. Kühne: *Second ELECON Workshop – Begleitband zum Workshop 2014*, 2014. ISBN 978-3-944722-23-8.

MAFO-63 Bernstein, P.: *Modellgestützte optimale Betriebsführung von PEM-Brennstoffzellen für autonome Anlagen*, 2015. ISBN 978-3-944722-24-5.

MAFO-64 Rabe, S.: *Betrieb einer Zweipunkt-Offshore-HGÜ-Verbindung – Modelluntersuchungen*, 2015. ISBN 978-3-944722-31-3.

MAFO-65 Arendarski, B.: *Reliability Assessment of Smart Grids*, 2015. ISBN 978-3-944722-32-0.

MAFO-66 Pan, X.: *Numerisches EMV-Simulationsverfahren zur Berechnung der Störaussendung elektrischer Antriebssysteme in Hybridfahrzeugen*, 2016. ISBN 978-3-944722-34-4.

MAFO-67 Richter, M.: *PMU-basierte Zustandsabschätzung in Smart Distribution*, 2016. ISBN 978-3-944722-43-6.

MAFO-68 Bielchev, I.: *Adaptiver Distanzschutz im Standard IEC 61850*, 2016. ISBN 978-3-944722-45-0.

MAFO-69 Hassan, A.: *Modeling of Single and Double-Shielded Cables for EMC Applications*, 2016. ISBN 978-3-944722-41-2.

MAFO-70 Liu, X.: *Control of Voltage Source Converter Based High Voltage Direct Current Transmission Systems for Grid Code Compliance*, 2016. ISBN 978-3-944722-46-7.

MAFO-71 Kaiser, M.: *Fusion of Interventional Ultrasound & X-ray*, 2016. ISBN 978-3-944722-51-1.

MAFO-72 Grieger, F.: *Ein Beitrag zur Bestimmung der Zuverlässigkeit von Leistungshalbleiterbauelementen unter Berücksichtigung der Anwendung*, 2016. ISBN 978-3-944722-52-8.

MAFO-73 Li, M.: *Towards a Robust Electromagnetic Tracking System for Use in Medical Applications*, 2018. ISBN 978-3-944722-66-5.

MAFO-74 Klabunde, C., J. Dancker, N. Gast, T. Schröter, F. Schulz, J. Rossberg und A. Richter: *Statusbericht der Otto-von-Guericke-Universität Magdeburg zum Verbundprojekt: Intelligentes Multi-Energie-System (SmartMES)*, 2018. ISBN 978-3-944722-69-6.

MAFO-75 Schröter, T.: *19. Dresdner Kreis Elektroenergieversorgung, Begleitband zum Workshop 2018 in Magdeburg*, 2018. ISBN 978-3-944722-79-5.

MAFO-76 Klabunde, C., J. Dancker, N. Gast, T. Schröter, F. Schulz und J. Rossberg: *Intelligentes Multi-Energie-System (SmartMES) – Statusbericht der Otto-von-Guericke-Universität Magdeburg zum Verbundprojekt, 2. Statusseminar 04. April 2019 in Magdeburg*, 2019. ISBN 987-3-944722-80-1.

MAFO-77 Helm, S., J. Dancker, M. Fritsch und T. Schröter: *Power and Energy Student Summit 2019, 09.–11. Juli*, 2019. ISBN 978-3-944722-84-9.

MAFO-78 Chychykina, I.: *Comparison of Different Redispatch Optimization Strategies*, 2019. ISBN 978-3-944722-89-4.

MAFO-79 Balischewski, S.: *Multifunktionaler Einsatz von Batteriespeichern in elektrischen Verteilnetzen*, 2020. ISBN 978-3-944722-92-4.

MAFO-80 Petzold, J.: *Analytische Beschreibung der Kopplung elektromagnetischer Felder durch Aperturen in Resonatoren*, 2020. ISBN 978-3-944722-91-7.

MAFO-81 Middelstädt, L.: *Transiente Effekte in leistungselektronischen Schaltungen mit schnellschaltenden Leistungshalbleitern unter besonderer Berücksichtigung der elektromagnetischen Verträglichkeit*, 2020. ISBN 978-3-944722-95-5.

MAFO-82 Liu, Y.: *Contribution to Improve the EMI Performance of Electrical Drive Systems in Vehicles With Special Consideration of Power Semiconductor Modules*, 2021. ISBN 978-3-948749-01-9.

MAFO-83 Gerlach, A.: *Regelung von direktangetriebenen elektrischen Maschinen für Verbrennungsmotoren*, 2021. ISBN 978-3-948749-03-3.